

Simplification is essential

The new European research commissioner deserves political support from member states of the European Union to drastically reduce the dead weight of Brussels bureaucracy.

The head of a major research institute who categorically refused to allow any of his staff to apply for European Commission research funding. The science grandee who stood down from an advisory council in disgust at the paperwork. The highly regarded bright young scientist who was successfully awarded a grant but never took it up because others spotted his potential before the Euro-paperwork could be completed.

These are just a few examples of accumulated bad will and lost opportunities from decades of the Brussels experience. The principle of pan-European research collaboration, policy and infrastructures is laudable. The practice is dreadful.

In the wake of a 1999 corruption scandal involving the then research commissioner Edith Cresson, the European Court of Auditors demanded an increase in the already strict level of financial control across European Union (EU) programmes. New EU financial guidelines were introduced in 2004, requiring the sort of detailed accounting that leaves no room for corruption. As a consequence, every cent in a research project has to be justified and accounted for both before and after it has been spent.

Current examples of that burden are all too easy to find. Following the discovery of a small number of accounting errors, the European Commission has instigated a mammoth re-audit of hundreds of completed projects — for example, the CNRS, the French research agency, is now having to audit about 900. This effort is out of all proportion to the amounts of money in question. Or consider the large projects in the current Framework research-funding programme. These require immense amounts of pre-auditing, leading to applications more than 100 pages long.

But it is when the applications succeed that the bureaucratic floodgates really open. The documentation provided in the approved project application must be updated at the end of each year, with explanations of why estimates of individual person-months may have slipped, why plans for costed new instruments might need to be changed and why exactly various deliverables have been delayed,

or modified or transferred between partners. The following year's money will not be released until this documentation is submitted and approved — a process that can take weeks.

The fear of criticism from the Court of Auditors is a miasma that envelops the commission, and in turn greatly undermines the motivation of the researchers it seeks to engage. Many scientific officers in Brussels are sympathetic and have managed to introduce some slight improvements, but their hands are tied. Moreover, others adopt a much more precautionary and burdensome interpretation.

The plain fact is that this rules- and process-based approach, appropriate enough for projects whose outcomes can be specified, is misguided in respect of research, whose outcomes are uncertain by definition. Risks that an investment might return less than hoped come with this territory, and need to be embraced as part of a funding culture by those ultimately responsible for the Brussels machine: its political overseers in the European Parliament and the council of ministers.

Here is an opportunity for the new research commissioner, Máire Geoghegan-Quinn, to take the initiative. The commission has already made high-level overtures to the European Parliament that point in the right direction. The Court of Auditors is sympathetic to 'simplification', and so too are elements in the European Parliament, where the committees responsible for budget and for research are influential.

The council of ministers will be another key element in building the political momentum for change. These EU member-state ministers need to fully appreciate that the burdens of bureaucracy are sufficient to constitute a real threat to the future of the commission's programmes. The new research commissioner is (by her own account) an energetic politician who also brings experience as a member of the Council of Auditors. She is on a steep learning curve. But if she can catalyse the political change in attitudes required, and embody them in risk-tolerant financial guidelines, she will have achieved something more visible and significant than most of her predecessors. Any country whose researchers and administrations see value in these research programmes should support her. ■

Bridges, not barriers

Industry talent should be welcomed into academia, not seen as a corrupting influence.

The recent announcement that William Chin, a top executive at the pharmaceutical giant Eli Lilly, is to become executive dean for research at Harvard Medical School, has drawn criticism. Chin, a Harvard-trained physician and researcher, spent 25 years at the Boston medical school and its affiliated hospitals before moving to Eli Lilly 11 years ago. There, he has risen to become head of drug

discovery and clinical research. By moving back, the critics charge, he has passed through a 'revolving door' between academia and industry that taints the academic enterprise. As proof, they point to some academic researchers' failure to disclose their industry income.

Such lapses have damaged the image of the biomedical enterprise, and taxpayers' trust in it. They justify close scrutiny of links between academia and industry. But the critics are misguided. They have conflated the very existence of industry-academia collaborations with failure to disclose those links.

Transparency is vital, and the National Institutes of Health (NIH) is preparing, appropriately, to tighten disclosure regulations for its extramural investigators collaborating with industry. But the

view that any and all cooperation between industry and academics is inherently suspect has created a poisonous atmosphere that has driven some young investigators to take up other careers. So charged have things become that Robert Califf, vice-chancellor for clinical research at Duke University Medical Center in Durham, North Carolina, last week told a conference at NIH headquarters in Bethesda, Maryland, about a recent meeting where the leaders of major academic medical centres were afraid to sit in the same room with industry leaders — with the goal of enhancing understanding and cooperation — for fear of an outcry either in Congress or the media.

Yet such meetings, and appointments such as Chin's, are not only appropriate, but essential for strengthening university research and for bridging the gap between lab and clinic — a gap that has bred a justifiable public impatience for cures at the advent of the 'century of biology'.

Chin has both a physician's appreciation of illness and an enviable scientific pedigree; the chairs of the medical school's basic-science departments endorsed his hiring unanimously. He has always sought

to connect laboratory discoveries to human disease. Just as importantly, he has run a huge drug-discovery enterprise, giving him the kind of management experience and insights into discovery and translation that can be got only in industry. This will particularly inform his efforts to guide the medical school's scientific interactions with industry, in the drive to meet critical medical needs.

Reject such people and the academy cuts off its nose to spite its face. Instead, it should take advantage of them, as the University of California, San Francisco (UCSF), did last year in naming Susan Desmond-Hellmann, previously president of product development at biotech company Genentech, as its chancellor. Last week, six months after she took the helm, UCSF announced a collaboration with Genentech aimed at generating small-molecule drug candidates, a step that has proven a major obstacle in drug discovery.

The notion, pushed implicitly by critics, that academia can and should remain a pristine bubble, untainted and uninformed by those with industry experience, reflects a failure to understand that industry-academia cooperation is essential if we are to speed the medical progress that everyone seeks. ■

An absurd law

Turkey's government is about to pass legislation that could cripple the country's biological research.

When politicians respond to popular distrust of genetically modified organisms (GMOs), they sometimes fail to grasp how intricately molecular technologies infiltrate different areas of science. A case in point is now playing out in Turkey, where an attempt to regulate GMOs in agriculture has morphed into a draft law that could wipe out the country's biomedical research.

Most of Turkey's scientists learnt about the situation only a few weeks ago. Some responded immediately, organizing meetings and petitions, and lobbying parliamentarians to try to stage a last-minute reprieve. But as *Nature* goes to press, it seems likely that the law will be voted in by parliament this week without change. Ironically, it will go through at a time when many universities in Turkey are expanding their activities in biomedical research.

The law was first drafted after Turkey signed up to the United Nations Environmental Programme's International Cartagena Protocol on Biosafety in 2000. This requires signatories to create legislation to regulate the international trade, handling and use of any GMO that might have adverse effects on biodiversity or human health.

Turkey was at the same time trying to align much of its legislation with that of the European Union, which it aspires to join. The first draft was prepared with input from Turkey's research council, TÜBİTAK, and followed European regulations that separate deliberate release of GMOs into the environment — cultivation of GM crops, for example — and the contained use of GMOs for research.

Before this draft could be made law, the government changed and the mildly Islamic AK Party took office in 2002. Responsibility for the law transferred from the environment ministry to the agriculture ministry, which did not consult with molecular biologists. Over the years,

the draft law's form changed. At the same time, popular opposition to genetic engineering in general, and GM food in particular, increased.

The version now being voted on fails to distinguish between deliberate release and contained use. It includes an outright ban on the cultivation of all GM crops, even those whose safety has been assessed and approved by expert bodies. It also bans the generation of genetically manipulated animals and microorganisms.

The law does not forbid research using GMOs or products derived from genetic engineering, but it makes such research impracticable. Every individual procedure would have to be approved by an inter-ministerial committee headed by the agriculture ministry, which is allowed 90 days to consider each application with the help of experts.

The committee would be responsible for approving applications to import tonnes of GM soya beans for food — but also for every experiment involving even the use of a standard plasmid to transfer genes into cells. Work with universally used model organisms, from mice and zebrafish to fruitflies and bacteria, would be rendered impossible. Even if scientists could afford to wait three months for approval of the simplest experiment, the committee would be overwhelmed by the number of applications. One Turkish scientist who has examined the law estimates that his lab alone would need to submit 50 or so separate applications in a year.

It is disappointing that so important a draft law should have got so far without full consultation with all the communities affected by it. It is also disappointing that TÜBİTAK, which is close to the government but should nevertheless defend scientific interests, has so far remained silent on the issue. The Turkish Academy of Sciences is planning to prepare a position paper, but it is moving too slowly.

Turkish scientists can only hope that their individual lobbying activities will influence the vote at the last minute. Officials insist that the law will not affect research but they misunderstand. The impact will be profound. The government, which almost certainly does not wish to harm its country's fragile research base, must open its eyes to the drastic consequences of this legislation. ■

RESEARCH HIGHLIGHTS

Carbon from the mountains

Environ. Sci. Technol. doi:10.1021/es903301j (2010)

The greenhouse-gas emissions of conventional coal-fired power plants are up to 17% higher when emissions relating to mountain-top coal-mining operations are factored in, research suggests.

The Southern Appalachian Mountains in the United States are the source of almost one-quarter of the country's coal. Using published data on factors such as forest and soil carbon, James Fox of the University of Kentucky in Lexington and Elliott Campbell at the University of California, Merced, calculated the carbon emitted when companies cut down trees and sheer off mountain tops to access coal.

The authors show that land disturbance increases emissions by 2–12%, depending on the practice. Those figures increase to 7–17% if emissions produced during coal extraction and transport are included.



L. STONE/CORBIS

NEUROSCIENCE

Baby blues

J. Neurosci. 30, 2571–2581 (2010)

Stress or trauma in very early life can lead to anxiety and depression in adulthood, and previous evidence has implicated corticotrophin-releasing hormone (CRH) as a contributor to this outcome.

Louis Muglia of Vanderbilt University in Nashville, Tennessee, and his colleagues have narrowed down CRH's involvement using mice in which they could control expression of the hormone in the forebrain. When the researchers raised CRH levels during the first 21 days after birth, the mice went on to show anxious and despairing behaviours as adults. These behaviours could be normalized with antidepressants.

The mice could serve as a model to help find a means of preventing long-term consequences of childhood stress.

atoms is easiest in atoms that have only a few electrons whirling around. But cooling dysprosium, which has many electrons, was thought to be near impossible. However, with the aid of a powerful blue laser, Mingwu Lu and his colleagues at the University of Illinois at Urbana-Champaign cooled half a billion dysprosium atoms to below 3 millikelvin, bringing them close to a standstill.

The authors suggest that, cooled a little further, dysprosium could spontaneously form new phases of quantum matter akin to the patterns seen in liquid crystals.

MOLECULAR IMAGING

Tumour glows out

Proc. Natl Acad. Sci. USA doi:10.1073/pnas.0910261107 (2010)

In cancer surgery, taking out every last bit of a tumour improves a patient's prognosis. By targeting glowing proteins to cancer cells and illuminating them with magnetic resonance and fluorescence imaging, researchers have succeeded in completely removing tumours in mice, increasing survival rates.

Roger Tsien and his team at the University of California, San Diego, injected tumour-bearing mice with a fluorescently tagged cell-penetrating peptide linked to a neutralizing peptide. Enzymes common in tumours

cleaved the two peptides, releasing the tagged one and allowing it to infiltrate tumour cells (pictured far left). After cutting out the tumour (large arrow, left), the team was able to spot the remaining cancer cells (small arrow).

On average, the enhanced

visibility allowed the researchers to remove 90% more residual cancer cells than when they didn't use the marker. Tumour-free survival rates increased by 50–500%, depending on the cancer type.

EVOLUTIONARY BIOLOGY

On the invasion front

Proc. R. Soc. B doi:10.1098/rspb.2009.2231 (2010)

The geographical spread of invasive, non-native species may be limited by how they adapt over climate gradients. To investigate, Robert Colautti of the University of Toronto in Canada and his co-workers combined mathematical modelling with field surveys and greenhouse experiments on purple loosestrife (*Lythrum salicaria*). This invasive wetland plant — native to Europe — is common in eastern North America, where its range is rapidly expanding. This allowed the researchers to see how changing conditions affect the plant's evolution.

The authors' model and experiments showed that plants that had adapted to more northern climates, where the growing season is shorter, had done so at a cost: they flowered earlier, but were smaller and produced fewer seeds. The authors suggest this constrained adaptation may ultimately limit the northern spread of this invasive plant.

CELL BIOLOGY

Lost in the mail

J. Cell Biol. doi:10.1083/jcb.200911115 (2010)

Many proteins carry signal sequences — segments that act like shipping labels, directing the protein to specific structures in the cell. Ramanujan Hegde at the National

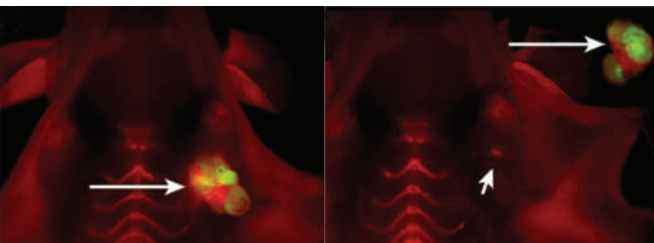
PARTICLE PHYSICS

Dazzling dysprosium

Phys. Rev. Lett. 104, 063001 (2010)

Physicists have trapped the first ultracold gas of dysprosium, prized for being one of the most magnetic atoms in the periodic table.

Using lasers and magnets to cool and trap



NATLACAD.SCI.

Institute of Child Health and Human Development in Bethesda, Maryland, and his colleagues looked at the efficiency of the signal sequence on the mammalian prion protein (PrP), which can cause neurodegenerative disease when misfolded or mutated.

They found that roughly 10% of PrP made by cells is misdirected, which is consistent with previous work. The authors engineered disease-causing versions of mutant PrP with signal sequences that more efficiently guide the protein to its destination. Mice producing the modified proteins were protected against neurodegeneration.

The work highlights a potential contributory factor to prion diseases.

ORGANIC CHEMISTRY

Catalysts cooperate

Science **327**, 986–990 (2010)

The products of chemical reactions often have different spatial arrangements, or stereoisomers, of which only one is useful (as a drug, for example). As a result, many chemists are focused on controlling such reactions to select only the desired product.

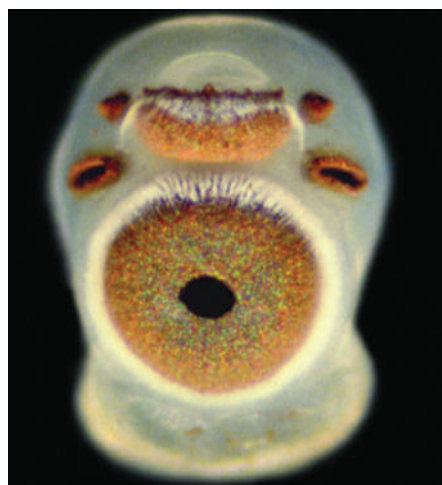
Eric Jacobsen and his colleagues at Harvard University in Cambridge, Massachusetts, have developed one such strategy involving two cooperating catalysts. They first use an acid catalyst to transform a molecule's nitrogen-based imide group into a reactive iminium ion. A second catalyst then cradles this ion through a network of weak intermolecular attractions — much like the way that biological enzymes position their substrates. This ensures that one reaction orientation is favoured, meaning that only one stereoisomer is formed. The reaction is 5–10 times slower than its one-catalyst variant, but highly selective.

BIOLOGY

Colour-blind

Proc. R. Soc. B doi:10.1098/rspb.2009.2248 (2010)
Box jellyfish (Cubomedusae) have a complex system of 24 eyes that comprises pits, slits and two types of lens (a set of six eyes is pictured below). But whether they can perceive colour has been a matter of debate.

Now, Megan O'Connor of Lund University in Sweden and her colleagues have identified the visual pigment present in the lens eyes of the *Chiropsella bronzie* jellyfish. Using microspectrophotometry and antibodies for zebrafish visual pigments, they found just one type of pigment. For colour vision, two or more are necessary.



GENETICS

Male regulator switched

PLoS Genet. **6**, e1000844 (2010)

'Jumping genes', or transposable elements, are tracts of DNA that can move around in the genome and are thought to offer potential for rapid rewiring of gene-regulatory networks.

Researchers have found evidence of this in medaka fish (*Oryzias latipes*).

About 10 million years ago in an ancestor of the medaka fish, a gene called *dmrt1a* — which occurs downstream in a sex-determination cascade — duplicated. One copy, *dmrt1bY*, later became a master 'maleness' regulator at the top of the cascade. To figure out how this happened, Amaury Herpin of the University of Würzburg in Germany and his colleagues analysed the regulatory region of *dmrt1bY*.

They found that a mobile piece of DNA had inserted into this region shortly after the gene duplication. Both the *Dmrt1a* and *Dmrt1bY* proteins bind to this transposable element to reduce expression of the *dmrt1bY* gene. This suggests that insertion of the mobile DNA rewired this gene network.

DEVELOPMENTAL BIOLOGY

Heads or tails

Dev. Biol. **339**, 188–199 (2010)

Non-parasitic flatworms called planarians readily regenerate damaged body parts by choreographing a large adult stem-cell population. Michael Levin at Tufts University in Medford, Massachusetts, and his colleagues have identified physiological signals that control regeneration in these creatures.

The researchers inhibited these signals with chemicals that block communication between cells. The worms then regenerated heads in abnormal positions, continuing to do so even after the new heads were amputated. The team suggests that the signals enable planarians to determine a wound's location and orientation, and decide which structure to regenerate.

Understanding the mechanisms that guide stem cells in forming complex tissues in three dimensions is key to unlocking the full potential of regenerative medicine.

JOURNAL CLUB

Luke Harmon
University of Idaho, Moscow

An evolutionary biologist ponders the pace of evolution.

Studies of evolution 'in action' in creatures such as sticklebacks, lizards and mice have taught us that evolution can proceed rapidly. Given this lightening-quick tempo, why are there so few species on Earth, and why are they so similar to each other?

One possible answer comes from long-term studies of

Galapagos finches. During drought years, when small seeds — the birds' preferred food — were scarce, the birds evolved larger beaks to help crack open bigger seeds. However, these changes were reversed during wet years, when smaller seeds again became prevalent. This sort of reversal can occur repeatedly, implying that much of the evolutionary change we observe over short timescales is only temporary.

A study of patterns of natural selection over time suggests that such evolutionary reversals might explain the slower pace of

evolution over longer timescales. Adam Siepielski of Dartmouth College in Hanover, New Hampshire, and his colleagues used published reports to gather more than 5,500 estimates of the strength and direction of natural selection in the wild (A. M. Siepielski *et al. Ecol. Lett.* **12**, 1261–1276; 2009). By focusing on studies in which selection was measured more than once, the authors were able to see for the first time that aspects of selection change rapidly in direction, strength and form from generation to generation.

This new perspective, if correct,

has profound implications. First, we should not be surprised to observe rapid evolution in natural settings, even over human lifetimes. At the same time, we should not expect evolutionary change that can be measured in real time to be permanent. More synthetic studies — combining observations of evolution in action with historical data — are needed to better understand the relationship between evolution in 'real time' and evolution in 'deep time'.

Discuss this paper at <http://blogs.nature.com/nature/journalclub>

NEWS BRIEFING

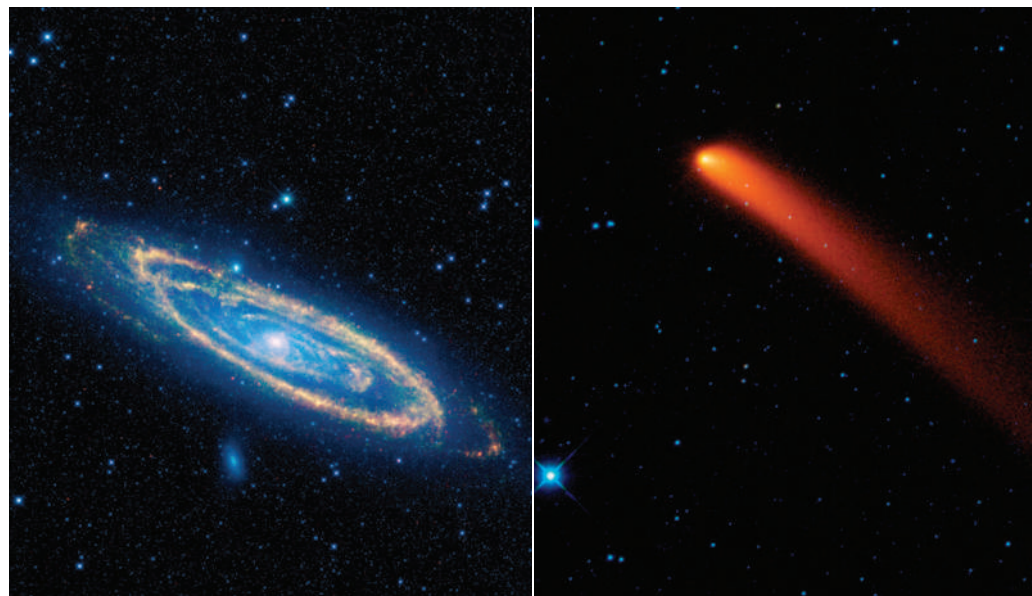
● POLICY

Stem-cell lines: The US National Institutes of Health (NIH) is considering extending the definition of human embryonic stem-cell lines eligible for federal funding, to include those from earlier-stage embryos than currently allowed. Pre-blastocyst embryos might become eligible under a revised rule proposed on 19 February. It is a “trivial, small change of the wording that could have enormous scientific benefit”, says Susan Fisher, a stem-cell biologist at the University of California, San Francisco, who recently submitted ten lines derived from pre-blastocyst embryos to the NIH. See go.nature.com/vmucio for more.

Avandia risks: Drug-maker GlaxoSmithKline (GSK) was aware of cardiac risks associated with its diabetes drug Avandia (rosiglitazone) years before they became public but sought to minimize the findings, said the US Senate finance committee in a report released last week. Two senators also challenged Margaret Hamburg, the commissioner of the US Food and Drug Administration (FDA), to justify an ongoing trial that compares Avandia with a competing drug.

The finance committee released documents from the FDA — where an advisory committee voted in 2007 to keep Avandia on the market — in which two FDA safety experts called the trial “unethical and exploitative”. GSK says that the Senate report cherry-picked information and mischaracterized its efforts to research and communicate the risks of Avandia.

Biomedical priorities: The Wellcome Trust, Britain's biggest charitable funder of biomedical research, has for the first time explicitly set out five priority areas it wants to fund, in a ten-year strategic plan announced on 22 February. The “research challenges” where funding will be focused include studies into chronic diseases and the effects



NASA/JPL-CALTECH/UCLA

WISE DELIVERS INFRARED WISDOM

NASA's Wide-field Infrared Survey Explorer (WISE) has offered up the first pictures since its 14 December launch, including these colour-altered images of the comet Siding Spring (right) and the Andromeda galaxy. WISE will mainly seek the cool glow of asteroids and brown dwarfs, almost-stars that aren't quite massive enough to ignite. Whereas the infrared Spitzer Space Telescope honed in on specific objects, WISE, with its huge field of view, will take an infrared census. It should complete 1.5 sweeps of the sky before its cryogenics run out around October.

of ageing on cell function, and the interplay between the environment, nutrition and health. In 2008–09 the trust spent a total of £720 million (US\$1.1 billion) on research.

● BUSINESS

Ethanol merger: The large Brazilian ethanol producer ETH Bioenergia announced on 18 February that it would take over the debt-ridden Brazilian Renewable Energy Company (Brenco) to create a world-leading company to make ethanol from biomass. The combined firm aims to produce 3 billion litres of ethanol annually by 2012, ETH stated, by which time the companies will have invested 3.5 billion reais (US\$2 billion) on top of existing investments of 3.8 billion reais. The move follows Shell's 2 February announcement of its joint venture with another big Brazilian ethanol firm, Cosan (see *Nature*, 463, 592; 2010).

SOUND BITES

“Being able to do science live from space every day of the week is going to be spectacular.”

Jeff Greason, president of XCOR Aerospace, based in Mojave, California, gets excited by the promise of cheap spaceflight, at a space-research conference in Boulder, Colorado, last week. See go.nature.com/AjykOj for more on the conference.

Nuclear guarantees: The US Department of Energy on 16 February issued an US\$8.3-billion loan guarantee for a pair of nuclear power plants in Georgia, potentially clearing the way for the first new commercial reactors to be granted permits in more than three decades. The federal support would cover debt in case of loan default, allowing a consortium led by Southern Company, based in Atlanta, Georgia, to secure lower-interest commercial loans from skittish Wall Street banks. The Obama administration hopes to issue loan guarantees for seven to ten plants country-wide, to build confidence in the industry.

● RESEARCH

Mission choices: Out of 52 initial proposals and a shortlist of 6, on 18 February the European Space Agency selected three medium-sized missions to continue development within its ‘Cosmic Vision 2015–2025’

programme, with an eye towards launching two of them in 2017–18. Cost-capped at €450 million (US\$610 million) each, the missions are: Euclid, to measure dark energy and dark matter; Planetary Transits and Oscillations of stars (PLATO), to detect extrasolar planets when they pass in front of their stars; and Solar Orbiter, which would sidle up to within 62 solar radii of the Sun. A decision on the two winners is expected in mid-2011.

Pebble-bed dashed: The company developing South Africa's pebble-bed nuclear reactor said on 18 February that it is contemplating shedding three-quarters of its 800-strong staff after losing government funding. See page 1007 for more.

CryoSat delay: The European Space Agency has postponed the planned 25 February launch of its satellite for monitoring variations in the extent and thickness of polar ice. The agency says that the Russian launch rocket that will carry CryoSat-2 into its required orbit did not have enough spare fuel in its second-stage engine. The delay could be around a month.

PEOPLE

NIH change: Raynard Kington, deputy director of the US National Institutes of Health (NIH), will leave the biomedical agency in late July to become president of Grinnell College in Iowa, NIH director Francis Collins announced on 17 February. Kington, a physician with a doctorate in health

NUMBER CRUNCH

523
Number of authors on two 2001 papers announcing the draft sequence of the human genome.

1,968
Number of authors on 2010 paper of initial results from the Compact Muon Solenoid detector at the Large Hadron Collider.

policy and economics, became a key administrator at the NIH over the past decade. As acting director before Collins took the helm last August, he oversaw the allocation of US\$10.4 billion in economic stimulus funds and the development of new guidelines for funding of human embryonic stem-cell research.

Research president: Austrian social scientist Helga Nowotny has been elected president of the European Research Council

(ERC), which funds cutting-edge research in Europe. Currently vice-president, Nowotny is based in Vienna and is an emeritus professor at the Swiss Federal Institute of Technology in Zurich. She will take up the position on 1 March, replacing the ERC's founding president, Fotis Kafatos, who resigned last month (see *Nature*, 463, 407; 2010).



Climate chief resigns: Yvo de Boer (pictured), executive secretary of the United Nations Framework Convention on Climate Change, unexpectedly announced his resignation on 18 February after almost four years leading climate negotiations. "I believe the time is ripe for me to take on a new challenge," he said, telling Associated Press that the failure of the climate talks in Copenhagen last year was not a factor in his decision to quit. De Boer leaves his post on 1 July, and will join consultancy group KPMG, where he will advise on climate and sustainability.

Anthrax case closed: Federal authorities in the United States announced on 19 February the conclusion of their investigation into the 2001 anthrax attacks, which killed five people. They determined that biodefence researcher Bruce Ivins was the

THE WEEK AHEAD

26 FEBRUARY

The World Health Organization reviews its Framework Convention on Tobacco Control, on the fifth anniversary of the treaty's entry into force.

go.nature.com/RMwxlo

1-5 MARCH

The 41st Lunar and Planetary Science Conference takes place at the Woodlands, Texas. Special sessions focus on recent findings from lunar orbiters LCROSS, Chandrayaan-1 and Chang'e-1.

go.nature.com/Qlbpzz

3-5 MARCH

The International Emissions Trading Association joins with various United Nations agencies to host the second Africa Carbon Forum in Nairobi, Kenya. The meeting aims to boost low-carbon projects in Africa under the Kyoto Protocol's Clean Development Mechanism.

go.nature.com/Nz7bZt

sole perpetrator; he committed suicide in July 2008, before indictment. A National Academy of Sciences panel commissioned last year is still reviewing the scientific evidence used in the case, such as analysis tracing mailed *Bacillus anthracis* spores back to a single-spore batch in Ivins's lab at the US Army Medical Research Institute of Infectious Diseases in Fort Detrick, Maryland.

BUSINESS WATCH

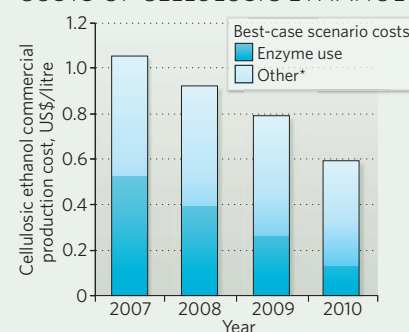
Enzymes that convert woodchips, maize leaves and stalks, and municipal waste to sugars are getting cheaper. At a national US ethanol conference in Orlando, Florida, last week, biotech companies Novozymes and Genencor launched new generations of enzymes that they claim will cut the enzyme-related production costs of cellulosic ethanol to less than US\$0.13 a litre.

Poul Ruben Andersen, global marketing director at Novozymes, based in Bagsværd, Denmark, says that a few years ago enzymes accounted for more than half the cost of cellulosic ethanol production, but now only contribute a quarter (see chart). "Enzyme costs are not the number-one concern any

more," agrees Aaron Kelley, a senior engineer at Genencor, based in California, which is a subsidiary of Danisco, headquartered in Copenhagen, Denmark.

Despite the economic downturn, cellulosic ethanol companies such as Poet, in Sioux Falls, South Dakota, are expecting to start commercial production in late 2011 or early 2012 at a total cost of under \$0.53 per litre — roughly on a par with that of 'corn' ethanol produced from sugar-rich maize cobs. Lower enzyme costs are already factored in to these projections, notes Kelley, but their progress — though expected — may bring confidence to wary investors.

COSTS OF CELLULOSIC ETHANOL



*Projected, includes feedstock, labour, plant build

SOURCE: NOVOZYMES

NEWS

'Seek, test and treat' slows HIV

Studies in several nations show that treating people before they fall ill can curb the spread of disease.

Treating HIV infection aggressively before symptoms appear could help to control the spread of the disease, according to data presented at a retroviral conference last week. Independent studies in Canada, the United States and Africa support the strategy in both the developed and developing world. However, the studies are not definitive and some scientists argue that improperly expanding treatment could cause problems.

Evidence in favour of 'treatment as prevention' has been building for more than a decade. Treating pregnant women who are HIV-positive, for instance, decreases disease transmission to their babies by lowering virus levels in the mother¹. Modellers with the World Health Organization last year predicted that HIV could be almost eliminated within 50 years by finding and treating every HIV-infected person immediately — rather than waiting for the disease to advance to the point at which treatment is recommended by current guidelines².

At the annual Conference on Retroviruses and Opportunistic Infections in San Francisco, California, on 16–19 February, Deborah Donnell of the Fred Hutchinson Cancer Research Center in Seattle, Washington, bolstered the 'seek, test and treat' strategy with data from a study of 3,408 couples from seven African nations in which only one partner had HIV. During the study, HIV-positive individuals who were receiving treatment almost never passed the virus on to their partner, whereas many untreated individuals did.

In another study, Moupali Das of the San Francisco Department of Public Health reported that as 'community viral load' — the amount of virus in the blood of all HIV-infected individuals tested in San Francisco — declined from 2005 to 2008 because of drug treatment and increased awareness, the number of new infections in the city also dropped. Julio Montaner, director of the British Columbia Centre for Excellence in HIV/AIDS, described similar results last year for a study of intravenous drug users in Vancouver³.

At the conference, he reported that when treatment was expanded to intravenous drug users with HIV throughout British Columbia, new HIV diagnoses in that group dropped by around 50%.

"The fact that more treatment would curb



Testing whole populations for HIV and treating those infected may slow the spread of the disease.

the epidemic is clear at a population level, and we would like to see the seek, test and treat strategy endorsed throughout the developed and developing world," Montaner says.

However, these studies do not prove that treatment itself caused the declines in new infections because there were many confounding factors beyond the investigators' control. And other data presented at the meeting introduced a cautionary note about the strategy.

Sally Blower of the University of California, Los Angeles, argued that scarce resources in developing countries would be better spent reaching the more than 9 million people who already need treatment and are not getting it. And she reported on model results suggesting that if therapies were offered to almost everyone in South Africa who needed them, drug-resistant strains could surge until they comprised up to 20% of circulating HIV strains.

Yet in Montaner's study, drug resistance actually dropped across the province when treatment was extended to all intravenous drug users.

Clinical trials of the seek, test and treat

strategy will begin this year in New York and Washington DC, and others are planned by French and British agencies. A randomized trial already under way in nine countries is testing whether early treatment leads to durable prevention of transmission within couples. That study will not report results for several years.

Even if the most optimistic models are not correct, more aggressive efforts to expand treatment to everyone will probably dent the spread of the epidemic, says Anthony Fauci, director of the US National Institute of Allergy and Infectious Diseases in Bethesda, Maryland.

"Rather than saying it's an all-or-nothing phenomenon — that we're going to eliminate the epidemic without anything else but test and treat — what I argue for is, why don't we let test and treat be part of a more aggressive prevention armamentarium," Fauci says. "I would be satisfied with the epidemic if not disappearing, then at least declining, and I see seek, test and treat as one of several tools in the tool kit that will get us there."

Erika Check Hayden

1. De Cock, K. M. *et al.* *J. Am. Med. Assoc.* **283**, 1175–1182 (2000).
2. Granich, R. M. *et al.* *Lancet* **373**, 48–57 (2009).
3. Wood, E. *et al.* *Br. Med. J.* **338**, b1649 (2009).

P.-A. PETTERSSON/GETTY



'JUNK' DNA HOLDS CLUES TO HEART DISEASE

Deleting non-coding region narrows arteries in mice.
go.nature.com/g89ldj

P. LECKO/ISTOCKPHOTO

Reserves 'win-win' for fish and fishermen

SAN DIEGO, CALIFORNIA

Although fisherman routinely fight bans on fishing, studies indicate that the creation of protected marine reserves in key areas can both raise the profits of fishermen and boost fish populations. Researchers presented evidence of these dual benefits in several sessions over the past week at the annual meeting of the American Association for the Advancement of Science (AAAS) in San Diego, and in a suite of papers published in the *Proceedings of the National Academy of Sciences*.

Marine reserves could help to make nearby fisheries profitable by acting as nurseries for fish larvae that are later spread by ocean currents, for example. "Reserves allow a win-win situation — better conservation and higher profitability for fishing," says Christopher Costello, a resource economist at the University of California, Santa Barbara (UCSB). His group's modelling study of southern Californian waters suggests that fishing profits are maximized when significant areas are closed to fishing¹.

Steven Gaines, a UCSB marine ecologist who organized an AAAS symposium on marine reserves, adds that his own team's research with ocean circulation models shows that protected areas do not need to be extensive. Strategic positioning of smaller reserves in a network can create pathways

for fish outside protected zones, which can boost the yields of fishermen.

Research on one of the world's largest marine conservation efforts, along Australia's Great Barrier Reef, shows how quickly such efforts can make a difference. Nearly one-third of the 2,000-kilometre-long reef off Queensland is set aside as 'no-take' zones, after stringent controls were put in place in 2004.

Terry Hughes, director of the Australian Research Council's Centre of Excellence for Coral Reef Studies in Townsville, Queensland, said at the symposium that his team's reef research² found that, in the no-take zones he studied, overall fish densities have doubled since they were created. On some reefs, the population of certain species, such as grouper, doubled within just two years of fishing closures. "The reef generates far more economic benefit to Australia than the cost of protecting it," he adds, estimating that the costs are less than 1% of annual revenue generated from other reef activities, such as tourism.

The experience of the Great Barrier Reef could inform an ongoing debate in California. The state is involved in a contentious process to create networks of reserves that could eventually encompass 10–20% of the state's coastline and stretch up to 5 kilometres from shore.

The Marine Life Protection Act was approved by Californian voters in 1999, but attempts to establish the reserves it mandated have been delayed by strong resistance. The battle between marine conservationists and fishermen has become so bitter that armed game wardens now attend public hearings about the plan. Fist fights have broken out at some meetings and, at one, Paul Dayton, a marine biologist at the Scripps Institution of Oceanography in La Jolla, was spat at by a fisherman.

A reserve system has so far been adopted for two regions along the central coast; a plan for a southern coastal region is under review; and plans are to be developed for the final two areas by the end of 2011.

Many complain that the scheme is too costly, and argue that there is little evidence that reserves successfully protect marine wildlife. But marine biologist Jennifer Caselle at the UCSB and her colleagues have put paid to this claim³.

Her team studied ten no-take and two fishing-restricted zones created in 2003 within the 100-kilometre-long Channel Islands National Marine Sanctuary off Santa Barbara. The scientists found that the number and size of the fish targeted for protection was greater in the reserve than outside. They also found that the ecosystem was healthier overall, with more predators such as spiny lobster and California sheephead helping to keep sea urchins under control. Because the urchins graze on kelp — an important habitat for many fish species — Caselle says that "the increased abundance of predators may help to prevent the transition of productive kelp forests into unproductive urchin barrens".

The research was greeted cautiously by Norman de Vall, president of Redwood Coast Watersheds Alliance in Elk, California, where reserve planning is now under way. Even if reserves produce larvae that move into unprotected areas, that may not be enough to help fishermen, says de Vall, a former commercial fisherman. What is needed, he said, is smarter management of fishing stocks overall and "less fishing everywhere".

Rex Dalton

1. Costello, C. et al. *Proc. Natl Acad. Sci. USA* doi:10.1073/pnas.0908057107 (2010).
2. McCook, L. J. et al. *Proc. Natl Acad. Sci. USA* doi:10.1073/pnas.0909335107 (2010).
3. Hamilton, S. L., Caselle, J. E., Malone, D. P. & Carr, M. H. *Proc. Natl Acad. Sci. USA* doi:10.1073/pnas.0908091107 (2010).



R. SCHWEMMER, CINIMS, NOAA

The diverse ecosystem of California's Monterey Bay is the focus of a National Marine Sanctuary.

Did design flaws doom the LHC?

Catastrophic failure that caused accelerator shutdown was not a freak accident, says project physicist.

Running more than a year behind schedule and at half its intended energy, the world's most powerful particle accelerator is slated to begin its first full scientific run this week. Along with relief, the occasion is bringing some soul-searching. One senior scientist who helped to build the Large Hadron Collider (LHC) at CERN, Europe's particle-physics laboratory near Geneva, Switzerland, is claiming that the cause of the delay — a major accident in 2008 — could have been avoided.

"Any technical fault is a human fault," says Lucio Rossi, a physicist who oversaw the production of the accelerator's superconducting magnets. In a paper published on 22 February (*L. Rossi Supercond. Sci. Technol.* 23, 034001; 2010), he concludes that the catastrophic failure of a splice between two magnets was not a freak accident but the result of poor design and lack of quality assurance and diagnostics. The project, he says, will be coping with the consequences for many months to come.

On 19 September 2008, just weeks before the LHC was first scheduled to start colliding protons, an electrical short caused massive damage. A connection between two superconducting

cables developed a small amount of resistance, which warmed the connection until the cables — cooled by liquid helium to superconducting temperatures — lost their ability to carry current. Thousands of amps arced through the machine, blowing a hole in its side and releasing several tonnes of liquid helium. The expanding helium gas created havoc, spewing soot into the machine's ultraclean beamline and ripping magnets from their stands. Repairs took more than a year, and the LHC successfully restarted last November.

An investigation revealed that technicians had not properly soldered the cables together. With tens of thousands of such connections, it is perhaps inevitable that some were faulty, Rossi says, but design flaws worsened the problem. The silver–tin solder that was used melted at high temperatures and did not flow easily into the cable joints. Moreover, workers did not adequately check to see if each connection was electrically secure. Sensors to detect an overheating circuit, which might have helped prevent the accident, were not installed until after it happened.

Worse, says Rossi, when the wires were

originally joined, the same silver–tin solder was used to connect them to an adjacent copper stabilizer, meant to provide an escape route for current in the event of a failure. That step risked reheating and destroying the original connection, he says. Making the second connection to the stabilizer with a different type of solder that had a lower melting point could have avoided the problem. Lyn Evans, who oversaw the LHC from 1994 to 2009, says that the idea was considered and rejected because the alternative solder contained lead, a hazard to workers.

A detailed analysis last summer revealed several more bad connections, and CERN now says that it will take a year to correct the problem throughout the machine. As a result, the LHC will not run at its full collision energy of 14 tera-electronvolts (10^{12} eV) until around 2013.

Many LHC scientists involved say that the accident was a natural consequence of constructing such a large and unique machine. "I personally think he [Rossi] is a bit too harsh on himself and the management of the time," says Steve Myers, the current project head of the LHC. "In such a technically complicated project with tight schedules it is almost inevitable that things go wrong."

"What we have to do is learn from our mistakes and make it better."

Pebble-bed nuclear reactor gets pulled

Hopes for the development of pebble-bed nuclear reactor technology, long held up as a safer alternative to conventional nuclear power, have suffered a blow. Last week, the South African government confirmed that it will effectively stop funding a long-term project to develop the technology.

The development company, Pebble Bed Modular Reactor (PBMR), based near Pretoria, says that it is now considering axing three-quarters of its 800 staff, about half of whom are scientists or engineers. "The resources available to the company will not sustain the current cost structure," the company says. The cuts could trigger an exodus of nuclear expertise from South Africa, although some argue that government funding has kept the project going for too long in the

face of growing problems.

South Africa started to develop its pebble-bed reactor design in the mid-1990s, hoping that it would deliver cheap electricity and open up a lucrative export industry. It licensed the technology from Germany's Jülich Research Centre, which abandoned a working prototype reactor in 1991 after citing poor business opportunities.

Eskom, South Africa's main electricity generator, based in Johannesburg, set up the PBMR in 1999 to develop the technology into an economically viable reactor. "It caught the mood in South Africa, and the feeling among South Africans was that their technology was as good as anybody's," says Steve Thomas, an energy-policy researcher at the University of Greenwich, London. "This was their



Bedtime for pebbles?

chance to show the world what they could do."

The proposed reactor would have used enriched uranium fuel embedded within tennis-ball-sized graphite spheres ('pebbles'). These should enable it to run at temperatures of between 750 °C and 1,600 °C yet resist a core

meltdown even if the helium-gas coolant is lost, an attractive safety feature.

But several of the firm's biggest investors, including the utility firm Exelon in Chicago, Illinois, withdrew during the feasibility phase, which ended in 2004. In the four years up to March 2007, the South African government contributed 7.2 billion rands (US\$935 million) in funding, on the condition that the PBMR "attract additional investment through investors other than government, and that it secure a customer for its product", according to a government statement. However, despite a revised business model and product offering, the firm has been unable to do either of these, the government says. Funding was last week slashed to 11 million rands over the next three years,

PEBBLE-BED MODULAR REACTOR (PTV)



DINOSAUR BREAKS THE MOULD

Fish-eating spinosaurs not restricted to land.

go.nature.com/xKFewR

M. SIMONETTI

German paper chase to end

Sometimes less is more — at least in grant proposals. That's the hope of the DFG, Germany's main research-funding agency, which plans to drastically restrict the number of papers that researchers can list in their grant applications.

From July, someone applying for a year's funding will be able to include only two publications closely related to the proposed project and a maximum of five other papers illustrating their scientific career. The agency hopes that the new rules will help ease the burden on reviewers faced with vast publication lists, and counter the pressure on scientists to publish as many papers as possible in order to win funding or academic appointments. "It is quality, not quantity, which matters," says Matthias Kleiner, president of the DFG.

But some fear that the new rules might deprive reviewers of crucial information, particularly in fields with high publication rates, such as molecular biology. "As a reviewer I am reliant on getting all the information," says Benedikt Grothe, dean of biology at Ludwig Maximilian University in Munich. "And as an applicant I find it dissatisfying not to be able to cite all the papers that I think reviewers should be aware of."

The DFG — which controls an annual budget of more than €2 billion (US\$2.7 billion) and funded about half of its 23,000 grant applications last year — is the first funding agency in Europe to cap citations in this way. In the United States, similar rules apply to grants from the National Science Foundation (NSF). But the DFG's plan goes a step further: it will not consider supporting papers that have been submitted to academic journals but not yet accepted for publication. The move aims to counter problems with seemingly impressive publication lists that were brought to light last year when members of a DFG-funded Collaborative Research Centre (SFB) at the University of Göttingen were reprimanded for including unfinished manuscripts in grant applications (see *Nature* 460, 791; 2009).

Quirin Schiermeier



It took months to repair magnets that were damaged in a major accident to the LHC in September 2008.

But Jim Strait, a physicist at Fermilab in Batavia, Illinois, says that Rossi's analysis is fundamentally right. The connections between the LHC's magnets aren't robust enough, Strait says. "The design looks like one that is optimized to make installation easy," he says. "These stupid little corners [of the design] get short shrift because they are boring." Only constant project

reviews and more-integrated management can catch such problems, he says.

Rossi says that he doesn't blame any one person for what happened at the LHC. "In Italian we say, '*Chi non fa, non sbaglia*': 'He who doesn't work makes no mistakes'. What we have to do is learn from our mistakes and make it better." ■

Geoff Brumfiel

which is "not enough to keep a nuclear design and engineering company going", according to the PBMR.

Runaway costs and technical problems helped to doom the project, says Thomas. "In 1998, they were saying that they would have the demo plant online in 2003" at a cost of 2 billion rands, he says. "The final estimate was that the demo plant would be online in 2018 and it would cost 30 billion rands." Furthermore, he adds, the PBMR has never been held to account for why costs rose every year, why the completion date was continually pushed back or the nature of its design problems.

In a final twist, the PBMR announced last year that it was indefinitely shelving plans to build a demonstration plant. The programme's demise will not help South Africa's goal of doubling its 35,000-megawatt power-generating capacity by 2025.

One problem was that the design became too ambitious, says John Walmsley, past president of the South African branch of the Nuclear Institute, a professional society for nuclear engineers. The PBMR hoped to push

"This was South Africa's chance to show the world what it could do."

the reactor's operating temperature as high as possible to enable not just electricity generation, but also 'process heat' applications such as turning coal into liquid fuels, he says. It also aimed to boost the power output to the very limits of the design to make the reactor more economical. "They tried to build a BMW when they maybe should have started with a Morris Minor," he says.

Although many scientists had hoped that the safety system of the pebble-bed design would win over opponents of nuclear power, a 2008 report from the Jülich Research Centre cast doubt on those claims, suggesting that core temperatures could rise even higher than the safe threshold.

Tsinghua University in Beijing now hosts the only operational prototype pebble-bed reactor, although similar reactors are being developed in the United States and the Netherlands. But the PBMR's problems are not unique, says Thomas. "Every nuclear nation in the world has had a programme to commercialize this type of reactor, and they all got nowhere."

Linda Nordling



THE FINAL FRONTIER BECKONS

Cheap spaceflight set to transform science.

go.nature.com/AjykoJ

XCOR AEROSPACE

Cosmic-ray theory unravels

Astrophysicists ponder whether ultrahigh-energy particles really do come from the centre of galaxies.

High-energy cosmic rays pack a punch: their particles hold some 10 million times more energy than can be produced by accelerators on Earth. Astronomers had thought that they were getting close to understanding the origins and composition of these intense particles. Now it seems they must think again.

Data collected three years ago by a team at the Pierre Auger Observatory in Mendoza, Argentina, suggested a tentative alignment between these incoming particles and active galactic nuclei (AGN). This hinted that the supermassive black holes in the AGN might be the long-sought cosmic particle accelerators that give the rays their huge energies (The Pierre Auger Collaboration *Science* **318**, 938–943; 2007).

The apparent connection with black holes electrified the astrophysics community. “We thought a new astronomy had been born: charged particle astronomy,” says Charles Dermer, a cosmic-ray astrophysicist at the US Naval Research Laboratory in Washington DC.

But at a meeting of the American Physical Society in Washington DC on 16 February, the Auger team began to backpedal on its original conclusions. The group revealed new data that weaken the link between the high-energy particles and the AGN.

Compounding the mystery, the team has found evidence that these highest-energy cosmic rays might be iron nuclei, rather than the protons that make up most cosmic rays. “There are some puzzles,” says Paul Sommers, co-spokesperson for the Auger collaboration at Pennsylvania State University in University Park. “We’re not close to writing the final chapter.”

Low-energy cosmic rays, made mostly of protons, strike Earth continually. They originate within the Milky Way but are seen coming from all directions in the sky because magnetic fields in the Galaxy bend their paths and obscure their original sources. Higher-energy cosmic rays from outside the Galaxy are much less frequent, but are potentially more valuable as astronomical tracers because they barrel into the Galaxy on straighter paths.

The most extreme of them hit the planet with enormous energies of 1×10^{20} electronvolts (eV; by comparison, protons produced by the Large Hadron Collider will top out at 7×10^{12} eV). These high-energy particles could provide a way to detect new physics



The black hole at the centre of the galaxy Centaurus A is just one potential source of cosmic rays.

beyond the standard model of subatomic particles and the forces that control them. When high-energy particles strike the upper atmosphere, they create ‘air showers’ of billions of particles and a faint flash of light that, on moonless nights, can be seen at places such as the Auger Observatory, a 3,000-square-kilometre array of detectors on the dry plains of Patagonia.

But gleaning clues about these cosmic rays is difficult because of their rarity; on average, fewer than one particle per century strikes a square kilometre of ground. Over the years, astronomers have considered a handful of possible origins besides the AGN for these rarest of rays. Some suspect the exploding stars that create γ -ray bursts, and Dermer says that it is possible that even small black holes and neutron stars could ramp the particles up to the necessary energies.

The latest results from the Auger scientists put all of these potential origins back in the game. Although the 2007 paper was based on just 13 of the highest energy cosmic rays, Sommers says that the team is preparing a new analysis for publication that is based on 44 more events. Fewer than 40% of these cosmic rays seemed to be coming from the AGN, a much weaker correlation than previously reported. The rays are not randomly distributed but follow the distribution of matter visible in the Universe.

The strangest aspect of the latest results relates to the particles’ composition. As the team reports

in a paper accepted for publication in *Physical Review Letters* (The Pierre Auger Collaboration, preprint at <http://arxiv.org/abs/1002.0699>; 2010), they are seeing small air showers that are indicative of iron nuclei, rather than the larger showers that point to protons. Ultrahigh-energy cosmic rays made of iron nuclei would be harder to explain because such nuclei are less common than protons and are more likely to be broken down by the violent mechanisms thought to accelerate cosmic rays.

Complicating the picture further is the fact that a rival experiment in the Northern Hemisphere — the older and smaller High Resolution Fly’s Eye (HiRes) experiment in Utah — has produced contradictory data. Spokesman Pierre Sokolsky of the University of Utah in Salt Lake City says that his team’s results, based on just ten cosmic rays, suggest that they are protons and come from a random distribution in the sky. The analysis is under review at *Astrophysical Journal Letters*.

Sokolsky points out that the cosmic-ray flux at HiRes could just be different from that seen in Argentina. Earth’s Northern Hemisphere (and therefore HiRes) generally faces away from the centre of the Milky Way, so the magnetic fields in that direction could differ. By contrast, several prominent and nearby potential sources of cosmic rays, such as the AGN of the galaxy Centaurus A, are visible from the Southern Hemisphere. “Nature is throwing us a few curve balls, it looks like,” says Sokolsky. ■

Eric Hand

“It looks like nature is throwing us a few curve balls.”

NASA/CXC/CFA/R. KRAFT ET AL.; MPIPR/ESO/APEX/A. WEISS ET AL.; ESO/WFI



THE CLIMATE MACHINE

A new generation of sophisticated Earth models is gearing up for its first major test. But added complexity may lead to greater uncertainty about the future climate, finds **Olive Heffernan**.

The government building in the south of England looks open and airy with its three-storey glass facade. But security measures such as guards stationed at the front serve as a reminder that this Ministry of Defence property is carrying out sensitive work important to the nation's future. Deep in the building's basement, two adjoining rooms house 27 big black boxes that churn through a million lines of computer code every hour to gaze into the future of Earth and its 7 billion inhabitants.

This massive supercomputer at the UK Met Office in Exeter is home to what is possibly the world's most sophisticated climate model. Developed by researchers at the Hadley Centre, the Met Office's climate-change branch, the newly finished model will be put to its first big test over the coming months. It will run a series of climate simulations out to the year 2100 for the next report of the Intergovernmental Panel on Climate Change (IPCC), on the physical-science basis of climate change, which is due out in 2013.

Four years in the making, the model is known as HadGEM2-ES, short for the Hadley Centre Global Environmental Model, version two, with an added Earth-system component. It is one of a dozen Earth-system models under development worldwide that reach far beyond their distant

forebears, which represented just the physical elements of the climate, such as air, sunlight and water. The new generation includes all that and much more: forests that can shrink or spread as conditions change; marine food webs that react as the oceans grow more acidic with carbon dioxide; aerosol particles in the atmosphere that interact with greenhouse gases, enhancing or sapping their warming power.

The Hadley Centre is at the forefront of efforts around the world to develop such complex climate models. "It's really pushing the envelope", says Andrew Weaver, a climate modeller at the University of Victoria in British Columbia, Canada.

Researchers hope that the added complexity will lead to more realistic predictions and help them to derive new insights about how elements of the climate interact with each other. But it is a bit of a gamble whether this monumental effort will actually help political leaders and researchers to plan for the future. Because models are simulating more components and each one is subject to variation, the extra complexity could make error bars expand greatly in forecasts of how temperatures or precipitation will change with time. "It's very likely that the generation of models that will be assessed for the next IPCC report will have a wider spread of possible climate outcomes as we move into

the future," says Jim Hurrell, who is heading development of the Earth-system model at the National Center for Atmospheric Research (NCAR) in Boulder, Colorado.

At its core, HadGEM2-ES is much like any climate model. It is a series of equations describing atmospheric circulation and thermodynamics, solved for a number of points that form a three-dimensional grid over the surface of Earth.

The grid for HadGEM2-ES has 192 evenly spaced points running east-west and 144 points in the north-south direction. Each box represents an area of roughly one degree latitude by two degrees longitude, which is about 100 kilometres by 200 kilometres at the equator. The atmosphere has 38 unequally divided levels, about 20 metres deep near the land and ocean surface but getting progressively thicker with height.

From slime to leaf

As with all modern global climate models, HadGEM2-ES couples the atmospheric model with an ocean model. In the 1980s and early 1990s, the oceans in the earliest of the Hadley coupled models were called swamps and were little more than large, shallow puddles connecting continents. They gradually evolved into 'slab oceans', which were rigid but could

MET OFFICE

absorb and release heat (see 'Model evolution'). The global ocean in HadGEM2-ES, by contrast, flows with currents and eddies. Its 40 layers reach down to 5,000 metres, with the top layer measuring just 10 metres thick, an important advance that allows models to simulate more realistically how the ocean takes up and retains carbon dioxide at different depths.

Amid the stark white walls and uniform desks of the Hadley Centre, researchers are wrestling with how to mimic the clouds and currents, trees and tundra and the myriad other aspects of the planet that can amplify or diminish global warming. Yet the only signs of the work that is done here are the lines of computer code scrolling across the computer monitors.

The coding that makes up HadGEM2-ES includes several other components of the Earth-system, such as a closed carbon cycle, which in theory can account for all of the carbon on Earth that might affect climate over the next few centuries. The model does this with detailed atmospheric chemistry, dynamic vegetation that can grow and die depending on the climate, and ocean biological and geochemical systems that can respond independently to changing greenhouse-gas levels.

On land, vegetation is split into nine categories from shrubs to needle-leaf trees — a major advance in how models represent the biosphere. The first attempts to include biology in a climate model gave rise to the 'green scum' model, which treated all of life as a uniform green layer from equator to pole. HadGEM1, the immediate forerunner of HadGEM2-ES, included the same types of vegetation as HadGEM2-ES but as a static layer. Now, the vegetation types can shift, and foliage can change with the seasonal cycle.

Merging these aspects together in a single model slows it considerably. Simulating one month takes an hour of computing time. "That's the price you pay," says Chris Jones, a carbon-cycle specialist who has been instrumental in developing HadGEM2-ES. HadGEM1 runs three times faster than the newer model.

Even with the fine resolution of HadGEM2-ES, there are climatically important processes that are simply too small for the model to simulate directly, such as clouds. To get around this, climate modellers use a technique called parameterization. Rather than trying to simulate individual clouds within a grid box, for example, the generalized effect of clouds on climate is represented by a series of equations that describe the conditions under which

clouds form and decay, and how they absorb or reflect radiation. These are then averaged for each grid box.

Parameterizations are a necessary evil that can introduce error into models. Perhaps more bothersome, though, are the random errors. Just one incorrectly entered bit of data can send the whole system haywire. So too can an imperfect representation of a seemingly simple aspect of the real world, as Hadley Centre scientists discovered when they put too little plant life in the world's arid regions, leaving insufficient vegetation to hold the soil in place. Soon, dust levels in the model atmosphere surged out of control, reaching three times higher than average, which in turn fertilized the ocean, causing phytoplankton to flourish.

Identifying culprits

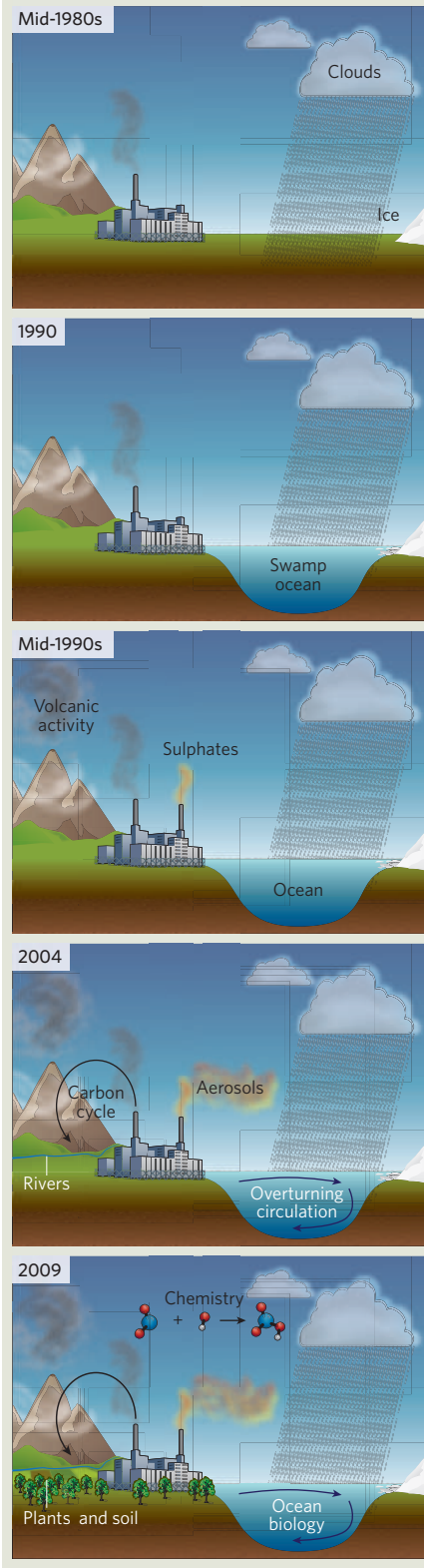
Model developers are only too familiar with the effects of errors. "That's not only common, that's the evolution that all of us go through," says Hurrell. To identify these quirks, each model goes through a rigorous testing phase. This involves putting the model through a series of 'control runs' in which its skill is tested by simulating a stable climate. The model is also commonly 'hindcast' to determine its ability to match historical changes. That's what HadGEM2-ES is currently doing and will finish up next month.

"Sometimes, you can get completely unrealistic results," says Jones. When the results don't correlate with reality, modellers use their knowledge of the climate system to try to identify the likely culprits within the model and then correct them. And occasionally what starts as a problem can lead to insights. The unrealistic dust storms in HadGEM2-ES, for example, revealed that even a small amount of plant life in the world's deserts can influence the whole climate.

The testing phase usually gets the model to a point at which it can simulate past and current climate well, but often certain aspects continue to cause problems. In fact, every model has a weak spot. When the Hadley Centre scientists developed HadGEM1, the model had difficulty simulating the El Niño Southern Oscillation, a phenomenon that drives much of the climate variability across the Pacific Ocean. "This led many to harp on that the Hadley Centre had lost its footing at the lead of the pack," says Bill Collins, the scientist responsible for the HadGEM2-ES model development. But the model used by NCAR scientists had an equally bad problem with El Niño. And Ronald Stouffer, a climate researcher at the Geophysical Fluid

MODEL EVOLUTION

Over the years, the Hadley Centre has improved its climate models by adding various oceanic and atmospheric components.



SOURCE: MET OFFICE/IPCC

"Once in a while you have to stop and think if this complexity is really warranted in light of our ignorance."

Dynamics Laboratory (GFDL) in Princeton, New Jersey, says the GFDL model was “the worst in the world” for simulating North Pacific sea ice in the last IPCC assessment.

But when it came to reproducing past and current climates on a global scale, these models were on top of their game. “That’s one of the joys of this business,” Stouffer says with a laugh. “You can make your model better overall but at any one point it might be worse.” Whether or not HadGEM2-ES has a blind spot should become apparent after running the simulations for the IPCC over the next few months.

Whatever flaws there are in HadGEM2-ES may be compensated for by its peers — the other Earth-system models that will be running simulations for the IPCC forecasts. These models hail from the research groups at the GFDL, NCAR and from centres in Australia, Canada, China, France, Germany, Japan and Norway. “It is important that there’s a good diversity of models,” says Weaver, because, when it comes to ways of modelling, “there’s no one right answer”. The advantage of having numerous groups developing models simultaneously is that they each approach the task differently.

Other institutes have not put as much work into their Earth-system models as the Hadley Centre, so most of them are not relying entirely on the new models. “Every one of these simulations is a challenge and we don’t know until the last moment whether everything will work out as we would like,” says Christian Reick, who is leading vegetation modelling for the Max Planck Institute for Meteorology in Hamburg, Germany. Many groups will run a hierarchy of simpler models as a way of hedging their bets. If the Earth-system models produce forecasts of, say, temperature change that have an unreasonably large uncertainty range, the teams can fall back on more familiar models for a simpler evaluation of what the future holds. That concern has led some to call for

The range of future climates

In its 2007 report, the Intergovernmental Panel on Climate Change (IPCC) issued a range of projections of what might happen to the climate under various scenarios. Some assumed that human population and consumption would grow quickly, whereas others envisioned the emergence of clean technologies or slower rates of development. But the panel did not examine deliberate efforts to rein in emissions of greenhouse gases.

For the next IPCC assessment of the physical-basis of climate change, due out in 2013, models will simulate emission-controlling scenarios called representative concentration pathways (RCP). Each RCP

is named after the level of radiative forcing, or overall warming power of human activities, expected in 2100. The current radiative forcing from past emissions is about 1.6 watts per square metre and the net concentration of greenhouse gases is more than 400 parts per million in terms of carbon dioxide equivalents. The new scenarios are:

RCP8.5 Emissions rise indefinitely, radiative forcing reaches 8.5 W m^{-2} and concentrations of all anthropogenic greenhouse gases reach at least 1,370 p.p.m. in CO_2 equivalents by the end of the century.

RCP6.0 Emissions level off

and radiative forcing reaches about 6 W m^{-2} sometime after 2100, with greenhouse-gas concentrations stabilizing at about 850 p.p.m. in CO_2 equivalents sometime after 2100.

RCP4.5 Emissions level off earlier and radiative forcing reaches roughly 4.5 W m^{-2} . Atmospheric greenhouse-gas concentrations stabilize at around 650 p.p.m. in CO_2 equivalents sometime after 2100.

RCP3.0-PD Radiative forcing peaks at about 3 W m^{-2} then declines; atmospheric greenhouse-gas concentrations reach around 490 p.p.m. in CO_2 equivalents and then decline. **O.H.**

caution in increasing the complexity of models. “Once in a while you have to stop and think if this complexity is really warranted in light of our ignorance,” says Syukuro Manabe, one of the founders of modern climate models and a researcher at the GFDL. “You don’t want to oversimplify,” says Manabe, adding that the key is to look at whether “the detail in the model is balanced with our knowledge of the process”.

Practical constraints

Although the new models are better from an academic perspective, they do not necessarily produce results that are more useful for policy-makers wrestling with how to plan for the future. Jones acknowledges that models are “only useful if we understand them to the point where we have confidence in them”. But, he says, “we’re going into a future that we can’t constrain with observations, and climate models are the only tool we have for making projections”.

During the report-writing process, the IPCC authors will analyse all the model projections to develop their best estimates for the climate of the future. The estimates will include how quickly temperatures will rise, where rainfall will increase or decrease and how vegetation patterns will shift.

But even as they run through the IPCC simulations with the current crop of models (see ‘The range of future climates’), Jones and his peers are thinking about how to improve them by adding more components. “We’re keen that we don’t stand still,” he says. One addition

they hope to make is the thawing of permafrost in the Arctic tundra that could accelerate warming by releasing methane, a potent greenhouse gas. HadGEM2-ES has factored in methane release from wetlands, but doesn’t account for permafrost. Also in the pipeline for the Hadley Centre’s next model is the nitrogen cycle and how it influences plant growth.

But the point of all of this “is not to develop a perfect model”, says Hurrell. “We develop new representations of aspects of the system based on our best understanding of the system, and when we are confident that we can represent that process well, we include it in the model.”

For climatologists, models are not just tools that can give a glimpse of what the future holds; they are also an experimental playground — a replica world on which they can test their knowledge of the climate system. Without the ability to conduct global-scale experiments in the lab or in the field, models are the only tool they have.

At the Hadley Centre, some staff joke that modellers will eventually try to include panda bears in their simulations. The bit of hyperbole no doubt riles some of the modellers, perhaps because they are only too keenly aware that their creations can never fully represent the real thing. “Part of our intellectual challenge is to find out what’s important to include,” says Jones. “There’ll always be some level of detail or complexity that we can’t get in there.”

Olive Heffernan is the editor of *Nature Reports Climate Change*.



The UK Met Office is home to the world’s most sophisticated climate model.

CORRESPONDENCE

Research thrives on integration of natural and social sciences

Emerging collaborations between social and natural scientists face challenges, as you acknowledge (*Nature* **462**, 825–826, 2009). But, like A. D. Manning and J. Fischer in Correspondence (*Nature* **463**, 425; 2010), you sidestep a practical question that keeps many laboratory doors closed: what if interactions with ‘soft’ scientists harm the quality of my ‘hard’ research?

The Center for Nanotechnology in Society at Arizona State University (ASU) has collaborated with natural scientists since 2005. It also hosts the Socio-Technical Integration Research project (<http://cns.asu.edu/stir>), which embeds social scientists in 20 labs across ten nations on three continents — represented by three authors of this letter, plus the project’s coordinator. Social researchers learn the theory and observe the methods of their laboratory counterparts, but they also introduce a protocol that unpacks social and ethical dimensions of the lab science itself in a real-time, hands-on, collaborative manner. The social scientists, their methods and enquiries become embedded in the laboratory during each 12-week engagement study.

We find that such integrative activities can trigger changes in laboratory practices — expanding the values and questions considered, and the alternatives that are perceived as viable. For example, reflections on responsible innovation generated novel ideas for antenna structures and nanoparticle synthesis for researchers at ASU’s Center for Single Molecule Biophysics. Such developments often advance research and sometimes advance deliberation on public values. For laboratory scientists, thinking and talking about the broader dimensions of their work in an integrated way need not entail a sacrifice in productivity.

Rather, efforts to enhance scientific creativity and societal responsiveness can be mutually reinforcing.

Erik Fisher School of Politics and Global Studies, Arizona State University, PO Box 873902, Tempe, Arizona 85287-390, USA

e-mail: efisher1@asu.edu

Simon Biggs School of Process, Environmental and Materials Engineering, University of Leeds, UK
Stuart Lindsay The Biodesign Institute, Arizona State University, USA
Jie Zhao School of Materials Science and Engineering, Dalian University of Technology, China

Rigid animal-rights views not useful to ethics debate

Fern Wickson calls for animal-rights activists to be formally consulted on university animal-research programmes (*Nature* **463**, 293; 2010). The UK practice of including lay members of the public on university animal-ethics committees might be a sounder strategy.

It is true that more productive dialogue ought to exist between scientists and protesters. But for the most vocal and militant activists, no compromise is acceptable. Their adherence to the cause is almost religious. Such rigid views are unlikely to add usefully to the discussion.

Rob Campbell Cold Spring Harbor Laboratory, Beckman Building, 1 Bungtown Road, Cold Spring Harbor, New York 11724, USA
e-mail: campbell@cshl.edu

New NMR machines are set to boost biomedical potential

You made some excessively pessimistic assessments in your News Feature about the arrival of the first 1-gigahertz high-resolution nuclear magnetic resonance (NMR) spectrometer at the European Centre for High

Field NMR, and its reception by the biological NMR community (*Nature* **463**, 605–606; 2010).

To predict potential benefits from this advance, we should remember NMR’s earlier contributions to biology and medicine, and not just focus on it as a structural tool.

By revealing the extent and timescale of conformational fluctuations in proteins, NMR enabled conformational selection to supplant induced fit as a paradigm for biomolecular recognition. Powerful approaches to drug discovery have been launched by protein NMR’s ability to pinpoint site-specific interactions very rapidly.

Far from evidence of donor fatigue, there are signs in the United States that federal support for ultra-high-field NMR is growing. As recently as 2007, only about a quarter of such instruments were purchased primarily with federal support. A rise in the cost limit for requests for high-end instrumentation from the US National Science Foundation and National Institutes of Health major-instrumentation programmes extends the reach of such requests to beyond 800-megahertz NMR machines.

Higher magnetic fields will soon be revealing biomedical insights we can scarcely imagine today.
Jeffrey C. Hoch Gregory P. Mullen NMR Structural Biology Facility, University of Connecticut Health Center, Farmington, Connecticut 06030, USA
e-mail: hoch@uchc.edu

Skewed assessment values have stifled textbook-writing

I welcome your Editorial encouraging career recognition for writers of science books (*Nature* **463**, 588; 2010). But nothing will change for British scientists unless books are properly valued within the new Research Excellence Framework, which assesses

the quality of research in UK higher-education institutions.

Under the previous system, the Research Assessment Exercise, a 400-page peer-reviewed science textbook was allocated the same value as a single journal article. It made no difference if the book was cited hundreds of times and well-reviewed in academic journals. I must declare an interest: I wrote such a book (*Pheromones and Animal Behaviour* Cambridge Univ. Press, 2003). Concerns about the chilling effects on textbook-writing by British academics have been highlighted before, to no avail (see, for example, go.nature.com/nmq3Vq).

The scientists finalizing the new rules have the power to change the criteria and give textbook-writing more recognition. I hope they will.

Tristram D. Wyatt Department of Zoology, University of Oxford, South Parks Road, Oxford OX1 3PS, UK
e-mail: tristram.wyatt@zoo.ox.ac.uk

Futures perfect — food for thought and welcome light relief

Please do not listen to the likes of Denis Alexander (*Nature* **463**, 425; 2010). Futures provides welcome light relief from the serious stuff preceding it, sometimes offering food for thought and — in the case quoted — such high comedy as to provoke what is colloquially known as a belly laugh, which I never dreamed I would experience in the company of your illustrious journal.

Robin Thompson Little Bookham Common, Surrey KT23 3HY, UK
e-mail: bookham@msn.com

Contributions may be submitted to correspondence@nature.com. Please see go.nature.com/cMCHno. Published contributions are edited. Comments and debate are also welcomed at our blog *Nautilus* (<http://blogs.nature.com/nautilus>).

OPINION

Globe still in grip of addiction

After five years, the World Health Organization's tobacco-control treaty is starting to have an effect, but we need to tackle the smoking epidemic in the developing world, say **Jonathan M. Samet** and **Heather L. Wipfli**.

At first glance, the past five years look like something of a triumph for anti-smoking campaigners, at least in the West. Legislation banning smoking in workplaces, bars and restaurants has helped to reduce tobacco use in many high-income countries. In Britain in 2008 just 22% of men smoked¹, compared with 65% in 1948 (ref. 2). Furthermore, the rates of some major tobacco-related diseases are falling. In the United States, for example, the death rate from lung cancer in men has fallen by about 2% per year from 1993 and is no longer increasing in women³, and in the United Kingdom, the number of men diagnosed with lung cancer has dropped by more than 45% from the peak in the late 1970s⁴.

Dig a little deeper, however, and the picture looks far from rosy. Decades after research first showed that active and passive smoking cause premature death, the world is still in the midst of an epidemic of tobacco-related illness. About 6 million people die each year because of tobacco, mainly from cancer, heart disease, stroke and chronic obstructive pulmonary disease, and without a rapid change in the epidemic's course this figure is estimated to rise to 8.3 million by 2030 (ref. 5). The substantial decline in smoking in the West has not happened elsewhere (see map): 1.2 billion people worldwide — about 40% of men and 10% of women — are smokers⁶. Tobacco remains a very common addiction among men in many low- and middle-income countries, although much less so among women. In fact, the proportions of cigarette production and consumption taking place in developing countries are rising by just under 1% a year⁷.

Clearly, more needs to be done to tackle the tobacco epidemic, especially in the developing world. One of the most formidable obstacles to progress is the tobacco industry. Some transnational tobacco groups continue to challenge the scientific evidence that links passive smoking to death and disease in non-smokers, and to use their immense financial resources to influence the political process, through lobbying, for example, and to challenge tobacco-control legislation in court. British American Tobacco (BAT) — the second largest transnational tobacco firm — has pushed to dilute legislation to keep public



places smoke-free⁸: in Argentina, the company is challenging the constitutionality of restricting smoking in enclosed public places⁹. In China, BAT's own documents show that the company had a strategy to divert attention away from the dangers of passive smoking¹⁰.

Captive markets

Tobacco companies are still making huge profits and are likely to continue doing so for the foreseeable future. Developing countries — particularly China, India and Indonesia, where about half of the world's male smokers reside⁶ — offer huge markets, with hundreds of millions of men already addicted to nicotine, and the prospect of many female customers. In China, where the majority of men but only a small percentage of women smoke¹¹, the largest multinational tobacco firm Philip Morris has entered into a joint agreement with government-owned China National Tobacco Corporation (CNTC) to market its Marlboro brand¹². Almost all the cigarettes in China are sold by the corporation.

Efforts to stamp out the global smoking epidemic have been under way for some time.

Five years ago this month, the World Health Organization's (WHO's) Framework Convention on Tobacco Control (FCTC) came into force. The 168 nations that have ratified it or its legal equivalent (that is, acceptance or approval) have committed themselves to a broad set of initiatives aimed at reducing tobacco's harmful effects. The treaty addresses issues such as advertising and promotion, price and taxes, labelling, protection against second-hand smoke, education and cessation, illicit trade and sales to minors, and sets deadlines for implementing measures to deal with them. In 2008, the process was reinforced by a package of six measures known as MPOWER, drawn up by the WHO to help countries cut demand for cigarettes. MPOWER focuses on improving monitoring, protecting people from second-hand smoke, offering smokers ways to stop, warning them of the dangers, enforcing bans on tobacco advertising and raising taxes.

The FCTC is a significant global campaign against the perils of tobacco. Even before it came into force, the process of negotiating it helped to foster a global network of researchers, campaigners and public-health and other governmental officials working on tobacco control. Funding has been forthcoming,

"The effort to control tobacco contains many lessons for those tackling other lifestyle-related epidemics."

too. The Bloomberg Family Foundation has pledged US\$375 million through its Initiative To Reduce Tobacco Use, which supports tobacco control in low- and middle-income countries and gives priority to high-burden countries including China, India, Indonesia, Russia and Bangladesh. The Bill & Melinda Gates Foundation has donated \$125 million, also aimed at control programmes in developing countries. As the first global public-health treaty, some hoped that the FCTC might also be a template for tackling other public-health challenges, such as obesity.

So how successful has it been? The news is mixed. Many places have now passed comprehensive smoke-free laws. A new survey of adults — the Global Adult Tobacco Survey, launched by the WHO and the US Centers for Disease Control and Prevention in Atlanta, Georgia, a few years ago — has greatly improved researchers' ability to track the epidemic. Little progress has been made, however, in raising prices and taxes, the most cost-effective way to reduce tobacco use. Taxes are at the recommended 75% of retail price for only 6.2% of the world's population. In China, cigarettes have become progressively more affordable since 1990 (ref. 13), and a recent tax increase did not affect prices because the CNTC held them steady¹⁴.

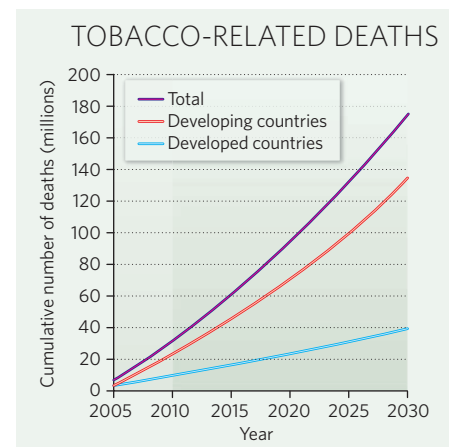
The FCTC is part of a global tobacco-control movement led competently by the WHO, yet this movement is not sustainable. Many countries depend on external funding, some governments remain reluctant to raise taxes and most governments are failing to take sufficient steps to persuade people to quit smoking. Only 8.2% of the world's population has access to a quit-smoking hot-line and free access to some form of cessation service and nicotine replacement

therapy¹³. Unless the rate of quitting is quickly increased worldwide, tobacco-control measures will have little immediate effect on death rates.

Five steps forward

To reduce global smoking and tobacco-related deaths worldwide, including stemming the power of the tobacco industry, we have the following five recommendations. First, nations should deliver on the low-cost but effective obligations laid out in the FCTC: to protect the public from exposure to second-hand smoke and to place larger, more-effective warnings on cigarette packets. Second, barriers that are hindering price and tax increases need to be quickly identified and overcome. The power to do this lies with finance ministries, many of which seem to be reluctant to accept the findings from global studies that taxes are an effective way to control tobacco use without reducing revenue. Third, governments need to put greater emphasis on helping people to stop smoking, using innovative, population-level approaches that will work in poorer areas, as well as more expensive clinical methods. Fourth, as deadlines pass for implementing FCTC measures over the next 5 years, government control programmes and tobacco-industry initiatives must be tracked. This should be done by the WHO through its annual reports, by the Conference of the Parties — the governing body for the treaty — through government reports, and by civil society through the Framework Convention Alliance. Finally, governments must take more responsibility for maintaining a tobacco-control programme that will last for decades.

The effort to control tobacco contains many lessons for those dealing with other lifestyle-related epidemics, in particular the use of



SOURCE: REF. 5

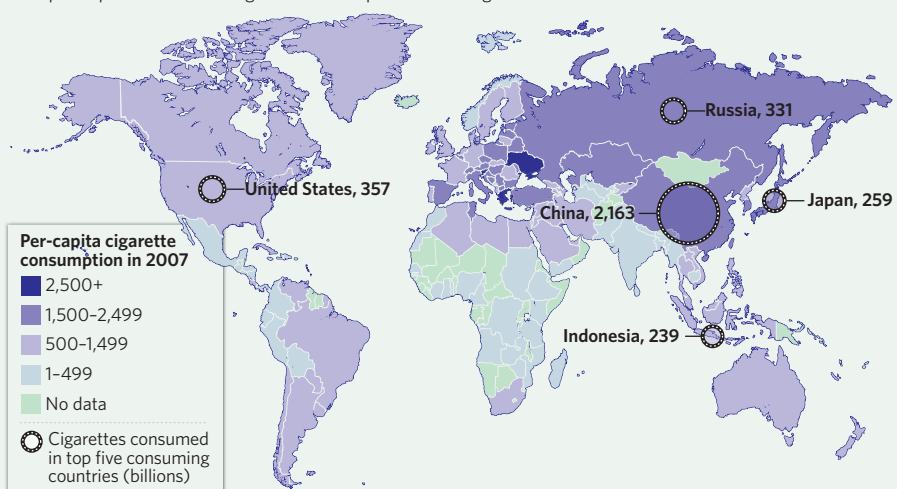
strategies such as product labelling, the economic costing of disease and the limiting of advertising and promotion. Health officials should also take heed of the tobacco industry's attempts to diminish the scientific base for action, to influence decision-makers, to interfere with policy-making and to target vulnerable populations, all tactics used by other multinational industries willing to sacrifice the public's health for their profit¹⁵. The extent to which the FCTC is a suitable model for other public-health treaties will become clear over its next five years.

Jonathan M. Samet and **Heather L. Wipfli** are at the University of Southern California, Keck School of Medicine, Department of Preventive Medicine and USC Institute for Global Health, Los Angeles, California 90033, USA.
e-mail: jsamet@usc.edu

- Robinson, S. & Bugler, C. *General Lifestyle Survey 2008* (UK Office for National Statistics, 2008).
- Wald, N. & Nicolaides-Bouman, A. *UK Smoking Statistics 2nd Edition* (Oxford Univ. Press, 1991).
- Centers for Disease Control and Prevention. Lung cancer trends (2009); available at go.nature.com/4PdC1V
- Cancer Research UK. *CancerStats Key Facts: Lung Cancer and Smoking Statistics* (2009); available at go.nature.com/2BBv4T
- Mathers, C. D. & Loncar, D. *PLoS Med.* **3**, e442 (2006).
- Shafey, O., Eriksen, M., Ross, H. & Mackay, J. *The Tobacco Atlas 3rd edn* (Am. Cancer Soc. 2009).
- WHO. *WHO Report on the Global Tobacco Epidemic, 2008 — The MPOWER package* (WHO, 2008).
- Corporate Accountability International. *Protecting Against Tobacco Industry Interference: The 2008 Global Tobacco Treaty Action Guide* (Corporate Accountability International, 2008).
- Noblez Piccardo S.A.I.C. y F. v. Provincia de Santa Fe Unconstitutionality claim 188/2006, Corte Suprema de Justicia de la Nación [Supreme Court] (Argentina).
- Muggli, M. E., Lee, K., Gan, Q., Ebbert, J. O. & Hurt, R. D. *PLoS Med.* **5**, 1729–1769 (2008).
- Yang, G. et al. *J. Am. Med. Assoc.* **282**, 1247–1253 (1999).
- Wright, A. A. & Katz, I. T. *N. Engl. J. Med.* **356**, 1493–1496 (2007).
- WHO. *WHO Report on the Global Tobacco Epidemic, 2009: Implementing Smoke-free Environments* (WHO, 2009).
- People's Daily Online. Expert: Tax hike has little effect on tobacco use (18 January 2010); available at go.nature.com/pu7ad5
- Michaels, D. *Doubt is their Product: How Industry's Assault on Science Threatens your Health* (Oxford Univ. Press, 2008).

A GLOBAL HABIT

Both per-capita and national cigarette consumption remain high.



SOURCE: THE TOBACCO ATLAS

BOOKS & ARTS

Theft or innovation?

A history of intellectual-property rights reveals how the pirating of ideas and goods has transformed science publishing, drug development and software, explains **Michael Gollin**.

Piracy: The Intellectual Property Wars from Gutenberg to Gates

by Adrian Johns

University of Chicago Press: 2010.

640 pp. \$35, £24

By allowing scientists, inventors and artists to assert property rights over their creative work, the intellectual-property system rewards the investment of time and money required to bring ideas to market. Piracy, or unauthorized copying, of creative works is usually seen as a simple violation of commercial rights, with pirates as thieves.

Historian Adrian Johns argues instead that piracy is a cultural force that has driven the development of intellectual-property law, politics and practices. As copying technologies have advanced, from the invention of printing in the sixteenth century to the present, acts of piracy have shaped endeavours from scientific publishing to pharmaceuticals and software.

Pirates duplicate an innovative idea, publication or thing, ignoring the objections of contemporaries who assert a dominant right. Arguments against piracy have changed little over the centuries: pirated books, machines, medicines and software are criticized as being dangerous or inferior to authentic ones; pirates destroy the social fabric of creativity by denying innovators their due compensation; pirates stand outside moral and legal norms. Industry giants attack companies who make cheap copies of drugs and software as pirates, and conservation organizations berate those who collect indigenous genetic material, particularly from the tropics, as biopirates.

But piracy has always had its supporters. Printers in revolutionary America saw their copying of British works as resisting an oppressive government, and some pirates today see themselves as patriots fighting foreign domination. Pirates champion the rights of private individuals against governments or monopolistic corporations — by making available unauthorized copies of movies, for example. Pirates claim to promote the flow of information in a free society, and to serve the poorer sectors of society with lower-priced drugs, hardware and software.

Johns suggests, counter-intuitively, that piracy can promote the development of technology. The resulting competition forces legitimate innovators to manoeuvre for



The cinchona plant was targeted for illicit export as it contains the antimalarial compound quinine.

advantage — by moving quickly, using technical countermeasures or banding together and promoting reputation as an indicator of quality, such as through trademarks. In the nineteenth century, US policy encouraged the free use of foreign technology to promote immigration and invention by talented craftspeople, scientists and engineers.

Today's debates about publishing genetic sequences in databases and the drive for open-access scientific journals have a history that is as old as printing. London's physicians joined together to publish the first national pharmacopoeia in 1618 as a way to avoid pirated drug formulations. Ironically, that book made it easier for others to copy the formulations in it, and the book itself was pirated. The evolution of peer-reviewed journals helped to distinguish authentic authors and inventors from the outsiders who copied their scientific works and instruments. But publication also aided copying, and the possibility of piracy became a rationale for introducing copyright and the patenting of scientific work to protect its commercial potential.

The exclusive rights granted by intellectual-property laws are always being reshaped by public opinion, and accused pirates have lobbied against these laws for centuries. The strongest form of their argument — that all property rights should be eliminated in publications, ideas and objects — has not prevailed, except

briefly during the French Revolution. Less radical ideas have been adopted into law, including the copyright defence of fair use and the compulsory licensing of patent rights on important inventions such as drugs. Governments have backed copyright-royalty tribunals to ensure distribution of music revenues to the copyright holders, and have instituted alternatives to privately funded innovation, such as state funding of research.

Piracy has led commerce to adopt countermeasures. Private, self-policing business associations were established as early as the seventeenth century, when booksellers formed their own registry of publications. In revolutionary America, printers such as Benjamin Franklin banded together, and today, international trade associations fight piracy for the recording, movie, pharmaceutical and agricultural industries.

Private associations can derive from piratical groups. Johns traces historical overlaps between pirate radio operators in the 1920s, ham radio operators of the 1960s, the 'phone phreakers' of the 1970s — who exchanged techniques for making free, long-distance phone calls — and the Homebrew computer club in the San Francisco Bay area of California, in which the sharing of ideas helped to incubate the personal computer. The open-source and open-access communities promote information sharing using sophisticated

BLICKWINKEL/ALAMY

practices that avoid the label of piracy and its legal consequences, which has helped them to become accepted in parts of the commercial and technological establishment.

Today's intellectual-property system is built on decisions made in the past. In revealing how piracy affected those decisions, Johns's history provides a valuable addition to the literature. However, the book does not deal with the future implications of piracy. Lacking a practical understanding of current intellectual-property law and practice, Johns is unable to draw lessons or make predictions or recommendations.

Piracy is an aspect of intellectual-property

dynamics that scientists, lawyers, policy-makers, business people and consumers should understand. When pirates gain the upper hand, innovators suffer and quality declines. But when exclusivity becomes too strong, society loses the benefits of access. A constant effort is required to balance the interests of innovators and copiers, and to nurture a healthy creative environment. ■

Michael Gollin is a law partner at Venable LLP in Washington DC and author of *Driving Innovation*. He chairs the group Public Interest Intellectual Property Advisors, whose forthcoming book is *Intellectual Property and Human Development*. e-mail: magollin@venable.com

of the central dogma — that information flows in one direction, from DNA to RNA to proteins — also dates from this period, along with the gradual realization that the structures and functions of molecules in cells are more complicated than he had earlier assumed.

Olby brilliantly follows Crick through these creative years. By highlighting the scientist's interactions with a growing group of others devoted to developing the field, he captures the excitement, false dawns and triumphs that followed the Watson–Crick model of DNA. Olby is fair to all of the early participants in DNA work: Linus Pauling, Maurice Wilkins and, above all, Rosalind Franklin and her collaborators at King's College London. Watson and Crick used Franklin's data, and benefited from a breakdown in relations between Franklin and Wilkins that interrupted Wilkins's work on the molecule. The full story emerged only after the Nobel prize was

awarded in 1962 to Watson, Crick and Wilkins; by then, Franklin had died, tragically young, of ovarian cancer. In 1952, both Franklin and Pauling were close to coming up with the structure themselves.

Issues of priority generate passion, but Olby's account can be recommended for its dispassionate analysis and mastery of archival sources.

Crick's long-time collaboration with Sydney Brenner, another scientific giant, is given its due. So, too, are Crick's later decades spent at the Salk Institute in La Jolla, California, where he became a neuroscientist. Crick led a privileged existence there, able to invite scientists whose work he admired to spend months with him.

Brash young physicist turned molecular biologist; successful molecular biologist turned neuroscientist: there is symmetry to Crick's discipline changes, but hubris as well. For Crick

Symmetry and hubris

Francis Crick: Hunter of Life's Secrets

by Robert Olby

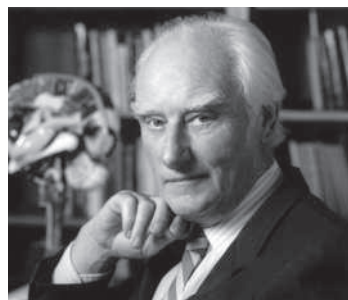
Cold Spring Harbor Laboratory Press: 2009. 450 pp. \$45, £30

Francis Crick was not your run-of-the-mill scientist, as Robert Olby makes clear in his superb biography. A tall man given to verbal diarrhoea and infectious laughter, Crick did his Nobel-prizewinning work before he finished his PhD. His thesis, on the X-ray analysis of protein structure, provided him with skills to appreciate the molecular arrangement of DNA, but his work with James Watson was done in his spare time. Crick included an off-print of their 25 April 1953 *Nature* paper, the most fundamental in twentieth-century life sciences, in the back of his thesis as proof that he was a published researcher.

The Cambridge thesis was his second attempt at a doctorate. His first, in physics at University College London, was interrupted by the outbreak of the Second World War, during

which he worked on mine research for the Admiralty. After the war, Crick convinced the Medical Research Council (MRC) to give him a studentship to apply physics to biology. He went to Cambridge, first to the Strangeways Research Laboratory, and then to what is now known as the MRC Laboratory of Molecular Biology (LMB).

Discovering the structure of DNA saved his career. Lawrence Bragg, director of the Cavendish Laboratories where the LMB was then housed, had grown tired of Crick's boisterous behaviour. After the DNA paper, Bragg held a different view and Crick stayed at the LMB until 1976. His contributions to the development of molecular biology and genetics, and to our understanding of the genetic code and of transfer RNA, ribosomes and messenger RNA, are without parallel. His formulation



Francis Crick: no ordinary scientist.

M. LIEBERMAN/SIEGEL & CALLAWAY

Stamps celebrate Royal Society scientists

To mark the Royal Society's 350th anniversary, the UK Royal Mail has issued a set of postage stamps featuring ten prominent fellows, each representing a 35-year period. Five are shown below (left to right): Alfred Russel Wallace, Joseph Lister, Ernest Rutherford, Dorothy Hodgkin and Nicholas Shackleton.



ROYAL MAIL GROUP

wanted to solve the ultimate problem, that of the physical basis of consciousness. The man who, in 1953, supposedly announced to drinkers in The Eagle pub in Cambridge that he had discovered the secret of life, was working in 2004, on his deathbed, on a paper proposing that the claustrum might be the key brain structure in producing consciousness. Olby works hard to put a positive spin on Crick's influence on consciousness research, in terms of support

and the number of workers in the field. He stops short of suggesting that Crick was yet another great scientist who did not know when to retire and let younger people take over. Nevertheless, that conclusion could be drawn. ■

W. F. Bynum is emeritus professor of the history of medicine at University College London and author of *The History of Medicine: A Very Short Introduction*.

e-mail: w.bynum@ucl.ac.uk

How lateral thinking saved lives

Martin Kemp is struck by the surreal quality of a home-made iron lung.

There is no more-telling formula associated with surrealism than the words of the nineteenth-century French poet Comte de Lautréamont, who aspired to create something "as beautiful as the chance encounter of a sewing machine and an umbrella on an operating table".

Currently on show at the Mori Art Museum in Tokyo is the perfect surrealist object. A giant pair of bellows, of exactly the type used to resuscitate a domestic fire, is operated by a rude wooden lever that is pivoted on an arch of jointed pipes. It is tethered to a coffin-like wooden box, which is in turn anchored to a rickety iron bed. Patches on the leather lung of the bellows testify to its sustained use. On the wooden lid a series of stained rings speak of its occasional use as a table for hot beverages. It is a truly extraordinary object. To understand what it is really is — or was — we must return to the seventeenth century.

John Mayow, a physician at All Souls College at the University of Oxford, UK, was a member of the illustrious circle that included Christopher Wren, Robert Hooke and Thomas Willis, founder members of the Royal Society. Mayow's 1688 treatise *On Respiration* established the first mechanical basis for how humans breathe.

Mayow wrote that "if a bladder with most of the air pressed out of it, and tied by a tight ligature around the sphincter, be placed in a glass from which the air is afterwards exhausted, we shall at once see the bladder swell and become greatly distended," adding that it is "a rather pretty sight". The plate accompanying the treatise shows a pair of bellows to support his argument. Mayow, who also showed that the life-giving properties of

air could be removed by combustion, died in 1679 aged 36, and is less well-known than he should be.

Given his early discovery of what came to be ponderously called external negative pressure ventilation, it is perhaps surprising that it was not until 1927 that a machine using this principle was invented to aid those whose respiratory systems were failing. The invention, which became known as the iron lung, is credited to the Harvard University physician Louis Agassiz Shaw and his colleague, the pioneer of industrial medicine, Philip Drinker. They had been sponsored in their research by the Consolidated Gas Company of New York. Their device consisted of an iron cabinet from which

air could be evacuated by two vacuum-cleaner power units. It made a spectacularly successful debut on 12 October 1928 at Boston Children's Hospital in Massachusetts, where it resuscitated a child who had faced what seemed an inevitable death.

The iron lung, in its sleeker version as a polished or enamelled metal cylinder punctuated by windows and equipped with an angled mirror that allowed patients to see their surroundings, came into its own during the polio outbreaks of the 1940s and 1950s. The respirators enabled those whose chest muscles had been paralysed by the disease to breathe, and stood in diagonally serried rows in large wards while solicitous nurses filed by.

Anyone acquainted with such high-tech versions would barely recognize the wooden cabinet with bellows as an iron lung. Indeed, iron is not the most evident material used in the device. But it is indeed a respirator, and one that performed sterling service for a dozen or more years at the Lansdowne Hospital in Cardiff, UK, before being retired in the late 1950s. It seems that the bellows lung was put together by resourceful hospital engineers, presumably to save money. Only immediately available materials were used, such as wood, leather and tacks, and a hospital bed was commandeered. The whole ensemble declares the potency of artisanal resourcefulness.

The utilitarianism of the bellows lung chimes with surrealism in two respects. The

first is that the leaps of lateral imagination that lay behind the incongruous juxtaposition of objects in surrealism find a clear

parallel in the Welsh engineers' brilliant insight that a giant pair of traditional bellows could be combined with a wooden box and bed to do the same job as the manufactured item. The second is that how we look at an object varies over time and in settings other than those for which it was conceived. Now that the bellows lung features in historical displays, we cannot help but see it as a strange and wondrous thing alongside the other technological dinosaurs that fascinate us in museums of science. ■

Martin Kemp is emeritus professor in history of art at the University of Oxford, Oxford, UK.



This makeshift respirator was used in a UK hospital until the late 1950s.

The iron lung is on display at the Mori Art Museum in Tokyo until 28 February, and is part of the Science Museum's permanent collection in London.

SCIENCE MUSEUM LONDON

Q&A: Georgina Ferry on writing biography

Acclaimed biographer **Georgina Ferry** has chronicled the lives of two Nobel prizewinning chemists, Dorothy Hodgkin and Max Perutz. In the fourth in our series of five interviews with authors who each write science books for a different audience, Ferry reveals how detachment is needed to turn an attic's worth of personal letters into a compelling story.

What do you like most about the biography format?

It has your narrative set out for you because the story has a beginning, a middle and an end. And also there's nosiness. You are given licence to go and read someone's personal letters and enter into their life in a way that you are rarely privileged to do.

What is the purpose of a biography?

The traditional idea is to show an exemplary life that we might all strive to live up to. But the advantage I see in scientific biography is that it provides a way of getting across to the public how scientists actually live; what doing science is really about.

Is it appropriate to tell the history of science through personal stories?

Within the history of science, biography has been disparaged for a long time because it puts too much focus on the individual. But that is beginning to change. If you do your biography properly, then you place your subject in context. It is not a question of individual heroes suddenly having some eureka moment.

Why did you choose Dorothy Hodgkin for your first biography?

She is the only British woman to have won a science Nobel prize, and yet most people don't even recognize her name. She was a mother who had three kids and a husband who was largely absent throughout her professional career. I was interested in finding out how she negotiated that.

Its title is *Dorothy Hodgkin: A Life*. Did you deliberately avoid science in the title?

I wanted it to look like a literary biography, not a science book. When people go into a book shop and browse, they are looking for something familiar. Science can be off-putting; if you've got science attached to a name you've never heard of, a person is not necessarily going to pick that book up and buy it.

Who makes a good subject?

The obvious candidates — Albert Einstein, Charles Darwin, Marie Curie — continue to be good choices because you don't



Georgina Ferry: scientists should archive e-mails.

have that initial recognition barrier to get across. You do need them to have reached the pinnacle of something. But that is not enough. If somebody has spent 60 years getting up, going to the lab and coming home, they are not going to be a great subject for a biography. It helps if there is some controversy in their life. Graham Farmelo's prize-winning book on physicist Paul Dirac, *The Strangest Man*, is fascinating because Dirac was so odd and had such a tragic life.

Do you need the permission of living relatives?

Biographies can be written without personal authorization, but I could not have done either of my books without the fantastic co-operation of the family members. The Hodgkin family never threw anything away, and they gave me carte blanche to read anything that I could find in the attic. I like to include direct quotes, and you need a family's permission to use that material.

Beyond family records, where do you go?

You can interview living colleagues but archives of professional and personal letters give you the bulk of your source material. You find out where things are, and then you travel around and look at them. Some

records are beginning to go up on the Internet, and one day we'll do this research from our desks. But that will take away a bit of the magic.

Is technology affecting archived material in other ways?

People don't write letters any more in the way that they used to. Scientists should think before they throw away e-mails, and archive anything that might be of interest to an audience in 20, 50 or 100 years time. The British Library set up the Digital Lives Research Project to look at this specific problem. [See *Nature* 459, 775–776; 2009.]

Do you have to step into the shoes of these people to write about them?

Actually you have to retain a certain detachment. You have got to be able to see their flaws as well as their triumphs, and you can't be so close that you feel it would be a betrayal to mention something that they wouldn't want revealed. But you do need to go and look at places where people were, so you can describe them accurately.

How might biographies be structured?

Currently the fashion is against the cradle-to-grave biography. Group biographies are popular, such as Richard Holmes's *Age of Wonder*. If you're determined to look at only one person, find a different way of doing it. A good example is Hermione Lee's biography of writer Virginia Woolf, in which each chapter is thematic.

How much money can an author make?

In my experience, you rarely get enough money to cover the time you spend doing the work. Each of those books took me about four years, working on other projects at the same time. Publishers offer an advance based on how many they think you will sell, perhaps around £10,000–£20,000 [US\$16,000–\$32,000] if you are lucky. So it is a labour of love. ■

Interview by **Nicola Jones**, a commissioning editor for *Nature's* Opinion section.

Georgina Ferry is author of *Dorothy Hodgkin: A Life* (Granta, 1998) and *Max Perutz and the Secret of Life* (Chatto & Windus, 2007).

D. LONG

APPLIED MATHEMATICS

The statistics of style

Bruno A. Olshausen and Michael R. DeWeese

A mathematical method has been developed that distinguishes between the paintings of Pieter Bruegel the Elder and those of his imitators. But can the approach be used to spot imitations of works by any artist?

What makes the style of an artist unique? For paintings or drawings, what comes to mind are specific brush or pen strokes, the manner in which objects are shaded, or how characters or landscapes are portrayed. Art historians are skilled at identifying such details through visual inspection, and art collectors and museums currently rely on this type of expert analysis to authenticate works of art. Might it be possible to automate this process to provide a more objective assessment? Is it possible to teach a computer to analyse art? In an article in *Proceedings of the National Academy of Sciences*, Hughes *et al.*¹ demonstrate that subtle stylistic differences between the paintings of Pieter Bruegel the Elder and those of his imitators, which were at one time misattributed by art historians, may be reliably detected by statistical methods.

Hughes and colleagues' work is the latest in a stream of research findings that have emerged over the past few decades in the field of 'image statistics'. The players in this field are an unlikely cadre of engineers, statisticians and neuroscientists who are seeking to characterize what makes images of the natural environment different from unstructured or random images (such as the 'static' on a computer monitor or television). Answering this question is central to the problem of coding and transmitting images over the airwaves and the Internet, and, it turns out, it is just as important for understanding how neurons encode and represent images in the brain.

The first image statisticians were television engineers, who, as early as the 1950s, were trying to exploit correlations in television signals to compress the signals into a more efficient format. Around the same time, pioneering psychologists and neuroscientists such as Fred Attneave and Horace Barlow were using ideas from information theory to work out how the particular structures contained in images shape the way that information is coded by neurons in the brain. Since then, others have succeeded in developing specific mathematical models of natural-image structure — showing, for example, that the two-dimensional power spectrum varies with spatial frequency, f , roughly as $1/f^2$ (ref. 2), and that the distribution of contrast in

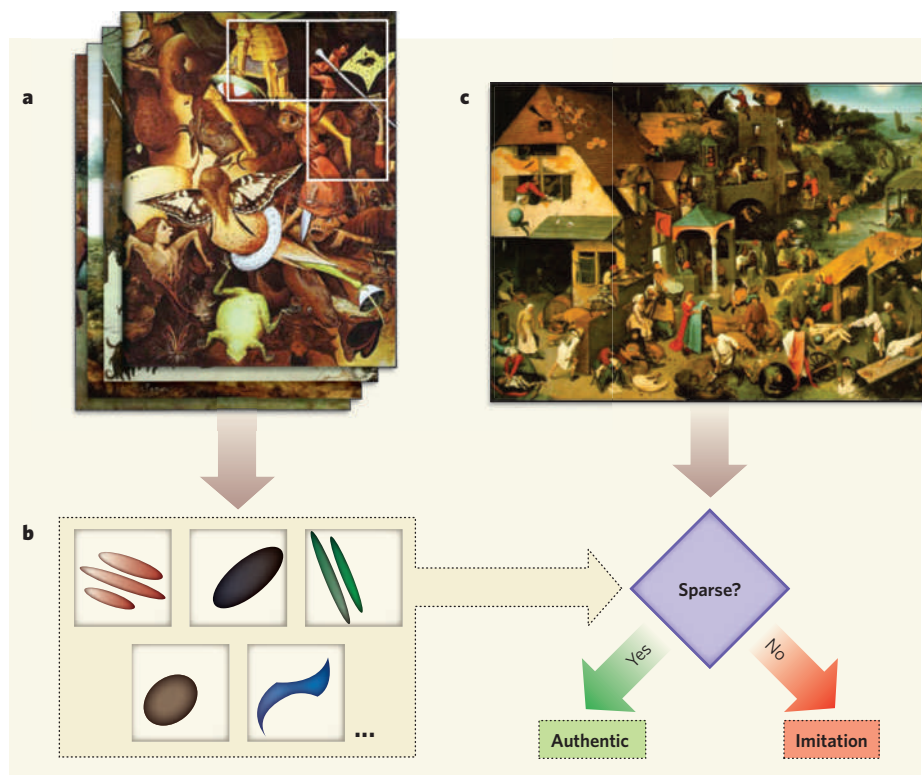


Figure 1 | Sparse-coding analysis of artistic style. Hughes and colleagues¹ show that small image patches taken from a collection of authentic works by Pieter Bruegel the Elder (a) can be used to generate a 'dictionary' of visual elements attuned to the statistics of his style (b). A test image (c) can then be authenticated by recreating it with a combination of dictionary elements. If recreation of the test image requires only a few dictionary elements, it is sparse, and labelled 'authentic', whereas if accurate encoding of the test image requires many dictionary elements, it is labelled as an 'imitation'.

local image regions is invariant across scale^{3–5}.

Investigators also began applying these and related models to characterize the statistical structure of paintings by particular artists. It was shown, for example, that Jackson Pollock's drip paintings have fractal structure⁶, and that Bruegel's drawings could be distinguished from those of his imitators by the shape of the histogram of wavelet filter outputs, which represent how much spatial structure is present at different scales and orientations⁷. It is this latter work that formed the basis for Hughes and colleagues' study¹. Instead of using standard wavelet filters, they apply a set of filters that are adapted to the statistics of Bruegel's drawings through a method known as sparse coding.

In a sparse-coding model, local regions of an image are encoded in terms of a 'dictionary' of spatial features; importantly, the dictionary is built up, or trained, from the statistics of an ensemble of images, so that only a few elements from the dictionary are needed to encode any given region. Essentially, sparsity forces the elements of the dictionary to match spatial patterns that tend to occur in the images with frequencies significantly higher than chance, thus providing a snapshot of structure contained in the data. Neuroscientists have shown that such dictionaries, when trained on a large ensemble of natural scenes, match the measured receptive-field characteristics of neurons in the primary visual cortex of mammals. These and

other empirical findings have lent support to the idea that sparse coding may be used by neurons for sensory representation in the cortex⁸.

Rather than attempting to form a generic code adapted to natural scenes, Hughes *et al.*¹ asked what sort of dictionary results from training on one specific class of image — the drawings of Pieter Bruegel the Elder. The dictionary that emerges, not surprisingly, differs from that adapted for natural scenes. In some sense, Hughes *et al.* have evolved an artificial visual system that is hyper-adapted to Bruegel's drawings. Such a visual system will be adept at representing other drawings from this class — that is, other authentic drawings by Bruegel — because they result in sparse encodings. However, it will not be so adept at representing images outside this class, such as drawings by other artists and even those attempting to imitate Bruegel, because they will result in denser encodings — more dictionary elements will be needed to describe each image region (Fig. 1). To put it another way, a picture may be worth a thousand words, but if it's an authentic Bruegel, it should take only a few Bruegel dictionary elements to represent it faithfully.

Can such an approach be used to authenticate works by any artist? And how robust can one expect it to be in practice? Key to the success of this study¹ is the fact that all of the analyses were performed on one particular type of artwork produced by Bruegel — drawings of landscapes. However, Bruegel worked in a variety of media, and his subject matter spanned a wide range of content. Moreover, an individual artist may use various styles. Developing algorithms capable of generalizing across these variations presents a much more challenging problem. Another concern is that it may be possible to defeat this method by generating images that are sparse for a wide range of dictionaries. For example, a geometrical abstract painting by Piet Mondrian would presumably yield a highly sparse representation using a dictionary trained on nearly any artist. Worse still, images randomly generated from the learned dictionary elements would also exhibit high sparsity but would look nothing like a real Bruegel. Thus, sparsity alone may be too fragile a measure for authentication.

One might question other technical choices made by the authors, such as the exclusive use of kurtosis (a statistical measure often used to quantify the degree of 'peakedness' of a probability distribution) to characterize the sparsity of filter outputs; and the analysis of statistical significance is at times puzzling. But Hughes and colleagues have taken a bold step. This is an exciting area of research that goes even beyond forgery detection. Indeed, it begs the question of whether it might be possible to fully capture the style of an artist using statistics. The field of natural-image statistics has advanced beyond the simple sparse-coding models used here, and it is now possible to characterize complex relationships among dictionary elements^{9,10}. Intriguingly, all of these models are

generative — that is, they can be used to synthesize images matching the statistics captured by the model, as has already been done successfully with textures¹¹. One exciting possibility is that computers could generate novel images that convincingly emulate the style of a particular artist. Perhaps someday the best Bruegel imitators will be computers. ■

Bruno A. Olshausen and Michael R. DeWeese are at the Redwood Center for Theoretical Neuroscience, Helen Wills Neuroscience Institute, School of Optometry (B.A.O.) and Department of Physics (M.R.D.), University of California, Berkeley, Berkeley, California 94720, USA.
e-mails: baolshausen@berkeley.edu;
deweese@berkeley.edu

1. Hughes, J. M., Graham, D. J. & Rockmore, D. N. *Proc. Natl Acad. Sci. USA* **107**, 1279–1283 (2010).
2. Field, D. J. *J. Opt. Soc. Am. A* **4**, 2379–2394 (1987).
3. Ruderman, D. L. *Network Comput. Neural Syst.* **5**, 517–548 (1994).
4. Geisler, W. S. *Annu. Rev. Psychol.* **59**, 167–192 (2008).
5. Hyvärinen, A., Hurri, J. & Hoyer, P. O. *Natural Image Statistics: A Probabilistic Approach to Early Computational Vision* (Springer, 2009).
6. Taylor, R. P., Micolich, A. P. & Jonas, D. *Nature* **399**, 422 (1999).
7. Lyu, S., Rockmore, D. & Farid, H. *Proc. Natl Acad. Sci. USA* **101**, 17006–17010 (2004).
8. Olshausen, B. A. & Field, D. J. *Curr. Opin. Neurobiol.* **14**, 481–487 (2004).
9. Karklin, Y. & Lewicki, M. S. *Nature* **457**, 83–86 (2009).
10. Cadieu, C. F. & Olshausen, B. A. *Adv. Neural Inf. Process. Syst.* **21**, 209–216 (2009).
11. Portilla, J. & Simoncelli, E. P. *Int. J. Computer Vision* **40**, 49–71 (2000).

CELL BIOLOGY

A brake on lipid synthesis

Fikadu G. Tafesse and Joost C. M. Holthuis

Although sphingolipids are vital cellular components, the path to their production is paved with toxic intermediates. Orm proteins allow cells to form these lipids without killing themselves in the process.

Sphingolipids are an unusually versatile class of membrane lipid that, besides providing mechanical stability, have roles in molecular signalling and sorting as well as in cell recognition. Not surprisingly, therefore, a block in sphingolipid synthesis compromises cell growth and survival¹. But sphingosine, ceramides and other intermediates of sphingolipid synthesis are also potent mediators of cellular stress pathways. When they accumulate in cells or are added experimentally, these compounds can trigger growth arrest and cell death^{2,3}. So how does a cell handle the dilemma of generating sufficient amounts of sphingolipids without jeopardizing its viability? On page 1048 of this issue, Breslow *et al.*⁴ identify Orm proteins as essential components of a sphingolipid rheostat that allows cells to fine-tune sphingolipid synthesis according to their needs.

Sphingolipid production starts in the intracellular organelle known as the endoplasmic reticulum with the condensation of serine and fatty acyl-CoA. This reaction is catalysed by the enzyme serine palmitoyltransferase (SPT) and yields the first of a series of long-chain bases (LCBs). The LCBs become acylated and are yet further modified to form ceramides — the backbone of all sphingolipids. Ceramides are transported to the Golgi complex, where they acquire a species-specific array of polar head groups to form the complex sphingolipids found primarily on the cell surface. In yeast, SPT consists of two related subunits, Lcb1 and Lcb2, which for maximal activity associate with a third subunit, Tsc3 (ref. 5). As the first and rate-limiting enzyme in sphingolipid synthesis, SPT is an attractive target

for homeostatic regulation of these lipids.

The ease of genetic manipulation in yeast has been invaluable for identifying the enzymes that mediate sphingolipid synthesis. The power of yeast genetics has gained further momentum with the advent of comprehensive strategies for mapping genetic interactions. Such interactions show how the effect of compromising one gene (such as impaired growth) is modulated by perturbing a second gene. An efficient way to study such functional relationships between genes is to create epistatic mini-array profiles, or E-MAPs⁶. This approach allows quantitative measurements to be made over the entire spectrum of possible genetic interactions — from those that aggravate the growth defect to those that alleviate it. E-MAPs also permit analysis of essential genes through the inclusion of hypomorphic alleles, which destabilize the genes' messenger RNAs.

Focusing on a collection of more than 1,400 yeast genes associated with the biology of the endoplasmic reticulum, Breslow *et al.*⁴ noticed a striking inverse correlation in the interaction patterns of the *LCB1/2* genes with the gene for the endoplasmic-reticulum membrane protein Orm2. Increased expression of Orm2 — or its relative Orm1 — had the same effect as a reduction in *Lcb1/2* expression, indicating that *Lcb1/2* and Orm1/2 proteins have opposing roles. Moreover, cells lacking Orm1/2 accumulated LCBs and ceramides, whereas cells expressing higher than normal levels of Orm1/2 contained reduced levels of these intermediates. The authors also found that Orm1/2 proteins form a complex with *Lcb1/2* and Tsc3. Together, these findings indicate that Orm

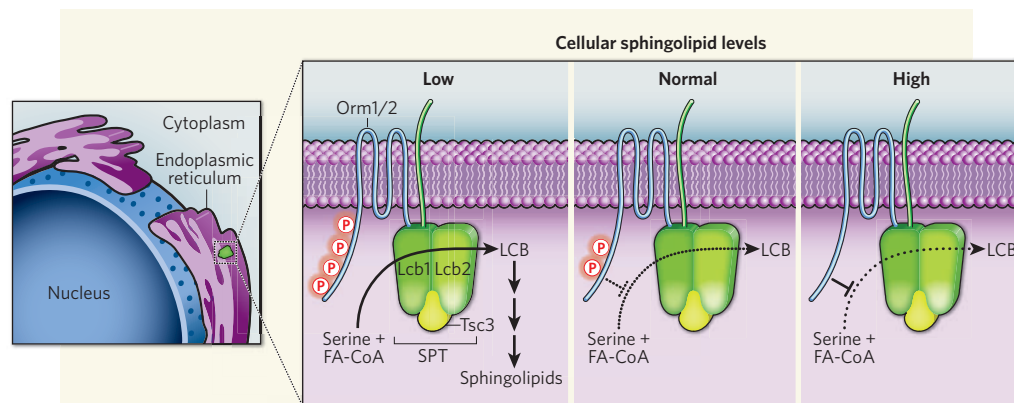


Figure 1 | Orm proteins control sphingolipid homeostasis in the endoplasmic reticulum. Sphingolipid synthesis starts with the formation of a long-chain base (LCB) from serine and fatty acyl-CoA (FA-CoA) in a reaction catalysed by serine palmitoyltransferase (SPT) on the cytoplasmic side of the endoplasmic reticulum. SPT subunits Lcb1, Lcb2 and Tsc3 form a complex with the proteins Orm1 and Orm2. When cellular sphingolipid levels are plentiful, Orm proteins act as negative regulators of LCB synthesis. But when sphingolipids are in short supply, multi-site phosphorylation of Orm proteins gradually relieves their inhibitory activity, thereby restoring sphingolipid homeostasis. The identity of the intermediate in the sphingolipid synthetic pathway whose levels are sensed to control Orm phosphorylation is not known.

proteins are negative regulators of sphingolipid synthesis, and act directly on SPT.

But why would cells include negative regulators as core components of an essential enzyme complex? A notable clue came when Breslow *et al.* examined the sensitivity of Orm-deficient cells to the SPT inhibitor myriocin. Unexpectedly, removal of Orm1/2 did not confer any resistance to this drug. Moreover, normal cells maintained constant LCB levels at myriocin concentrations that effectively suppressed LCB accumulation in Orm-deficient cells. This observation implies that cells can generate a constant sphingolipid output in the face of increasing SPT inhibition by gradually relieving an Orm1/2-mediated brake on LCB synthesis.

Curiously, myriocin did not affect Orm1/2 expression or binding to Lcb1/2. So how is the Orm1/2-mediated brake on LCB synthesis removed? Breslow *et al.* convincingly show that the brake is operated by a phosphorylation-based feedback loop (Fig. 1). Myriocin induces a dose-dependent addition of phosphate groups to Orm1/2 proteins at several sites in their amino-terminal region⁴. Mutations of these phosphorylation sites reduce basal LCB levels and make cells highly sensitive to myriocin. These elegant experiments establish the mechanistic basis of a sphingolipid rheostat with a central role for Orm1/2 proteins as homeostatic regulators of SPT.

The control of Orm1/2 activity by multi-site phosphorylation has a distinct advantage. Besides allowing cells to respond rapidly to undesirable fluctuations in sphingolipid levels, this arrangement may provide a graded mechanism for finely adjusting sphingolipid synthesis to match cellular needs. Importantly, such a device would ensure an adequate supply of complex sphingolipids, while minimizing the risk of accumulation of the toxic intermediates.

But there are still some outstanding questions.

How do Orm proteins regulate SPT? Do they alter the catalytic activity of Lcb1/2, or do they modulate the enzyme's access to its substrates? Which kinase and phosphatase enzymes control Orm phosphorylation? And what is the identity of the sphingolipid intermediate whose levels are sensed to regulate Orm activity? Preliminary evidence⁴ suggests that Orm phosphorylation is sensitive to fluctuations in ceramide levels. This raises the question of whether a recently identified ceramide sensor in the endoplasmic reticulum⁷ is part of the mechanism by which Orm proteins

control sphingolipid homeostasis.

Two recent studies^{8,9} report that, in the absence of Orm proteins, the process of protein quality control at the endoplasmic reticulum is impaired. Together with the findings of Breslow *et al.*, these studies provide a fresh starting point for investigating how protein and lipid synthesis is coordinated during membrane biogenesis. Breslow and colleagues' work might also have clinical implications. Because one of the human *ORM* genes has recently been implicated in childhood asthma¹⁰, the present study indicates that dysregulation of sphingolipid metabolism may contribute to the development of this disease. This hypothesis merits verification, because it holds the promise of new therapies.

Fikadu G. Tafesse and Joost C. M. Holthuis are in the Bijvoet Center and the Institute of Biomembranes, Utrecht University, 3584 CH Utrecht, the Netherlands.
e-mail: j.c.holthuis@uu.nl

1. Hanada, K., Nishijima, M. & Akamatsu, Y. *J. Biol. Chem.* **265**, 22137–22142 (1990).
2. Zhang, X., Skrzypek, M. S., Lester, R. L. & Dickson, R. C. *Curr. Genet.* **40**, 221–233 (2001).
3. Hannun, Y. A. & Obeid, L. M. *J. Biol. Chem.* **277**, 25847–25850 (2002).
4. Breslow, D. K. *et al.* *Nature* **463**, 1048–1053 (2010).
5. Gable, K., Slife, H., Bacikova, D., Monaghan, E. & Dunn, T. M. *J. Biol. Chem.* **275**, 7597–7603 (2000).
6. Schuldiner, M. *et al.* *Cell* **123**, 507–519 (2005).
7. Vacaru, A. M. *et al.* *J. Cell Biol.* **185**, 1013–1027 (2009).
8. Han, S., Lone, M. A., Schneider, R. & Chang, A. *Proc. Natl Acad. Sci. USA* (in the press).
9. Cantero-Recasens, G., Fandos, C., Rubio-Moscardo, F., Valverde, M. A. & Vicente, R. *Hum. Mol. Genet.* **19**, 111–121 (2010).
10. Moffatt, M. F. *et al.* *Nature* **448**, 470–473 (2007).

LOW-TEMPERATURE PHYSICS

Surprise in the strong regime

Yong-il Shin

The finding that the normal phase of an ultracold gas of fermionic atoms in the strongly interacting regime is close to a Fermi liquid isn't quite what theorists expected for these systems.

During the past decade, ultracold gases of fermions (particles with half-integer spin, such as electrons) gained renown as a tool for modelling the physics of strongly interacting many-body systems. In the vicinity of a Feshbach resonance, these systems can be conveniently controlled with a magnetic field to reach the unitary limit, the point at which the interactions between particles become strongest and the thermodynamic properties of the system become universal — that is, independent of the nature of the interactions¹. As such, ultracold Fermi gases with tunable interactions allow us to probe the crossover from the Bardeen–Cooper–Schrieffer (BCS)

superfluid state, which describes the frictionless flow of weakly interacting electron pairs in superconductors, to the Bose–Einstein condensate (BEC) superfluid state, which occurs in systems made of bosons (particles with whole-integer spin) such as helium-4 (ref. 2); the gas's weakly interacting fermions can be made to interact strongly and bind together into bosonic molecules that ultimately condense into a BEC. On page 1057 of this issue, Nascimbène *et al.*³ provide insight into the strongly interacting, BCS–BEC crossover regime by devising an experiment that yields the equation of state for a unitary Fermi gas.

The equation of state of a physical system is a



50 YEARS AGO

In my opinion the trouble with African agriculture is not that information is not properly co-ordinated, but that the basic facts are simply not known. So little fundamental agricultural research has been done ... Even attempts at developments like the Groundnut Scheme ... seem less wasteful when it is realized that for every pound lost in this and in all agricultural schemes attempted in Africa since the War, much more than a hundred pounds has been spent in subsidizing British agriculture at home. More money will have to be spent on research in Africa. We need to have more and better research workers in the laboratories and in the field; I believe they will use the limited resources better than those who fritter away so much time and money attending international conferences and endless meetings of co-ordinating committees which lack the basic facts to co-ordinate. **Kenneth Mellanby**
From *Nature* 27 February 1960.

100 YEARS AGO

The Irish Fairy Book. By Alfred Perceval Graves — There is a greater demand for fairy books than there is for works on folklore, and the readers differ greatly in taste and requirements. Some fairy books are worse than useless to the folklorist, books in which the authors treat their sources in a thoroughly irresponsible fashion. On the other hand, those who could handle such materials discreetly, learnedly, and reverently cannot be induced to write fairy books. But such books must be written, and Mr. Graves has produced one which is in every respect commendable ... Many of the tales are in proper form for scientific examination, being evidently faithful records of oral traditions ... As in Welsh folklore, the fairies are in high glee at the seasonal festivals. Puck, for instance, is definitely associated with November. Lughnassad, Lug's marriage — the old name for the August festival — survives in dialect as "Lunacy day in harvest." From *Nature* 24 February 1910.

formula that describes the relationship between the system's thermodynamic parameters, such as pressure, volume, temperature and internal energy. From the history of physics, we know that a new formulation or modification of a system's equation of state represents an advance in our understanding of the system. The most famous equation of state, the ideal-gas law, was formulated in the early 1800s. It describes the state of an ideal gas, a hypothetical gas composed of non-interacting point particles. Despite its simple form ($PV = nRT$, where P is the pressure, V the volume, n the density, T the temperature and R a constant) the ideal-gas law provides a good description of the behaviour of many ordinary gases under normal conditions.

The procedure to obtain the equation of state for a gas is straightforward: fill a box with a 'cloud' of gas; measure how its pressure changes with temperature or volume, or vice versa; do so for all possible phases of the system; and, finally, combine and translate all of the information into an equation. In their experiment, Nascimbène *et al.*³ did just that, but with two differences. First, their sample, a fermionic gas of lithium-6 atoms in a mixture of two spin states, was confined in a harmonic trap instead of a box. Second, they measured the shape — that is, the gas density distribution — of the cloud.

In a harmonic trap, the trapping potential changes quadratically as a function of distance from the trap centre, so a sample in the trap has an inhomogeneous density distribution: a high density at the centre and a low density in the outer regions. As a consequence, the phase of the system varies spatially across the sample. This spatial inhomogeneity makes it difficult to measure the thermodynamic properties of the system, and so the equation of state. However, because in thermal equilibrium neighbouring local points in the sample have a well-defined thermodynamic relationship, it turns out that from the precise measurement of the gas density distribution one can access the thermodynamic quantities⁴. Nascimbène and colleagues measured the equation of state for the gas in the unitary regime for both a spin-balanced (with no net spin) sample at finite temperature and a spin-imbalanced sample in the zero-temperature limit.

Interestingly, the authors find that the thermodynamic behaviour of the normal (non-superfluid) phase of the gas in the unitary regime, for both balanced and imbalanced samples, is very close to that of a Fermi liquid. In the BEC regime, fermions pair up and form spatially localized molecules before undergoing a phase transition to a superfluid; the low-temperature normal phase is a Bose liquid of thermal molecules. In the BCS regime, fermion pairing and superfluidity occur at the same time, so the normal phase is a Fermi liquid of atoms (Fig. 1). In attempts to model the BCS-BEC crossover, theorists have anticipated that the normal phase of Fermi gases in the unitary limit might be a non-Fermi-liquid phase such as the pseudo-gap state that is

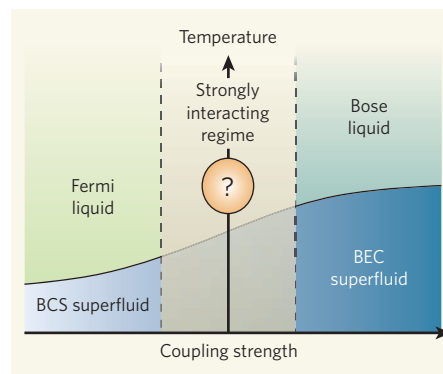


Figure 1 | Nature of the strongly interacting regime. A strongly interacting Fermi gas lies at the crossover between a Bardeen–Cooper–Schrieffer (BCS) superfluid and a Bose–Einstein condensate (BEC) superfluid. As the coupling strength between particles is increased, the BCS superfluidity (frictionless flow) of weakly interacting pairs of fermions (Cooper pairs) smoothly evolves into the BEC superfluidity of tightly bound bosonic molecules made of fermions. In the BEC regime, the low-temperature normal (non-superfluid) phase is a Bose liquid of molecules; in the BCS regime, the low-temperature normal phase is a Fermi liquid of atoms. Nascimbène *et al.*³ demonstrate that the hitherto uncharacterized normal phase of a strongly interacting Fermi gas in the unitary regime is very close to a Fermi liquid.

thought to be a precursor phase of the high-temperature superconducting state of copper oxide compounds⁵. Nascimbène and colleagues' experiment now shows unambiguously that this is not the case.

One novelty of their experiment lies in the use of a Bose gas to measure the temperature of the system. Lack of accurate thermometry has long been the bottleneck for determining the thermodynamic properties of strongly interacting Fermi gases. The observation of a lattice of vortices in such a system has provided conclusive evidence of high-temperature superfluidity⁶. But until now, the critical temperature at which a balanced Fermi gas becomes superfluid has not been determined in a model-independent way. Because the heat capacity of ultracold (nanokelvin temperature) atomic gases is extremely small, a normal thermometer cannot be used as the sample would immediately vaporize. Inspired by an earlier demonstration⁷, Nascimbène *et al.*³ overcome this problem by introducing a small amount of a Bose gas into the sample and measuring its temperature. The Bose gas used by the authors has the advantage of being sufficiently weakly interacting to not perturb the sample, but strong enough to be in thermal equilibrium with it. This technique allowed the researchers to measure the temperature of their samples directly.

Ultracold atomic-gas systems have been developed to simulate a variety of quantum phenomena and to tackle long-standing problems in condensed-matter physics. Nascimbène

and colleagues' determination of the equation of state for a unitary Fermi gas represents an outstanding example of quantum simulation, providing valuable qualitative and quantitative information on a regime for which a comprehensive theoretical description is inevitably difficult. In the long run, their technique might be generalized to all other cold atomic systems and become a useful tool with which to probe thermodynamic properties and thus search for exotic quantum states of matter. ■

Yong-il Shin is in the School of Physics and Astronomy, Seoul National University,

Seoul, 151-747, Republic of Korea.

e-mail: yishin@snu.ac.kr

1. Ho, T.-L. *Phys. Rev. Lett.* **92**, 090402 (2004).
2. Inguscio, M., Ketterle, W. & Salomon, C. *Ultracold Fermi Gases Proc. Int. School Phys. "Enrico Fermi" Course CLXIV* (IOS Press, Amsterdam, 2008).
3. Nascimbène, S., Navon, N., Jiang, K. J., Chevy, F. & Salomon, C. *Nature* **463**, 1057-1060 (2010).
4. Ho, T.-L. & Zhou, Q. *Nature Phys.* **6**, 131-134 (2010).
5. Chen, Q., Stajic, J., Tan, S. & Levin, K. *Phys. Rep.* **412**, 1-88 (2005).
6. Zwiernlein, M. W., Abo-Shaeer, J. R., Schirotzek, A., Schunck, C. H. & Ketterle, W. *Nature* **435**, 1047-1051 (2005).
7. Spiegelhalter, F. *et al. Phys. Rev. Lett.* **103**, 223203 (2009).

REGENERATIVE MEDICINE

Cell reprogramming gets direct

Cory R. Nicholas and Arnold R. Kriegstein

In a feat of biological wizardry, one type of differentiated cell has been directly converted into another, completely distinct type. Notably, the approach does not require a stem-cell intermediate stage.

Barriers to transdifferentiation — the direct conversion or reprogramming of one cell type into another — are falling fast. On page 1035 of this issue, Vierbuchen *et al.*¹ maintain the pace of this research by describing a potential innovation for generating disease-specific and patient-specific tissues of the central nervous system (CNS) that does not rely on stem cells. The route to possible regenerative-medicine-based treatment of CNS disorders such as epilepsy, stroke and Parkinson's disease may have taken another unexpected turn.

In 2006, the ability to reprogram fibroblasts, a type of cell found in connective tissue throughout the body, to embryonic-like stem cells (called induced pluripotent stem, iPS, cells)² was a breakthrough: it cleared the way to create disease- and patient-specific stem cells and sidestepped the thorny ethical issues associated with embryonic stem (ES) cells from human embryos. Disease-specific iPS cells, derived from patients with specific genetic disorders, such as some cases of amyotrophic lateral sclerosis (Lou Gehrig's disease), are already being used to study disease mechanisms and to search for new drug targets. Patient-specific iPS cells hold the promise of replacement-cell therapy without the risk of immune rejection. But such are the developments in cell transdifferentiation^{1,3} that one might ask if stem cells will be dispensable in the quest for regenerative medicine.

It was once thought that cells are irreversibly instructed to become specific cell types in the body. We now know that this is not the case. Reprogramming of cell fates began with work in the 1960s that harnessed the ability of the oocyte (egg) to instruct differentiated adult cell nuclei to revert to an undifferentiated state. This process, called somatic-cell nuclear

transfer (SCNT)⁴, can result in an embryo and ES cells with the genetic make-up of the adult cell. Similarly, fusing ES cells with adult cells can convert the adult cell nucleus to an undifferentiated state⁵ (Fig. 1). But the clinical relevance has remained doubtful: human SCNT has not yet succeeded, and cell fusion results in tetraploidy, a clinically unacceptable duplication of nuclear material.

The 2006 paper² boosted the reprogramming field with the discovery that adult fibroblasts

can be induced to undergo a dramatic cell-fate reversal to an undifferentiated iPS cell state through the transient expression of four master-regulatory genes that encode transcription factors. The iPS cell approach has unquestionable clinical relevance. But adult cells must first be completely de-differentiated to an ES-cell-like state, and then subsequently re-differentiated to an adult cell type of interest — a time-consuming and inefficient detour (Fig. 1).

This detour raised the question of whether cell reprogramming could be optimized by directly inducing other adult cell fates without complete de-differentiation. Transdifferentiation of mammalian cells took a knock when reports of lineage reprogramming turned out to represent cell fusion⁶. But other studies suggested that conversion of one cell type to another could be achieved by activation of a few core factors⁷. An especially notable advance was the 2008 discovery³ that transient activation of three transcription factors induced the direct reprogramming of pancreatic exocrine cells into insulin-producing endocrine cells with robust (20%) efficiency. In this and most other studies, however, reprogramming occurred only between closely related cell lineages.

This is where Vierbuchen and colleagues¹ come in. Beginning with a set of 19 candidate genes that encode transcription factors involved in neuronal development or function, they eventually found that a combination of only three factors was sufficient to convert fibroblasts into neurons (Fig. 1). The fibroblasts were derived from mouse embryos and newborn or adult tail-tips of 'reporter' mice engineered to express a green fluorescent marker when the gene for the protein tau was turned on. Because

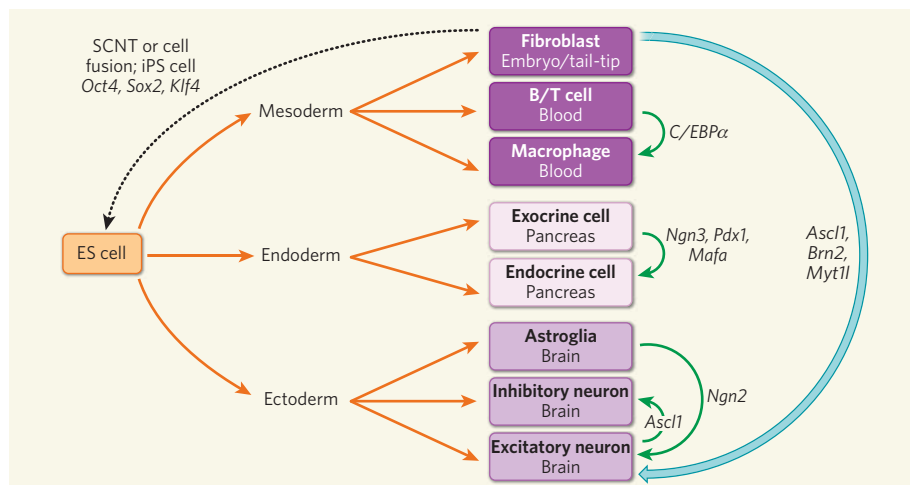


Figure 1 | Indirect and direct routes to cell-lineage reprogramming. The indirect routes involve reprogramming of a variety of adult cell types from different lineages to produce a de-differentiated embryonic stem (ES) cell state. Indirect routes (dotted arrow) include somatic-cell nuclear transfer (SCNT) or cell fusion, or creation of induced pluripotent stem (iPS) cells by the introduction of genes such as *Oct4*. But the de-differentiated cells must then be re-differentiated to adult cell types along the respective mesodermal, endodermal or ectodermal lineages. Vierbuchen *et al.*¹ demonstrate that a direct route can be taken (blue arrow): by inducing lineage-specific transcription factors encoded by genes including *Ascl1*, *Brn2* and *Myt1l*, they show that fibroblasts can be directly converted into distantly related cortical excitatory neurons. This is an advance over the intra-lineage conversion achieved between cells of the blood, pancreas or brain by induction of the other genes noted. Intra-lineage conversion studies not shown include fibroblast to macrophage and fibroblast to muscle cell by *PU.1* and *MyoD*, respectively.



50 YEARS AGO

In my opinion the trouble with African agriculture is not that information is not properly co-ordinated, but that the basic facts are simply not known. So little fundamental agricultural research has been done ... Even attempts at developments like the Groundnut Scheme ... seem less wasteful when it is realized that for every pound lost in this and in all agricultural schemes attempted in Africa since the War, much more than a hundred pounds has been spent in subsidizing British agriculture at home. More money will have to be spent on research in Africa. We need to have more and better research workers in the laboratories and in the field; I believe they will use the limited resources better than those who fritter away so much time and money attending international conferences and endless meetings of co-ordinating committees which lack the basic facts to co-ordinate. **Kenneth Mellanby**
From *Nature* 27 February 1960.

100 YEARS AGO

The Irish Fairy Book. By Alfred Perceval Graves — There is a greater demand for fairy books than there is for works on folklore, and the readers differ greatly in taste and requirements. Some fairy books are worse than useless to the folklorist, books in which the authors treat their sources in a thoroughly irresponsible fashion. On the other hand, those who could handle such materials discreetly, learnedly, and reverently cannot be induced to write fairy books. But such books must be written, and Mr. Graves has produced one which is in every respect commendable ... Many of the tales are in proper form for scientific examination, being evidently faithful records of oral traditions ... As in Welsh folklore, the fairies are in high glee at the seasonal festivals. Puck, for instance, is definitely associated with November. Lughnassad, Lug's marriage — the old name for the August festival — survives in dialect as "Lunacy day in harvest." From *Nature* 24 February 1910.

formula that describes the relationship between the system's thermodynamic parameters, such as pressure, volume, temperature and internal energy. From the history of physics, we know that a new formulation or modification of a system's equation of state represents an advance in our understanding of the system. The most famous equation of state, the ideal-gas law, was formulated in the early 1800s. It describes the state of an ideal gas, a hypothetical gas composed of non-interacting point particles. Despite its simple form ($PV = nRT$, where P is the pressure, V the volume, n the density, T the temperature and R a constant) the ideal-gas law provides a good description of the behaviour of many ordinary gases under normal conditions.

The procedure to obtain the equation of state for a gas is straightforward: fill a box with a 'cloud' of gas; measure how its pressure changes with temperature or volume, or vice versa; do so for all possible phases of the system; and, finally, combine and translate all of the information into an equation. In their experiment, Nascimbène *et al.*³ did just that, but with two differences. First, their sample, a fermionic gas of lithium-6 atoms in a mixture of two spin states, was confined in a harmonic trap instead of a box. Second, they measured the shape — that is, the gas density distribution — of the cloud.

In a harmonic trap, the trapping potential changes quadratically as a function of distance from the trap centre, so a sample in the trap has an inhomogeneous density distribution: a high density at the centre and a low density in the outer regions. As a consequence, the phase of the system varies spatially across the sample. This spatial inhomogeneity makes it difficult to measure the thermodynamic properties of the system, and so the equation of state. However, because in thermal equilibrium neighbouring local points in the sample have a well-defined thermodynamic relationship, it turns out that from the precise measurement of the gas density distribution one can access the thermodynamic quantities⁴. Nascimbène and colleagues measured the equation of state for the gas in the unitary regime for both a spin-balanced (with no net spin) sample at finite temperature and a spin-imbalanced sample in the zero-temperature limit.

Interestingly, the authors find that the thermodynamic behaviour of the normal (non-superfluid) phase of the gas in the unitary regime, for both balanced and imbalanced samples, is very close to that of a Fermi liquid. In the BEC regime, fermions pair up and form spatially localized molecules before undergoing a phase transition to a superfluid; the low-temperature normal phase is a Bose liquid of thermal molecules. In the BCS regime, fermion pairing and superfluidity occur at the same time, so the normal phase is a Fermi liquid of atoms (Fig. 1). In attempts to model the BCS–BEC crossover, theorists have anticipated that the normal phase of Fermi gases in the unitary limit might be a non-Fermi-liquid phase such as the pseudo-gap state that is

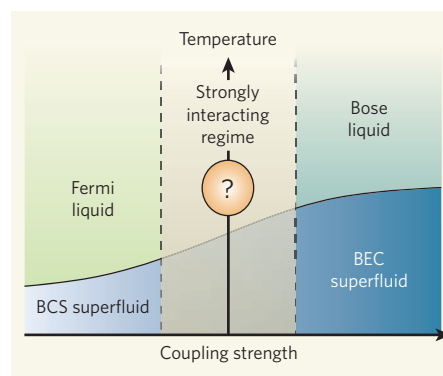


Figure 1 | Nature of the strongly interacting regime. A strongly interacting Fermi gas lies at the crossover between a Bardeen–Cooper–Schrieffer (BCS) superfluid and a Bose–Einstein condensate (BEC) superfluid. As the coupling strength between particles is increased, the BCS superfluidity (frictionless flow) of weakly interacting pairs of fermions (Cooper pairs) smoothly evolves into the BEC superfluidity of tightly bound bosonic molecules made of fermions. In the BEC regime, the low-temperature normal (non-superfluid) phase is a Bose liquid of molecules; in the BCS regime, the low-temperature normal phase is a Fermi liquid of atoms. Nascimbène *et al.*³ demonstrate that the hitherto uncharacterized normal phase of a strongly interacting Fermi gas in the unitary regime is very close to a Fermi liquid.

thought to be a precursor phase of the high-temperature superconducting state of copper oxide compounds⁵. Nascimbène and colleagues' experiment now shows unambiguously that this is not the case.

One novelty of their experiment lies in the use of a Bose gas to measure the temperature of the system. Lack of accurate thermometry has long been the bottleneck for determining the thermodynamic properties of strongly interacting Fermi gases. The observation of a lattice of vortices in such a system has provided conclusive evidence of high-temperature superfluidity⁶. But until now, the critical temperature at which a balanced Fermi gas becomes superfluid has not been determined in a model-independent way. Because the heat capacity of ultracold (nanokelvin temperature) atomic gases is extremely small, a normal thermometer cannot be used as the sample would immediately vaporize. Inspired by an earlier demonstration⁷, Nascimbène *et al.*³ overcome this problem by introducing a small amount of a Bose gas into the sample and measuring its temperature. The Bose gas used by the authors has the advantage of being sufficiently weakly interacting to not perturb the sample, but strong enough to be in thermal equilibrium with it. This technique allowed the researchers to measure the temperature of their samples directly.

Ultracold atomic-gas systems have been developed to simulate a variety of quantum phenomena and to tackle long-standing problems in condensed-matter physics. Nascimbène

the *Tau* gene is specifically expressed in neurons, cells that had converted into neurons could be easily identified. Vierbuchen *et al.* observed that, when they introduced all 19 genes together, some of the fibroblasts turned green. These presumptive neurons were called induced neuronal (iN) cells.

Fewer genes were then tested, and eventually a combination of only five of them — *Brn2*, *Myt1l*, *Zic1*, *Olig2* and *Ascl1* — was shown to be enough to convert fibroblasts to neurons in 12 days of culture. These iN cells expressed a variety of neuronal markers and were capable of firing action potentials, a basic function of neurons. Furthermore, when cultured with mouse neural cells, the iN cells received both excitatory and inhibitory synaptic connections from the mouse neurons, and were able to form functional synapses with each other.

Vierbuchen *et al.*¹ found that they could further reduce the pool of transforming genes to *Ascl1*, *Brn2* and either *Myt1l* or *Zic1*, increasing the efficiency of conversion by two- to threefold, up to around 20%. *Ascl1* alone was able to produce cells with immature neuronal features, but co-infection with *Brn2* and *Myt1l* was required to produce cells with more mature neuronal features. Surprisingly, most of the iN cells resemble excitatory cortical neurons of the forebrain — they express a protein called TBR1, and they mostly form excitatory synapses.

Why this should be so is a mystery, especially given the role of *Ascl1* in the developing brain. *Ascl1* encodes a transcription factor that is expressed by progenitor cells in the inhibitory neuron lineage⁸ that does not express TBR1. Furthermore, forced expression of *Ascl1* in excitatory cortical neuron progenitor cells is sufficient to induce them to express inhibitory neuronal cell markers⁹. It is unclear how to reconcile this observation with the role of *Ascl1* in producing excitatory iN neurons. Interestingly, a previous study showed that forced expression of *Neurog2* (*Ngn2*), a gene encoding a transcription factor required for the development of excitatory neurons, can induce TBR1 expression and excitatory neuron conversion from astroglia¹⁰.

Multipotent precursor cells of neural crest ectodermal origin have been isolated from rodent and human skin¹¹; they have yielded neural cells, although most of them seemed to be peripheral glia or non-functional neurons. Vierbuchen and colleagues' approach, by contrast, generated functional excitatory neurons of the CNS. If their approach could be modified to produce large numbers of neurons, including other types, such as inhibitory neurons that produce the neurotransmitter γ -aminobutyric acid (GABA) or dopamine-producing neurons, it could alter strategies for regenerative medicine.

However, there are obstacles to be overcome. Importantly, it must be shown that iN reprogramming has been established after silencing the expression of the three exogenous transcription factors to confirm that an intrinsic

and stable conversion of cell fate has occurred. This would also pave the way for safe, transient and non-viral reprogramming methods similar to those used in iPS cell production¹². Moreover, it remains to be seen whether adult human fibroblasts from a skin biopsy, or alternative accessible cell types such as blood cells, could be efficiently converted into functional neurons. Only mouse fibroblasts were used by Vierbuchen *et al.*, and the authors did not determine the functionality of the iN cells derived from adult mouse fibroblasts.

In addition, transplantation experiments will be necessary to see whether iN cells can integrate into the brain and ameliorate disease in animal models. A way of expanding cell numbers is also required. As many as millions of cells might be needed for therapeutic applications in humans; unlike iPS cells, there is no current step for expanding iN cell number. This same limitation, by contrast, may give iN cells an advantage over iPS cells, because they are unlikely to form tumours in the way that pluripotent stem cells can.

Nonetheless, we have an exciting prospect. If iN conversion is possible with human cells,

it could be quickly applied to the creation of disease-specific neurons for disease modelling and drug discovery, and to understanding the genetic and epigenetic mechanisms that determine cell fate. The question is no longer whether cell fates can be substantially manipulated without reversion to an undifferentiated pluripotent state. Rather, it is how many different cell types can now be generated by activating distinct combinations of lineage-specific factors. ■

Cory R. Nicholas and Arnold R. Kriegstein are at the Eli and Edythe Broad Center of Regeneration Medicine and Stem Cell Research, UCSF School of Medicine, San Francisco, California 94143-0525, USA.

e-mail: kriegsteina@stemcell.ucsf.edu

1. Vierbuchen, T. *et al.* *Nature* **463**, 1035–1041 (2010).
2. Takahashi, K. & Yamanaka, S. *Cell* **126**, 663–676 (2006).
3. Zhou, Q. *et al.* *Nature* **455**, 627–632 (2008).
4. Gurdon, J. B. & Uehlinger, V. *Nature* **210**, 1240–1241 (1966).
5. Han, D. W. *et al.* *Stem Cells* **26**, 445–454 (2008).
6. Wagers, A. J. & Weissman, I. L. *Cell* **116**, 639–648 (2004).
7. Zhou, Q. & Melton, D. A. *Cell Stem Cell* **3**, 382–388 (2008).
8. Letinic, K., Zoncu, R. & Rakic, P. *Nature* **417**, 645–649 (2002).
9. Fode, C. *et al.* *Genes Dev.* **14**, 67–80 (2000).
10. Berninger, B. *et al.* *J. Neurosci.* **27**, 8654–8664 (2007).
11. Toma, J. G. *et al.* *Nature Cell Biol.* **3**, 778–784 (2001).
12. Kim, D. *et al.* *Cell Stem Cell* **4**, 472–476 (2009).

CLIMATE CHANGE

Tropical cyclones in the mix

Ryan L. Sriver

What was responsible for the unusual climatic conditions that prevailed during the early Pliocene, 5 million to 3 million years ago? Modelling studies point to intense tropical-cyclone activity as a possible answer.

During the early Pliocene, many factors that affect climate were similar to those of today, including the positions of the continents, the intensity of sunlight and the atmospheric concentrations of carbon dioxide¹. But at this time, 5 million to 3 million years ago, the global mean temperature was about 4 °C warmer; and surface conditions in the tropical oceans resembled a permanent El Niño, marked by anomalously warm temperatures in the eastern tropical Pacific. Currently, El Niño events are intermittent, occurring roughly every 3–8 years, and can alter temperature and precipitation patterns worldwide.

On page 1066 of this issue, Fedorov *et al.*² propose that increased tropical-cyclone activity was a key contributor to the climate of the early Pliocene, part of a positive-feedback mechanism that maintained warmth with permanent El Niño-like conditions. These results may provide clues to understanding not only the climate of the early Pliocene, but also the nature of future climate change in a greenhouse world.

Much attention has been focused on understanding how the frequency and intensity of tropical cyclones might alter in response to changes in Earth's climate. However, it now

seems that these events do not just passively respond to climate change. Rather, there is mounting evidence that tropical cyclones have an active role in the dynamics of the climate system, primarily as a source of vertical mixing in the ocean^{3–6}. This mixing contributes to maintaining the large-scale ocean circulation⁷ that transports heat around the globe. Thus, tropical cyclones may be closely tied to global temperature patterns through feedbacks associated with vertical ocean mixing and transport. These feedbacks may help in understanding past climate paradoxes in which conditions were demonstrably different from those of today. But such conditions are difficult to simulate in the current generation of climate models, which do not typically include feedbacks from tropical cyclones.

Fedorov *et al.*² show how tropical cyclones may have contributed to the climate of the early Pliocene. Using a multifaceted modelling approach, they demonstrate that the large-scale atmospheric conditions could have favoured widespread cyclone activity, with the global frequency of events being almost double that of the present day. This increased activity would have led to more of the vertical ocean mixing

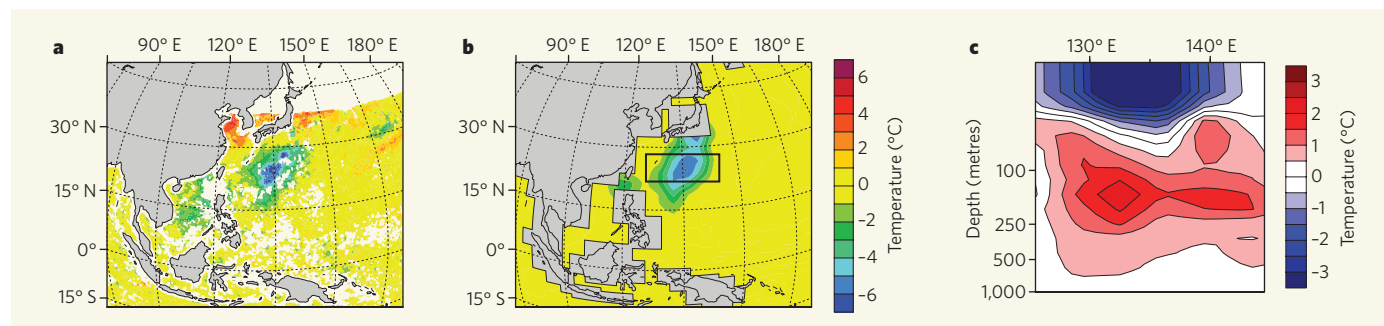


Figure 1 | The tropical-cyclone heat pump. **a**, In this satellite image of Typhoon Kirogi (year 2000), a cold wake can be seen that has been created by cool water brought to the surface by enhanced vertical mixing. **b**, Simulation in an ocean-circulation model of the wake forced by tropical-cyclone winds at the ocean's surface. **c**, The vertical structure of the modelled wake (boxed area in **b**) shows warming below the cold anomaly owing to heat from the surface that has been pumped down into the ocean interior, where it can be

transported by the large-scale circulation. In regions such as the subtropical central Pacific, cyclone mixing may influence the shallow wind-driven 'overturning' circulation, which flows towards the Equator at depth and feeds into the equatorial undercurrent. The warm water returns to the surface in the eastern equatorial Pacific. Fedorov *et al.*² argue that increased tropical-cyclone activity in the Pacific, and the heat pump produced by vertical mixing, contributed to permanent El Niño-like conditions during the early Pliocene.

that pumps heat from the surface down into the oceanic interior (Fig. 1).

This scenario sets up a possible feedback mechanism able to sustain El Niño-like temperature patterns in the equatorial Pacific, as follows. Extreme tropical-cyclone surface winds vigorously stir the normally well-stratified waters of the upper ocean, bringing cold water up to the surface and pumping warm surface water downwards (Fig. 1). In the central Pacific, much of the heat pumped downwards is carried by the shallow wind-driven 'overturning' circulation towards the Equator, where it eventually returns to the surface in the equatorial upwelling regions in the eastern Pacific. The net result is warmer surface waters in the equatorial Pacific and, more generally, warmer ocean surface temperatures throughout the tropics. These conditions contribute to sustaining the increased tropical-cyclone activity and the associated vertical ocean mixing, thus closing the feedback loop.

Using a fully coupled ocean-atmosphere general circulation model, Fedorov *et al.*² include an idealized representation of tropical cyclones by prescribing additional ocean mixing along latitudes at which tropical cyclones occur. In doing so, they are able to simulate a climate state very similar to that thought to have occurred during the early Pliocene — including the permanent El Niño-like surface-temperature structure.

These results are promising but represent only a preliminary step in including the effects of tropical cyclones in climate models. Tropical cyclones trigger short episodes of extremely vigorous ocean mixing. The transient and extreme nature of these events cannot be captured using prescribed mixing values that are constant in space and time. Furthermore, it is not yet clear how much ocean mixing is done by tropical cyclones on a global scale. The authors use mixing estimates from previous work based on the global surface-temperature response to cyclones^{4,8}, but those findings were largely exploratory and are first-order estimates at best. Additional

insight into the question could be provided by using, for example, a more sophisticated ocean-modelling approach that incorporates tropical-cyclone wind-forcing on a global scale.

Tropical cyclones may be transient, but they can modify the large-scale atmospheric and oceanic environments. Thus, feedbacks may occur that limit their intensity and formation. Idealized modelling approaches that prescribe the effects of cyclones cannot capture such feedbacks, which could influence the amount of ocean mixing, and the eventual heat transport. Further work is needed to reflect the full extent of ocean-atmosphere feedbacks associated with tropical cyclones.

As to the future, much of what we presume to understand about oceanic responses to global warming rests on the assumption that a warmer (and therefore more strongly stratified) tropical ocean will undergo less mixing^{1,9}. Fedorov and colleagues' findings² challenge this idea: they suggest that warmer tropical oceans will actually mix more because warmer climates will experience more tropical cyclones. If they are correct, a fundamental shift will be needed in our perception of processes in the tropical

ocean in the context of a changing climate.

Furthermore, given the strong evidence that there will be a substantial increase in the frequency of intense tropical cyclones over the next century¹⁰, and the fact that the strongest cyclones cause the largest amount of ocean mixing⁸, the results of Fedorov *et al.* may have implications for the future incidence of El Niño events. Such events could become a much more prevalent feature of Earth's climate.

Ryan L. Sriver is in the Department of Meteorology, The Pennsylvania State University, University Park, Pennsylvania 16802-5013, USA. e-mail: rsriver@psu.edu

1. Fedorov, A. V. *et al. Science* **312**, 1485–1489 (2006).
2. Fedorov, A. V., Brierley, C. M. & Emanuel, K. *Nature* **463**, 1066–1070 (2010).
3. Emanuel, K. J. *Geophys. Res.* **106**, 14771–14781 (2001).
4. Sriver, R. L. & Huber, M. *Nature* **447**, 577–580 (2007).
5. Korty, R. L. *et al. J. Clim.* **21**, 638–654 (2008).
6. Jansen, M. & Ferrari, R. *Geophys. Res. Lett.* **36**, doi:10.1029/2008GL036796 (2009).
7. Wunsch, C. & Ferrari, R. *Annu. Rev. Fluid Mech.* **36**, 281–314 (2004).
8. Sriver, R. L., Huber, M. & Nusbaumer, J. *Geochim. Geophys. Geosyst.* **9**, doi:10.1029/2007GC001842 (2008).
9. Philander, S. G. & Fedorov, A. V. *Paleoceanography* **18**, doi:10.1029/2002PA000837 (2003).
10. Bender, M. A. *et al. Science* **327**, 454–458 (2010).

GEOMICROBIOLOGY

Sediment reactions defy dogma

Kenneth H. Nealson

Redox reactions in widely spatially separated layers of marine sediments are coupled to each other. This suggests that bacteria mediate the flow of electrons between the layers — an idea that would previously have been dismissed.

To a human, 12 millimetres doesn't seem like much of a distance. But to a bacterium it amounts to 10,000 body lengths — equivalent to about 20 kilometres in human terms. With this in mind, the report by Nielsen *et al.*¹ on page 1071 of this issue is truly astonishing. The authors show that microbes can

respond to chemical changes across millimetre distances in marine sediments, thus altering the subsurface chemistry of those sediments. The phenomenon is initiated so quickly that it can't involve molecular diffusion — the usual means by which chemical changes are transmitted through sedimentary layers.

Marine sediments typically become anoxic because the bacteria within them consume oxygen as it diffuses down from the overlying water. This process establishes a series of sedimentary layers, within which a different kind of molecule (or ion) accepts electrons from oxygen and is consumed to form a chemically reduced product (Fig. 1). In one of the lower layers, sulphate (SO_4^{2-}) is converted to highly toxic hydrogen sulphide (H_2S), which accumulates and poisons the environment for most oxygen-consuming microorganisms. The hydrogen sulphide can, in turn, be converted into sulphate or other oxidized forms of sulphur by bacteria that use inorganic material as an energy source.

Nielsen *et al.*¹ worked with sediments in which oxygen could diffuse to a depth of a couple of centimetres. When they replaced oxygenated water in this region (the oxic zone) with anoxic water, they observed a rapid chemical response in the underlying sediments: within an hour, the sulphide layer began to move upward, most probably because less hydrogen sulphide was being consumed by bacteria than before. By contrast, when the authors replenished the water overlying the sediments with oxygen, creating a new oxic zone, the sulphide layer began to recede within an hour as more hydrogen sulphide was consumed. In concert with this increase in sulphide consumption, Nielsen and colleagues recorded a rise in pH near the oxic–anoxic interface. This is consistent with a reaction taking place in the zone in which oxygen reacts to produce water, consuming protons in the process (and so increasing the pH).

The authors argue¹ that the only explanation for these results is that some mechanism operates in which bacteria allow electrons to flow from deeper sediments to the surface, coupling redox reactions in the sulphide layer with those in the oxic zone (Fig. 1). What's more, they propose that this unknown mechanism allows not only chemical communication, but also the transport of energy (in the form of electrons) across distances normally regarded as being far greater than any distance-scale associated with bacterial metabolism. They argue convincingly that the rapidity of these responses requires nearly real-time connections, which can't be explained by diffusive processes across such distances. They also contend that the rise in pH in the oxic zone is not caused by the direct reaction of oxygen with other chemical species found in anoxic sediments, as such reactions would not consume protons.

Instead, the authors propose three possible mechanisms to account for the observed electron flow: enzymes on bacterial outer membranes might transport electrons to solid substrates in the subsurface; conductive 'nanowires' might connect microbial cells, creating a network of bacteria that spans large distances in sediments; or other sedimentary components might be responsible, such as metallic conductors or the mineral pyrite. Such hypotheses would at one time have been

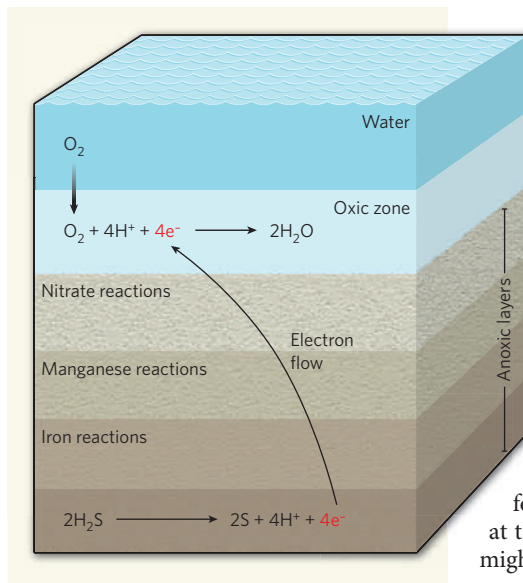


Figure 1 | Coupled reactions in marine sediments. Marine sediments typically consist of several layers. Oxygen from overlying water diffuses into the top layer of sediment (the oxic zone), where it is reduced by bacteria to form water. Lower sedimentary layers are anoxic, and are characterized by different reaction cycles in which nitrate, manganese(IV) or iron(III) ions are reduced and re-oxidized by microbial activity. Nielsen *et al.*¹ report that a reaction in one of the anoxic layers, in which hydrogen sulphide (H_2S) is oxidized by bacteria to produce sulphur, is coupled to the oxygen-reduction reaction in the oxic layer. The coupling of these reactions can be explained only if electrons (e^-) produced from the oxidation are rapidly transported to the oxic layer, to be used in the reduction. The authors propose that bacteria mediate the electron flow.

considered heretical to those in the field, but discoveries made in the past few years now make these arguments tenable.

Let's start with the first proposed mechanism. Two groups of bacteria, *Geobacter*² and *Shewanella*³, have well-characterized enzymes in their outer membranes that are capable of extracellular electron transport — the bacteria use the enzymes for the respiration of solid substrates, such as metal oxides. In support of the second hypothesis, the same two groups of bacteria also have conductive nanowires, either in the form of pilins⁴ (hair-like appendages) or pilin-like proteins that are associated with multi-haem cytochrome enzymes^{5,6} (which are capable of electron transport). Although pilins and pilin-like proteins contain conductive materials, to date, no one has demonstrated that they can actually conduct electrons along their lengths.

As for the third suggested mechanism (that sedimentary components mediate electron flow), Nielsen and colleagues¹ note several lines of evidence in support of this idea, including conductivity measurements of sediments^{7,8} and demonstrations of electric-current production by sediment batteries^{9–11} (which exploit naturally occurring voltage differences between anoxic sedimentary layers and the overlying

oxic zone). No mechanism for the conductivity recorded in these studies^{7–11} has been established, however.

So why should we care about Nielsen and colleagues' findings? One reason is that their data may be relevant to energy transfer and electron flow through many different environments, not just the sediments studied¹. If so, the microbe-mediated, electronic coupling of distant regions might act as much more than just a rapid mechanism for removing toxic hydrogen sulphide from subsurface sediments.

In fact, the authors note¹ that even if all of the subsurface hydrogen sulphide was consumed, it would account for only part of the electron flow measured at the oxic surface of the sediments. This might mean that a variety of other reactions in anoxic sediments are also mediated by rapid electron flow to the surface, such as the oxidation of organic carbon, or of inorganic electron acceptors found in such environments. This in turn would implicate electron flow in processes such as bioremediation, corrosion and carbon sequestration in sediments.

Finally, one of the tenets of anaerobic microbiology is that of 'interspecies hydrogen exchange' — a mechanism in which hydrogen is consumed by one microorganism to drive an otherwise slow or thermodynamically unfavourable reaction performed by another. Processes such as anaerobic methane oxidation are thought to use such a mechanism, although no hydrogen transfer has yet been proved. Microbial electron transfer could accomplish the same catalytic feat, perhaps faster and more specifically (so that electrons are transferred directly between only the right kinds of organisms) than hydrogen transfer. If so, new paradigms will emerge in the fields of microbial energetics and metabolism, and perhaps also in ecology and evolution. As Nielsen and colleagues' study¹ has shown, the time is ripe for microbiologists to open themselves up to unusual ideas.

Kenneth H. Nealson is in the Department of Earth Sciences, University of California, Los Angeles, Los Angeles, California 90089-0740, USA.
e-mail: knealson@usc.edu

1. Nielsen, L. P., Risgaard-Petersen, N., Fossing, H., Christensen, P. B. & Sayama, M. *Nature* **463**, 1071–1074 (2010).
2. Lovley, D. R. *Nature Rev. Microbiol.* **4**, 497–508 (2006).
3. Fredrickson, J. K. *et al.* *Nature Rev. Microbiol.* **6**, 592–603 (2008).
4. Reguera, G. *et al.* *Nature* **435**, 1098–1101 (2005).
5. Gorby, Y. A. *et al.* *Proc. Natl Acad. Sci. USA* **103**, 11358–11363 (2006).
6. El-Naggar, M. Y., Gorby, Y. A., Xia, W. & Nealson, K. H. *Biophys. J.* **95**, L10–L12 (2008).
7. Sato, M. & Mooney, H. M. *Geophysics* **25**, 226–249 (1960).
8. Ntarlagiannis, D., Atekwana, E. A., Hill, E. A. & Gorby, Y. *Geophys. Res. Lett.* **34**, L17305 (2007).
9. Rabaey, K. *et al.* *ISME J.* **1**, 9–18 (2007).
10. Reimers, C. E., Tender, L. M., Fertig, S. & Wang, W. *Environ. Sci. Technol.* **35**, 192–195 (2001).
11. Ryckelynck, N., Stecher, H. A. & Reimers, C. E. *Biogeochemistry* **76**, 113–139 (2005).

Direct conversion of fibroblasts to functional neurons by defined factors

Thomas Vierbuchen^{1,2}, Austin Ostermeier^{1,2}, Zhiping P. Pang³, Yuko Kokubu¹, Thomas C. Südhof^{3,4} & Marius Wernig^{1,2}

Cellular differentiation and lineage commitment are considered to be robust and irreversible processes during development. Recent work has shown that mouse and human fibroblasts can be reprogrammed to a pluripotent state with a combination of four transcription factors. This raised the question of whether transcription factors could directly induce other defined somatic cell fates, and not only an undifferentiated state. We hypothesized that combinatorial expression of neural-lineage-specific transcription factors could directly convert fibroblasts into neurons. Starting from a pool of nineteen candidate genes, we identified a combination of only three factors, *Ascl1*, *Brn2* (also called *Pou3f2*) and *Myt1l*, that suffice to rapidly and efficiently convert mouse embryonic and postnatal fibroblasts into functional neurons *in vitro*. These induced neuronal (iN) cells express multiple neuron-specific proteins, generate action potentials and form functional synapses. Generation of iN cells from non-neural lineages could have important implications for studies of neural development, neurological disease modelling and regenerative medicine.

The diverse cell types present in the adult organism are produced during development by lineage-specific transcription factors that define and reinforce cell-type-specific gene expression patterns. Cellular phenotypes are further stabilized by epigenetic modifications that allow faithful transmission of cell-type-specific gene expression patterns over the lifetime of an organism^{1,2}. Recent work showing that four transcription factors are sufficient to induce pluripotency in primary fibroblasts demonstrated that fully differentiated cells can be induced to undergo dramatic cell fate changes³. Similarly, the transfer of somatic cell nuclei into oocytes, as well as cell fusion of pluripotent cells with differentiated cells, have proven to be capable of inducing pluripotency^{4–9}. This remarkable transformation has been interpreted as a reversion of mature into more primitive developmental states, with a concomitant erasure of developmentally relevant epigenetic information¹⁰. Therefore, direct reprogramming between divergent lineages could be unique to reprogramming into an embryonic state, and might not be possible between different somatic cell states. However, cell fusion or forced expression of lineage-specific genes in somatic cells can induce traits of other cell types^{11,12}. For example, the basic helix–loop–helix (bHLH) transcription factor *MyoD* (also called *Myod1*) can induce muscle-specific properties in fibroblasts but not hepatocytes^{13,14}; ectopic expression of interleukin (IL)-2 and granulocyte–macrophage colony-stimulating factor receptors can lead to myeloid conversion in committed lymphoid progenitor cells¹⁵; expression of *Cebpa* in B cells or *PU.1* (also called *Sfp1*) and *Cebpa* in fibroblasts induces characteristics of macrophages^{16–18}; deletion of *Pax5* can induce B cells to de-differentiate towards a common lymphoid progenitor¹⁹; and the bHLH transcription factor neurogenin 3, in combination with *Pdx1* and *Mafa*, can efficiently convert pancreatic exocrine cells into functional β -cells *in vivo*²⁰. Here, we set out to determine whether specific transcription factors could directly convert fibroblasts into functional neurons.

A screen for neuronal-fate-inducing factors

Reasoning that multiple transcription factors would probably be required to reprogram fibroblasts to a neuronal fate, we cloned a

total of 19 genes that are specifically expressed in neural tissues, have important roles in neural development, or have been implicated in epigenetic reprogramming (Supplementary Table 1). A pool of lentiviruses containing all 19 genes (19F pool) was prepared to infect mouse embryonic fibroblasts (MEFs) from TauEGFP knock-in mice, which express EGFP specifically in neurons^{21,22} (see Fig. 1a for experimental outline). Great care was taken to exclude neural tissue from the MEF preparation, and we were unable to detect evidence for the presence of neurons or neural progenitor cells in these cultures using immunofluorescence, fluorescence activated cell sorting (FACS) and polymerase chain reaction with reverse transcription (RT–PCR) analyses (Supplementary Fig. 1). However, uninfected MEFs did contain rare Tuj1-positive, TauEGFP-negative cells with fibroblast-like morphology, indicative of weak Tuj1 (that is, β -III-tubulin) expression in non-neuronal cells (Fig. 1b, c and Supplementary Fig. 1a). In contrast, 32 days after infection with the 19F pool, we detected Tuj1-positive cells with typical neuronal morphologies and bright TauEGFP fluorescence (Fig. 1d,e). Thus, some combination(s) of the genes in the 19F pool was capable of converting MEFs into iN cells.

We next set out to narrow down the number of transcription factors required for generation of iN cells. Given their important roles in neuronal cell fate determination^{23–26} we first tested the bHLH transcription factors *Ascl1* (also known as *Mash1*) and *Neurod1* individually. Notably, we observed occasional Tuj1-positive, TauEGFP-positive cells exhibiting a simple mono- or bipolar morphology after infection with only *Ascl1* (Supplementary Fig. 2b). However, 19F iN cells showed more complex morphologies, which indicated that the activity of *Ascl1* alone was not sufficient to recapitulate the full activity of the 19F pool (compare to Fig. 1d, e). We therefore tested the neuron-inducing activity of *Ascl1* in combination with each of the remaining 18 candidate genes (Supplementary Fig. 2a). Five genes (*Brn2*, *Brn4* (*Pou3f4*), *Myt1l*, *Zic1* and *Olig2*) substantially potentiated the neuron-inducing activity of *Ascl1* (Supplementary Fig. 2a, b). Importantly, none of these five genes generated iN cells when tested individually (data not shown). Next, we tested whether combinatorial expression of these factors with *Ascl1* could further increase the induction of neuron-like cells by infecting

¹Institute for Stem Cell Biology and Regenerative Medicine, Department of Pathology, ²Program in Cancer Biology, ³Department of Molecular and Cellular Physiology, ⁴Howard Hughes Medical Institute, Stanford University School of Medicine, 1050 Arastradero Road, Palo Alto, California 94304, USA.

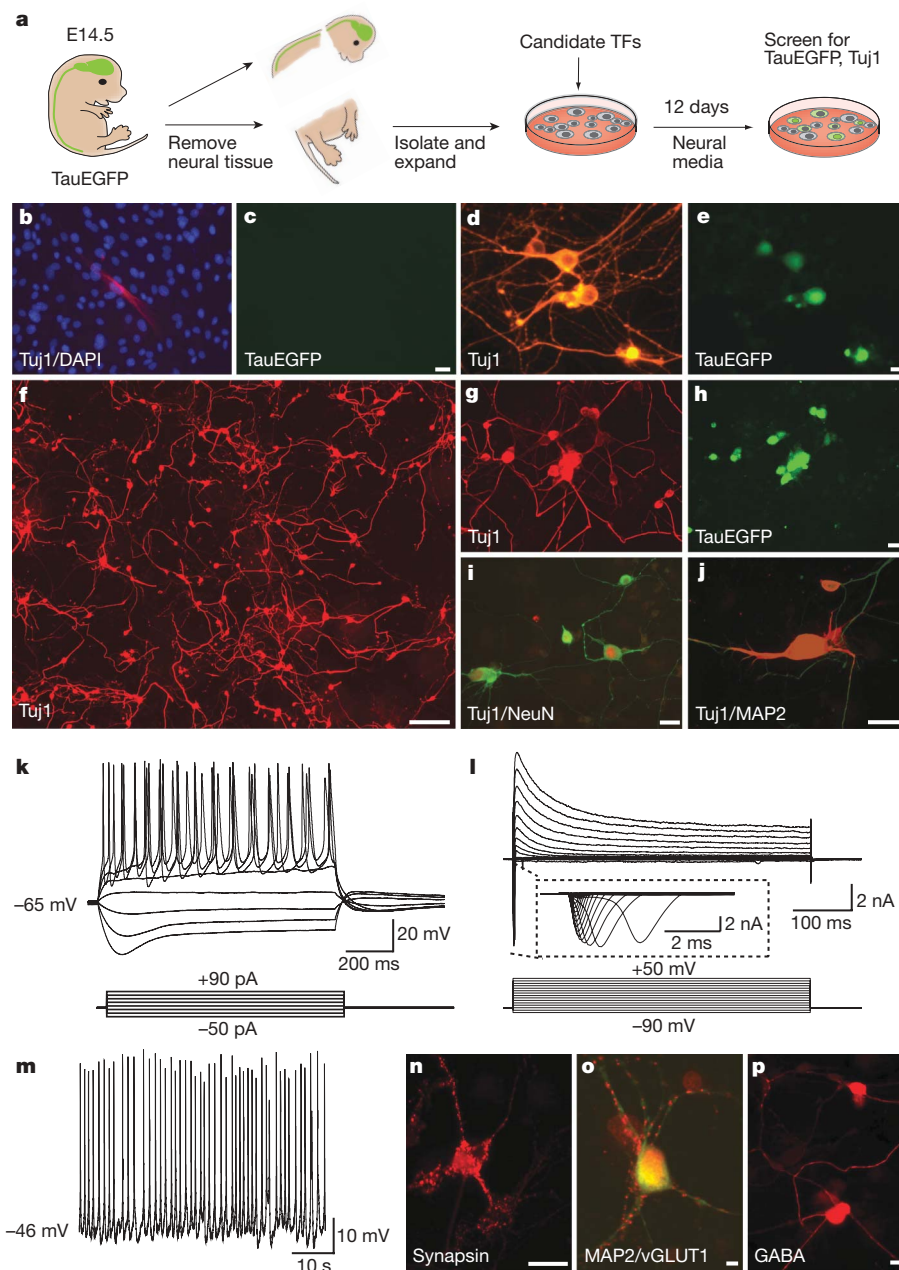


Figure 1 | A screen for neuronal-fate-inducing factors and characterization of MEF-derived iN cells **a**, Experimental rationale. **b**, Uninfected, p3 TauEGFP MEFs contained rare Tuj1-positive cells (red) with flat morphology. Blue indicates 4,6-diamidino-2-phenylindole (DAPI) counterstain. **c**, Tuj1-positive fibroblasts do not express visible TauEGFP. **d**, **e**, MEF iN cells express Tuj1 (red) and TauEGFP (green) and display complex neuronal morphologies 32 days after infection with the 19-factor (19F) pool. **f**, Tuj1 expression in MEFs 13 days after infection with the 5F pool. **g**–**j**, MEF-derived Tuj1-positive iN cells co-express the pan-neuronal markers TauEGFP (**h**), NeuN (**i**) and MAP2 (**j**). **k**, Representative TauEGFP MEFs with a pool of *Brn2*, *Myt1l*, *Zic1*, *Olig2* and *Ascl1* viruses (5F pool). Given its close similarity to *Brn2*, we did not include *Brn4* in the 5F pool. Twelve days after infection, we detected frequent Tuj1-positive iN cells with highly complex morphologies (Fig. 1f). These 5F iN cells also expressed the pan-neuronal markers MAP2, NeuN and synapsin (Fig. 1i–j, n). Similar results were obtained with iN cells derived from BALB/c MEFs (Supplementary Fig. 3a).

Characterization of 5-factor iN cells

To explore whether iN cells have functional membrane properties similar to neurons, we performed patch-clamp recordings of

traces of membrane potential responding to step depolarization by current injection (lower panel). Membrane potential was current-clamped at around -65 mV. **l**, Representative traces of whole-cell currents in voltage-clamp mode; cells were held at -70 mV; step depolarization from -90 mV to $+50$ mV at 10-mV intervals was delivered (lower panel). The inset shows Na^+ currents. **m**, Spontaneous action potentials recorded from a 5F MEF iN cell 8 days after infection. No current injection was applied. **n**–**p**, Twenty-two days after infection 5F MEF iN cells expressed synapsin (red, **n**) and vesicular glutamate transporter 1 (vGLUT1; red, **o**) or GABA (**p**). Scale bars: 5 μm (**o**), 10 μm (**e**, **j**, **n**, **p**) 20 μm (**c**, **h**, **i**) and 200 μm (**f**).

TauEGFP-positive cells on days 8, 12 and 20 after infection. For the majority of the iN cells analysed (85.1%, $n = 47$), action potentials could be elicited by depolarizing the membrane in current-clamp mode (Fig. 1k). Six cells (14.2%, $n = 42$) showed spontaneous action potentials, some as early as 8 days after transduction (Fig. 1m). These action potentials could be blocked by tetrodotoxin (TTX), a specific inhibitor of Na^+ ion channels (Supplementary Fig. 3e). Moreover, in voltage-clamp mode we observed both fast, inactivating inward and outward currents, which probably correspond to opening of voltage-dependent K^+ - and Na^+ -channels, respectively, with a possible contribution of Ca^{2+} channels to the whole-cell currents (Fig. 1l and

Supplementary Fig. 3f). The resting membrane potentials ranged between -30 and -69 mV with an average of ~ -55 mV on day 20 ($n = 12$, Supplementary Tables 2 and 3). Additionally, we asked whether these cells possessed functional ligand-gated ion channels. Induced neuronal cells responded to exogenous application of GABA (γ -aminobutyric acid), and this response could be blocked by the GABA receptor antagonist picrotoxin (Supplementary Fig. 3g). Thus, MEF-derived iN cells seem to exhibit the functional membrane properties of neurons and possess ligand-gated GABA receptors.

We then sought to characterize the neurotransmitter phenotype of iN cells. After 21 days of culture in minimal neuronal media, we detected vGLUT1-positive puncta outlining MAP2-positive neurites of some cells, indicating the presence of excitatory, glutamatergic neurons (Fig. 1o). In addition, we found iN cells labelled with antibodies against GABA, the major inhibitory neurotransmitter in brain (Fig. 1p). Some iN cells (9 out of ~ 500) contained the Ca^{2+} -binding protein calretinin, a marker for cortical interneurons and other neuronal subtypes (Supplementary Fig. 3c). No expression of tyrosine hydroxylase, choline acetyltransferase or serotonin was detected. The vast majority of iN cells were negative for peripherin, an intermediate filament characteristic of peripheral neurons (data not shown)²⁷.

Functional neurons from tail fibroblasts

To evaluate whether iN cells could also be derived from postnatal cells, we isolated tail-tip fibroblasts (TTFs) from 3-day-old TauEGFP and Rosa26-rtTA mice²⁸. Similar to our MEF cultures, we could not detect pre-existing neurons, glia, or neural progenitor cells (Supplementary Fig. 1a). Twelve days after infecting TTFs with the 5F pool,

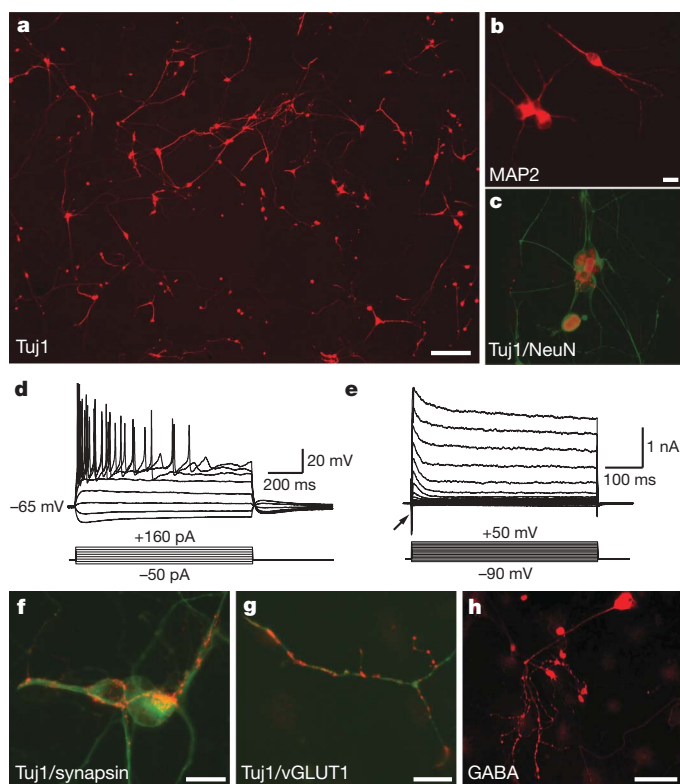


Figure 2 | Efficient induction of neurons from perinatal tail-tip fibroblasts **a**, Tuj1-stained tail-tip fibroblast (TTF) 13 days after infection with the 5F pool. **b**, **c**, TTF iN cells express the pan-neuronal markers MAP2 (**b**) and NeuN (**c**). **d**, Representative traces showing action potentials elicited at day 13 after infection. Nine of eleven cells recorded exhibited action potentials. **e**, Whole-cell currents recorded in voltage-clamp mode. Inward fast inactivating Na^+ currents (arrow) and outward currents can be observed. **f–h**, At 21 days after infection TTF iN cells express synapsin (**f**), vGLUT1 (**g**) and GABA (**h**). **c**, **f** and **g** are overlay images with the indicated marker (red) and Tuj1 (green). Scale bars: 20 μm (**b**, **f**, **g**), 100 μm (**h**), 200 μm (**a**).

Tuj1-positive iN cells with a complex, neuronal morphology could be readily detected (Fig. 2a). TTF iN cells expressed the pan-neuronal markers NeuN, MAP2 and synapsin (Fig. 2b, c, f). Electrophysiological recordings 12 days after infection demonstrated an average resting membrane potential of ~ -57 mV (range: -35 to -70 mV, $n = 11$), firing of action potentials (81.8%, $n = 11$) (Fig. 2d),

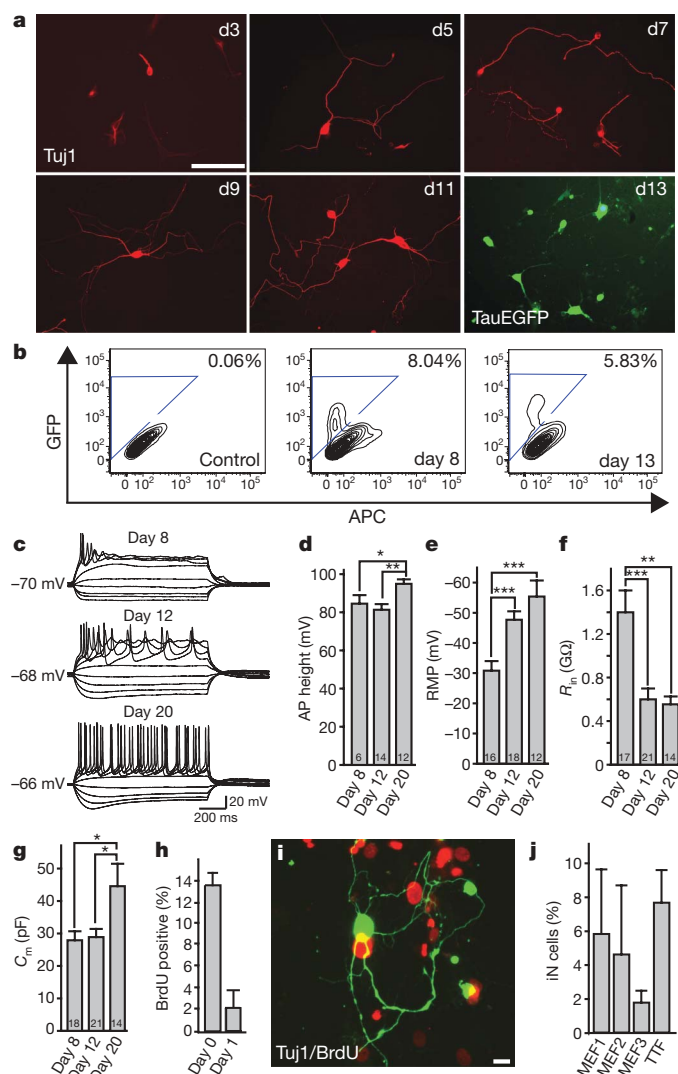


Figure 3 | The 5F-pool-induced conversion is rapid and efficient **a**, Tuj1-positive iN cells (red) show morphological maturation over time after viral infections. At day 13, TauEGFP expression outlines neuronal processes. **b**, FACS analysis of TauEGFP expression 8 and 13 days after infection. Control indicates uninfected TauEGFP MEFs. APC, allophycocyanin. **c**, Representative traces showing action potentials elicited from MEF iN cells at days 8, 12 and 20 after infection. Cells were maintained at a potential of approximately -65 to -70 mV. Step current injection protocols were used from -50 to $+70$ pA. Scale bar applies to all traces. **d–g**, Quantification of membrane properties in MEF iN cells at 8, 12 and 20 days after infection. Numbers in the bars represent the numbers of recorded cells. Data are presented as mean \pm s.e.m. * $P < 0.05$; ** $P < 0.01$; *** $P < 0.001$ (Student's *t*-test). AP, action potential; C_m , membrane capacitance; R_{in} , membrane input resistances; RMP, resting membrane potential. Action potential heights were measured from the baseline. **h**, BrdU-positive iN cells after BrdU treatment from day 0–13 or day 1–13 after transgene induction. **i**, Example of a Tuj1 (green) positive cell not labelled with BrdU (red) when added at day 0 after addition of doxycycline. Data are presented as mean \pm s.d. **j**, Efficiency estimates for iN cell generation 13 days after infection (see Methods). Every bar represents an independent experiment. Doxycycline was added 48 h after plating in MEF experiment 1 and after 24 h in MEF experiments 2 and 3. Error bars indicate \pm s.d. of cell counts. Scale bars: 10 μm (**i**), 100 μm (**a**).

and expression of functional voltage-gated membrane channel proteins (Fig. 2e and Supplementary Tables 2 and 3). We were also able to detect vGLUT1-positive as well as GABA-positive cells (Fig. 2g, h). Despite extensive screening (>1,000 iN cells analysed), we were unable to detect tyrosine hydroxylase, choline acetyltransferase, or serotonin expression. Induced neuronal cells exhibited rare peripherin-positive filaments (Supplementary Fig. 3d).

Neuronal induction is fast and efficient

Next, we assessed the kinetics and efficiency of 5F iN conversion. In MEFs, Tuj1-positive cells with immature neuron-like morphology were found as early as 3 days after infection (Fig. 3a). After 5 days, neuronal cells with long, branching processes were readily detected, and over time increasingly complex morphologies were evident, suggesting an active process of maturation in newly formed iN cells (Fig. 3a). Similarly, we detected TauEGFP expression as early as day five (Supplementary Fig. 3h). The fraction of TauEGFP-positive cells remained similar at 8 and 13 days after infection, as determined by FACS analysis, indicating no *de novo* generation of iN cells after day 8 (Fig. 3b). Electrophysiological parameters such as action potential height, resting membrane potential, membrane input resistance and membrane capacitance also showed signs of maturation over time (Fig. 3c–g and Supplementary Tables 2 and 3).

To estimate the conversion efficiency, we first determined how many of the MEF-derived iN cells divided after induction of the viral transgenes by treating the cells with 5-bromodeoxyuridine (BrdU) throughout the duration of the culture period and beginning 1 day after gene induction. The results showed that the vast majority of iN cells became post mitotic by 24 h after transgene activation (Fig. 3h, i). This allowed us to roughly estimate the conversion efficiency of our

method by quantifying the total number of Tuj1-positive iN cells in the entire dish on day 12, and dividing this number by the number of plated cells (see Methods). Using this method, the efficiency ranged from 1.8% to 7.7% in MEF and TTF iN cells (Fig. 3j) presumably due to slight variations in titres of the viruses. These calculations might be an underestimation of the true conversion rate because not all cells receive the necessary complement of viral transgenes.

iN cells form functional synapses

Because iN cells exhibited the membrane properties of neurons, we next wanted to assess whether iN cells have the capacity to form functional synapses. To accomplish this we used two independent methods. First, we determined whether iN cells were capable of synaptically integrating into pre-existing neural networks. We used FACS to purify TauEGFP-positive iN cells 7 days after infection and re-plated the 5F iN cells onto neonatal cortical neurons that had been cultured for 7 days *in vitro*. One week after re-plating, we performed patch-clamp recordings from TauEGFP-positive iN cells and observed spontaneous and rhythmic network activity typical of cortical neurons in culture (Fig. 4a, b). Both excitatory and inhibitory postsynaptic currents (EPSCs and IPSCs) could be evoked after electrical stimulation delivered from a concentric electrode placed 100–150 μm away from the patched iN cells (Fig. 4b–d). In the presence of the α -amino-3-hydroxy-5-methyl-4-isoxazole propionic acid (AMPA) and NMDA (*N*-methyl-D-aspartate) receptor channel blockers 6-cyano-7-nitroquinoxaline-2,3-dione (CNQX) and D(-)-2-amino-5-phosphonovaleric acid (D-AP5), spontaneous IPSCs were reliably detected (Fig. 4c, upper panel). Evoked IPSCs could be blocked by further addition of picrotoxin (Fig. 4c, middle panel). Similarly, at a holding potential of -70 mV and in the presence of picrotoxin, fast-decaying EPSCs mediated by AMPA receptors could be evoked (Fig. 4d, middle panel). Conversely, at a holding potential of $+60$ mV (which relieves the voltage-dependent blockade of

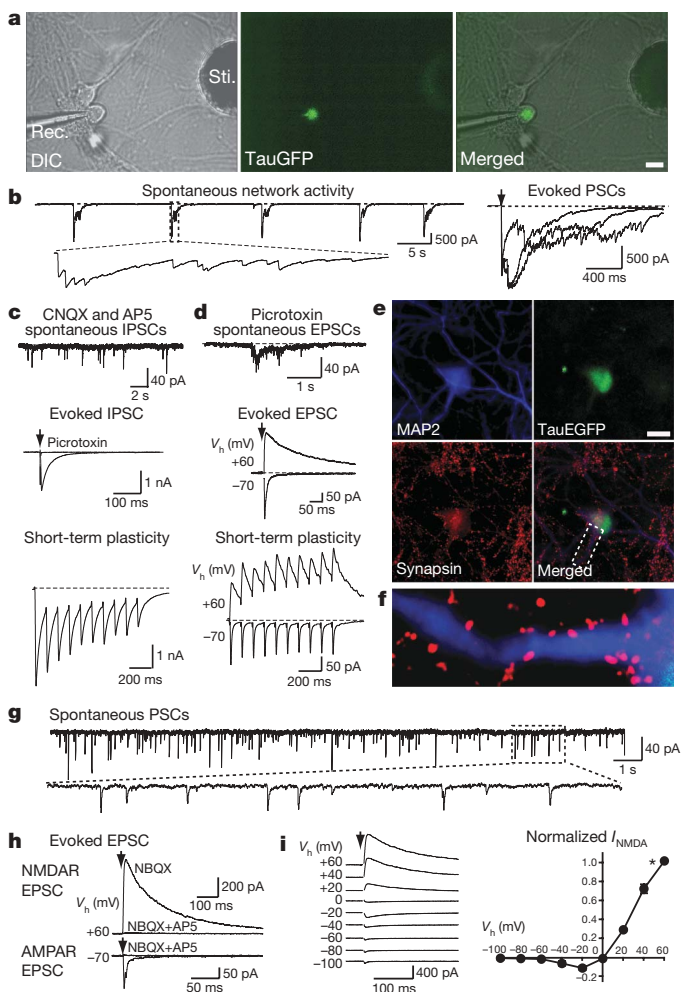


Figure 4 | MEF-derived iN cells show functional synaptic properties.

TauEGFP-positive iN cells were FACS purified 7–8 days after infection of MEFs and plated on cortical neuronal cultures (7 days *in vitro*, **a–f**) or on monolayer glia cultures (**g–i**). Electrophysiological recordings were performed 7–20 days after sorting. **a**, Recording electrode (Rec.) patched onto an TauEGFP-positive cell (middle panel) with a stimulation electrode (Sti.). The right panel is a merged picture of DIC and fluorescence images showing that the recorded cell is TauEGFP positive. **b**, Representative traces of spontaneous synaptic network activities and representative evoked postsynaptic currents (PSCs) after stimulation. **c**, In the presence of 20 μM CNQX and 50 μM D-AP5, a representative trace of spontaneous IPSCs is shown (upper panel). Evoked IPSCs could be elicited (middle panel) and blocked by the addition of picrotoxin. When a train of 10 stimulations was applied at 10 Hz, evoked IPSCs show depression (lower panel). **d**, In the presence of 30 μM picrotoxin, excitatory synaptic activities from EGFP-positive cells were observed. Spontaneous (upper panel) and evoked (middle panel) EPSCs are shown. At a holding potential (V_h) of -70 mV, AMPA receptor (AMPA)-mediated EPSCs were monitored. When the holding potentials were set at $+60$ mV, both AMPAR- and NMDAR-mediated EPSCs could be recorded. The lower panel shows the short-term synaptic plasticity of both AMPAR- and NMDAR-mediated synaptic activities. Arrows indicate time of stimulation. **e**, Example of a TauEGFP-positive iN cell expressing MAP2 among cortical neurons. **f**, Higher magnification ($\times 7$) of area marked in **e**. **g**, Representative spontaneous postsynaptic currents (PSCs) recorded from MEF iN cells co-cultured with glia. **h**, Representative traces of evoked EPSCs. NMDAR-mediated EPSCs in the presence of 10 μM NBQX (2,3-dihydroxy-6-nitro-7-sulphamoyl-benzo[f]quinoxaline-2,3-dione), an AMPA-receptor antagonist, were recorded at a holding potential (V_h) of $+60$ mV. Application of D-AP5 blocked the response. AMPAR-mediated EPSCs were recorded at a V_h of -70 mV. The AMPAR-evoked response is blocked by NBQX and AP5. **i**, Current–voltage (I – V) relationship of NMDAR-mediated EPSCs (left panel); representative traces of evoked EPSCs at different V_h as indicated. The right panel shows the summarized I – V relationship. NMDAR EPSC amplitudes (I_{NMDA}) are normalized to EPSCs at a V_h of $+60$ mV (indicated by an asterisk, $n = 5$). NMDAR EPSCs show ratifications at negative holding potentials, presumably because of the blockade of NMDAR by Mg^{2+} . Scale bars: 10 μm (**a**, **e**).

Mg²⁺ to NMDA receptors), slow-decaying NMDA-receptor-mediated EPSCs could be recorded (Fig. 4d, middle panel).

Moreover, synaptic responses recorded from iN cells showed signs of short-term synaptic plasticity, such as depression of IPSCs and facilitation of EPSCs during a high-frequency stimulus train (Fig. 4c, d, lower panels). The presence of synaptic contacts between iN cells and cortical neurons was independently corroborated by the immunocytochemical detection of synapsin-positive puncta surrounding MAP2-positive dendrites originating from EGFP-positive cells (Fig. 4e, f). We were also able to observe synaptic responses in similar experiments performed with iN cells derived from TTFs (Supplementary Fig. 4). These data demonstrate that iN cells can form functional postsynaptic compartments and receive synaptic inputs from cortical neurons.

Next we asked whether iN cells were capable of forming synapses with each other. To address this question we plated FACS-sorted TauEGFP-positive, MEF-derived 5F iN cells 8 days after infection onto a monolayer culture of primary astrocytes, which are thought to have an essential role in synaptogenesis^{29,30}. Importantly, we confirmed that these cultures were free of pre-existing Tuj1- or MAP2-positive neurons (data not shown). Patch-clamp recordings at 12–17 days after sorting indicated the presence of spontaneous postsynaptic currents in 5 out of 11 cells (Fig. 4g). Upon extracellular stimulation, evoked EPSCs could be elicited in a majority of the cells (9 out of 11 cells, Fig. 4h). Similar to iN cells cultured with primary cortical neurons, we were able to record both NMDA-receptor-mediated (9 out of 11 cells) and AMPA-receptor-mediated EPSCs (8 out of 11 cells; Fig. 4h, i). Interestingly, we were unable to detect obvious IPSCs in a total of 15 recorded 5F iN cells. These data indicate that iN cells are capable of forming functional synapses with each other, and that the majority of iN cells exhibit an excitatory phenotype.

Genes sufficient for neuronal conversion

As stated earlier, *Ascl1* was the only gene from the 5F pool that was sufficient to induce neuron-like cells in MEFs. We next attempted to determine the relative contribution of each of the five genes by removing each gene from the pool and assessing the efficiency of iN cell generation. Surprisingly, only the omission of *Ascl1* had a marked effect on induction efficiency (Supplementary Fig. 6a). Thus, we tested the effects of removing two genes at a time by evaluating all possible three-gene combinations. Our results indicated that either *Ascl1* or both *Brn2* and *Myt1l* must be present to generate iN cells (Fig. 5a). The most efficient conversions were achieved when *Ascl1* and *Brn2* were combined with either *Myt1l* (BAM pool) or *Zic1* (BAZ pool). The efficiencies in these conditions were two- to three-fold higher than the 5F pool when the total amount of virus was kept constant (Fig. 5a–d). In this experiment the BAM iN cells appeared to have a more complex morphology than the BAZ cells (Fig. 5c, d and Supplementary Fig. 7). Therefore, we focused our further analysis on the BAM pool.

MEF-derived BAM iN cells expressed the pan-neuronal markers MAP2 and synapsin (Fig. 5f). The BAM pool was capable of efficiently generating iN cells from perinatal TTFs (Fig. 5e and Supplementary Fig. 8a–e). After infecting TTFs from adult mice with these three factors, we could detect neuronal cells expressing TauEGFP, Tuj1, NeuN and MAP2 (Supplementary Fig. 9). Importantly, when co-cultured with astrocytes, both MEF and perinatal TTF-derived BAM iN cells were capable of forming functional synapses as determined by the presence of both NMDA- and AMPA-receptor mediated EPSCs (Fig. 5g, h). Similar to 5F iN cells, no IPSCs were detected in MEF-derived ($n = 16$) or TTF-derived ($n = 12$) BAM iN cells. This functional evidence indicates that a majority of BAM iN cells are excitatory. Indeed, 53% (111 out of 211 cells) of MEF BAM iN cells expressed Tbr1, a marker of excitatory cortical neurons, whereas less than 1% (3 out of ~500 cells) were GAD-positive (Supplementary Fig. 8f).

Our results left open the possibility that one or two factors might be able to induce functional neuronal properties in MEFs. Thus, we tested

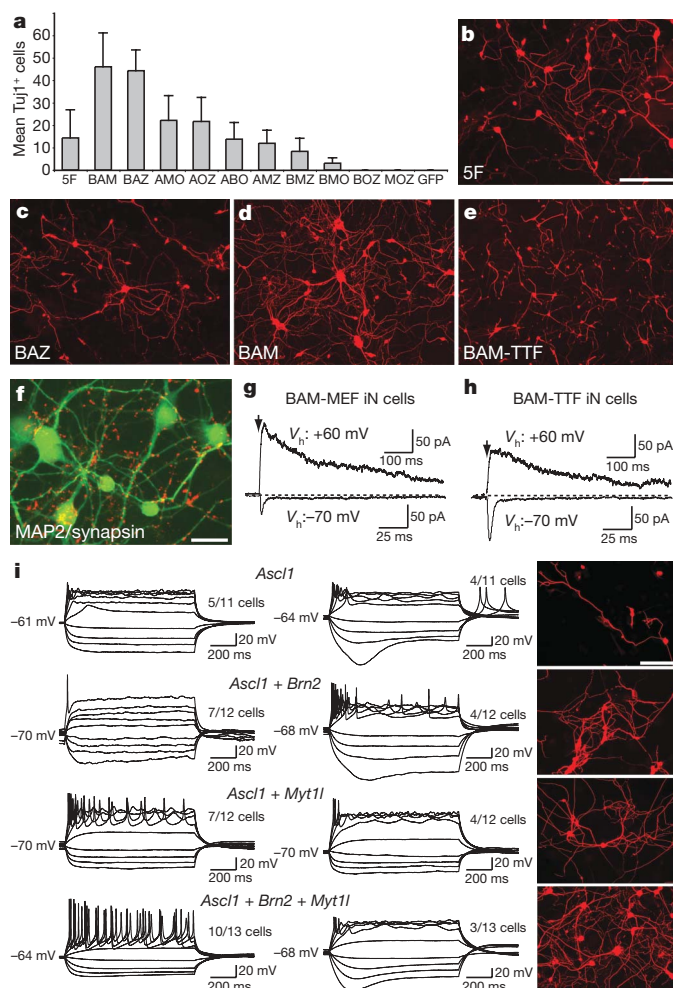


Figure 5 | Defining a minimal pool for efficient induction of functional iN cells **a**, Quantification of Tuj1-positive iN cells from TauEGFP MEFs infected with different three-factor combinations of the five genes. Each gene is represented by the first letter in its name. **A**, *Ascl1*; **B**, *Brn2*; **M**, *Myt1l*; **O**, *Olig2*; **Z**, *Zic1*. Averages from 30 randomly selected visual fields are shown (error bars indicate \pm s.d.). **b–d**, Representative images of Tuj1 staining of MEFs infected with the 5F (**b**), *Ascl1* + *Brn2* + *Zic1* (BAZ; **c**) and *Ascl1* + *Brn2* + *Myt1l* (BAM; **d**) pools. **e**, Tuj1 staining of perinatal TTF iN cells 13 days after infection with the BAM pool. **f**, BAM-induced MEF iN cells express MAP2 (green) and synapsin (red) 22 days after infection. **g**, Representative traces of synaptic responses recorded from MEF-derived BAM (3F) iN cells co-cultured with glia after isolation by FACS. V_h , holding potential. At a V_h of -70 mV, AMPAR-mediated EPSCs were recorded; at a V_h of $+60$ mV, NMDAR-mediated EPSCs were revealed. **h**, Synaptic responses recorded from TTF-derived 3F iN cells. **i**, Representative traces of action potentials elicited from MEF-derived iN cells transduced with the indicated gene combinations, recorded 12 days after infection. Cells were maintained at a resting membrane potential of approximately -65 to -70 mV. Step current injection protocols were used from -50 to $+70$ pA. Traces in each subgroup (left or right panels) represent subpopulations of neurons with similar responses. Numbers indicate the fraction of cells from each group that were qualitatively similar to the traces shown. Right panels: representative images of Tuj1 staining after recordings from each condition. Scale bars: 20 μ m (**f**) and 100 μ m (**b**, **i**).

smaller subsets of the BAM pool to determine their functionality. In many *Ascl1*-induced cells, current injection elicited action potentials, but their properties appeared to be immature, consistent with their simple neurite morphology (Fig. 5i and Supplementary Fig. 2b). MEFs infected with *Ascl1* and *Brn2* or *Myt1l* generated more mature action potentials and displayed more complex neuronal morphologies. In contrast, the majority of BAM iN cells exhibited repetitive action potentials with more mature characteristics, and displayed the most

complex neuronal morphologies. Thus, it seems likely that *Ascl1* alone is sufficient to induce some neuronal traits, such as expression of functional voltage-dependent channel proteins that are necessary for the generation of action potentials; however, co-infection of additional factors is necessary to facilitate neuronal conversion and maturation.

Discussion

Here we show that expression of three transcription factors can rapidly and efficiently convert mouse fibroblasts into functional neurons (iN cells). Although the single factor *Ascl1* was sufficient to induce immature neuronal features, the additional expression of *Brn2* and *Myt1l* generated mature iN cells with efficiencies of up to 19.5% (Supplementary Fig. 6b). Three-factor iN cells displayed functional neuronal properties such as the generation of trains of action potentials and synapse formation. These transcription factors were identified from a total of 19 candidates that we selected because of their specific expression in neural cell types or their roles in reprogramming to pluripotency (see Methods).

Despite the heterogeneity of embryonic and TTF cultures, the highly efficient nature of this process effectively rules out the possibility that directed differentiation of rare stem or precursor cells with neurogenic potential can explain our observations. Future studies will have to be performed to unequivocally demonstrate that terminally differentiated cells such as mature B or T lymphocytes can be directly converted into neurons using this approach^{31,32}.

It will now be of great interest to decipher the molecular mechanism of this fibroblast to neuron conversion. We assume that high expression levels of strong neural cell-fate-determining transcription factors can activate salient features of the neuronal transcriptional program. Auto-regulatory feedback and feed forward activation of downstream transcriptional regulators could then reinforce the expression of important cell-fate-determining genes and help to further stabilize the induced transcriptional program. Robust changes in transcriptional activity could also lead to genome-wide adjustments of repressive and active epigenetic features such as DNA methylation, histone modifications and changes of chromatin remodelling complexes that further stabilize the new transcriptional network^{12,33}. It is possible that certain subpopulations of cells are 'primed' to respond to these factors, depending on their pre-existing transcriptional or epigenetic states³⁴.

The majority of iN cells described in this report are excitatory and express markers of cortical identity. A low proportion of iN cells expressed markers of GABAergic neurons, but no other neurotransmitter phenotypes were detected. Our data indicate the intriguing possibility that additional combinations of neural transcription factors might also be able to generate functional neurons whose phenotypes remain to be explored. One of the next important steps will be to generate iN cells of other specific neuronal subtypes and from human cells.

Future studies will be necessary to determine whether iN cells could represent an alternative method to generate patient-specific neurons. The generation of iN cells is fast, efficient and devoid of tumorigenic pluripotent stem cells, a key complication of induced pluripotent stem cell approaches in regenerative medicine. Therefore, iN cells could provide a novel and powerful system for studying cellular identity and plasticity, neurological disease modelling, drug discovery and regenerative medicine.

METHODS SUMMARY

Fibroblast isolation, cell culture and molecular cloning. Homozygous TauEGFP knock-in mice²¹ were purchased from the Jackson Laboratories and bred with C57BL/6 mice (Taconic) to generate TauEGFP heterozygous embryos. MEFs were isolated from E14.5 embryos using a dissection microscope (Leica). Tail tips were sliced into small pieces, trypsinized and plated to derive fibroblast cultures. All fibroblasts were expanded for three passages before being used for experiments. Complementary DNAs for candidate genes were cloned into doxycycline-inducible lentiviral vectors, as described previously³⁵. MEFs were infected overnight and

cultured in MEF media with doxycycline for 48 h before being transferred into N3 media with doxycycline.

FACS analysis, cortical cultures, glia cultures. For glia and cortical co-cultures cells were trypsinized 8 days after infection and EGFP-positive cells were isolated using a FACS Aria II (Becton Dickinson). EGFP-positive cells were replated on 7 days *in vitro* cortical cultures from wild-type p0 mice, or alternatively, passage three primary astrocytes isolated from p5 pups (as described previously^{30,36,37}).

Electrophysiology and immunofluorescence analysis. Cells were analysed at indicated times after infection. Action potentials were recorded with current-clamp whole-cell configuration. The pipette solution for current-clamp experiments contained (in mM) 123 K-gluconate, 10 KCl, 1 MgCl₂, 10 HEPES, 1 EGTA, 0.1 CaCl₂, 1 K₂ATP, 0.2 Na₄GTP and 4 glucose, pH adjusted to 7.2 with KOH. Membrane potentials were kept around -65 to -70 mV, and step currents were injected to elicit action potentials. Whole-cell currents including sodium currents, potassium currents were recorded at a holding potential of -70 mV, voltage steps ranging from -80 mV to +90 mV were delivered at 10 mV increments. Synaptic responses were measured as described previously^{36,37}. For immunofluorescence experiments, cells were fixed in 4% paraformaldehyde in PBS for 10 min. Antibodies were diluted to indicated concentrations (see Methods).

Full Methods and any associated references are available in the online version of the paper at www.nature.com/nature.

Received 9 October 2009; accepted 6 January 2010.

Published online 27 January 2010.

- Jenuwein, T. & Allis, C. D. Translating the histone code. *Science* **293**, 1074–1080 (2001).
- Bernstein, B. E., Meissner, A. & Lander, E. S. The mammalian epigenome. *Cell* **128**, 669–681 (2007).
- Takahashi, K. & Yamanaka, S. Induction of pluripotent stem cells from mouse embryonic and adult fibroblast cultures by defined factors. *Cell* **126**, 663–676 (2006).
- Briggs, R. & King, T. J. Transplantation of living nuclei from blastula cells into enucleated frogs' eggs. *Proc. Natl Acad. Sci. USA* **38**, 455–463 (1952).
- Gurdon, J. B., Elsdale, T. R. & Fischberg, M. Sexually mature individuals of *Xenopus laevis* from the transplantation of single somatic nuclei. *Nature* **182**, 64–65 (1958).
- Campbell, K. H., McWhir, J., Ritchie, W. A. & Wilmut, I. Sheep cloned by nuclear transfer from a cultured cell line. *Nature* **380**, 64–66 (1996).
- Tada, M., Takahama, Y., Abe, K., Nakatsuji, N. & Tada, T. Nuclear reprogramming of somatic cells by *in vitro* hybridization with ES cells. *Curr. Biol.* **11**, 1553–1558 (2001).
- Do, J. T. & Scholer, H. R. Nuclei of embryonic stem cells reprogram somatic cells. *Stem Cells* **22**, 941–949 (2004).
- Cowan, C. A., Atienza, J., Melton, D. A. & Eggan, K. Nuclear reprogramming of somatic cells after fusion with human embryonic stem cells. *Science* **309**, 1369–1373 (2005).
- Silva, J. & Smith, A. Capturing pluripotency. *Cell* **132**, 532–536 (2008).
- Blau, H. M. How fixed is the differentiated state? Lessons from heterokaryons. *Trends Genet.* **5**, 268–272 (1989).
- Zhou, Q. & Melton, D. A. Extreme makeover: converting one cell into another. *Cell Stem Cell* **3**, 382–388 (2008).
- Davis, R. L., Weintraub, H. & Lassar, A. B. Expression of a single transfected cDNA converts fibroblasts to myoblasts. *Cell* **51**, 987–1000 (1987).
- Schäfer, B. W., Blakely, B. T., Darlington, G. J. & Blau, H. M. Effect of cell history on response to helix-loop-helix family of myogenic regulators. *Nature* **344**, 454–458 (1990).
- Kondo, M. *et al.* Cell-fate conversion of lymphoid-committed progenitors by instructive actions of cytokines. *Nature* **407**, 383–386 (2000).
- Bussmann, L. H. *et al.* A robust and highly efficient immune cell reprogramming system. *Cell Stem Cell* **5**, 554–566 (2009).
- Feng, R. *et al.* PU.1 and C/EBP α / β convert fibroblasts into macrophage-like cells. *Proc. Natl Acad. Sci. USA* **105**, 6057–6062 (2008).
- Xie, H., Ye, M., Feng, R. & Graf, T. Stepwise reprogramming of B cells into macrophages. *Cell* **117**, 663–676 (2004).
- Cobaleda, C., Jochum, W. & Busslinger, M. Conversion of mature B cells into T cells by dedifferentiation to uncommitted progenitors. *Nature* **449**, 473–477 (2007).
- Zhou, Q., Brown, J., Kanarek, A., Rajagopal, J. & Melton, D. A. *In vivo* reprogramming of adult pancreatic exocrine cells to β -cells. *Nature* **455**, 627–632 (2008).
- Tucker, K. L., Meyer, M. & Barde, Y. A. Neurotrophins are required for nerve growth during development. *Nature Neurosci.* **4**, 29–37 (2001).
- Wernig, M. *et al.* Tau EGFP embryonic stem cells: an efficient tool for neuronal lineage selection and transplantation. *J. Neurosci. Res.* **69**, 918–924 (2002).
- Lee, J. E. *et al.* Conversion of *Xenopus* ectoderm into neurons by NeuroD, a basic helix-loop-helix protein. *Science* **268**, 836–844 (1995).
- Guillemot, F. *et al.* Mammalian achaete-scute homolog 1 is required for the early development of olfactory and autonomic neurons. *Cell* **75**, 463–476 (1993).
- Farah, M. H. *et al.* Generation of neurons by transient expression of neural bHLH proteins in mammalian cells. *Development* **127**, 693–702 (2000).
- Guillemot, F. Cellular and molecular control of neurogenesis in the mammalian telencephalon. *Curr. Opin. Cell Biol.* **17**, 639–647 (2005).
- Escurat, M., Djabali, K., Gumpel, M., Gros, F. & Portier, M. M. Differential expression of two neuronal intermediate-filament proteins, peripherin and the

- low-molecular-mass neurofilament protein (NF-L), during the development of the rat. *J. Neurosci.* **10**, 764–784 (1990).
28. Beard, C., Hochedlinger, K., Plath, K., Wutz, A. & Jaenisch, R. Efficient method to generate single-copy transgenic mice by site-specific integration in embryonic stem cells. *Genesis* **44**, 23–28 (2006).
 29. Christopherson, K. S. *et al.* Thrombospondins are astrocyte-secreted proteins that promote CNS synaptogenesis. *Cell* **120**, 421–433 (2005).
 30. Wu, H. *et al.* Integrative genomic and functional analyses reveal neuronal subtype differentiation bias in human embryonic stem cell lines. *Proc. Natl Acad. Sci. USA* **104**, 13821–13826 (2007).
 31. Hochedlinger, K. & Jaenisch, R. Monoclonal mice generated by nuclear transfer from mature B and T donor cells. *Nature* **415**, 1035–1038 (2002).
 32. Hanna, J. *et al.* Direct reprogramming of terminally differentiated mature B lymphocytes to pluripotency. *Cell* **133**, 250–264 (2008).
 33. Jaenisch, R. & Young, R. Stem cells, the molecular circuitry of pluripotency and nuclear reprogramming. *Cell* **132**, 567–582 (2008).
 34. Yamanaka, S. Elite and stochastic models for induced pluripotent stem cell generation. *Nature* **460**, 49–52 (2009).
 35. Wernig, M. *et al.* A drug-inducible transgenic system for direct reprogramming of multiple somatic cell types. *Nature Biotechnol.* **26**, 916–924 (2008).
 36. Maximov, A., Pang, Z. P., Tervo, D. G. & Sudhof, T. C. Monitoring synaptic transmission in primary neuronal cultures using local extracellular stimulation. *J. Neurosci. Methods* **161**, 75–87 (2007).
 37. Maximov, A. & Sudhof, T. C. Autonomous function of synaptotagmin 1 in triggering synchronous release independent of asynchronous release. *Neuron* **48**, 547–554 (2005).

Supplementary Information is linked to the online version of the paper at www.nature.com/nature.

Acknowledgements We would like to thank S. Marro and P. Lovelace for help with FACS sorting, S. Hafeez and Y. Huh for assistance with molecular cloning and mouse husbandry, and K. Jann for assistance with the diagram in Fig. 1. We would also like to thank I. Graef, R. Bajpai, J. Wysocka, J.-R. Lin and J.-Y. Chen for contributing reagents and help with analysis. This work was supported by start-up funds from the Institute for Stem Cell Biology and Regenerative Medicine at Stanford (M.W.), the Donald E. and Delia B. Baxter Foundation (M.W.), an award from William Stinehart Jr and the Reed Foundation (M.W.), the National Institute of Health Training Grant 1018438-142-PABCA (A.O.) and the Ruth and Robert Halperin Stanford Graduate Fellowship (T.V.). Z.P.P. is supported by NARSAD Young Investigator Award and NIH/NINDS Epilepsy Training Grant 5T32NS007280.

Author Contributions T.V., A.O. and M.W. designed and conceived the experiments. T.V., Y.K. and M.W. produced the lentiviral vectors. T.V. and A.O. performed the lentiviral infections, isolated the fibroblasts and completed the molecular characterization of the iN cells. Z.P.P. and T.C.S. designed, performed and analysed the electrophysiological assays. T.V., A.O., Z.P.P., T.C.S. and M.W. wrote and edited the manuscript and produced the figures.

Author Information Reprints and permissions information is available at www.nature.com/reprints. The authors declare no competing financial interests. Correspondence and requests for materials should be addressed to M.W. (wernig@stanford.edu).

METHODS

Embryonic fibroblast isolation. Homozygous TauEGFP knock-in mice²¹ were purchased from the Jackson Laboratories and bred with C57BL/6 mice (Taconic) to generate TauEGFP heterozygous embryos. BALB/c mice were purchased from Taconic. Rosa26-rtTA mice were obtained from R. Jaenisch²⁸. MEFs were isolated from E14.5 embryos under a dissection microscope (Leica). The head, vertebral column (containing the spinal cord), dorsal root ganglia and all internal organs were removed and discarded to ensure the removal of all cells with neurogenic potential from the cultures. The remaining tissue was manually dissociated and incubated in 0.25% trypsin (Sigma) for 10–15 min to create a single cell suspension. The cells from each embryo were plated onto a 15-cm tissue culture dish in MEF media (Dulbecco's Modified Eagle Medium; Invitrogen) containing 10% fetal bovine serum (FBS; Hyclone), β -mercaptoethanol (Sigma-Aldrich), non-essential amino acids, sodium pyruvate and penicillin/streptomycin (all from Invitrogen). Cells were grown at 37 °C for 4–7 days until confluent, and then split once before being frozen. After thawing, cells were cultured on 15-cm plates and allowed to become confluent before being split onto plates for infections using 0.25% trypsin. Postnatal TTFs were prepared by removing the bottom third of tail from 3-day-old pups using surgical scissors. Cells were rinsed in ethanol, washed with HBSS (Sigma), and then dissociated using scissors and 0.25% trypsin. TTFs were cultured in MEF media until confluent and passaged once before being pooled together and frozen down for further use.

Cell culture, molecular cloning and viral infections. We had three criteria for identifying candidates with neuron-inducing activity: (1) we reasoned that cell-fate-inducing factors should be enriched in the gene category of transcriptional regulators. (2) We included factors previously involved in reprogramming to pluripotency (*Klf4*, *c-Myc* and *Sox2*). (3) We searched for genes specifically expressed in neural tissues. Those were selected based on published expression arrays of MEFs, embryonic stem cells and neural progenitor cells retrieved from the Gene Expression Omnibus database (GSE8024, <http://www.ncbi.nlm.nih.gov/gds>) and the EST Profile function of NCBI's Unigene database (<http://www.ncbi.nlm.nih.gov/unigene>). cDNAs for the factors included in the 19 factor pool were cloned into lentiviral constructs under the control of the tetracycline operator³⁵. Replication-incompetent, VSVg-coated lentiviral particles were packaged in 293T cells as described³⁵. Passage three TauEGFP and BALB/c MEFs were infected in MEF media containing polybrene (8 $\mu\text{g ml}^{-1}$). After 16–20 h in media containing lentivirus, the cells were switched into fresh MEF media containing doxycycline (2 $\mu\text{g ml}^{-1}$) to activate expression of the transduced genes. After 48 h in MEF media with doxycycline (Sigma), the media was replaced with N3 media²² containing doxycycline. The media was changed every 2–3 days for the duration of the culture period. For BrdU experiments, 10 μM BrdU was added to the culture media and was maintained throughout media changes until the cells were fixed.

Immunofluorescence, RT-PCR and flow cytometry. Neuronal cells were defined as cells that stained positive for Tuj1 and had a process at least three times longer than the cell body. For immunofluorescence staining, cells were washed with PBS and then fixed with 4% paraformaldehyde for 10 min at room temperature. Cells were then incubated in 0.2% Triton X-100 (Sigma) in PBS for 5 min at room temperature. After washing twice with PBS, cells were blocked in a solution of PBS containing 4% BSA, 1% FBS for 30 min at room temperature. Primary and secondary antibodies were diluted in a solution of PBS containing 4% BSA and 1% FBS. Fields of cells for staining were outlined with a PAP pen (DAKO). Primary and secondary antibodies were typically applied for 1 h and 30 min, respectively. Cells were washed three times with PBS between primary and secondary staining. For anti-BrdU staining, cells were treated with 2 N HCl in PBS for 10 min and washed twice with PBS before permeabilization with Triton X-100 (Sigma). The following antibodies were used for our analysis: goat anti-choline acetyltransferase (Millipore, 1:100), rabbit anti-GABA (Sigma, 1:4,000), rabbit-GFAP (DAKO, 1:4,000), mouse anti-MAP2 (Sigma, 1:500), mouse anti-NeuN (Millipore, 1:100), mouse anti-peripherin (Sigma, 1:100), mouse anti-Sox2 (R&D Systems, 1:50), rabbit anti-serotonin (Biogenesis, 1:1,000), rabbit anti-Tuj1 (Covance, 1:1,000), mouse anti-Tuj1 (Covance, 1:1,000), goat anti-BrdU (Santa Cruz Biotechnology, 1:100), mouse anti-BrdU (Becton Dickinson, 1:3.5), mouse anti-calretinin (DAKO, 1:100), sheep anti-tyrosine hydroxylase (Pel-Freez, 1:1,000), E028 rabbit anti-synapsin (gift from T. Südhof, 1:500), guinea-pig anti-vGLUT1 (Millipore, 1:2,000), mouse anti-GAD6 (Developmental Studies Hybridoma Bank (DSHB), 1:500), mouse anti-Pax3 (DSHB, 1:250), mouse anti-Pax6 (DSHB, 1:50), mouse anti-Pax7 (DSHB, 1:250), mouse anti-Nkx2.2 (DSHB, 1:100), mouse anti-Olig1 (NeuroMab, 1:100). FITC- and Cy3-conjugated secondary antibodies were obtained from

Jackson Immunoresearch. Alexa-488-, Alexa-546- and Alexa-633-conjugated secondary antibodies were obtained from Invitrogen. TauEGFP-expressing cells were analysed and sorted on a FACS Aria II (Becton Dickinson). Flow cytometry data were analysed using FlowJo (Tree Star). After sorting, cells were plated on cortical cultures or glia cultures derived from neonatal brains. Cells were kept in 50% N3 media and 50% growth media (see media composition below) and 2 $\mu\text{g ml}^{-1}$ doxycycline for 1 week before being switched to growth media without doxycycline until electrophysiological analysis was completed. For RT-PCR analysis, RNA was isolated using Trizol (Invitrogen) following the manufacturer's instructions, treated with DNase (NEB) and 1.5 μg was reverse-transcribed with Superscript II (Invitrogen). PCR was performed using the following primers: *Sox1*, forward 5'-TCGAGCCCTTCTCACTTGT-3', reverse 5'-TTGATGCATTTTGGGGGTAT-3'; *Sox10*, forward 5'-GAAGTGGCAAGG TCAAGAA-3', reverse 5'-CGCTTGCTACTTTCGTTTCAG-3'; β -actin, forward 5'-CGTGGGCGCCCTAGGCACCA-3', reverse 5'-CTTAGGGTTCAGGGG GC-3'. PCR products were analysed on a 1% gel.

Efficiency calculation. The following method was used to calculate the efficiency of neuronal induction. The total number of Tuj1⁺ cells with a neuronal morphology, defined as cells having a circular, three-dimensional appearance that extend a thin process at least three times longer than their cell body, were quantified 12 days after infection. This estimate was based on the average number of iN cells present in 30 randomly selected $\times 20$ visual fields. The area of a $\times 20$ visual field was then measured, and we used this estimated density of iN cells to determine the total number of neurons present in the entire dish. We then divided this number by the number of cells plated before infection to get a percentage of the starting population of cells that adopted neuron-like characteristics.

Cortical cultures. Primary cortical neurons were isolated from newborn wild-type mice as described³⁶ with modifications. Briefly, cortices were dissociated by papain (10 U ml^{-1} , with 1 μM Ca^{2+} , and 0.5 μM EGTA) digestions and plated on Matrigel-coated circle glass coverslips (\varnothing 11 mm). The neurons were cultured *in vitro* in growth media consisting of MEM (Invitrogen) supplemented with B27 (Invitrogen), glucose, transferrin, FBS and Ara-C (Sigma).

Glia cell isolation. Forebrains were dissected from postnatal day five wild-type mice and were manually dissociated into $\sim 0.5 \text{ mm}^2$ pieces in a total of 2 ml of HBSS. A total of 500 μl of 2.5% trypsin and 1% DNase were added and dissociated tissue was incubated at 37 °C for 15 min. Solution was mixed every 5 min. The supernatant was then transferred into 1.5 ml FBS. A total of 4 ml HBSS, 500 μl 2.5% trypsin, and 500 μl DNase were again added to the remaining dissociated tissue and incubated at 37 °C for 15 min, mixing every 5 min. The supernatant was again removed and added to the FBS-containing solution. Using a pipette, the remaining tissue was further dissociated and passed through a 70 μm nylon mesh filter (BD Biosciences) into the FBS-containing solution. The cell mixture was then spun at 1,000 r.p.m. for 5 min and re-suspended in MEF media. Glia cells were passaged three times before culturing with MEF or TTF-derived iN cells. Contaminating neurons in p3 glia cell cultures could not be detected when stained for either Tuj1 or MAP2.

Electrophysiology. Recordings were performed from MEF- and tail-cell-derived iN cells at 8, 12 and 20 days after viral infection, or 7–13 days after co-culturing with cortical neurons. Spontaneous or evoked synaptic responses were recorded in the whole-cell voltage-clamp mode. Evoked synaptic responses were triggered by 1-ms current injection through a local extracellular electrode (FHC concentric bipolar electrode, Catalogue number CBAEC75) with a Model 2100 Isolated Pulse Stimulator (A-M Systems), and recorded in whole-cell mode using a Multiclamp 700B amplifier (Molecular Devices)³⁷. Data were digitized at 10 kHz with a 2 kHz low-pass filter. The whole-cell pipette solution for synaptic current recordings contained (in mM): CsCl 135, HEPES 10, EGTA 1, Mg-ATP 4, Na_4GTP 0.4, and QX-314 10, pH 7.4. The bath solution contained (in mM): NaCl 140, KCl 5, CaCl_2 2, MgCl_2 2, HEPES 10, and glucose 10, pH 7.4. IPSCs were pharmacologically isolated by addition of 50 μM D-AP5 and 20 μM CNQX to the bath solution. EPSCs were pharmacologically isolated by addition of 30 μM picrotoxin. Data were analysed using Clampfit 10.02 (Axon Instruments). Action potentials were recorded with the current-clamp whole-cell configuration. The pipette solution for current-clamp experiments contained (in mM): 123 K-gluconate, 10 KCl, 1 MgCl_2 , 10 HEPES, 1 EGTA, 0.1 CaCl_2 , 1 K_2ATP , 0.2 Na_4GTP , and 4 glucose, pH adjusted to 7.2 with KOH. Membrane potentials were kept around -65 to -70 mV , and step currents were injected to elicit action potential. Whole-cell currents including sodium currents and potassium currents were recorded at a holding potential of -70 mV ; voltage steps ranging from -80 mV to $+90 \text{ mV}$ were delivered at 10-mV increments.

ARTICLES

Reprogramming towards pluripotency requires AID-dependent DNA demethylation

Nidhi Bhutani^{1*}, Jennifer J. Brady^{1*}, Mara Damian^{1,2}, Alessandra Sacco¹, Stéphane Y. Corbel¹ & Helen M. Blau¹

Reprogramming of somatic cell nuclei to yield induced pluripotent stem (iPS) cells makes possible derivation of patient-specific stem cells for regenerative medicine. However, iPS cell generation is asynchronous and slow (2–3 weeks), the frequency is low (<0.1%), and DNA demethylation constitutes a bottleneck. To determine regulatory mechanisms involved in reprogramming, we generated interspecies heterokaryons (fused mouse embryonic stem (ES) cells and human fibroblasts) that induce reprogramming synchronously, frequently and fast. Here we show that reprogramming towards pluripotency in single heterokaryons is initiated without cell division or DNA replication, rapidly (1 day) and efficiently (70%). Short interfering RNA (siRNA)-mediated knockdown showed that activation-induced cytidine deaminase (AID, also known as AICDA) is required for promoter demethylation and induction of *OCT4* (also known as *POU5F1*) and *NANOG* gene expression. AID protein bound silent methylated *OCT4* and *NANOG* promoters in fibroblasts, but not active demethylated promoters in ES cells. These data provide the first evidence that mammalian AID is required for active DNA demethylation and initiation of nuclear reprogramming towards pluripotency in human somatic cells.

Reprogramming of somatic cell nuclei towards pluripotency has been achieved by nuclear transfer into enucleated oocytes^{1,2} and the introduction of four defined factors to generate iPS cells^{3–6}. These remarkable advances enable the generation of patient-specific cells for tissue replacement, modelling human diseases in tissue culture, and drug discovery. However, an understanding of the molecular mechanisms underlying nuclear reprogramming has been elusive, largely due to the technical challenges associated with nuclear transfer and the low efficiency of iPS cell generation.

To identify new early regulators essential for nuclear reprogramming towards pluripotency, we capitalized on our previous experience with heterokaryons—cell fusion products that proved useful in determining the principles inherent to the maintenance of the differentiated state of somatic cells^{7–11}. Specifically, these earlier studies, by us and others, showed that the ‘terminally differentiated’ state of human cells was not fixed, but could be altered, and the expression of previously silent genes typical of other differentiated states could be induced^{11–15}. We showed that reprogramming in heterokaryons was influenced by DNA methylation status, tissue of origin, and the relative ratio of nuclei that dictates the balance of regulators^{11,15–17}, consistent with recent experiments in iPS cells^{18–23}. We reasoned that heterokaryons, generated by fusing mouse ES cells and human fibroblasts, could be used to elucidate mechanisms and identify new genes with a role at the onset of reprogramming towards pluripotency because reprogramming takes place in the presence of all ES cell factors, and the onset of reprogramming is synchronously initiated after fusion. The advantages of interspecies heterokaryons over previously used same-species cell fusion hybrids^{24,25} are that species differences allow a distinction of transcripts derived from the two fused cell types, and reprogramming is assessed immediately after fusion without the need for cell division or DNA replication. Heterokaryons

constitute a third complementary approach to nuclear reprogramming that overcomes some of the limitations of nuclear transfer and iPS cell generation by facilitating mechanistic studies.

The use of heterokaryons in this report allowed us to study epigenetic and transcriptional changes critical to the initiation of reprogramming towards pluripotency. We focused on DNA demethylation—a known block to reprogramming that leads to partially reprogrammed iPS cells²³, and also a key step for reprogramming by nuclear transfer²⁶. Despite decades of effort, so far no consensus mammalian DNA demethylase has been identified²⁷. Recently, AID has been implicated in DNA demethylation in zebrafish within hours after fertilization, acting in a complex that mediates deamination followed by DNA repair²⁸. In mammals, AID is primarily known for its role in the generation of antibody diversity in B lymphocytes²⁹, but has recently been detected in germ cells³⁰. Our studies demonstrate a new role for AID in active DNA demethylation and reprogramming of mammalian somatic cells towards pluripotency.

Efficient reprogramming towards pluripotency in heterokaryons

To produce interspecies heterokaryons, mouse ES cells transduced with a green fluorescent protein (GFP) reporter gene were co-cultured with primary human fibroblasts transduced with a DsRed reporter gene, and fused using polyethylene glycol (PEG) (Fig. 1a and scheme in Supplementary Fig. 1). Fused GFP⁺ DsRed⁺ heterokaryons, which were readily sorted by fluorescence-activated cell sorting (FACS) (Fig. 1b) and identified using fluorescence microscopy, contained distinctly stained human and mouse nuclei when visualized with Hoechst dye (Fig. 1c, f). Because the efficiency of PEG fusion is low (0.6–1.0%), GFP⁺ DsRed⁺ heterokaryons were sorted twice and enriched to 80% purity (Fig. 1b). Using an antibody for Ki67, a nuclear protein present only in proliferating cells, we determined that cell

¹Baxter Laboratory for Stem Cell Biology, Institute for Stem Cell Biology and Regenerative Medicine, Department of Microbiology and Immunology, Stanford University School of Medicine, Stanford, California 94305-5175, USA. ²Department of Biology, Stanford University, Stanford, California 94305-5020, USA.

*These authors contributed equally to this work.

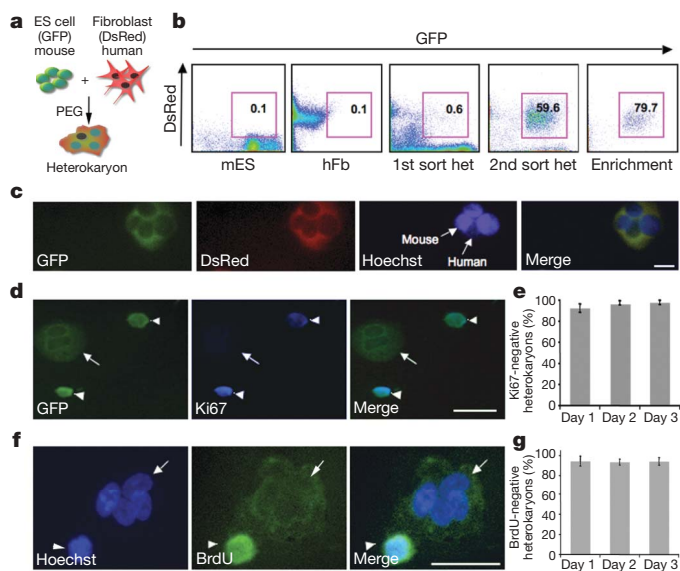


Figure 1 | Absence of cell division and DNA replication in heterokaryons. **a**, Heterokaryon fusion scheme. GFP⁺ mouse ES (mES) cells were co-cultured with DsRed⁺ primary human fibroblasts (hFb) and then fused using PEG. **b**, FACS profiles of GFP⁺ mES, DsRed⁺ hFb, and GFP⁺ DsRed⁺ day 2 heterokaryons (het). **c**, Representative image of GFP⁺ DsRed⁺ day 2 heterokaryons. Hoechst 33342 (blue) denotes the nuclei. The heterokaryon shown has three distinct, unfused bright mouse nuclei, and one uniformly stained human nucleus. Scale bar, 50 μ m. **d**, GFP⁺ DsRed⁺ day 2 heterokaryons were cytospun and stained for Ki67 (blue) to assess cell division. The GFP⁺ heterokaryon has two distinct nuclei (arrow) that are negative for Ki67 (blue) in contrast to the mononuclear cells (arrowheads) that stain positive for Ki67. Scale bar, 50 μ m. **e**, Heterokaryons on days 1, 2 and 3 after fusion were scored on the basis of Ki67 staining, and $98 \pm 2\%$ heterokaryons were non-dividing (mean \pm s.e.m., $P < 0.05$). **f**, Heterokaryons, generated using GFP⁺ ES cells, were enriched using a human fibroblast marker THY1.1 (see Methods) on day 1 post fusion, and stained for BrdU (green) and nuclei (blue) using Hoechst 33258. The heterokaryon (arrow) has three uniformly stained human nuclei and one bright, punctate mouse nucleus, and is negative for BrdU staining. In contrast, the indicated human mononuclear cell (arrowhead) stains positive for BrdU. Scale bar, 50 μ m. **g**, Day 1, 2 and 3 heterokaryons were scored on the basis of nuclear and BrdU staining. DNA replication did not occur in $94 \pm 3\%$ heterokaryons (mean \pm s.e.m., $P < 0.05$).

division did not occur in $98 \pm 2\%$ (mean \pm s.e.m.) of heterokaryons over the 3-day time period assayed after fusion (Fig. 1d, e). Furthermore, BrdU labelling was not detected in $94 \pm 4\%$ of heterokaryons over the same time period, indicating the absence of DNA replication (Fig. 1f, g and Supplementary Figs 2 and 3). To favour reprogramming towards a pluripotent state, we skewed the ratio of the input cells so that ES cells outnumbered the fibroblasts as gene dosage and the proportion of proteins contributed by each cell type determines the direction of nuclear reprogramming in somatic cells^{16,31}.

To determine whether ES-cell-specific genes were induced in the human fibroblast nuclei, the induction of human *OCT4* and *NANOG* was assayed relative to ubiquitous *GAPDH* using species-specific primers (Supplementary Fig. 4). Messenger RNA isolated from sorted heterokaryons 1, 2 and 3 days after fusion was assessed by reverse transcription followed by semiquantitative PCR (RT-PCR) and real-time PCR (Fig. 2a, b). The day 0 controls tested initially were (1) human fibroblasts alone, (2) pre-PEG, unfused co-cultures of mouse ES cells and human fibroblasts, or (3) human fibroblasts treated with PEG to control for the effects of PEG and fusion. All of these day 0 controls gave similar results (data not shown) and the unfused co-culture control was used for all subsequent experiments. Notably, the induction of both human *OCT4* and *NANOG* transcripts was evident as early as day 1 after fusion in heterokaryons but not in controls (Fig. 2a, b and Supplementary Fig. 5), indicating that the onset of expression of two

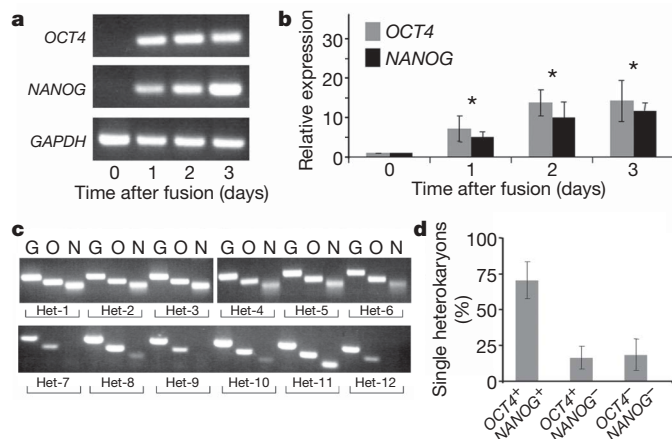


Figure 2 | Time course of human fibroblast pluripotency gene expression in heterokaryons at the single-cell level. **a**, Human-specific primers against *OCT4*, *NANOG* and *GAPDH* were used for transcript analysis by RT-PCR of unfused co-cultures on day 0 and heterokaryons (mES \times hFb) isolated on days 1, 2 and 3 after fusion. **b**, Real-time PCR to assess the upregulation of *OCT4* (grey) and *NANOG* (black) in day 1, 2 and 3 heterokaryons using human-specific primers (mean \pm s.e.m., $*P < 0.03$). Unfused co-cultures served as day 0 controls and the expression of *OCT4* and *NANOG* was normalized to *GAPDH* expression. Data shown are from three independent fusion experiments. **c**, Single heterokaryon nested PCR was used to assess the efficiency of reprogramming in the heterokaryon population. Direct reverse transcription and nested PCR were performed simultaneously on day 3 single heterokaryons, using human-specific primers for *GAPDH* (G), *OCT4* (O) and *NANOG* (N) as indicated. Twelve heterokaryons analysed from a single fusion experiment are shown. Supplementary Fig. 3 shows 41 heterokaryons analysed from two additional fusion experiments. **d**, The frequency of heterokaryons expressing both *OCT4* and *NANOG* is $70 \pm 13\%$, showing that a high proportion of heterokaryons initiate reprogramming towards pluripotency. Data shown are a summary of three independent fusion experiments (mean \pm s.e.m.).

key human pluripotency genes is rapid in heterokaryons. By day 1, expression of human *OCT4* and *NANOG* (normalized to the control (day 0) and persisted at 10-fold higher levels on days 2 and 3 (Fig. 2b). Human-specific primers were used to determine whether other key pluripotency genes in addition to *OCT4* and *NANOG* were induced using real-time PCR, including *KLF4*, *ESRRB*, *TDGF1* (also known as *CRIP1*), *SOX2* and *c-Myc* (also known as *MYC*) (Supplementary Fig. 6). *ESRRB*³² and *TDGF1* (ref. 33), which have been shown to be essential for maintaining ES cell self-renewal³² and are targets of *OCT4* and *NANOG*³⁴, were found to be upregulated 3-fold and 2.5-fold, respectively, in heterokaryons on day 2 after fusion (Supplementary Fig. 6). *SOX2* is already expressed in human fibroblasts and its promoter is extensively demethylated pre-fusion, in agreement with findings in mouse fibroblasts²³; its expression did not increase after fusion. Expression of *KLF4* (ref. 35), which is functionally interchangeable with *ESRRB*, did not change in heterokaryons at day 2 after fusion (Supplementary Fig. 6).

To assess the efficiency of nuclear reprogramming in human fibroblasts after fusion, single FACS-sorted heterokaryons were analysed by nested RT-PCR for the three human transcripts *OCT4*, *NANOG* and *GAPDH* (control), using two sets of human-specific primers in each case (Fig. 2c). As expected, no human gene products were detected in mouse ES cells (control), and only human *GAPDH* was detected in human fibroblasts (control) (Supplementary Fig. 4). Notably, 70% of single FACS-sorted heterokaryons from three independent fusion experiments isolated on day 3 after fusion expressed both human *OCT4* and *NANOG* (Fig. 2c, d and Supplementary Fig. 7), showing that a high proportion of heterokaryons initiated reprogramming towards pluripotency. This is in marked contrast to the slow and inefficient induction of *OCT4* and *NANOG* expression in iPS cells ($<0.1\%$ of the total population) in 2–3 weeks^{3–5,36}.

Active DNA demethylation in heterokaryons

Because DNA demethylation has been shown to be a major limiting step in reprogramming fibroblasts towards iPS cells²³, we analysed the time course and extent of demethylation of the human *OCT4* and *NANOG* promoters in heterokaryons. DNA was isolated from heterokaryons on days 1, 2 and 3 after fusion and subjected to bisulphite conversion. Human *OCT4* and *NANOG* promoter regions were amplified by PCR using human- and bisulphite-specific primers (Supplementary Fig. 4) and the products were cloned and sequenced. DNA demethylation was evident at the human *OCT4* and *NANOG* promoters and progressively increased through day 3 (Fig. 3a). In contrast, the β -globin (*HBB*) HS2 locus remained methylated throughout, indicating that the DNA demethylation was specific (data not shown). The time course and progressive accumulation of demethylated CpG sites in the human *OCT4* and *NANOG* promoters (Fig. 3b) parallel the progressive increase in transcript accumulation observed over the same 3-day time period using real-time PCR (Fig. 2b). Notably, promoter demethylation and activation of pluripotency genes in human somatic cells take place in the absence of Ki67 or BrdU labelling (Fig. 1e, g); thus, demethylation is active and independent of cell division and DNA replication.

AID requirement for DNA demethylation and pluripotency

We focused on AID as a candidate factor with a role in mammalian DNA demethylation as it has been detected in mammalian pluripotent germ cells³⁰ and implicated in DNA demethylation in zebrafish post fertilization²⁸. We assayed mouse ES cells and human fibroblasts for AID expression using real-time PCR. Although AID expression in somatic cells is generally thought to be restricted to B lymphocytes, we detected AID mRNA in human fibroblasts as well as mouse ES cells, albeit at greatly reduced levels (5% and 15%, respectively) compared to Ramos, a B-lymphocyte cell line (Supplementary Fig. 8). To investigate

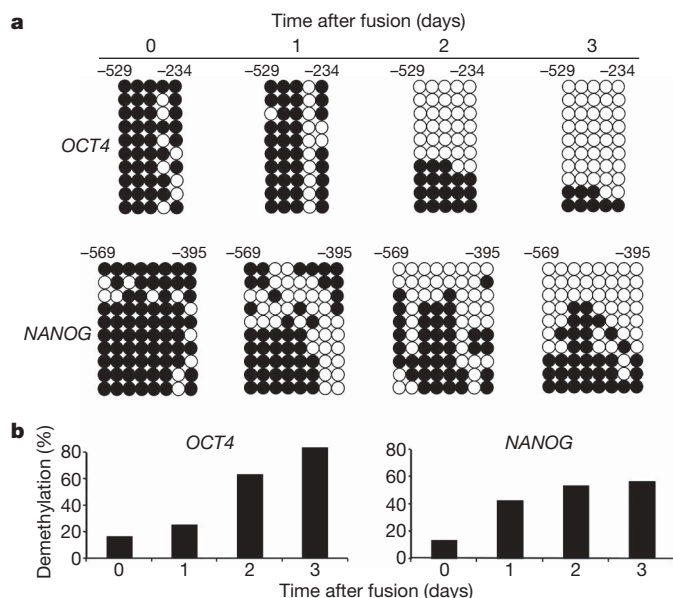


Figure 3 | Time course of DNA demethylation at pluripotency gene promoters in heterokaryons. **a**, Bisulphite sequencing analysis of methylation status of the human *OCT4* and *NANOG* promoter in heterokaryons. Both human *OCT4* and *NANOG* promoters in heterokaryons show rapid and progressive DNA demethylation on days 1, 2 and 3 after fusion compared to the co-culture control. White circles indicate unmethylated, black circles indicate methylated CpG dinucleotides. **b**, The percentage of demethylation at the human *OCT4* and *NANOG* promoters in heterokaryons after fusion shows a progressive increase in demethylation. Thirty clones were analysed at each time point in two to three independent experiments; ten representative clones are shown.

the role of AID in these cells, we performed a transient knockdown of mouse and human AID mRNAs by transfection of three distinct, non-overlapping siRNAs to different sequences within the AID coding region, and a fourth siRNA specific to the non-coding 3' untranslated region (UTR) of AID, to rule out off-target effects and ensure that the results were specific to AID (Supplementary Fig. 9). A fifth siRNA with 50% identity to the AID coding region was used as a control. The extent and timing of knockdown was first confirmed in control mouse ES cells in which siRNA-1, -2, -3 and -4 reduced AID transcripts at day 3 post-transfection as compared to the control siRNA (Supplementary Fig. 10, top). AID protein was detected in ES cell lysates. Knockdown of AID protein by 88% correlated well with the mRNA reduction by 81% (Supplementary Fig. 11). In human fibroblasts, AID transcripts were reduced by all of the siRNAs (Supplementary Fig. 10, bottom). These data show that AID is present and can be efficiently reduced by four distinct siRNAs in both ES cells and fibroblasts.

To assess the initiation of reprogramming in heterokaryons subjected to AID knockdown, the expression of human *OCT4* and *NANOG* relative to *GAPDH* was assessed by real-time PCR. For heterokaryon experiments, siRNAs were transfected into both the mouse ES cells and the human fibroblasts 24 h before fusion (see Supplementary Fig. 1 for scheme). A persistent knockdown of AID was detected by real-time PCR in heterokaryons using each of the four siRNAs on days 2 and 3 after fusion relative to heterokaryons transfected with the control siRNA (Fig. 4a). Notably, both *OCT4* and *NANOG* gene induction was greatly inhibited using siRNA-1

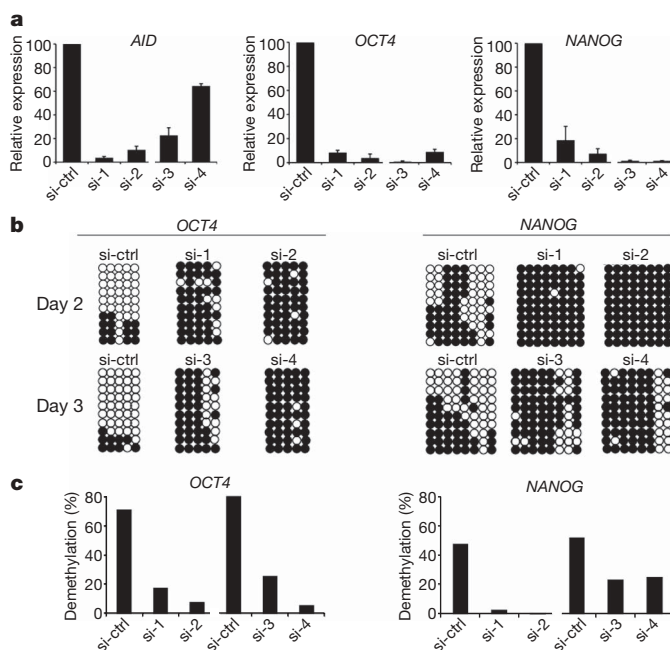


Figure 4 | Requirement of AID-dependent DNA demethylation for initiation of reprogramming towards pluripotency in heterokaryons. **a**, AID and human pluripotency gene expression in heterokaryons subjected to siRNA treatment, as assessed by real time PCR. Day 2 heterokaryons were treated with siRNA-1 and -2 (si-1 and si-2), and day 3 heterokaryons were treated with si-3 and si-4. Total levels of mouse and human AID transcripts were assessed using a set of degenerate primers, whereas human-specific primers were used for human *OCT4* and *NANOG*. Gene expression was normalized internally to *GAPDH* (degenerate primers) for AID expression, and to human *GAPDH* for human *OCT4* and *NANOG* expression. The samples were then normalized to the corresponding day 2 or 3 sample treated with the control siRNA (si-ctrl), represented as 100%. **b**, Human *OCT4* and *NANOG* promoters on days 2 and 3 post fusion after AID knockdown remain methylated. **c**, The percentage of demethylation at the human *OCT4* and *NANOG* promoters after AID knockdown shows a block in demethylation compared to their respective day 2 and day 3 control samples treated with control siRNA.

and siRNA-2 on day 2 after fusion, and siRNA-3 and siRNA-4 on day 3 after fusion, as compared to using the control siRNA (Fig. 4a). All siRNAs resulted in a similar block of *OCT4* and *NANOG* activation. These observations indicate that the effect of AID is extremely dosage-sensitive, as a 35% knockdown led to a similar inhibition of pluripotency gene induction as a 96% knockdown. Together, these data show that all four siRNAs to AID used here efficiently inhibited *OCT4* and *NANOG* activation by at least 80%.

To assess the effect of AID knockdown on promoter demethylation, we assayed the CpG methylation status of the human *OCT4* and *NANOG* promoters in heterokaryons. Both day 2 and 3 heterokaryons subjected to AID knockdown using each of the four siRNAs showed a profound inhibition of CpG demethylation in the human *OCT4* and *NANOG* promoters as compared to the control (Fig. 4b, c). A summary of the bisulphite sequencing data for all the siRNA knockdown experiments is shown in Supplementary Fig. 12. In parallel with the reduction in demethylation of the *OCT4* and *NANOG* promoters after AID knockdown, the induction of *OCT4* and *NANOG* transcripts was reduced by at least 80% on days 2 and 3, relative to the control (Fig. 4a). These data show that promoter demethylation is critical to the expression of these two pluripotency genes and that AID is required for mammalian DNA demethylation in somatic cell reprogramming.

To investigate further the requirement and specificity of AID for initiating reprogramming, we tested its ability to accelerate reprogramming, and to rescue the DNA demethylation block caused by the siRNA knockdown in heterokaryons. Therefore, human AID (hAID) was transiently overexpressed in mouse ES cells before siRNA transfection (see scheme in Supplementary Fig. 1). In two separate experiments, when AID was overexpressed twofold or fourfold relative to the control in heterokaryons at day 1 after fusion, there was no acceleration in promoter demethylation or reprogramming (Supplementary Fig. 13). However, after overexpression of hAID in heterokaryons undergoing transient knockdown by siRNA-3, there was a complete rescue of *NANOG* promoter demethylation and gene expression and a partial rescue of *OCT4* promoter demethylation and gene expression (Supplementary Fig. 14). The lack of reprogramming acceleration and partial rescue observed for *OCT4* could possibly be due to the kinetics of human *OCT4* and *NANOG* promoter demethylation, which in heterokaryons may require at least 1 day to occur, or by the lack of other factors that work together with AID. These data show that the added hAID is functional and rule out any non-specific effects of the siRNA, further confirming the specific and essential role of AID in DNA demethylation at the onset of reprogramming towards pluripotency.

Binding of AID to methylated pluripotency gene promoters

To validate the role of AID in DNA demethylation of human *OCT4* and *NANOG* promoters further, we tested whether AID specifically binds to these promoter regions by performing chromatin immunoprecipitation (ChIP) experiments using an anti-AID antibody, previously validated for ChIP³⁷. The promoter regions assessed in ChIP experiments were designed to be within the *OCT4* and *NANOG* promoter regions that were analysed for CpG demethylation by bisulphite sequencing (Fig. 5 and Supplementary Fig. 15). In human fibroblasts, the ChIP analyses showed significant binding of AID to both human *OCT4* (sixfold) and human *NANOG* (eightfold) promoters (Fig. 5). Thus, AID binds to the heavily methylated promoter regions of human *OCT4* and *NANOG* in fibroblasts that undergo demethylation during reprogramming. As controls, AID binding to the promoter of the IgM constant region (C μ) was significant, as expected³⁸, whereas no binding was observed for *THY1.1* (also known as CD90.1), which is expressed in fibroblasts.

In contrast to fibroblasts, no AID binding was observed at the promoter regions of *Oct4* and *Nanog* in mouse ES cells despite the higher levels of AID protein in ES cells, presumably because these promoters are active and demethylated (Fig. 5). As controls, AID binding was detected at the promoter of *Cdx2*, a gene not expressed

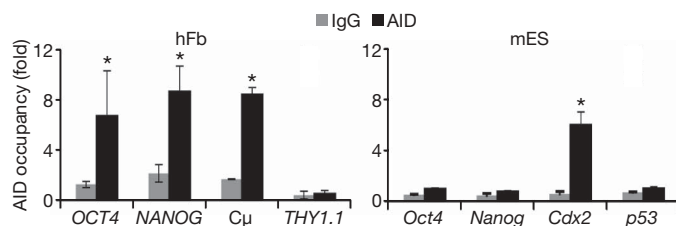


Figure 5 | AID binding to pluripotency gene promoters by chromatin immunoprecipitation. ChIP with anti-AID antibody was performed in human fibroblasts (left) and mouse ES cells (right). AID occupancy is shown relative to background IgG signal (mean \pm s.e.m.). Significant AID binding was detected in human fibroblasts for the methylated *NANOG* and *OCT4* promoters as well as for the positive control *Cμ* ($P < 0.002$). In mouse ES cells, AID binding was detected only in the positive control, *Cdx2* promoter region ($P < 0.007$), whereas no significant binding was observed for the unmethylated *Oct4* and *Nanog* promoters.

in undifferentiated ES cells³⁹, but was absent from the *p53* (also known as *Trp53*) promoter, as previously reported³⁷. Together, these findings provide strong support for a direct involvement of AID in DNA demethylation and the sustained expression of human *NANOG* and *OCT4* leading to the onset of reprogramming towards pluripotency.

Discussion

DNA demethylation is essential to overcome gene silencing and induce temporally and spatially controlled expression of mammalian genes, yet no consensus mammalian DNA demethylase has been identified despite years of effort²⁷. Evidence of DNA demethylation by 5-methyl-cytosine DNA glycosylases has been shown in plants^{40,41}, but mammalian homologues such as thymine DNA glycosylase (TDG) or the methyl-CpG-binding domain protein 4 (MBD4) have not exhibited comparable functions^{42,43}. As an alternative to direct demethylation, it has been postulated that the deamination of cytosine followed by DNA repair could lead to DNA demethylation⁴⁴. AID belongs to a family of cytosine deaminases (AID, APOBEC1, 2 and 3 subgroups) that have established roles in generating antibody diversity in B cells, RNA editing and antiviral response⁴⁵. Both AID and APOBEC1 are expressed in progenitor germ cells, oocytes and early embryos and have a robust 5-methyl-cytosine deaminase activity *in vitro*³⁰, resulting in a T-G mismatch that is repaired through the base excision DNA repair (BER) pathway, and could theoretically lead to DNA demethylation without replication. Recently in zebrafish embryos, AID was implicated as a member of a tripartite protein complex along with MBD4 and GADD45A, causing cytosine deamination and leading to base excision by MBD4 (ref. 28). The third component GADD45A lacks enzymatic activity and its role in repair-mediated DNA demethylation and gene activation in *Xenopus* oocytes remains a matter of debate^{46,47}.

Our data provide new evidence implicating AID in active DNA demethylation in mammalian cells, and demonstrate that AID-dependent DNA demethylation is an early epigenetic change necessary for the induction of pluripotency genes in human fibroblasts. Knockdown of AID in heterokaryons prevented DNA demethylation of the human *OCT4* and *NANOG* promoters and the expression of these pluripotency factors by fibroblast nuclei. Indeed, initiation of nuclear reprogramming towards pluripotency was inhibited in human somatic fibroblasts when AID-dependent DNA demethylation was reduced, providing strong evidence that AID is a crucial regulator for the onset of reprogramming. The inhibitory effects of AID reduction were rescued by hAID overexpression with a complete rescue observed for *NANOG* and a partial rescue observed for *OCT4*. Moreover, AID binding was observed at silent methylated *OCT4* and *NANOG* promoters in fibroblasts but not in active unmethylated *OCT4* and *NANOG* promoters in ES cells, demonstrating its specific role in DNA demethylation. Previous studies that used cell fusion to

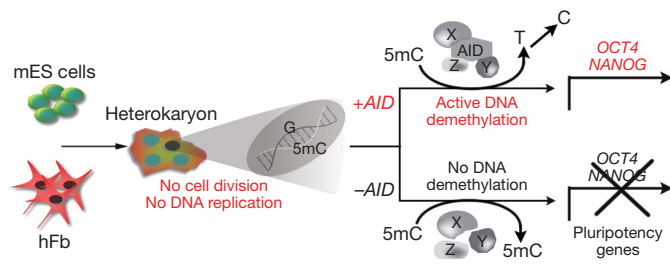


Figure 6 | Model for AID-dependent active DNA demethylation in reprogramming. AID-mediated reprogramming and DNA demethylation in heterokaryons takes place in the absence of cell division or DNA replication, showing that AID is a component of an active DNA demethylation complex in mammals. The other putative components of this mammalian DNA demethylase complex (X, Y and Z) that may act together with the deaminase, AID, remain to be identified. 5mC, 5-methyl-cytosine.

analyse reprogramming to pluripotency could not distinguish the products of the two nuclei because the cells were derived from the same species^{24,25}. A recent study used heterokaryons to reprogram lymphocytes towards pluripotency, however, only modest demethylation changes at the *OCT4* promoter were observed that did not increase with time⁴⁸, possibly owing to differences in the cell types and methods used for isolating heterokaryons. The high efficiency of reprogramming in heterokaryons achieved here allowed the discovery of a regulator critical to the induction of five pluripotency genes including *OCT4* and *NANOG*, the first known markers of stable reprogramming leading to the generation of iPS cells. The heterokaryon platform can now be exploited (1) to determine the other components of the mammalian DNA demethylation complex (glycosylase and other DNA repair enzymes) that are likely to work together with AID to mediate active DNA demethylation (Fig. 6), and (2) to perform an unbiased search for other regulators of nuclear reprogramming by screening for human genes that are expressed immediately after cell fusion. Future studies will determine whether expression of AID alone or in conjunction with these other molecules will enhance the generation of iPS cells.

METHODS SUMMARY

Heterokaryon generation and isolation. GFP⁺ mouse ES cells and DsRed⁺ human fetal lung primary fibroblasts were generated by transduction with retroviral constructs and fused to form non-dividing, multinucleated heterokaryons as previously described³¹. GFP⁺ DsRed⁺ heterokaryons were sorted twice by flow-cytometry (FACSVantage SE, BD Biosciences) and analysed for gene expression and methylation.

Immunofluorescence. For antibody staining, GFP⁺ DsRed⁺ heterokaryons were cytopun and stained. Images were acquired using an epifluorescent microscope (Axioplan2, Carl Zeiss MicroImaging), Fluor $\times 20/0.75$ or $\times 40/0.90$ objective lens, and a digital camera (ORCA-ER C4742-95, Hamamatsu Photonics). The software used for acquisition was OpenLab 4.0.2 (Improvision).

BrdU was added to mouse ES cell and human fibroblast co-cultures 3 h after PEG-induced fusion. Labelling and antibody staining was performed using the BrdU Labelling and Detection Kit I (Roche).

Single-cell RT-PCR. Single cells were directly sorted by FACS. Collection of cells and the subsequent two-step multiplex nested RT-PCR were performed directly from cell lysates using all three human and gene-specific primers (*OCT4*, *NANOG* and *GAPDH*) as described in Methods.

DNA methylation analyses. Bisulphite treatment was performed on DNA isolated from FACS sorted heterokaryons (2,000–10,000 cells) using the Epitect Bisulphite Kit (Qiagen). Nested PCR for regions of the human *OCT4* (ref. 18) and *NANOG* promoters was performed using human- and bisulphite-specific primers. PCR products from second-round bisulphite-specific PCR amplification were cloned and sequenced as described previously¹⁷.

siRNA transfection. For siRNA transfection, ES cells and primary fibroblasts were plated at 50–60% confluence the day before transfection. siRNAs (Dharmacon) were transfected using siImporter (Millipore).

ChIP. ChIP was performed as previously described⁴⁹. ChIP data was presented as normalized to input DNA and as the mean \pm s.e.m.

Statistical analysis. Data are presented as the mean \pm s.e.m. Comparisons between groups used the Student's *t*-test assuming two-tailed distributions.

Full Methods and any associated references are available in the online version of the paper at www.nature.com/nature.

Received 10 June; accepted 14 December 2009.

Published online 21 December 2009.

- Gurdon, J. B. Adult frogs derived from the nuclei of single somatic cells. *Dev. Biol.* **4**, 256–273 (1962).
- Briggs, R. & King, T. J. Transplantation of living nuclei from blastula cells into enucleated frogs' eggs. *Proc. Natl Acad. Sci. USA* **38**, 455–463 (1952).
- Takahashi, K. *et al.* Induction of pluripotent stem cells from adult human fibroblasts by defined factors. *Cell* **131**, 861–872 (2007).
- Takahashi, K. & Yamanaka, S. Induction of pluripotent stem cells from mouse embryonic and adult fibroblast cultures by defined factors. *Cell* **126**, 663–676 (2006).
- Wernig, M. *et al.* In vitro reprogramming of fibroblasts into a pluripotent ES-cell-like state. *Nature* **448**, 318–324 (2007).
- Okita, K., Ichisaka, T. & Yamanaka, S. Generation of germline-competent induced pluripotent stem cells. *Nature* **448**, 313–317 (2007).
- Blau, H. M., Chiu, C. P. & Webster, C. Cytoplasmic activation of human nuclear genes in stable heterokaryons. *Cell* **32**, 1171–1180 (1983).
- Chiu, C. P. & Blau, H. M. Reprogramming cell differentiation in the absence of DNA synthesis. *Cell* **37**, 879–887 (1984).
- Chiu, C. P. & Blau, H. M. 5-Azacytidine permits gene activation in a previously noninducible cell type. *Cell* **40**, 417–424 (1985).
- Blau, H. M. *et al.* Plasticity of the differentiated state. *Science* **230**, 758–766 (1985).
- Blau, H. M. & Baltimore, D. Differentiation requires continuous regulation. *J. Cell Biol.* **112**, 781–783 (1991).
- Baron, M. H. & Maniatis, T. Rapid reprogramming of globin gene expression in transient heterokaryons. *Cell* **46**, 591–602 (1986).
- Wright, W. E. Expression of differentiated functions in heterokaryons between skeletal myocytes, adrenal cells, fibroblasts and glial cells. *Exp. Cell Res.* **151**, 55–69 (1984).
- Spear, B. T. & Tilghman, S. M. Role of α -fetoprotein regulatory elements in transcriptional activation in transient heterokaryons. *Mol. Cell. Biol.* **10**, 5047–5054 (1990).
- Blau, H. M. Differentiation requires continuous active control. *Annu. Rev. Biochem.* **61**, 1213–1230 (1992).
- Pavlati, G. K. & Blau, H. M. Expression of muscle genes in heterokaryons depends on gene dosage. *J. Cell Biol.* **102**, 124–130 (1986).
- Zhang, F., Pomerantz, J. H., Sen, G., Palermo, A. T. & Blau, H. M. Active tissue-specific DNA demethylation conferred by somatic cell nuclei in stable heterokaryons. *Proc. Natl Acad. Sci. USA* **104**, 4395–4400 (2007).
- Park, I. H. *et al.* Reprogramming of human somatic cells to pluripotency with defined factors. *Nature* **451**, 141–146 (2008).
- Yu, J. *et al.* Induced pluripotent stem cell lines derived from human somatic cells. *Science* **318**, 1917–1920 (2007).
- Aoi, T. *et al.* Generation of pluripotent stem cells from adult mouse liver and stomach cells. *Science* **321**, 699–702 (2008).
- Eminli, S. *et al.* Differentiation stage determines potential of hematopoietic cells for reprogramming into induced pluripotent stem cells. *Nature Genet.* **41**, 968–976 (2009).
- Aasen, T. *et al.* Efficient and rapid generation of induced pluripotent stem cells from human keratinocytes. *Nature Biotechnol.* **26**, 1276–1284 (2008).
- Mikkelsen, T. S. *et al.* Dissecting direct reprogramming through integrative genomic analysis. *Nature* **454**, 49–55 (2008).
- Cowan, C. A., Atienza, J., Melton, D. A. & Eggan, K. Nuclear reprogramming of somatic cells after fusion with human embryonic stem cells. *Science* **309**, 1369–1373 (2005).
- Silva, J., Chambers, I., Pollard, S. & Smith, A. Nanog promotes transfer of pluripotency after cell fusion. *Nature* **441**, 997–1001 (2006).
- Simonsson, S. & Gurdon, J. DNA demethylation is necessary for the epigenetic reprogramming of somatic cell nuclei. *Nature Cell Biol.* **6**, 984–990 (2004).
- Ooi, S. K. & Bestor, T. H. The colorful history of active DNA demethylation. *Cell* **133**, 1145–1148 (2008).
- Rai, K. *et al.* DNA demethylation in zebrafish involves the coupling of a deaminase, a glycosylase, and Gadd45. *Cell* **135**, 1201–1212 (2008).
- Muramatsu, M. *et al.* Class switch recombination and hypermutation require activation-induced cytidine deaminase (AID), a potential RNA editing enzyme. *Cell* **102**, 553–563 (2000).
- Morgan, H. D., Dean, W., Coker, H. A., Reik, W. & Petersen-Mahrt, S. K. Activation-induced cytidine deaminase deaminates 5-methylcytosine in DNA and is expressed in pluripotent tissues: implications for epigenetic reprogramming. *J. Biol. Chem.* **279**, 52353–52360 (2004).
- Palermo, A. *et al.* Nuclear reprogramming in heterokaryons is rapid, extensive, and bidirectional. *FASEB J.* **23**, 1431–1440 (2009).
- Ivanova, N. *et al.* Dissecting self-renewal in stem cells with RNA interference. *Nature* **442**, 533–538 (2006).
- Bhattacharya, B. *et al.* Gene expression in human embryonic stem cell lines: unique molecular signature. *Blood* **103**, 2956–2964 (2004).
- Loh, Y. H. *et al.* The Oct4 and Nanog transcription network regulates pluripotency in mouse embryonic stem cells. *Nature Genet.* **38**, 431–440 (2006).

35. Feng, B. *et al.* Reprogramming of fibroblasts into induced pluripotent stem cells with orphan nuclear receptor Esrrb. *Nature Cell Biol.* **11**, 197–203 (2009).
36. Wernig, M. *et al.* A drug-inducible transgenic system for direct reprogramming of multiple somatic cell types. *Nature Biotechnol.* **26**, 916–924 (2008).
37. Vuong, B. Q. *et al.* Specific recruitment of protein kinase A to the immunoglobulin locus regulates class-switch recombination. *Nature Immunol.* **10**, 420–426 (2009).
38. Okazaki, I. M., Kinoshita, K., Muramatsu, M., Yoshikawa, K. & Honjo, T. The AID enzyme induces class switch recombination in fibroblasts. *Nature* **416**, 340–345 (2002).
39. Deb, K., Sivaguru, M., Yong, H. Y. & Roberts, R. M. *Cdx2* gene expression and trophectoderm lineage specification in mouse embryos. *Science* **311**, 992–996 (2006).
40. Gong, Z. *et al.* *ROS1*, a repressor of transcriptional gene silencing in *Arabidopsis*, encodes a DNA glycosylase/lyase. *Cell* **111**, 803–814 (2002).
41. Choi, Y. *et al.* DEMETER, a DNA glycosylase domain protein, is required for endosperm gene imprinting and seed viability in *Arabidopsis*. *Cell* **110**, 33–42 (2002).
42. Cortázar, D., Kunz, C., Saito, Y., Steinacher, R. & Schar, P. The enigmatic thymine DNA glycosylase. *DNA Repair (Amst.)* **6**, 489–504 (2007).
43. Millar, C. B. *et al.* Enhanced CpG mutability and tumorigenesis in MBD4-deficient mice. *Science* **297**, 403–405 (2002).
44. Gehring, M., Reik, W. & Henikoff, S. DNA demethylation by DNA repair. *Trends Genet.* **25**, 82–90 (2009).
45. Conticello, S. G., Langlois, M. A., Yang, Z. & Neuberger, M. S. DNA deamination in immunity: AID in the context of its APOBEC relatives. *Adv. Immunol.* **94**, 37–73 (2007).
46. Barreto, G. *et al.* Gadd45a promotes epigenetic gene activation by repair-mediated DNA demethylation. *Nature* **445**, 671–675 (2007).
47. Jin, S. G., Guo, C. & Pfeifer, G. P. GADD45A does not promote DNA demethylation. *PLoS Genet.* **4**, e1000013 (2008).
48. Pereira, C. F. *et al.* Heterokaryon-based reprogramming of human B lymphocytes for pluripotency requires Oct4 but not Sox2. *PLoS Genet.* **4**, e1000170 (2008).
49. Dahl, J. A. & Collas, P. A rapid micro chromatin immunoprecipitation assay (microChIP). *Nature Protocols* **3**, 1032–1045 (2008).

Supplementary Information is linked to the online version of the paper at www.nature.com/nature.

Acknowledgements We thank O. Alkan for generating retroviral constructs for GFP and DsRed expression; R. Doyonnas for helping to standardize FACS isolation of heterokaryons; Y. Liao for performing the initial experiments showing demethylation in heterokaryons; M. Pajcini for technical assistance with the BrdU experiments; D. Schatz and S. Unniraman for providing the human AID construct; F. Alt for his generous provision of antibody to AID; J. A. Dahl for discussions about chromatin immunoprecipitation assays; H. Chang for use of the Bioruptor sonicator; and M. Wernig, G. Sen, C.-Z. Chen and J. Pomerantz for comments on the manuscript. This work was supported by a National Science Foundation Graduate Research Fellowship awarded to J.J.B., National Institutes of Health (NIH) training grant AI007328 to M.D., and NIH grants AG009521, AG024987 and support from the Baxter Foundation to H.M.B.

Author Contributions N.B. and H.M.B. designed the research, N.B., J.J.B. and M.D. performed the experiments and analysed the data. M.D. assisted with western blots, and conducted the ChIP analyses. A.S. and S.Y.C. performed FACS isolation of heterokaryons and provided expert help in figure preparation. N.B., J.J.B. and H.M.B. discussed the results and wrote the paper.

Author Information Reprints and permissions information is available at www.nature.com/reprints. The authors declare no competing financial interests. Correspondence and requests for materials should be addressed to H.M.B. (hblau@stanford.edu).

METHODS

Heterokaryon generation and isolation by flow cytometry. GFP⁺ mouse ES cells and DsRed⁺ human fetal lung primary fibroblasts were generated by transduction with retroviral constructs as previously described³¹, and fused to form non-dividing, multinucleated heterokaryons. Cells were first co-cultured for 12 h in ES cell media and then treated with PEG 1500 (Roche) for 2 min at 37 °C, followed by four successive washes with DMEM. ES cell media was replaced after washing and every 12 h thereafter. GFP⁺ DsRed⁺ heterokaryons were sorted twice by flow-cytometry (FACS Vantage SE, BD Biosciences) and analysed for gene expression and methylation.

Immunofluorescence. Heterokaryons were sorted twice in PBS with 2.5% (v/v) goat serum and 1 mM EDTA, and cytospun for 5 min. The cytospun GFP⁺ DsRed⁺ heterokaryons were stained with Hoechst 33342, and imaged. For antibody staining, cytospun cells were fixed, permeabilized and blocked using 20% FBS in PBS. Cells were incubated with the mouse anti-Ki67 antibody (Dako Denmark A/S) at 1:100 dilution in blocking buffer for 1 h, rinsed three times in PBS, and then incubated with a goat anti-mouse Cascade blue secondary antibody (Millipore) at 1:500 dilution for 30 min, rinsed three times, mounted with Fluoromount-G and imaged. Images were acquired using an epifluorescent microscope (Axioplan2, Carl Zeiss MicroImaging), Fluor $\times 20/0.75$ or $\times 40/0.90$ objective lens, and a digital camera (ORCA-ER C4742-95, Hamamatsu Photonics). The software used for acquisition was OpenLab 4.0.2 (Improvision).

BrDU was added to mouse ES cell and human fibroblast co-cultures 3 h after PEG-induced fusion. Labelling and antibody staining was performed using the BrDU Labelling and Detection Kit I (Roche).

Analysis of gene expression. RNA was prepared from ES cells, fibroblasts and twice-sorted heterokaryons at different times post fusion or after siRNA treatment using the RNeasy micro kit (Qiagen). Total RNA for each sample was reverse transcribed using the Superscript First-Strand Synthesis System for RT-PCR (Invitrogen). The reverse-transcribed material was subjected to PCR using Go GreenTaq DNA polymerase (Promega). Human-specific primers were designed for analysing the expression of *OCT4*, *NANOG* and *GAPDH*. Primers used for *AID* and *GAPDH* in the siRNA treatment experiments amplify both human and mouse transcripts to assess the total levels of AID and GAPDH in heterokaryons. Human-specific primers used for RT-PCR and quantitative PCR are: *OCT4* F 5'-TCGAGAACCGAGTGAGAGGC-3', R 5'-CACACTCGG ACCACATCCTTC-3'; *NANOG* F 5'-CCAACATCCTGAACCTCAGCTAC-3', R 5'-GCCTTC TCGGTCACACATT-3'; *GAPDH* F 5'-TGTCCCCACTGCCA ACGTGTCA-3', R 5'-AGCGTCAAAGGTGGAGGAGTGGGT-3'. Non-species-specific primer sequences for assessing knockdown after siRNA treatment are as follows: *GAPDH* F 5'-ACCACAGTCCATGCCATCAC-3', R 5'-TCCACCACCC TGTTGCTGTA-3'; *AID* F 5'-AAAATGTCCGCTGGGCTAAG-3', R 5'-AGGT CCCAGTCCGAGATGTAG-3'.

Real-time PCR. Real-time PCR was performed using an ABI 7900HT Real time PCR system using the Sybr Green PCR mix (Applied Biosystems). Samples were cycled at 94 °C for 2 min, 40 cycles of: 94 °C for 20 s, 58 °C for 45 s.

DNA methylation analyses. FACS-sorted heterokaryons (2,000–10,000 cells) were collected in 20 μ l PBS. DNA was extracted using the DNeasy Tissue Kit (Qiagen). Bisulphite treatment was performed using the Epiect Bisulfite Kit (Qiagen). Nested PCR for regions of the human *OCT4* and *NANOG* promoters

was performed using human- and bisulphite-specific primers. Samples were cycled for the first and second nested PCR at 94 °C for 2 min, 30 cycles of 94 °C for 20 s, 61 °C for 30 s, 68 °C for 30 s. PCR products from second-round bisulphite-specific PCR amplification were cloned and sequenced as described before¹⁷.

Single heterokaryon nested RT-PCR. Single-cell collection. Single heterokaryons were directly sorted by FACS (FACS Vantage SE, BD Biosciences) into PCR tubes containing 9- μ l aliquots of RT-PCR lysis buffer. The buffer components included commercial RT-PCR buffer (SuperScript One-Step RT-PCR Kit Reaction Buffer, Invitrogen), RNase inhibitor (Protector RNase Inhibitor, Roche) and 0.15% IGEPAL detergent (Sigma). After a short pulse-spin, the PCR-tubes were immediately shock-frozen and stored at -80 °C for subsequent analysis.

Two-step multiplex nested single-cell RT-PCR. Cell lysates were first reverse-transcribed using the human-specific primer pairs for *OCT4*, *NANOG* and *GAPDH* (Supplementary Table 2, external primers; Supplementary Fig. 1b) using SuperScript One-Step RT-PCR Kit (Invitrogen). In brief, the RT-PCR was performed in the same PCR cell-lysis tubes by addition of an RT-PCR-reaction mix containing the gene-specific primer pairs and RNase inhibitor. Genomic products were excluded by designing and using intron-spanning primer sets for the first and second round PCR and nested RT-PCR to ensure greater specificity. In the first step, the reverse transcription reactions were carried out at 55 °C for 30 min, followed by a 2-min step at 94 °C. Subsequently, 30 cycles of PCR amplification were performed as follows: 94 °C for 30 s; 58 °C for 30 s; 68 °C for 30 s. In the final PCR step, the reactions were incubated for 3 min at 68 °C. The completed reactions were stored at 4 °C.

In the second step of the PCR protocol, the completed RT-PCR reaction from the first step was diluted 1:1 with water. One per cent of these reactions were replica transferred into new reaction tubes for the second round of PCR, which was performed for each of the genes separately using nested gene-specific internal primers, for greater specificity, in a total reaction volume of 20 μ l (Platinum Taq Super-Mix HF, Invitrogen). Thirty cycles of PCR amplification were performed as follows: 94 °C for 30 s; 58 °C for 30 s; 68 °C for 30 s. In the final PCR step, the reactions were incubated for 3 min at 68 °C. The completed reactions were stored at 4 °C. The second-round PCR products were then subjected to gel electrophoresis using one-fifth of the reaction volumes and 1.4% agarose gels.

THY1.1 enrichment of heterokaryons. GFP⁻ (non-GFP) mES and DsRed⁺ hFB co-cultures treated with PEG were trypsinized and resuspended in 3 ml FACS buffer. Cells were incubated for 30 min at room temperature with biotin mouse anti-human CD90.1 (BD Pharmingen) at a dilution of 1:5,000. The cells were washed once, resuspended in 3 ml FACS buffer, and incubated for 30 min at room temperature with 10 μ l of Dynabeads Biotin Binder (Invitrogen). Beads were collected by magnetic isolation, washed twice and the enriched heterokaryons were cytospun.

Western blots. To visualize AID protein knockdown in mouse ES cells, cell lysates were collected 3 days after transfection with control siRNA or siRNA-3. Detection of AID in these samples was performed from 170 μ g of whole cell lysate using anti mouse-AID (L7E7, Cell Signaling, dilution 1:500). The membrane was stripped and probed with anti-mouse α -tubulin (Sigma, dilution 1:20,000) for the loading control.

ARTICLES

Orm family proteins mediate sphingolipid homeostasis

David K. Breslow^{1,2,3,4}, Sean R. Collins^{1,2,4}†, Bernd Bodenmiller⁵†, Ruedi Aebersold^{5,6,7}, Kai Simons⁸, Andrej Shevchenko⁸, Christer S. Ejsing^{8,9} & Jonathan S. Weissman^{1,2,4}

Despite the essential roles of sphingolipids both as structural components of membranes and critical signalling molecules, we have a limited understanding of how cells sense and regulate their levels. Here we reveal the function in sphingolipid metabolism of the *ORM* genes (known as *ORMDL* genes in humans)—a conserved gene family that includes *ORMDL3*, which has recently been identified as a potential risk factor for childhood asthma. Starting from an unbiased functional genomic approach in *Saccharomyces cerevisiae*, we identify Orm proteins as negative regulators of sphingolipid synthesis that form a conserved complex with serine palmitoyltransferase, the first and rate-limiting enzyme in sphingolipid production. We also define a regulatory pathway in which phosphorylation of Orm proteins relieves their inhibitory activity when sphingolipid production is disrupted. Changes in *ORM* gene expression or mutations to their phosphorylation sites cause dysregulation of sphingolipid metabolism. Our work identifies the Orm proteins as critical mediators of sphingolipid homeostasis and raises the possibility that sphingolipid misregulation contributes to the development of childhood asthma.

As cells grow, divide and respond to their environment, they must synthesize lipids to meet metabolic demands while ensuring the correct balance of a wide array of structurally and functionally diverse lipid species. At the same time, cells need to maintain the correct distribution of lipids within the membrane bilayers of different organelles and the plasma membrane. Regulatory mechanisms that ensure proper levels of some lipid species including sterols^{1–3} and various glycerolipids^{4–6} have been identified, with loss of such controls leading to a variety of disease states^{1,7}. Although remarkable progress has been made in defining the protein machinery responsible for synthesizing^{8,9} and transporting sphingolipids^{10–13}, insights into how cells sense and maintain their levels are only now emerging^{14,15}. The need for precise regulation of sphingolipids may be particularly acute as, in addition to the structural roles of the terminal products, several biosynthetic intermediates—including sphingosine, ceramide and their phosphorylated derivatives—are signalling molecules that participate in key physiological and pathological processes^{16,17}.

Our investigations into how cells achieve sphingolipid homeostasis stem from analysis of the *ORM* (or *ORMDL*) genes, which have been implicated recently in asthma. Asthma has emerged as a major health problem, with rates of childhood disease increasing markedly over the past three decades¹⁸. There is a strong heritable component that modulates susceptibility to asthma, and many studies have been undertaken to identify genetic risk factors¹⁹. A breakthrough in these efforts came with a recent genome-wide association study²⁰, which identified single nucleotide polymorphisms at chromosome 17q21 near the *ORMDL3* gene that confer an increased risk of childhood asthma. Subsequent studies have reproduced this finding in multiple ethnic groups^{21–23}. Furthermore, the disease-associated polymorphisms have been shown to modulate expression of *ORMDL3* and the adjacent gene *GSDMB*^{20,24}, suggesting that dysregulation of one or both of these genes may contribute to childhood asthma. Thus

genetic variants near *ORMDL3* are a widespread risk factor for developing childhood asthma that may raise the incidence of the disease by up to approximately 20% (refs 22, 25). However, translating these findings into an increased understanding of how *ORMDL3* may contribute to the pathogenesis of asthma has been hampered by the lack of information on the function of *ORM*-family genes.

Members of the *ORM* gene family encode transmembrane proteins localized in the endoplasmic reticulum (ER) and include two genes in the budding yeast *S. cerevisiae* (*ORM1/2*) and three genes in humans (*ORMDL1/2/3*)²⁶. The Orm proteins have no known functional domains, and little is known about their cellular role; however, they are strongly conserved and have been proposed to share a common function²⁶. Here we use a combination of global and targeted studies to identify Orm proteins as homeostatic regulators of the first and rate-limiting step in sphingolipid biosynthesis.

Orm1/2 negatively regulate sphingolipid synthesis

We began our investigation of *S. cerevisiae* *ORM1* and *ORM2* by using a global approach to characterize gene function based on large-scale measurements of genetic interactions, termed epistatic mini-array profiles (E-MAPs)²⁷. In this strategy, the function of a given gene can be inferred without a priori hypotheses by comparing the spectrum of genetic interactions resulting from mutation of that gene with interaction patterns caused by mutations in other genes of defined function. When we compared the genetic interaction profile resulting from deletion of *ORM2* with those obtained for a collection of more than 1,400 yeast mutants in a study focused on ER biology (manuscript in preparation and ref. 27), we observed a strong anti-correlation with the interaction patterns seen for hypomorphic alleles that reduce expression of *LCB1* and *LCB2* (*lcb1-DAmP* and *lcb2-DAmP*²⁷), thus suggesting that *ORM2* and *LCB1/2* have opposing cellular roles (Fig. 1a and Supplementary Information). We also

¹Department of Cellular and Molecular Pharmacology, ²Howard Hughes Medical Institute, ³Graduate Program in Chemistry and Chemical Biology, ⁴The California Institute for Quantitative Biomedical Research, University of California, San Francisco, 1700 4th Street, San Francisco, California 94158, USA. ⁵Institute of Molecular Systems Biology, ETH Zurich, 8093 Zurich, Switzerland. ⁶Institute for Systems Biology, Seattle, Washington 98103, USA. ⁷Faculty of Science, University of Zurich, 8057 Zurich, Switzerland. ⁸Max Planck Institute of Molecular Cell Biology and Genetics, Pfotenhauerstrasse 108, 01307 Dresden, Germany. ⁹Department of Biochemistry and Molecular Biology, University of Southern Denmark, Campusvej 55, 5230 Odense, Denmark. †Present addresses: Chemical and Systems Biology, Bio-X Program, Stanford University, Stanford, California 94305, USA (S.R.C.); Department of Microbiology and Immunology, Baxter Laboratory in Genetic Pharmacology, Stanford University, 269 Campus Drive, Stanford, California 94305, USA (B.B.).

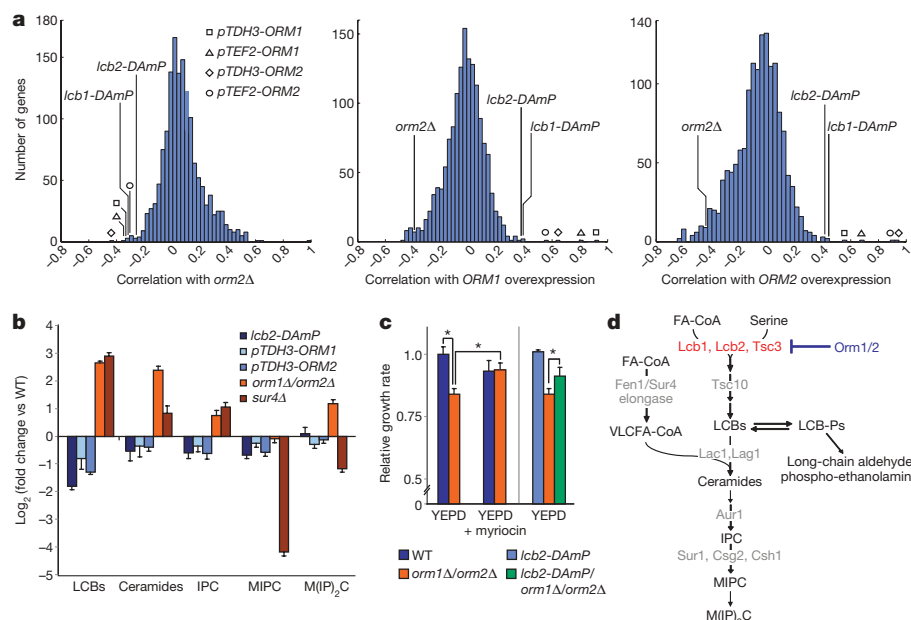


Figure 1 | Orm1/2 are negative regulators of sphingolipid synthesis.

a, Genetic interaction (E-MAP) profiles were generated for strains containing *ORM2* deletion, *ORM1* overexpression and *ORM2* overexpression alleles (*orm2Δ*, *pTDH3-ORM1* and *pTEF2-ORM1*, and *pTDH3-ORM2* and *pTEF2-ORM2*, respectively). Correlations between the E-MAP profiles of these strains and those of more than 1,400 other yeast mutants are shown in histograms (see Methods and Supplementary Information). **b**, Lipids were extracted from the indicated strains and analysed using a global mass spectrometry approach³⁰. Amounts of the indicated metabolites are shown relative to wild type (WT; average \pm s.d.,

$n = 4$; see Methods and Supplementary Information). **c**, Logarithmic-phase growth rates for the indicated strains were measured in standard media (YEPD) or media supplemented with myriocin at 150 ng ml⁻¹. Growth rates (average \pm s.d., $n \geq 3$) are shown normalized to wild type; asterisks denote statistical significance ($P < 0.05$). **d**, Schematic of the sphingolipid biosynthesis pathway in *S. cerevisiae*, with selected metabolites and genes indicated. FA-CoA, fatty acid co-enzyme A; LCB-Phs, long-chain base phosphates; IPC, inositolphosphorylceramide; MIPC, mannosyl-inositolphosphorylceramide; M(IP)₂C, mannosyl-diinositolphosphorylceramide; VLCFA-CoA, very long-chain fatty acid co-enzyme A.

examined the genetic interactions that result from overexpression of *ORM1* or *ORM2* by using the strong promoters *pTDH3* and *pTEF2*, as it was shown that the asthma-associated polymorphisms near *ORMDL3* are associated with increased expression of this gene^{20,24}. Overexpression of *ORM1* or *ORM2* produced a pattern of genetic interactions that was highly correlated with those seen for the *lcb1-DAmP* and *lcb2-DAmP* strains, indicating that increased Orm expression phenocopies reduced Lcb1/2 activity (Fig. 1a).

LCB1 and *LCB2* encode serine palmitoyltransferase, an essential heterodimeric enzyme that catalyses the first and rate-limiting step in sphingolipid biosynthesis^{9,28}. The synthesis of sphingolipids begins in the ER, where two classes of lipid metabolite, long-chain bases (LCBs) and very long-chain fatty acids, are formed (Fig. 1d). LCBs are produced by the condensation of serine with fatty acids by serine palmitoyltransferase (Lcb1/2 in yeast and SPTLC1/2/3 in mammals), followed by Tsc10-mediated reduction^{8,9,29}. LCBs can then be phosphorylated or *N*-acylated with very long-chain fatty acids to form long-chain base phosphates or ceramides, respectively, with the latter undergoing further modification to generate complex sphingolipids (Fig. 1d).

Thus, our E-MAP data showing a correlation between increased *ORM* expression and decreased *LCB1/2* function implicate the Orm proteins as negative regulators of sphingolipid synthesis and highlight the reaction performed by Lcb1/2 as the possible step in the pathway at which Orm1/2 may act (Fig. 1a, d). We therefore examined the effects of altering Orm levels on cellular lipid composition using a mass-spectrometry-based global lipidomic technique³⁰. In agreement with the genetic interaction data, overexpression of *ORM1* or *ORM2* resulted in changes to the lipidome, including reduced levels of LCBs and ceramides, which closely resembled those seen for the *lcb2-DAmP* mutant (Fig. 1b and Supplementary Information). Conversely, cells deleted for *ORM1/2* had highly increased levels of LCBs and ceramides. In principle, this accumulation of LCBs caused by deletion of *ORM1/2* could result from a failure to consume these species by reaction with very long-chain fatty acids to form ceramides, as is seen

when *SUR4* is deleted (Fig. 1b and ref. 30). However, in contrast to the *sur4Δ* strain, the increased LCB levels in the *orm1Δ/orm2Δ* strain are also accompanied by increased amounts of the terminal sphingolipid mannosyl-diinositolphosphorylceramide. Thus, *ORM1/2* deletion causes increased flux throughout the sphingolipid pathway. This increased flux is also the primary cause of the growth defect seen in *orm1Δ/orm2Δ* cells, as artificially decreasing Lcb1/2 activity, either through the use of myriocin, a drug that specifically inhibits Lcb1/2 (ref. 31), or through the *lcb2-DAmP* allele, significantly suppresses the growth defect caused by loss of *ORM1/2* (Fig. 1c).

A complex with Orm1/2, Lcb1/2 and Sac1

We next explored how Orm proteins modulate sphingolipid production by identifying proteins bound by Orm1 and Orm2 *in vivo*. Isolation of functional 3×Flag-tagged forms of Orm1 and Orm2 expressed from their endogenous loci revealed a previously uncharacterized, roughly stoichiometric complex (Fig. 2a). Mass spectrometry showed that this complex comprises the serine palmitoyltransferase proteins Lcb1, Lcb2 and Tsc3, in addition to the phosphoinositide phosphatase Sac1 (ref. 32) (Supplementary Table 1). To characterize physical interactions among these proteins further, we used a 3×Flag-tagged form of Lcb1 that is able to rescue the inviability seen upon loss of *LCB1* (although this allele does exhibit mild sensitivity to myriocin). Purification of 3×Flag-Lcb1 yielded the same components seen in the Orm1/2 pull-downs (Fig. 2b), indicating that the Orm-associated proteins are likely to exist in a single complex. Orm proteins and potentially their binding partners may also form higher-order oligomers, as we detected Orm2 co-immunoprecipitation with 3×Flag-Orm1 (and vice versa) and self-association of differently tagged copies of the same Orm protein (Fig. 2a and see later).

The presence of Sac1 in association with Lcb1/2 suggests a new connection between this phosphoinositide phosphatase and sphingolipid biosynthesis. Deletion of *SAC1* leads to increased levels of

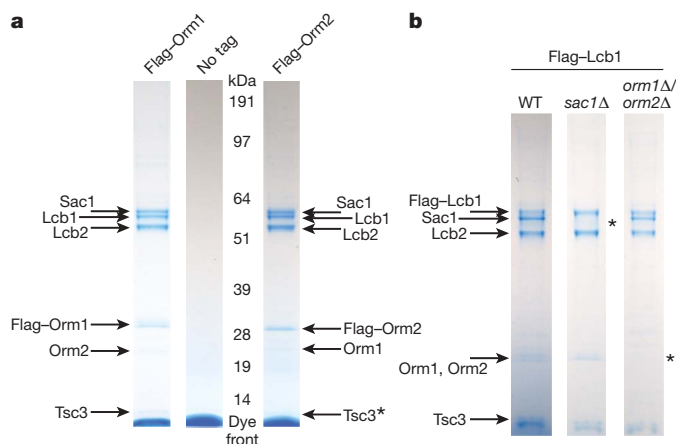


Figure 2 | Orm proteins form a complex with serine palmitoyltransferase. **a**, Colloidal-stained gels are shown for proteins eluted after affinity purifications from strains expressing 3×Flag-Orm1 or 3×Flag-Orm2, or from an untagged control strain. Immunoprecipitated proteins were identified by mass spectrometry (Supplementary Table 1; asterisk indicates the partly obscured protein Tsc3, whose presence was confirmed by mass spectrometry). **b**, Affinity purifications of 3×Flag-Lcb1 from wild-type, *sac1Δ* and *orm1Δ/orm2Δ* strains were performed as in **a**. Asterisks indicate bands that are lost in deletion backgrounds.

LCBs (Supplementary Fig. 1a and ref. 33) and resistance to the Lcb1/2 inhibitor myriocin (Supplementary Fig. 1b). This resistance was also seen in cells expressing the *sac1-8* (ref. 34) catalytically inactive mutant of *SAC1*. Additionally, we found that Sac1 and Orm1/2 bind independently to Lcb1/2 (Fig. 2b) and that *SAC1* and *ORM1/2* deletions exhibit synthetic lethality (Supplementary Fig. 1c). These findings together suggest that Sac1 modulates serine palmitoyltransferase activity directly, but in a mode distinct from Orm1/2.

Finally, we showed that the functional complex between Orm proteins and serine palmitoyltransferase is conserved in human cells. Immunoprecipitations from HEK293T cells expressing 3×Flag-tagged ORMDL3 led to a prominent SPTLC1 band detected by western blot (Fig. 3a). Furthermore, we found that simultaneous knock-down by RNA interference of *ORMDL1/2/3* in HeLa cells causes an approximately threefold increase in ceramide levels (Fig. 3b, Supplementary Fig. 2 and Supplementary Information).

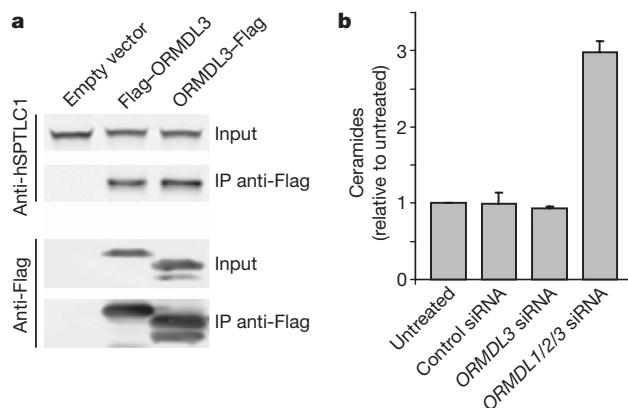


Figure 3 | ORM gene function is conserved in human cells. **a**, HEK293T cells were transfected with either an empty vector or a vector encoding ORMDL3 fused to the 3×Flag epitope (N- or carboxy-terminal fusion). Immunoprecipitations with anti-Flag agarose were analysed by western blot against human serine palmitoyltransferase (anti-hSPTLC1) and against the Flag epitope (anti-Flag). **b**, HeLa cells were transfected with short interfering RNAs (siRNAs) directed against the indicated genes. After 72 h, cells were collected and their lipids were analysed by mass spectrometry. Ceramide levels normalized to phosphatidylcholine are shown (moles of ceramide per mole of phosphatidylcholine, relative to untreated cells; average \pm s.d., $n = 3$).

Together, these results establish that Orm proteins are components of a novel and conserved protein complex, which we term the SPOTS complex (serine palmitoyltransferase, Orm1/2, Tsc3, and Sac1). Additionally, our data indicate that Orm1/2 negatively regulate sphingolipid synthesis by acting directly on Lcb1/2 (for example by altering Lcb1/2 catalytic activity, accessibility of substrates to the enzyme or its subcellular localization).

Homeostatic regulation of Orm1/2 activity

Why would cells include negative regulators of serine palmitoyltransferase, Orm1/2, as core components of this essential enzyme complex? This seemingly paradoxical arrangement prompted us to investigate whether Orm-mediated inhibition of LCB production might be regulated in response to changes in the cellular need for sphingolipid synthesis. We therefore examined how *ORM1/2* deletion affects sensitivity to the Lcb1/2 inhibitor myriocin. Growth in the presence of myriocin is strongly dependent on the cellular capacity for LCB production, as the *lcb2-DAmP* strain is highly sensitive to myriocin (Fig. 4a); in addition, *SAC1* deletion, which leads to increased LCB levels, confers myriocin resistance (Fig. 4a). Thus, naively, we might expect deletion of *ORM1/2* also to confer pronounced resistance to this drug. However, we observed that wild-type and *orm1Δ/orm2Δ* strains exhibit comparable growth in the presence of myriocin (Fig. 4a). Thus, loss of *ORM1/2* strongly affects cell growth under standard conditions but has little apparent effect when sphingolipid synthesis is disrupted, suggesting that Orm1/2 may be inactivated in response to myriocin treatment.

To investigate this possibility further, we compared the effects of myriocin on the LCB levels of wild-type and *orm1Δ/orm2Δ* strains. As described earlier, the *ORM1/2* deletion strain exhibits highly increased LCB levels in the absence of myriocin. However, with increasing doses of myriocin, LCB levels in the *orm1Δ/orm2Δ* strain decrease strongly and approximately converge with those of the wild-type strain (Fig. 4b), supporting our growth data indicating that Orm1/2 may be inactivated in response to myriocin treatment (Fig. 4a). Interestingly, we also found that wild-type cells maintain roughly constant LCB levels even at intermediate concentrations of myriocin (up to about 40 ng ml⁻¹). This robustness is not due to a failure of myriocin to affect Lcb1/2 at these concentrations, as LCB levels in the *orm1Δ/orm2Δ* strain are reduced strongly by the same drug concentrations (Fig. 4b; for further evidence see Fig. 4d). Rather, these results indicate that progressive inactivation of Orm1/2 may provide cells with a homeostatic mechanism to maintain nearly constant sphingolipid output in the face of increasing Lcb1/2 inhibition. Consistent with this hypothesis, LCB levels in the wild-type strain begin to decline only at myriocin concentrations where Orm-mediated inhibition of LCB synthesis appears to be fully relieved, as evidenced by convergence of wild-type and *orm1Δ/orm2Δ* LCB levels (Fig. 4b).

Orm1/2 regulation by phosphorylation

We next investigated the mechanism by which Orm1/2 activity might be decreased in response to myriocin treatment. Growth in myriocin did not alter Orm1/2 expression levels (Fig. 4c and Supplementary Fig. 7) or abolish their ability to interact with Lcb1/2 and Sac1 (Supplementary Fig. 3). However, we observed a notable reduction in localization of green fluorescent protein (GFP)-Orm2 to the cortical but not perinuclear ER after treatment with myriocin (Supplementary Fig. 4), raising the possibility that changes in subcellular localization contribute to regulation of SPOTS complex activity. We also found a strong reduction in Orm protein co-immunoprecipitation in cells treated with myriocin (Fig. 4c), both for Orm1-Orm2 interaction and for self-association of Orm1 and of Orm2. A weak reduction in Orm-Lcb1 binding was also observed in response to myriocin (Fig. 4c). These findings suggest a model in which Orm-Lcb1/2 sub-complexes can self-associate into higher-order oligomers in a

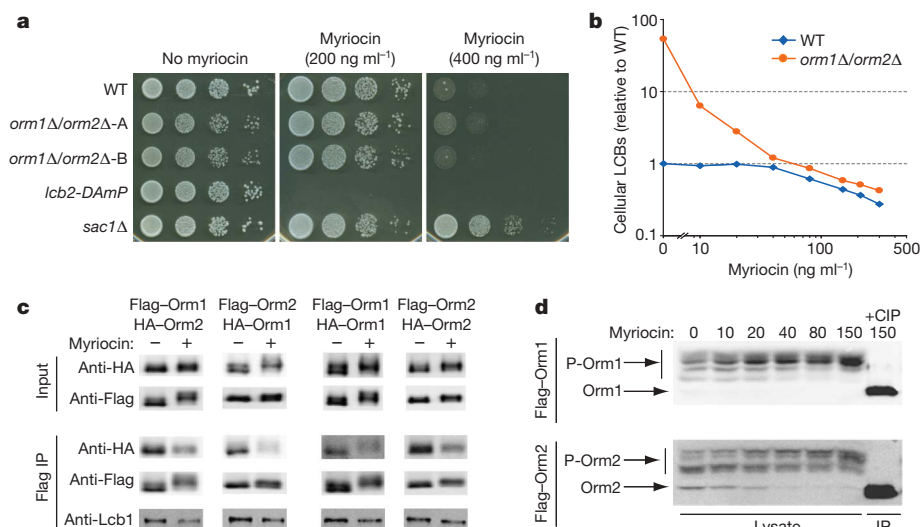


Figure 4 | Orm1/2 are regulated in response to disruption of sphingolipid synthesis. **a**, Serial dilutions of the indicated strains were spotted on plates containing 0, 200 or 400 ng ml⁻¹ myriocin and imaged after growth for 24–48 h. **b**, LCBs were extracted and analysed from wild-type and *ORM1/2* deletion strains grown in media supplemented with the indicated concentrations of myriocin. The combined amounts of C18 dihydrosphingosine and C18 phytosphingosine are shown (relative to wild-type LCB levels in the absence of myriocin; average of $n \geq 2$ experiments). **c**, Native immunoprecipitations of 3×Flag-tagged Orm1 and Orm2 were performed from strains grown in standard media or media supplemented

with 150 ng ml⁻¹ myriocin, and analysed by western blot. The indicated strains also expressed 3×HA–Orm1/2 from their endogenous loci (diploid strains were used to examine self-association of Orm1 and Orm2). **d**, Lysates were prepared from yeast expressing 3×Flag–Orm1/2 after growth in media containing the indicated concentrations of myriocin. Western blots show phosphorylated forms of 3×Flag–Orm1 (P–Orm1) and 3×Flag–Orm2 (P–Orm2) after separation on phosphate-affinity gels³⁵. An immunoprecipitated (IP) sample treated with calf intestine phosphatase (CIP) shows the position of unphosphorylated Orm1/2.

manner that is inhibited in response to disruptions to sphingolipid synthesis.

We also detected in our Orm1/2 co-immunoprecipitations a slight shift in the electrophoretic mobility of Orm1 isolated from myriocin-treated cells, indicating that Orm proteins may be post-translationally modified (see Fig. 4c, Flag–Orm1 and haemagglutinin (HA)–Orm1 inputs). Analysis of 3×Flag–Orm1 and 3×Flag–Orm2 in SDS–polyacrylamide gel electrophoresis (SDS–PAGE) gels that incorporated a phosphate-binding agent to improve the separation of phosphorylated species³⁵ resolved multiple phosphorylated forms for both Orm1 and Orm2 that collapsed to faster-migrating species upon phosphatase treatment (Fig. 4d). Importantly, growth in myriocin induced a dose-dependent shift to more highly phosphorylated forms, and this response occurred over the same concentrations of myriocin that led to homeostatic inactivation of Orm1/2, as determined by measurements of LCBs (compare Fig. 4b and 4d). We also observed increased Orm1/2 phosphorylation after shutting off expression of downstream sphingolipid synthetic enzymes such as Tsc10 or Lag1 (in a *lac1Δ* background; Supplementary Fig. 5), further indicating that phosphorylation of Orm proteins is a homeostatic response to disruption of sphingolipid production (see Fig. 5c). Finally, we did not observe substantial changes in Orm1/2 phosphorylation upon shutting off expression of *AUR1* or *CSG2* (Supplementary Fig. 5), thus providing preliminary evidence that a metabolite upstream of these enzymes, such as ceramide, is an intermediate whose levels are sensed to regulate Orm1/2 activity.

To test our phosphorylation-mediated feedback model directly, we identified residues of Orm1 and Orm2 that are phosphorylated. Through a combination of targeted mutagenesis and mass spectrometry, we found several sites of Orm1 and Orm2 phosphorylation in the amino-terminal regions of these proteins (Fig. 5a and Supplementary Fig. 6). Importantly, mutation of these sites to alanine blocks formation of the slower-migrating phosphorylated species seen in phosphate-affinity gels (Fig. 5a). This loss of phosphorylation is unlikely to be due to these mutations resulting in non-functional Orm proteins, as the phospho-mutants are expressed at levels comparable to wild type and rescue the slow growth of the *orm1Δ/orm2Δ*

strain (Supplementary Fig. 7 and data not shown). Furthermore, immunoprecipitations of phospho-mutant Orm1 and Orm2 revealed that these proteins not only maintain the ability to interact with Lcb1 and each other, but that blocking phosphorylation prevents the change in higher-order assembly of the SPOTS complex normally seen in response to myriocin (Fig. 5b). Thus Orm1/2 phosphorylation appears to be the event that triggers dynamic regulation of SPOTS complex oligomerization.

We next investigated the *in vivo* role of Orm1/2 phosphorylation. Consistent with a basal level of Orm1/2 phosphorylation that is important for steady-state LCB production, we observed a substantial (twofold) reduction in LCB levels in the *ORM1/2* phospho-mutant strain under standard growth conditions (Fig. 5d). Furthermore, we found that this strain is highly sensitive to treatment with myriocin (Fig. 5e). This result therefore confirms a key prediction of our homeostatic model and indicates that although cells may possess additional mechanisms to regulate sphingolipid biosynthesis, such pathways cannot compensate for disruption of the critical feedback control provided by Orm1/2. Thus, Orm proteins are dynamic negative regulators of serine palmitoyltransferase, whose inhibitory activity is dependent on adequate levels of downstream sphingolipids (Fig. 5c).

Discussion

Our studies identify Orm proteins as homeostatic regulators of sphingolipid metabolism and demonstrate that alteration of these controls leads to misregulation of sphingolipid production (Fig. 5c). Specifically, loss of the Orm1/2-mediated brake on serine palmitoyltransferase activity results in toxic accumulation of sphingolipids, whereas mutations that prevent this brake from being removed render cells unable to survive disruptions to sphingolipid synthesis.

A phosphorylation-based feedback loop provides a mechanistic basis for homeostatic regulation of sphingolipid production and exhibits several features that make it well suited to control sphingolipid levels precisely. First, phosphorylation of a direct regulator of serine palmitoyltransferase may enable cells to respond rapidly to changing environments. Second, Orm1/2 exhibit partial phosphorylation under standard growth conditions, which may position the

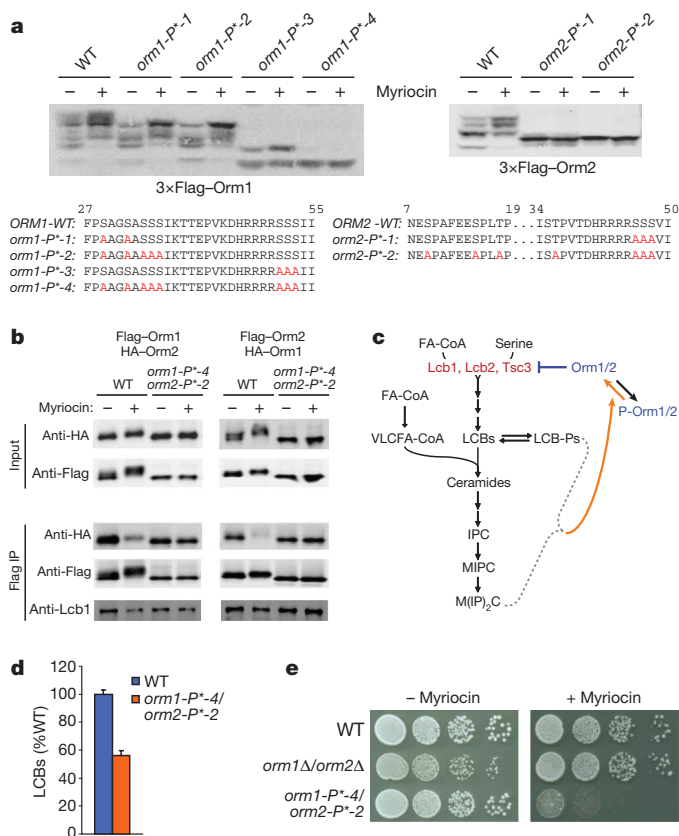


Figure 5 | Mutation of phosphorylated Orm1/2 residues impairs sphingolipid homeostasis. **a**, Lysates were prepared from strains expressing wild-type or phospho-site mutant 3×Flag-Orm1 or 3×Flag-Orm2 after growth in standard media or media supplemented with 150 ng ml⁻¹ myriocin. Western blots are shown after protein separation on phosphate-affinity gels. Residues mutated to alanine in the indicated phospho-mutants are highlighted in red below. **b**, Native immunoprecipitations of 3×Flag-tagged wild-type or phospho-mutant Orm1 and Orm2 were performed from strains expressing wild-type or phospho-mutant 3×HA-Orm1/2 after growth in standard media or media supplemented with 100 ng ml⁻¹ myriocin. Western blots were analysed as in Fig. 4c. **c**, Model for homeostatic regulation of Orm1/2, in which Orm proteins act as negative regulators of serine palmitoyltransferase (Lcb1, Lcb2 and Tsc3), whose inhibitory activity is dependent on levels of downstream sphingolipids. See Fig. 1d for abbreviations used. **d**, LCBs were extracted and analysed from wild-type and 3×Flag-tagged *ORM1/2* double phospho-mutant strains grown in standard media. Data were analysed as in Fig. 4b (average ± s.d., *n* = 3). **e**, Serial dilutions of wild-type, *ORM1/2* deletion and 3×Flag-tagged *ORM1/2* double-phospho-mutant strains were spotted on plates with 0 or 280 ng ml⁻¹ myriocin and imaged after growth for 24–36 h.

Orm1/2-based sphingolipid rheostat for maximal sensitivity to changes in lipid metabolism. Furthermore, multi-site phosphorylation of Orm1 and Orm2 has the potential to generate several distinct and stable phospho-states, which may provide cells with a graded mechanism to adjust lipid production finely to match cellular needs. Finally, several phosphorylation sites may also render Orm1/2 responsive to multiple physiological or metabolic cues.

Our identification of the SPOTS complex reveals a new mechanism by which cells may be able to coordinate a variety of important secretory pathway processes. Although a link between sphingolipids and phosphoinositides has been appreciated for some time^{29,33,36}, we provide evidence that the phosphoinositide phosphatase Sac1 directly modulates sphingolipid metabolism, as it is associated physically with serine palmitoyltransferase. These results are of particular interest given the role of phosphoinositides, including the Sac1 substrate phosphatidylinositol-4-phosphate, in the trafficking of both proteins and sphingolipids from the ER and Golgi apparatus^{10,11,32}. Additionally, changes in Sac1 localization from the ER to the Golgi

have been shown in both yeast and mammals to regulate protein flux through the secretory pathway in response to nutrient levels³⁷. We therefore suggest that the SPOTS complex may represent a dynamic coordinating centre that couples changes in sphingolipid and nutrient levels to the activity and localization of key enzymes of lipid metabolism and trafficking. This model is consistent with our finding that Orm proteins self-associate in a regulated fashion and with evidence that mammalian serine palmitoyltransferase is part of a high-molecular-mass complex³⁸.

Finally, our characterization of *ORM* gene function provides a framework for investigating whether alterations in *ORMDL3* activity and sphingolipid metabolism play a role in the pathogenesis of asthma. Several studies support a role for sphingolipids such as ceramide and sphingosine-1-phosphate in asthma-associated inflammatory processes, including mast-cell degranulation, airway hyper-responsiveness and immune-cell trafficking^{39–43}. Our findings now link this growing body of evidence to the identification of single nucleotide polymorphisms near *ORMDL3* that are associated with childhood asthma²⁰. Specifically, our observation that altered Orm levels strongly impact sphingolipid metabolism raises the testable hypothesis that misregulation of sphingolipids may have a direct and causative role in the development of asthma. A broader potential role for sphingolipids in inflammatory disease is also suggested by reports that single nucleotide polymorphisms near *ORMDL3* are associated with Crohn's disease⁴⁴, type I diabetes⁴⁵ and primary biliary cirrhosis⁴⁶. Finally, the existence of a rich set of pharmacological tools targeting the sphingolipid pathway³¹ raises the possibility of therapeutic intervention to counteract the potential effects of changes in *ORMDL3* activity.

METHODS SUMMARY

Phosphorylation analysis by phosphate-affinity SDS-PAGE. Lysates for phosphorylation analysis were prepared by pelleting and immediately resuspending logarithmically growing yeast in SDS lysis buffer (50 mM Tris-Cl, pH 6.8, 2% SDS, 10% glycerol) with protease inhibitors (Complete EDTA-free Protease Inhibitor Tablets; Roche) at 65 °C. SDS-PAGE gels with phosphate affinity reagent³⁵ (synthesized according to standard synthetic procedures) were prepared with a 7.5% acrylamide resolving gel with 50 μM MnCl₂ and 25 μM phosphate affinity reagent (375 mM Tris, pH 8.8, 0.1% SDS). Gels were run at 70 V for 2.5 h, rinsed twice for 5 min in transfer buffer with 1 mM EDTA and rinsed twice more for 5 min in transfer buffer without EDTA before transfer to nitrocellulose membranes.

Western blots. Proteins were transferred from SDS-PAGE gels to nitrocellulose membranes and probed for proteins of interest by using standard western blot procedures. Antibodies used were as follows: rabbit anti-Flag (Sigma Aldrich), mouse anti-Flag (M2; Sigma Aldrich), mouse anti-HA antibodies 12CA5 (Roche) and HA.11 (Covance), mouse anti-yPgk1 (Molecular Probes), rabbit anti-yLcb1 (raised against peptide antigen SYIKKSHHDDPYRTTC; Abgent), mouse anti-hSPTLC1 (Becton Dickinson) and rabbit anti-*ORMDL1/2/3* (raised against peptide antigen KGTPFETPDQGKARLC; Abgent). Western blots were scanned using an Odyssey fluorescent scanner (Li-Cor Biosciences).

Full Methods and any associated references are available in the online version of the paper at www.nature.com/nature.

Received 23 August; accepted 17 December 2009.

- Brown, M. S. & Goldstein, J. L. Cholesterol feedback: from Schoenheimer's bottle to Scap's MELADL. *J. Lipid Res.* 50 (suppl.), S15–S27 (2009).
- Hampton, R. Y. & Garza, R. M. Protein quality control as a strategy for cellular regulation: lessons from ubiquitin-mediated regulation of the sterol pathway. *Chem. Rev.* 109, 1561–1574 (2009).
- Burg, J. S. *et al.* Insig regulates HMG-CoA reductase by controlling enzyme phosphorylation in fission yeast. *Cell Metab.* 8, 522–531 (2008).
- Loewen, C. J. *et al.* Phospholipid metabolism regulated by a transcription factor sensing phosphatidic acid. *Science* 304, 1644–1647 (2004).
- Martin, C. E., Oh, C. S. & Jiang, Y. Regulation of long chain unsaturated fatty acid synthesis in yeast. *Biochim. Biophys. Acta* 1771, 271–285 (2007).
- Kurat, C. F. *et al.* Cdk1/Cdc28-dependent activation of the major triacylglycerol lipase Tgl4 in yeast links lipolysis to cell-cycle progression. *Mol. Cell* 33, 53–63 (2009).
- Fischer, J. *et al.* The gene encoding adipose triglyceride lipase (PNPLA2) is mutated in neutral lipid storage disease with myopathy. *Nature Genet.* 39, 28–30 (2007).

8. Dickson, R. C., Sumanasekera, C. & Lester, R. L. Functions and metabolism of sphingolipids in *Saccharomyces cerevisiae*. *Prog. Lipid Res.* **45**, 447–465 (2006).
9. Cowart, L. A. & Obeid, L. M. Yeast sphingolipids: recent developments in understanding biosynthesis, regulation, and function. *Biochim. Biophys. Acta* **1771**, 421–431 (2007).
10. Hanada, K. *et al.* Molecular machinery for non-vesicular trafficking of ceramide. *Nature* **426**, 803–809 (2003).
11. D'Angelo, G. *et al.* Glycosphingolipid synthesis requires FAPP2 transfer of glucosylceramide. *Nature* **449**, 62–67 (2007).
12. Kumagai, K., Kawano, M., Shinkai-Ouchi, F., Nishijima, M. & Hanada, K. Interorganelle trafficking of ceramide is regulated by phosphorylation-dependent cooperativity between the PH and START domains of CERT. *J. Biol. Chem.* **282**, 17758–17766 (2007).
13. Klemm, R. W. *et al.* Segregation of sphingolipids and sterols during formation of secretory vesicles at the trans-Golgi network. *J. Cell Biol.* **185**, 601–612 (2009).
14. Aronova, S. *et al.* Regulation of ceramide biosynthesis by TOR complex 2. *Cell Metab.* **7**, 148–158 (2008).
15. Vacaru, A. M. *et al.* Sphingomyelin synthase-related protein SMSr controls ceramide homeostasis in the ER. *J. Cell Biol.* **185**, 1013–1027 (2009).
16. Hannun, Y. A. & Obeid, L. M. Principles of bioactive lipid signalling: lessons from sphingolipids. *Nature Rev. Mol. Cell Biol.* **9**, 139–150 (2008).
17. Leberman, D. A. & Spiegel, S. Cross-talk at the crossroads of sphingosine-1-phosphate, growth factors, and cytokine signaling. *J. Lipid Res.* **49**, 1388–1394 (2008).
18. Akinbami, L. J., Moorman, J. E., Garbe, P. L. & Sondik, E. J. Status of childhood asthma in the United States, 1980–2007. *Pediatrics* **123** (suppl. 3), S131–S145 (2009).
19. Vercelli, D. Discovering susceptibility genes for asthma and allergy. *Nature Rev. Immunol.* **8**, 169–182 (2008).
20. Moffatt, M. F. *et al.* Genetic variants regulating ORMDL3 expression contribute to the risk of childhood asthma. *Nature* **448**, 470–473 (2007).
21. Galanter, J. *et al.* ORMDL3 gene is associated with asthma in three ethnically diverse populations. *Am. J. Respir. Crit. Care Med.* **177**, 1194–1200 (2008).
22. Wu, H. *et al.* Genetic variation in ORM1-like 3 (ORMDL3) and gasdermin-like (GSDML) and childhood asthma. *Allergy* **64**, 629–635 (2009).
23. Bouzigon, E. *et al.* Effect of 17q21 variants and smoking exposure in early-onset asthma. *N. Engl. J. Med.* **359**, 1985–1994 (2008).
24. Verlaan, D. J. *et al.* Allele-specific chromatin remodeling in the ZBP2/GSDMB/ORMDL3 locus associated with the risk of asthma and autoimmune disease. *Am. J. Hum. Genet.* **85**, 377–393 (2009).
25. Tavendale, R., Macgregor, D. F., Mukhopadhyay, S. & Palmer, C. N. A polymorphism controlling ORMDL3 expression is associated with asthma that is poorly controlled by current medications. *J. Allergy Clin. Immunol.* **121**, 860–863 (2008).
26. Hjelmqvist, L. *et al.* ORMDL proteins are a conserved new family of endoplasmic reticulum membrane proteins. *Genome Biol.* **3**, doi:10.1186/gb-2002-3-6-research0027 (2002).
27. Schuldiner, M. *et al.* Exploration of the function and organization of the yeast early secretory pathway through an epistatic miniarray profile. *Cell* **123**, 507–519 (2005).
28. Hanada, K. Serine palmitoyltransferase, a key enzyme of sphingolipid metabolism. *Biochim. Biophys. Acta* **1632**, 16–30 (2003).
29. Beeler, T. *et al.* The *Saccharomyces cerevisiae* TSC10/YBR265w gene encoding 3-ketosphinganine reductase is identified in a screen for temperature-sensitive suppressors of the Ca²⁺-sensitive *csg2Δ* mutant. *J. Biol. Chem.* **273**, 30688–30694 (1998).
30. Ejsing, C. S. *et al.* Global analysis of the yeast lipidome by quantitative shotgun mass spectrometry. *Proc. Natl Acad. Sci. USA* **106**, 2136–2141 (2009).
31. Delgado, A., Casas, J., Llebaria, A., Abad, J. L. & Fabrias, G. Inhibitors of sphingolipid metabolism enzymes. *Biochim. Biophys. Acta* **1758**, 1957–1977 (2006).
32. Strahl, T. & Thorner, J. Synthesis and function of membrane phosphoinositides in budding yeast, *Saccharomyces cerevisiae*. *Biochim. Biophys. Acta* **1771**, 353–404 (2007).
33. Brice, S. E., Alford, C. W. & Cowart, L. A. Modulation of sphingolipid metabolism by the phosphatidylinositol-4-phosphate phosphatase Sac1p through regulation of phosphatidylinositol in *Saccharomyces cerevisiae*. *J. Biol. Chem.* **284**, 7588–7596 (2009).
34. Kearns, B. G. *et al.* Essential role for diacylglycerol in protein transport from the yeast Golgi complex. *Nature* **387**, 101–105 (1997).
35. Kinoshita, E., Kinoshita-Kikuta, E., Takiyama, K. & Koike, T. Phosphate-binding tag, a new tool to visualize phosphorylated proteins. *Mol. Cell. Proteomics* **5**, 749–757 (2006).
36. Tabuchi, M., Audhya, A., Parsons, A. B., Boone, C. & Emr, S. D. The phosphatidylinositol 4,5-bisphosphate and TORC2 binding proteins Slm1 and Slm2 function in sphingolipid regulation. *Mol. Cell. Biol.* **26**, 5861–5875 (2006).
37. Blagoveshchenskaya, A. & Mayinger, P. SAC1 lipid phosphatase and growth control of the secretory pathway. *Mol. Biosyst.* **5**, 36–42 (2009).
38. Hornemann, T., Wei, Y. & von Eckardstein, A. Is the mammalian serine palmitoyltransferase a high-molecular-mass complex? *Biochem. J.* **405**, 157–164 (2007).
39. Rivera, J., Proia, R. L. & Olivera, A. The alliance of sphingosine-1-phosphate and its receptors in immunity. *Nature Rev. Immunol.* **8**, 753–763 (2008).
40. Ammit, A. J. *et al.* Sphingosine 1-phosphate modulates human airway smooth muscle cell functions that promote inflammation and airway remodeling in asthma. *FASEB J.* **15**, 1212–1214 (2001).
41. Masini, E. *et al.* Ceramide: a key signaling molecule in a guinea pig model of allergic asthmatic response and airway inflammation. *J. Pharmacol. Exp. Ther.* **324**, 548–557 (2008).
42. Ryan, J. J. & Spiegel, S. The role of sphingosine-1-phosphate and its receptors in asthma. *Drug News Perspect.* **21**, 89–96 (2008).
43. Idzko, M. *et al.* Local application of FTY720 to the lung abrogates experimental asthma by altering dendritic cell function. *J. Clin. Invest.* **116**, 2935–2944 (2006).
44. Barrett, J. C. *et al.* Genome-wide association defines more than 30 distinct susceptibility loci for Crohn's disease. *Nature Genet.* **40**, 955–962 (2008).
45. Barrett, J. C. *et al.* Genome-wide association study and meta-analysis find that over 40 loci affect risk of type 1 diabetes. *Nature Genet.* **41**, 703–707 (2009).
46. Hirschfield, G. M. *et al.* Primary biliary cirrhosis associated with HLA, IL12A, and IL12RB2 variants. *N. Engl. J. Med.* **360**, 2544–2555 (2009).

Supplementary Information is linked to the online version of the paper at www.nature.com/nature.

Acknowledgements We acknowledge A. Falick, S. Zhou and D. King for identification of proteins by mass spectrometry; M. Schuldiner and S. Wang for E-MAP data collection; D. Fiedler and K. Shokat for providing the phosphate-binding acrylamide reagent; E. Griffis and M. D'Ambrosio for assistance with fluorescence microscopy; N. Ingolia for a codon-optimized mCherry-tagging plasmid; E. Burchard and J. Galanter for discussions of asthma genetics; I. Poser and A. Hyman for advice and providing the HeLa-Kyoto cell line; and M. Bassik, G. Brar, V. Denic, A. Frost, N. Ingolia, E. Quan, B. Toyama and other members of the Weissman laboratory for discussions. This work was supported by funding from Deutsche Forschungsgemeinschaft SFB/TR 13 projects A1 (K.S.) and D1 (A.S.), EUFP6 PRISM (K.S.), ETH Zurich (R.A.), the National Heart, Lung, and Blood Institute, National Institute of Health (N01-HV-28179) (R.A.), SystemsX.ch, the Swiss initiative for systems biology (R.A.), the Boehringer Ingelheim Fonds and the Swiss National Science Foundation (B.B.), the Howard Hughes Medical Institute (J.S.W.), the University of California, San Francisco Strategic Asthma Basic Research Center (J.S.W.), the National Science Foundation Graduate Research Fellowship Program (D.K.B.) and the Fannie and John Hertz Foundation (D.K.B.).

Author Contributions D.K.B. designed, performed and interpreted experiments. S.R.C. oversaw E-MAP data collection and analysis. B.B. performed and analysed protein mass spectrometry experiments to identify sites of phosphorylation under the supervision of R.A. C.S.E. performed and analysed lipidomic measurements with the support of A.S. and K.S. J.S.W. designed and interpreted experiments. D.K.B. and J.S.W. prepared the manuscript.

Author Information Reprints and permissions information is available at www.nature.com/reprints. The authors declare no competing financial interests. Correspondence and requests for materials should be addressed to J.S.W. (weissman@cmp.ucsf.edu).

METHODS

Growth media, plasmids and strain construction. All yeast experiments were conducted in strain BY4741 (ATCC), a related strain suitable for E-MAP experiments²⁷, and derivatives thereof. Strains were grown in YEPD media or media supplemented with myriocin (Sigma Aldrich; at least 12 h growth in myriocin in all cases), with the exception of samples prepared for lipidome analysis, which were grown in synthetic defined media.

Deletion, DAMP, overexpression (*pTEF2* and *pTHD3*), mCherry fusion and tetracycline-repressible promoter strains were constructed by standard PCR-based methods (see Supplementary Information). Strains expressing N-terminally epitope-tagged or GFP-tagged forms of wild-type or mutant Orm1, Orm2, Lcb1 and Sac1 were made by integration of DNA fragments encoding these gene variants into strains in which these genes had been deleted with the *URA3* counter-selectable marker. For the essential gene *LCB1*, a diploid strain was used for integration of the tagged allele containing the 3×Flag epitope inserted between codons 9 and 10, as previously reported⁴⁷. *ORM1* and *ORM2* mutants, as well as the previously described *sac1-8* mutation³⁴, were created by standard PCR mutagenesis.

HEK293T cells (ATCC) and HeLa-Kyoto cells (a gift from A. Hyman) were grown in DMEM high-glucose media supplemented with penicillin, streptomycin, glutamine and 10% heat-inactivated fetal calf serum. *ORMDL3* was cloned from HEK293T cDNA into expression plasmids containing N- or C-terminal 3×Flag epitopes (p3XFLAG-CMV-10 and p3XFLAG-CMV-14; Sigma Aldrich). **E-MAP data collection and analysis.** E-MAP data were collected and analysed as described previously²⁷ (manuscript in preparation). Genetic interaction patterns were compared for pairs of mutants by first identifying those genetic backgrounds for which E-MAP data were available for both mutants of interest. The similarity of the genetic interaction scores for the two mutants was then calculated by computing the cosine correlation between their interaction scores across these shared mutant backgrounds. For a given mutant of interest such as *orm2Δ*, these pairwise comparisons were performed with all other mutant strains having at least 200 shared genetic interaction data points. For the *ORM1* and *ORM2* overexpression mutants, an average of the *pTDH3* and *pTEF2* interaction profiles was used as the query profile for correlation calculations.

Lipidome analysis by mass spectrometry. Lipidome analyses were conducted as described previously³⁰ with minor modifications based on an existing method⁴⁸ for LCB analysis. Samples were collected from 20-ml cultures of yeast cells growing logarithmically in synthetic defined media or from about 4×10^6 to 6×10^6 HeLa cells grown as described earlier. Cells were washed in water or 155 mM ammonium bicarbonate at 4 °C, and cell pellets were then frozen immediately in liquid nitrogen. Yeast data are from two independent samples each analysed twice; HeLa cell data are from samples analysed in triplicate.

Growth rate measurements. Logarithmic growth rates were measured by OD₆₀₀ from $n \geq 3$ replicate samples. Saturated cultures of the relevant strains were diluted into fresh media and grown for more than 7 h before growth analysis. Myriocin-treated cultures were grown for 3 h in the presence of the drug before analysis of growth rate.

Native affinity purifications of solubilized membrane proteins (large scale, yeast). ER-derived microsomes were prepared from yeast cells grown in YEPD (~4,000 OD₆₀₀ units collected at OD₆₀₀ ~1.4). Cells were collected, washed in water at 4 °C, resuspended in lysis buffer (50 mM HEPES-KOH, pH 6.8, 150 mM potassium acetate (KOAc), 2 mM MgOAc, 1 mM CaCl₂, 200 mM sorbitol) supplemented with protease inhibitors (Complete EDTA-free Cocktail; Roche) and frozen in a drop-by-drop fashion in liquid nitrogen. Frozen cells were then pulverized in a ball mill (6 × 3 min at 30 Hz; Retsch), thawed in lysis buffer at 4 °C and dounced ten times to homogeneity. After clarification by two consecutive centrifugations at 1,000g, microsomes were pelleted at 44,000g, resuspended in 0.5 ml lysis buffer and then diluted with 14 ml immunoprecipitation buffer (50 mM HEPES-KOH, pH 6.8, 150 mM KOAc, 2 mM MgOAc, 1 mM CaCl₂, 15% glycerol) with 2% digitonin (Calbiochem) supplemented with protease inhibitors. After nutating for 1.5 h at 4 °C, unsolubilized material was removed by centrifugation at 44,000g, and the remaining supernatant was added to anti-Flag resin (150 µl bed volume; Sigma Aldrich). Immunoprecipitations were nutated for 3 h at 4 °C and then washed 4 × 10 ml with immunoprecipitation buffer with 0.1% digitonin. Bound proteins were eluted twice with 150 µl immunoprecipitation buffer with 0.25% digitonin and 2 mg ml⁻¹ 3×Flag peptide (Sigma Aldrich). Eluates were combined, separated on SDS-PAGE gels and stained with a colloidal blue staining kit (Invitrogen). Samples were prepared for phospho-site mapping using the same protocol, except that phosphatase inhibitors (Halt Phosphatase Inhibitor Cocktail; Pierce) were included in the buffers used.

Native affinity purifications of solubilized membrane proteins (small scale, yeast). Lysates for small-scale immunoprecipitations were prepared from logarithmically growing yeast cells (~25 OD₆₀₀ units) grown in YEPD. Cultures were

collected, washed in water at 4 °C and resuspended in 500 µl immunoprecipitation buffer (see above) with 0.1% digitonin and supplemented with protease and phosphatase inhibitors. Cell lysates were prepared by bead-beating at 4 °C, followed by addition of 500 µl immunoprecipitation buffer with 1.9% digitonin to raise the final digitonin concentration to 1%. Membrane proteins were solubilized by nutating lysates at 4 °C for 40 min. Unsolubilized material was next removed by centrifugation at 100,000g, and clarified lysates were incubated with anti-Flag resin (25 µl bed volume) for 2.5 h. The anti-Flag resin was then washed four times with 1 ml immunoprecipitation buffer containing 0.1% digitonin, and bound proteins were eluted by addition of 30 µl immunoprecipitation buffer with 0.25% digitonin and 2 mg ml⁻¹ 3×Flag peptide.

Native affinity purifications of solubilized membrane proteins (small scale, human cells). HEK293T cells grown in DMEM high-glucose media supplemented with penicillin, streptomycin, glutamine and 10% heat-inactivated fetal calf serum were transfected using Fugene6 transfection reagent (Roche) according to the manufacturer's instructions. After approximately 48 h growth, transfected cells were collected by trypsinization and washed with PBS. Cell pellets were then resuspended at 4 °C in 1 ml immunoprecipitation buffer (see above) with 2% digitonin and protease inhibitors and nutated for 45 min to solubilize membrane proteins. Insoluble material was removed by centrifugation at 100,000g, and the clarified supernatant was incubated with anti-Flag resin (25 µl bed volume) for 2.5 h. The remainder of the immunoprecipitation was done in the same fashion as the yeast small-scale affinity purifications (see earlier).

Denaturing immunoprecipitations and phosphatase treatment. A 50-ml yeast culture in logarithmic phase growth was collected and resuspended in 10 ml 5% trichloroacetic acid (TCA) and incubated for 10 min at 4 °C. Cell pellets were washed once in 1 ml 5% TCA, washed twice in 1 ml acetone and then air-dried. Acid-washed glass beads (200 µl) and 150 µl SDS lysis buffer (50 mM Tris-Cl, pH 7.8, 1 mM EDTA, 1% SDS, 2 M urea) supplemented with protease inhibitors were added to the dried pellets, which were then lysed by bead-beating (3 × 60 s at 4 °C). Lysates were diluted by addition of 1,350 µl Tween immunoprecipitation buffer (100 mM Tris-Cl, pH 7.8, 200 mM NaCl, 0.5% Tween-20, also supplemented with protease inhibitors) and clarified at 20,000g. Supernatants were then added to anti-Flag agarose (25 µl bed volume) and immunoprecipitated for 2.5 h at 4 °C. The anti-Flag resin was then washed 2 × 1 ml with Tween immunoprecipitation buffer, 1 × 1 ml with Tween/urea wash buffer (100 mM Tris-Cl, pH 7.8, 100 mM NaCl, 0.5% Tween-20, 2 M urea), and 2 × 1 ml in phosphatase buffer (NEBuffer 3; New England Biolabs), with 0.1% Tween-20. The washed resin was then resuspended in 54 µl phosphatase buffer plus 6 µl calf intestine phosphatase (New England Biolabs) and incubated for 1 h at 37 °C. After phosphatase treatment, the resin was sequentially washed with 1 ml Tween immunoprecipitation buffer and 1 ml SDS-DOC wash buffer (50 mM Tris-Cl, pH 7.8, 0.1% SDS, 0.1% Na-deoxycholate). Bound proteins were then eluted by addition of 60 µl SDS buffer (100 mM Tris-Cl, pH 6.8, 4% SDS, 20% glycerol) and incubation for 10 min at 65 °C.

RNA interference in HeLa cells. HeLa cells grown in DMEM high-glucose media supplemented with penicillin, streptomycin, glutamine and 10% heat-inactivated fetal calf serum were transfected using HiPerFect transfection reagent (Qiagen) according to the manufacturer's instructions. After approximately 72 h growth, transfected cells were collected by trypsinization for lipidomic and gene expression analysis. For each targeted gene, a pool of four siRNAs was used (ON-TARGETplus SMARTpool; Dharmacon), with siRNA sequences as follows: *ORMDL1*: 5'-UGGCAAGUUUCUAUACGAA-3', 5'-GGAGUUGGCUUGCUUCAUA-3', 5'-GCUUAUAAGUUAAGGGCA-3', 5'-GGACCAGCUUAACUUAUAA-3'; *ORMDL2*: 5'-UGGUAGGAUUGCUGCAUAU-3', 5'-AGUUAUAUCAGGAUGGGUA-3', 5'-GUGUACUGCUGCCGAAGUU-3', 5'-AGUAUGAUGCUGCGCACUU-3'; *ORMDL3*: 5'-GAACAUGGACCAGCAGUU-3', 5'-ACACUAAGUACGACCAAGAU-3', 5'-CGGUACGGCUUCUGGAUUG-3', 5'-UGGGUAGGGAGCUGUCUAA-3'.

RT-PCR analysis of gene expression in HeLa cells. RNA was extracted from HeLa cells using the RNeasy kit (Qiagen) after cell homogenization (QIAshredder; Qiagen). Extracted RNA was reverse-transcribed using AMV RT (Promega) and amplified with Taq polymerase (GoTaq; Promega). Real-time SYBR green fluorescence was monitored using a DNA Engine Opticon System (MJ Research), and the following primers were used: *RPL19*: 5'-ATGTATCACAGCCTGTACCTG-3', 5'-TTCTTGGTCTCTCTCCTCTTG-3'; *ORMDL1*: 5'-CTGACCAGGGTAAAGCAAGG-3', 5'-TCCAAAGATCCGAACACCAT-3'; *ORMDL2*: 5'-CATACGGTGAACGGACACC-3', 5'-CGGCAGCAGTACACTTAGCA-3'; *ORMDL3*: 5'-AACCCTTGCTCACTTGTTG-3', 5'-CAAAGACCCATCCACACTT-3'.

Live-cell yeast fluorescence microscopy. Yeast cells expressing Sec63-mCherry and GFP-Orm1 or GFP-Orm2 were grown in rich media with or without myriocin and spotted on a concanavalin-A-coated 25 × 50 mm coverslip covered with a 22 × 22 mm coverslip. Cells were imaged through the 25 × 50 mm coverslip using a Zeiss Axiovert 200M microscope (Carl Zeiss Microimaging) equipped

with a spinning disk confocal scanhead and laser system (Yokogawa CS10, Yokogawa Electronics; Solamere). Images were collected as Z-stacks with 0.5 μm spacing between frames using $\mu\text{Manager}$ software and an ImagEM C9100-13 EM-CCD camera (Hamamatsu Photonics).

Serial-dilution cell-spotting assays. Logarithmically growing yeast were spotted onto agar plates in tenfold serial dilutions from a starting OD_{600} density of 0.3 to a final OD_{600} density of 3×10^{-4} . Plates were imaged after growth for 24–48 h. Plates with myriocin were standard YEPD supplemented with 0.1% tergitol and 2 mM citric acid.

LCB extraction and analysis by high-performance liquid chromatography. LCB extraction and analysis was performed as described⁴⁸. Myriocin-treated samples were grown for 14–16 h in the presence of drug before extractions. For extractions, 50 ml of a logarithmically growing culture was collected and resuspended in 10 ml 5% TCA at 4 °C. After a 10 min incubation, cells were washed once in 5% TCA and three times in H_2O at 4 °C. Cell pellets were then resuspended in 75 μl H_2O followed by addition of 425 μl 70.6 mM TEA/ethanol. Lipids were extracted by bath sonication (3×99 s, 30 W) and incubation at 65 °C for 30 min. Of this extract, 150 μl was derivatized by reaction for 40 min at room temperature with 30 μl of AccQ Fluor reagent (Waters Corporation). Ester-linked lipids were de-acylated by addition of 22.5 μl of 1.5 M KOH/methanol. After 30 min incubation at 37 °C, the reaction was neutralized by addition of 22.5 μl 1.74 M acetic acid/methanol. Samples were analysed on an Agilent Chemstation high-performance liquid chromatography using a reverse-phase C18 column (ZORBAX Eclipse XDB-C18; Agilent).

Protein identification by mass spectrometry. Gel slices were trypsinized and mass spectra were acquired on a Bruker Reflex III MALDI-TOF mass spectrometer. Proteins were identified by searching the NCBI database using the MS-Fit program on Protein Prospector (University of California, San Francisco, <http://prospector.ucsf.edu>)⁴⁹.

Identification of phosphorylation sites by mass spectrometry. Proteins eluted from native affinity purifications of 3 \times Flag-Orm1 or 3 \times Flag-Orm2 (see earlier) were precipitated using ice-cold acetone. After incubation overnight at –20 °C, proteins were pelleted at 4 °C by centrifugation. Protein pellets were then processed, and the resulting peptide mixtures were analysed on a hybrid LTQ-Orbitrap mass spectrometer, as described previously⁵⁰. Database searches were performed using the Saccharomyces Genome Database non-redundant database, as described⁵⁰.

47. Gable, K., Slife, H., Bacikova, D., Monaghan, E. & Dunn, T. M. Tsc3p is an 80-amino acid protein associated with serine palmitoyltransferase and required for optimal enzyme activity. *J. Biol. Chem.* **275**, 7597–7603 (2000).
48. Lester, R. L. & Dickson, R. C. High-performance liquid chromatography analysis of molecular species of sphingolipid-related long chain bases and long chain base phosphates in *Saccharomyces cerevisiae* after derivatization with 6-aminoquinolyl-N-hydroxysuccinimidyl carbamate. *Anal. Biochem.* **298**, 283–292 (2001).
49. Jiménez, C. R., Huang, L., Qiu, Y. & Burlingame, A. L. in *Current Protocols in Protein Science* (eds Coligan, J. E., Dunn, B. M., Ploegh, H. L., Speicher, D. W. & Wingfield, P. T.) 16.4.1–16.4.5 (John Wiley, 1998).
50. Huber, A. *et al.* Characterization of the rapamycin-sensitive phosphoproteome reveals that Sch9 is a central coordinator of protein synthesis. *Genes Dev.* **23**, 1929–1943 (2009).

LETTERS

WASP-12b as a prolate, inflated and disrupting planet from tidal dissipation

Shu-lin Li^{1,2,†}, N. Miller³, Douglas N. C. Lin^{1,3} & Jonathan J. Fortney³

The class of exotic Jupiter-mass planets that orbit very close to their parent stars were not explicitly expected before their discovery¹. The recently discovered² transiting planet WASP-12b has a mass $M = 1.4 \pm 0.1$ Jupiter masses (M_J), a mean orbital distance of only 3.1 stellar radii (meaning it is subject to intense tidal forces), and a period of 1.1 days. Its radius $1.79 \pm 0.09 R_J$ is unexpectedly large and its orbital eccentricity 0.049 ± 0.015 is even more surprising because such close orbits are usually quickly circularized. Here we report an analysis of its properties, which reveals that the planet is losing mass to its host star at a rate of about $10^{-7} M_J$ per year. The planet's surface is distorted by the star's gravity and the light curve produced by its prolate shape will differ by about ten per cent from that of a spherical planet. We conclude that dissipation of the star's tidal perturbation in the planet's convective envelope provides the energy source for its large volume. We predict up to 10 mJy CO band-head ($2.292 \mu\text{m}$) emission from a tenuous disk around the host star, made up of tidally stripped planetary gas. It may also contain a detectable resonant super-Earth, as a hypothetical perturber that continually stirs up WASP-12b's eccentricity.

Gas giant planets contract as they age and cool. Theoretical models^{3,4} predict an upper radius limit of around $1.2 R_J$ for mature Jupiter-like gas giants. The radii (R_p) of ~ 60 short-period (mostly $P < 5$ days) gas giants have been measured from transit light curves. In the mass range $M_p \approx (1 \pm 0.5) M_J$, most planets have $R_p \approx (1.2 \pm 0.2) R_J$. However, several planets have observed R_p of about $1.5\text{--}1.8 R_J$. The rate of heat loss from these planets increases with their radius. The over-sized WASP-12b has an intrinsic radiative luminosity of $L_p \approx (1\text{--}2) \times 10^{28} \text{ erg s}^{-1}$. If gravity provides the only source with which to replenish this heat loss, WASP-12b would contract^{3,5} significantly over 100 million years. The small orbital separation from its host star means that WASP-12b is one of the most intensely heated planets known. Stellar photons deposit energy onto a planet's day side, and reduce the internal heat loss⁶, but the absorbed stellar irradiation is efficiently re-radiated along with the heat flux from a planet's interior on its night side⁷. Although surface evaporation enlarges a planet's tenuous atmosphere⁸, it cannot alone significantly modify its internal structure and evolution⁹.

To account for the inflated sizes of gas giants that are gigayears old, we consider additional heating mechanisms. Given its measured eccentricity $e_p \approx 0.05$ and its proximity to its host star, one potential suitable energy source for WASP-12b (and other close-in planets) is the dissipation of the stellar tidal disturbance¹⁰ well below its photosphere. A planet's tidal heating rate $\dot{E}_{\text{tidal}} \approx e^2 G M_p M_* / a \tau_e$ (where G is the gravitational constant and a is the semi-major axis) is determined by its circularization timescale τ_e (where subscript e indicates eccentricity damping), which is proportional to its tidal quality factor¹¹, Q'_p . (Here M_* is the stellar mass.) We note that many long-period planets have elongated orbits ($0 < e_p < 1$), whereas those

of short-period gas giants are mostly circular (within the detection limit, $e_p < 0.02$). If this transition is due to their own lifelong tidal dissipation, their inferred $Q'_p \approx 10^6$ to 10^7 .

For its orbit, WASP-12b's $\tau_e \approx 0.033 Q'_p (X_R/R_p)^5$ years, where $X_R \equiv (M_p/3M_*)^{1/3} a$ is the distance from the planet's core to its inner Lagrangian (L_1) point (that is, the Roche radius). If WASP-12b's $Q'_p \approx 10^7$, then its eccentricity would be damped within ten million years and the associated tidal heating rate would balance its current intrinsic radiative luminosity (that is, $\dot{E}_{\text{tidal}} \approx L_p$). Depending on their internal structure and orbital periods, the magnitudes of Q'_p for gas giants and their host stars are thought to vary over a large magnitude range^{12,13} (see below). If WASP-12b's Q'_p is comparable to that inferred for Jupiter¹⁴ ($\sim 10^6$), its tidal heating would over-compensate beyond its intrinsic luminosity and would drive ongoing envelope expansion. Once the planet's atmosphere filled its Roche lobe, mass would be lost at a rate of $\dot{M}_p \approx \dot{E}_{\text{tidal}} R_p / 2GM_p$.

To show that WASP-12b is currently losing mass, we analyse the amount of stellar light blocked during its primary transit by its cross-section in the (Y - Z) direction normal to the line (X) joining it and its host star (see Fig. 1). At the planet's occultation radius R_p and maximum Y distance ($Y_R = 2X_R/3$) on the planet's Roche lobe, we estimate the atmosphere density to be $\rho(R_p) \approx 5 \times 10^{-8} \text{ g cm}^{-3}$ and $\rho(Y_R) \approx 3 \times 10^{-12} \text{ g cm}^{-3}$ respectively (see Supplementary Information). An interesting consequence of the planet's prolate shape is that, as a function of orbital phase, it will scatter incident stellar flux, and emit its own thermal radiation, differently from how a spherical planet would. We estimate that this effect leads to 10% more flux during first and third quarters. Optical and mid-infrared orbit-modulated flux has been detected from several planets¹⁵ and WASP-12b is a promising candidate for detection as well.

Near L_1 , gas falls towards the host star through a nozzle with a radius $\Delta Y \approx 0.22 X_R$ (see Supplementary Information). The resultant pressure gradient on the Roche lobe drives gas from other regions to flow towards L_1 . This advection along equipotential surfaces offsets the hydrostatic equilibrium normal to these surfaces. Consequently, the planet's lower atmosphere expands (see Fig. 1) at the speed of sound in space (c_{sound}) across the Roche lobe (which has a total surface area of $A_R \approx 4\pi X_R Y_R$) with a mass flux $\dot{M}_{\text{observed}} = \rho(Y_R) c_{\text{sound}} A_R \approx 10^{-7} M_J$ per year. If WASP-12b's $Q'_p \approx 10^6$, its $\dot{M}_p \approx \dot{M}_{\text{observed}}$ and its atmosphere loss would be continually replenished by the tidal inflation of its envelope.

Gas slightly beyond the nozzle accelerates towards the star and attains a free-fall speed v_f and a local density $\rho(L_1) \approx \rho(Y_R)$ ($c_{\text{sound}} A_R / v_f \pi \Delta Y^2 \approx \rho(Y_R)$). Because $\rho(L_1) \ll \rho(R_p)$, this stream remains optically thin. It does not directly strike WASP-12b but forms a disk that is tidally truncated¹⁶ by WASP-12b at about $0.7a = 3R_\odot$, where R_\odot is the radius of the Sun. Provided WASP-12's magnetic field has a subsolar strength, the disk extends to the stellar surface and

¹Kavli Institute for Astronomy and Astrophysics, ²Department of Astronomy, Peking University, Beijing 100871, China. ³Department of Astronomy and Astrophysics, University of California, Santa Cruz 95064, USA. [†]Present address: National Astronomical Observatories of China, Chinese Academy of Sciences, Beijing 100012, China.

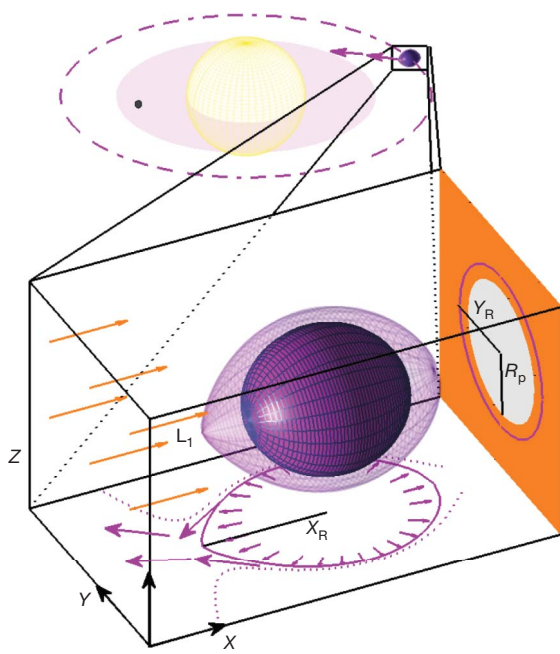


Figure 1 | WASP-12b's surfaces. The inner opaque purple surface (we note its prolate shape) contains the planet's envelope, which contributes to the eclipse of the stellar light, as inferred from transit observations. The stellar photons are represented by the orange arrows. The planet's outer transparent surface is the L_1 equipotential surface and its projection onto the orbital plane is shown as the solid purple line. The equipotential surfaces are computed assuming that the planet is a point mass on a nearly circular orbit. WASP-12b has a thin atmosphere that extends between these two surfaces; some of this atmosphere flows through the inner Lagrange point and eventually onto WASP-12. The purple dotted lines indicate the projection of the equipotential surface which channels the flow (purple arrows) from the planet's expanding envelope. The presence of a tenuous disk (light purple disk) with a hypothetical embedded planet (black dot) around WASP-12 (light yellow sphere) is illustrated at the top. The planet's orbit is traced by the purple dashed line. All variables are defined in the text.

intercepts a significant fraction (~ 0.1) of the stellar visual luminosity¹⁷. Viscous stress also generates heat at a rate of about $10^{-2}L_{\odot}$ while it transfers mass and angular momentum¹⁸ (with an efficiency factor $\alpha \approx 10^{-2}$ – 10^{-3}) to produce a disk surface density $\Sigma \approx \alpha^{-1} \text{ g cm}^{-2}$.

The disk's warm ($\sim 3,000$ – $4,000$ K) midplane is sandwiched by heated surface layers that emit continuum and line radiation, respectively. At these temperatures, CO molecules are preserved and their 2-0 band-head emission at $\sim 2.292 \mu\text{m}$ (1–10 mJy at WASP-12's 267-kiloparsec distance from the Sun) is comparable to that of their continuum¹⁹. Although the expected flux is 1–2 orders of magnitude below that found around some known young stellar objects, this disk signature may be marginally observable with existing near-infrared spectrometers. Pollution of a few Earth masses of metals may also enhance the [Fe/H] of the star's low-mass ($< 10^{-3}M_{\odot}$) convection zone, depending on the efficiency of a double diffusive instability²⁰.

As its tidal debris flows through the disk onto the surface of its host star, WASP-12b gains orbital angular momentum. Its orbit also exchanges angular momentum with its host star at a rate that is regulated by the dissipative efficiency of its tidal perturbation within the stellar envelope^{21,22}. WASP-12b would spiral towards its host star on a timescale of $\tau_a \approx 10$ million years if the quality factor Q'_* of its slowly spinning host star is comparable to that ($\sim 10^6$) estimated from the circularization periods of binary stars in open clusters²³.

The low probability of catching a brief glimpse of WASP-12b's rapid orbital evolution and mass loss can be circumvented with variable Q'_* values¹³. We suggest that during WASP-12's main sequence evolution, its Q'_* may have been larger than 10^8 , such that its planet's orbit did

not evolve significantly. But, as it evolved onto its subgiant track, WASP-12's intrinsic oscillation frequencies would have been modified with the expansion of its radius, deepening of its convective zone, and slowdown of its spin. When these frequencies are tuned to match those of the planet's tidal perturbation, the star's dynamical response is greatly amplified. In these resonant episodes, Q'_* may have decreased¹³ below $\sim 10^7$, leading to the present epoch of intense star–planet tidal interaction and dissipation.

Our result for the mass loss from WASP-12b is robust, whereas the tidal heating scenario depends on the assumed value of $Q'_p < 10^7$ today. But the preservation of WASP-12b's finite eccentricity implies that its $Q'_p > 10^9$ for most of its lifetime. It is possible that during its recent accelerated orbital decay (owing to a decline in Q'_*), the evolving stellar perturbation frequency and strength may have intensified the planet's tidal response and dissipation over some ranges of its orbital period. The subsequent expansion of the heated envelope could have led to further changes in the planet's oscillation frequencies and enlarged the range of efficient tidal dissipation. We estimate an effective $Q'_p \approx 10^6$ to 10^7 for the present-day WASP-12b, which is comparable to the value needed to maintain its inflated size.

It is also possible that WASP-12b's eccentricity is continually excited by one or more super-Earths with periods $P_2 < P$ and masses $M_2 < M_p(P_2/P)^{13/3}$. Their convergent paths would lead to resonant capture²⁴ followed by lock-step orbital decay and e growth to an equilibrium²⁵. Episodic declines of Q'_* and Q'_p (over a few million years) would excite WASP-12b's equilibrium eccentricity and inflate its radius to their observed values. Such a hypothetical planet would be embedded¹⁶ in the circumstellar disk and the orbital migration induced by its tidal interaction with the disk²⁶ (on timescales $> 10^8$ years) would not affect its resonant interaction with WASP-12b. The sensitivity of its radial velocity detection would need to be $< 1 \text{ m s}^{-1}$ and its transit observation would need to be 10^{-4} magnitude.

Our analysis can be used to constrain the efficiency of tidal dissipation of other close-in planets, such as the recently discovered²² massive ($10M_J$), short-period (0.94 days) planet WASP-18b. If it and its host star have similar Q' values of $\sim 10^6$, WASP-18b's tidal dissipation (at a rate of about $10^{30} \text{ erg s}^{-1}$) would maintain the synchronization of its spin¹⁰ and induce mass loss through Roche-lobe overflow during the decay of its orbit (induced by the star's tidal dissipation) on a timescale of about one million years. However, WASP-18b is observed to have a normal radius ($1.1R_J$) for massive gas giants, which places an upper limit ($< 10^{28} \text{ erg s}^{-1}$) on the planetary dissipation rate⁵, which implies either $Q'_* > 10^7$ or $Q'_p > 10^{10}$ (or both). This constraint includes the possibility that WASP-18b will be preserved (with $Q'_* > 10^9$) until the end of its host star's main-sequence evolution.

Received 27 April; accepted 25 November 2009.

- Mayor, M. & Queloz, D. A. Jupiter-mass companion to a solar-type star. *Astrophys. J.* **378**, 355–359 (1995).
- Hebb, L. et al. WASP-12 b: the hottest transiting extra solar-planet yet discovered. *Astrophys. J.* **693**, 1920–1928 (2009).
- Bodenheimer, P., Laughlin, G. & Lin, D. N. C. On the radii of extrasolar giant planets. *Astrophys. J.* **592**, 555–563 (2003).
- Fortney, J. J., Marley, M. S. & Barnes, J. W. Planetary radii across five orders of magnitude in mass and stellar insolation: application to transits. *Astrophys. J.* **659**, 1661–1672 (2007).
- Bodenheimer, P., Lin, D. N. C. & Mardling, R. A. On the tidal inflation of short-period extrasolar planets. *Astrophys. J.* **548**, 466–472 (2001).
- Guillot, T., Burrow, A., Hubbard, W. B., Lunine, J. I. & Saumon, D. Giant planets at small orbital distances. *Astrophys. J.* **459**, L35–L38 (1996).
- Dobbs-Dixon, I. & Lin, D. N. C. Atmospheric dynamics of short-period extrasolar gas giant planets. I. Dependence of nightside temperature on opacity. *Astrophys. J.* **673**, 513–525 (2008).
- Garcia Munoz, A. Physical and chemical aeronomy of HD 209458b. *Planet. Space Sci.* **55**, 1426–1455 (2007).
- Hubbard, W. B., Hattori, M. F., Burrows, A., Hubeny, I. & Sudarsky, D. Effects of mass loss for highly-irradiated giant planets. *Icarus* **187**, 358–364 (2007).
- Dobbs-Dixon, I., Lin, D. N. C. & Mardling, R. A. Spin-orbit evolution of short-period planets. *Astrophys. J.* **610**, 464–476 (2004).
- Goldreich, P. & Soter, S. Q in the Solar System. *Icarus* **5**, 375–389 (1966).

12. Ogilvie, G. I. & Lin, D. N. C. Tidal dissipation in rotating giant planets. *Astrophys. J.* **610**, 477–509 (2004).
13. Ogilvie, G. I. & Lin, D. N. C. Tidal dissipation in rotating solar-type stars. *Astrophys. J.* **661**, 1180–1191 (2007).
14. Yoder, C. F. & Peale, S. J. The tide of Io. *Icarus* **47**, 1–35 (1981).
15. Knutson, H. *et al.* A map of the day-night contrast of the extrasolar planet HD 189733b. *Nature* **447**, 183–186 (2007).
16. Lin, D. N. C. & Papaloizou, J. C. B. in *Protostars and Planets III* (eds Black, D. & Mathews, M.) 749–835 (University of Arizona Press, 1993).
17. Adams, F. C., Shu, F. H. & Lada, C. J. The disks of T Tauri stars with flat infrared spectra. *Astrophys. J.* **326**, 865–883 (1988).
18. Hartmann, L., Calvet, N., Gullbring, E. & D'Alessio, P. Accretion and the evolution of T Tauri disks. *Astrophys. J.* **495**, 385–400 (1998).
19. Najita, J., Carr, J. S., Glassgold, A. E., Shu, F. H. & Tokunaga, A. T. Kinematic diagnostics of disks around young stars: CO overtone emission from WL 16 and 1548C27. *Astrophys. J.* **462**, 919–936 (1996).
20. Vauclair, S. Metallic fingers and metallicity excess in exoplanets' host stars: the accretion hypothesis revisited. *Astrophys. J.* **605**, 874–879 (2004).
21. Sasselov, D. D. The new transiting planet OGLE-TR-56b: orbit and atmosphere. *Astrophys. J.* **596**, 1327–1331 (2003).
22. Hellier, C. *et al.* An orbital period of 0.94 days for the hot-Jupiter planet WASP-18b. *Nature* **460**, 1098–1100 (2009).
23. Meibom, S., Mathieu, R. D. & Stassun, K. G. An observational study of tidal synchronization in solar-type binary stars in the open clusters M35 and M34. *Astrophys. J.* **653**, 621–635 (2006).
24. Peale, S., Cassen, P. & Reynolds, R. T. Melting Io by tidal dissipation. *Science* **203**, 892–894 (1979).
25. Lin, D. N. C. & Papaloizou, J. On the structure of circumbinary accretion disks and the tidal evolution of commensurable satellites. *Mon. Not. R. Astron. Soc.* **188**, 191–201 (1979).
26. Tanaka, H., Takeuchi, T. & Ward, W. R. Three-dimensional interaction between a planet and an isothermal gaseous disk. I. Corotation and Lindblad torques and planet migration. *Astrophys. J.* **565**, 1257–1274 (2002).

Supplementary Information is linked to the online version of the paper at www.nature.com/nature.

Acknowledgements This work is supported by the Kavli Foundation, which enabled the initiation and development of this work at KIAA-PKU. It is also supported by NASA, JPL and the NSF.

Author Contributions S.-I.L. and D.N.C.L. constructed arguments for mass loss and tidal heating of WASP-12b, and also composed the draft of the paper. N.M. brought WASP-12b's large radius to the attention of the team and designed the illustration. J.J.F. contributed information on the planet's opacity and improved the presentation of the manuscript.

Author Information Reprints and permissions information is available at www.nature.com/reprints. The authors declare no competing financial interests. Correspondence and requests for materials should be addressed to D.N.C.L. (lin@ucolick.org).

Exploring the thermodynamics of a universal Fermi gas

S. Nascimbène¹, N. Navon¹, K. J. Jiang¹, F. Chevy¹ & C. Salomon¹

One of the greatest challenges in modern physics is to understand the behaviour of an ensemble of strongly interacting particles. A class of quantum many-body systems (such as neutron star matter and cold Fermi gases) share the same universal thermodynamic properties when interactions reach the maximum effective value allowed by quantum mechanics, the so-called unitary limit^{1,2}. This makes it possible in principle to simulate some astrophysical phenomena inside the highly controlled environment of an atomic physics laboratory. Previous work on the thermodynamics of a two-component Fermi gas led to thermodynamic quantities averaged over the trap^{3–5}, making comparisons with many-body theories developed for uniform gases difficult. Here we develop a general experimental method that yields the equation of state of a uniform gas, as well as enabling a detailed comparison with existing theories^{6–15}. The precision of our equation of state leads to new physical insights into the unitary gas. For the unpolarized gas, we show that the low-temperature thermodynamics of the strongly interacting normal phase is well described by Fermi liquid theory, and we localize the superfluid transition. For a spin-polarized system^{16–18}, our equation of state at zero temperature has a 2 per cent accuracy and extends work^{19,20} on the phase diagram to a new regime of precision. We show in particular that, despite strong interactions, the normal phase behaves as a mixture of two ideal gases: a Fermi gas of bare majority atoms and a non-interacting gas of dressed quasi-particles, the fermionic polarons^{10,18,20–22}.

In this Letter we study the thermodynamics of a mixture of the two lowest spin states ($i = 1, 2$) of ⁶Li prepared at a magnetic field $B = 834$ G (see Methods), where the dimensionless number $1/k_F a$ characterizing the s -wave interaction is equal to zero, the unitary limit. (Here k_F is the Fermi momentum and a the scattering length.) Understanding the universal thermodynamics at unitarity is a challenge for many-body theories because of the strong interactions between particles. Despite this complexity at the microscopic scale, all the macroscopic properties of an homogeneous system are encapsulated within a single equation of state (EOS), $P(\mu_1, \mu_2, T)$, that relates the pressure P of the gas to the chemical potentials μ_i of the species i and to the temperature T . In the unitary limit, this relationship can be expressed as¹:

$$P(\mu_1, \mu_2, T) = P_1(\mu_1, T) h\left(\eta = \frac{\mu_2}{\mu_1}, \zeta = \exp\left(\frac{-\mu_1}{k_B T}\right)\right) \quad (1)$$

where $P_1(\mu_1, T) = -k_B T \lambda_{dB}^{-3}(T) f_{5/2}(-\zeta^{-1})$ is the pressure of a single component non-interacting Fermi gas. Here k_B is the Boltzmann constant, $\lambda_{dB}(T)$ is the de Broglie wavelength and $f_{5/2}(z) = \sum_{n=1}^{\infty} z^n / n^{5/2}$. $h(\eta, \zeta)$ is a universal function which contains all the thermodynamic information of the unitary gas (Fig. 1). In cold atomic systems, the inhomogeneity due to the trapping potential makes the measurement of $h(\eta, \zeta)$ challenging. However, this inhomogeneity of the trap can be turned into an advantage, as shown in refs 20 and 23.

We directly probe the local pressure of the trapped gas using *in situ* images, following a recent proposal²³. In the local density approximation, the gas is locally homogeneous with local chemical potentials:

$$\mu_i(\mathbf{r}) = \mu_i^0 - V(\mathbf{r}) \quad (2)$$

here μ_i^0 is the chemical potential at the bottom of the trap for species i and $V(\mathbf{r})$ is the trapping potential. Then a simple formula relates the pressure P to the doubly-integrated density profiles²³:

$$P(\mu_{1z}, \mu_{2z}, T) = \frac{m\omega_r^2}{2\pi} (\bar{n}_1(z) + \bar{n}_2(z)) \quad (3)$$

where $\bar{n}_i(z) = \int n_i(x, y, z) dx dy$, n_i being the atomic density. ω_r and ω_z are respectively the transverse and axial angular frequency of a cylindrically symmetric trap (see Fig. 2), m is the ⁶Li mass, and $\mu_{iz} = \mu_i(0, 0, z)$ is the local chemical potential along the z axis. From a single image, we thus measure the EOS, equation (1), along the parametric line $(\eta, \zeta) = (\mu_{2z}/\mu_{1z}, \exp(-\mu_{1z}/k_B T))$; see below.

The interest of this method is straightforward. First, one directly measures the EOS of the uniform gas. Second, each pixel row z_i gives a point $h(\eta(z_i), \zeta(z_i))$ whose signal to noise ratio is essentially given by that of $\bar{n}_1(z) + \bar{n}_2(z)$; typically one experimental run leads to ~ 100 points with a signal to noise ratio between 3 and 10. With about 40 images one gets $\sim 4,000$ points $h(\eta, \zeta)$, which after averaging provides a low-noise EOS of standard deviation $\sigma = 2\%$. In the following we illustrate the efficiency of our method on two important sectors of the parameter space (η, ζ) in Fig. 1: the balanced gas at finite temperature $(1, \zeta)$ and the zero-temperature imbalanced gas $(\eta, 0)$.

We first measure the EOS of the unpolarized unitary gas at finite temperature, $P(\mu_1, \mu_2, T) = P(\mu, T)$. The measurement of $h(1, \zeta)$ through the local pressure, equation (3), can be done provided one knows the temperature T of the cloud and its central chemical potential μ^0 .

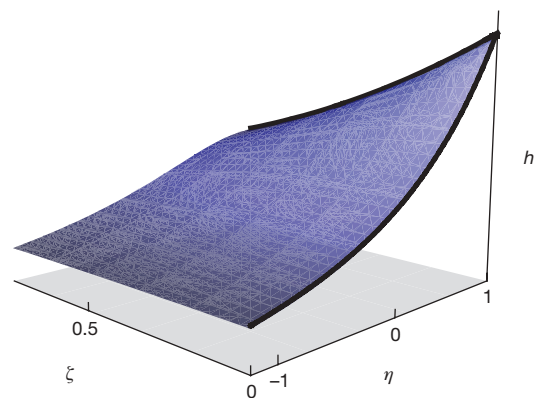


Figure 1 | Schematic representation of the universal function $h(\eta, \zeta)$. It fully describes the thermodynamics of the unitary gas as a function of chemical potential imbalance $\eta = \mu_2/\mu_1$ and of the inverse of the fugacity $\zeta = \exp(-\mu_1/k_B T)$. In this paper we measure the function h over the black lines $(1, \zeta)$ and $(\eta, 0)$, which correspond to the balanced unitary gas at finite temperature and to the spin-imbalanced gas at zero temperature, respectively.

¹Laboratoire Kastler Brossel, CNRS, UPMC, École Normale Supérieure, 24 rue Lhomond, 75231 Paris, France.

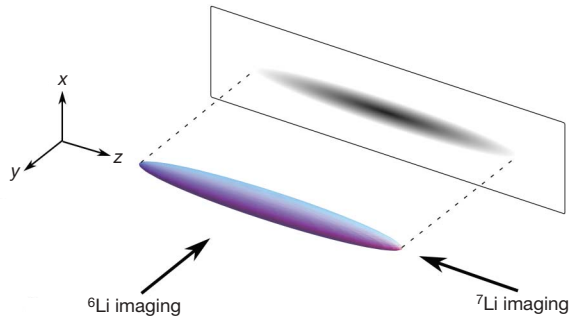


Figure 2 | Schematic representation of our atomic sample. The ^6Li atomic cloud is imaged in the direction y ; the column density is then integrated along the direction x to give $\bar{n}(z)$. The ^7Li atoms are imaged after a time of flight along the z direction.

In the balanced case, model-independent thermometry is notoriously difficult because of the strong interactions. Inspired by ref. 24, we overcome this issue by measuring the temperature of a ^7Li cloud in thermal equilibrium with the ^6Li mixture (see Methods).

The central chemical potential μ^0 is fitted on the hottest clouds so that the EOS agrees in the classical regime $\zeta \gg 1$ with the second-order virial expansion $h(1, \zeta) \approx 2(1 + \zeta^{-1}/\sqrt{2})$ (ref. 25). For colder clouds we proceed recursively. The EOS of an image recorded at temperature T has some overlap with the previously determined EOS from all images with $T' > T$. In this overlap region, μ^0 is fitted to minimize the distance between the two EOSs. This provides a new portion of the EOS at lower temperature. Using 40 images of clouds prepared at different temperatures, we thus reconstruct a low-noise EOS from the classical part down to the degenerate regime, as shown in Fig. 3a.

We now comment on the main features of the EOS. At high temperature, the EOS can be expanded in powers of ζ^{-1} as a virial expansion¹¹:

$$\frac{h(1, \zeta)}{2} = \frac{\sum_{k=1}^{\infty} ((-1)^{k+1} k^{-5/2} + b_k) \zeta^{-k}}{\sum_{k=1}^{\infty} (-1)^{k+1} k^{-5/2} \zeta^{-k}}$$

where b_k is the k^{th} virial coefficient. As we have $b_2 = 1/\sqrt{2}$ in the measurement scheme described above, our data provide for the first time the experimental values of b_3 and b_4 . $b_3 = -0.35(2)$ is in excellent agreement with the recent calculation $b_3 = -0.291 - 3^{-5/2} = -0.355$ from ref. 11, but not with $b_3 = 1.05$ from ref. 12. $b_4 = 0.096(15)$ involves the four-fermion problem at unitarity and could interestingly be computed along the lines of ref. 11.

Let us now focus on the low-temperature regime of the normal phase $\zeta \ll 1$. As shown in Fig. 3b, we observe a T^2 dependence of the pressure with temperature. This behaviour is reminiscent of a Fermi liquid, and indicates that pseudogap effects expected for strongly interacting Fermi superfluids²⁶ do not show up at the thermodynamic level within our experimental precision. In analogy with ^3He or heavy-fermion metals, we fit our data with the EOS:

$$P(\mu, T) = 2P_1(\mu, 0) \left(\xi_n^{-3/2} + \frac{5\pi^2}{8} \xi_n^{-1/2} \frac{m^*}{m} \left(\frac{k_B T}{\mu} \right)^2 \right) \quad (4)$$

Here $P_1(\mu, 0) = 1/15\pi^2(2m/\hbar^2)^{3/2}\mu^{5/2}$ is the pressure of a single-component Fermi gas at zero temperature, m^* is the quasi-particle mass, and ξ_n^{-1} is the compressibility of the normal gas extrapolated to zero temperature, and normalized to that of an ideal gas of same density. We deduce two new parameters $m^*/m = 1.13(3)$ and $\xi_n = 0.51(2)$. Despite the strong interactions, m^* is close to m , unlike the weakly interacting ^3He liquid for which $2.7 < m^*/m < 5.8$, depending on pressure. Our ξ_n value is in agreement with the variational fixed-node Monte Carlo calculations $\xi_n = 0.54$ in ref. 27 and

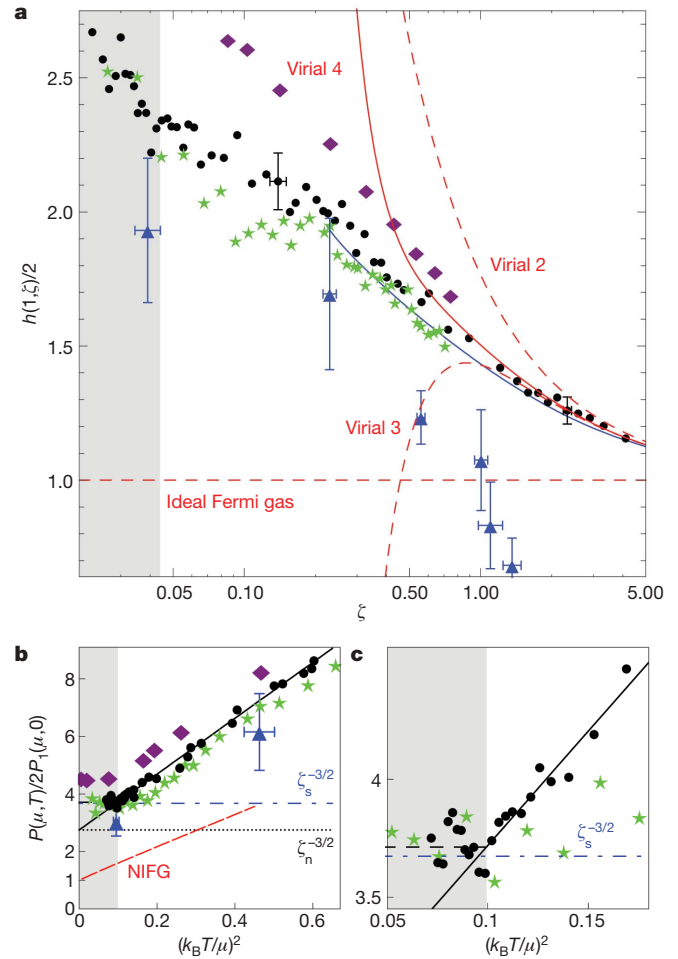


Figure 3 | Equation of state of a spin-balanced unitary Fermi gas. **a**, Finite-temperature equation of state (EOS) $h(1, \zeta)$ (black dots). The error bars represented at $\zeta = 0.14$ and $\zeta = 2.3$ indicate the 6% accuracy in ζ and h of our EOS. The red curves are the successive virial expansions up to fourth order. The blue triangles are from ref. 6, the green stars from ref. 7, the purple diamonds from ref. 8, and the blue solid line from ref. 9. The grey region indicates the superfluid phase. **b**, EOS $P(\mu, T)/2P_1(\mu, 0)$ as a function of $(k_B T/\mu)^2$, fitted by the Fermi liquid EOS, equation (4). The red dashed line is the non-interacting Fermi gas (NIFG). The horizontal dot-dashed and dotted lines indicate respectively the zero-temperature pressure of the superfluid phase $\propto \xi_s^{-3/2}$ and that of the normal phase $\propto \xi_n^{-3/2}$. **c**, Expanded view of **b** near T_c . The sudden deviation of the data from the fit occurs at $(k_B T/\mu)_c = 0.32(3)$ that we interpret as the superfluid transition. The black dashed line indicates the mean value of the data points below T_c .

$\xi_n = 0.56$ in ref. 10, and with the quantum Monte Carlo calculation $\xi_n = 0.52$ in ref. 28. This yields the Landau parameters $F_0^s = \xi_n m^*/m - 1 = -0.42$ and $F_1^s = 3(m^*/m - 1) = 0.39$.

In the lowest temperature points (Fig. 3c) we observe a sudden deviation of the data from the fitted equation (4) at $(k_B T/\mu)_c = 0.32(3)$ (see Supplementary Information). We interpret this behaviour as the transition from the normal phase to the superfluid phase. This critical ratio has been extensively calculated in recent years. Our value is in close agreement with the diagrammatic Monte Carlo calculation $(k_B T/\mu)_c = 0.32(2)$ of ref. 6 and with the quantum Monte Carlo calculation $(k_B T/\mu)_c = 0.35(3)$ of ref. 28; but it differs from the self-consistent approach in ref. 8 that gives $(k_B T/\mu)_c = 0.41$, from the renormalization group prediction 0.24 in ref. 29, and from several other less precise theories. From equation (4) we deduce the total density $n = n_1 + n_2 = \partial P(\mu_i = \mu, T)/\partial \mu$ and the Fermi energy $E_F = k_B T_F = \hbar^2/2m(3\pi^2 n)^{2/3}$ at the transition point. We obtain $(\mu/E_F)_c = 0.49(2)$ and $(T/T_F)_c = 0.157(15)$, in very good agreement with ref. 6. Our measurement is the first direct determination of $(\mu/E_F)_c$

and $(T/T_F)_c$ in the homogeneous gas. It agrees with the extrapolated value of the MIT measurement¹⁹.

Below T_c , advanced theories^{7,8} predict that $P(\mu, T)/2P_1(\mu, 0)$ is nearly constant (Fig. 3b). Therefore at $T = T_c$, $P/2P_1 \approx \xi_s^{-3/2} \approx 3.7$, and is consistent with our data. Here $\xi_s = 0.42(1)$ is the fundamental parameter characterizing the EOS of the balanced superfluid at zero temperature, a quantity extensively measured and computed in recent years².

Our data are compared at all temperatures with the calculations from refs 6–9 in Fig. 3a. The agreement with ref. 7 is very good for a large range of temperatures. Concerning ref. 6, the deviation from our data is about one error bar of the Monte Carlo method below $\zeta = 0.2$, and the deviation increases with temperature (Fig. 3a). Furthermore, we show in the Supplementary Information that $h(1, \zeta)/2$ must be greater than 1, an inequality violated by the two hottest Monte Carlo points of ref. 6.

From our homogeneous EOS we can deduce the EOS of the harmonically trapped unitary gas by integrating $h(1, \zeta)$ over the trap (see Supplementary Information). In particular, we find a critical temperature for the trapped gas $(T/T_F)_c = 0.19(2)$, where $T_F = \hbar(3\omega_r^2\omega_z N)^{1/3}$ and N is the total atom number. This value agrees very well with the recent measurement of ref. 30, and with less precise measurements^{5,31,32}.

Let us now explore a second line in the universal diagram $h(\eta, \zeta)$ (Fig. 1) by considering the case of the $T = 0$ spin-imbalanced mixture $\mu_2 \neq \mu_1$, that is, $\eta \neq 1$. Previous work^{16–18} has shown that phase separation occurs in a trap. Below a critical population imbalance a fully paired superfluid occupies the centre of the trap. It is surrounded by a normal mixed phase and an outer rim consisting of an ideal gas of the majority component. In two out of the three previous experiments including ours^{16,18}, the local density approximation has been carefully checked. We are therefore justified in using equation (3) to analyse our data.

As in the previous case, the relationship between the pressure and the EOS requires the knowledge of the chemical potentials μ_1^0 and μ_2^0 at the centre of the trap. μ_1^0 is determined using the outer shell of the majority spin component ($i = 1$). The pressure profile $P(\mu_{1,2}, 0)$ corresponds to the Fermi–Dirac distribution and is fitted with the Thomas–Fermi formula $P_1 = \alpha(1 - z^2/R_1^2)^{5/2}$, providing $\mu_1^0 = \frac{1}{2}m\omega_z^2 R_1^2$. Using P_1 for the calculation of $h = P/P_1$ cancels many systematic effects on the absolute value of the pressure. Moreover, fitting the outer shell using a finite-temperature Thomas–Fermi profile¹⁹, we measure a temperature $k_B T = 0.03(3)\mu_1^0$. μ_2^0 is fitted by comparison in the superfluid region with the superfluid EOS at zero temperature²¹:

$$h(\eta, 0) = (1 + \eta)^{5/2} / (2\xi_s)^{3/2} \quad (5)$$

Our measured EOS $h(\eta, 0)$ is displayed in Fig. 4. By construction our data agree for $\eta \gtrsim 0.1$ with equation (5). In Fig. 4 the slope of $h(\eta, 0)$ displays an obvious discontinuity for $\eta = \eta_c = 0.065(20)$. This is a signature of a first-order quantum phase transition to the partially polarized normal phase. The error bar is dominated by the uncertainty on ξ_s . This value is slightly higher than the prediction $\eta_c = 0.02$ given by the fixed-node Monte Carlo¹⁰ and than the value $\eta_c = 0.03(2)$ measured in ref. 19.

From the relations $n_i = \partial P / \partial \mu_i$, we deduce from $h(\eta, 0)$ the density ratio n_2/n_1 (Fig. 4 inset). This ratio is discontinuous at the phase transition, from a maximum value in the normal phase $(n_2/n_1)_c = 0.5(1)$ to $n_2 = n_1$ in the superfluid phase. Our value is close to the zero-temperature calculation 0.44 (ref. 10) and agrees with the coldest MIT samples^{19,20}. It confirms that the temperature is much smaller than the tricritical point temperature $T = 0.07T_F$ (ref. 19) where the discontinuity vanishes, justifying our $T = 0$ assumption made above.

For $\eta < \eta_c$ our data display a good agreement with a simple polaron model, based on the pioneering work in ref. 10. A polaron is a quasi-particle describing a single minority atom immersed in the majority Fermi sea^{15,18,21,22}. It is characterized¹⁰ by a renormalized

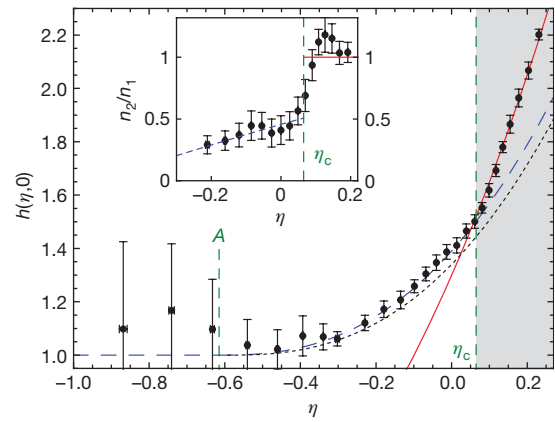


Figure 4 | Equation of state of the zero-temperature spin-imbalanced unitary gas $h(\eta, 0)$. The EOS is shown as filled black circles; error bars are equal to one standard error. The red solid line is the superfluid EOS, the blue dashed line is the ideal Fermi liquid, equation (7), with $A = -0.615$, $m^* = 1.20m$ and the black dotted line is the Monte Carlo calculation from ref. 10. Inset, local density ratio n_2/n_1 as a function of η . The red solid line $n_2/n_1 = 1$ corresponds to the fully paired superfluid and blue dashed line to the model, equation (7).

chemical potential $\mu_2 - A\mu_1$ and an effective mass m_p^* . Following this picture, we write the pressure as the sum of the Fermi pressures of ideal gases of majority atoms and of polarons:

$$P = \frac{1}{15\pi^2} \left(\frac{2m}{\hbar^2} \right)^{3/2} \left(\mu_1^{5/2} + \left(\frac{m_p^*}{m} \right)^{3/2} (\mu_2 - A\mu_1)^{5/2} \right) \quad (6)$$

which can be written as:

$$h(\eta, 0) = 1 + \left(\frac{m_p^*}{m} \right)^{3/2} (\eta - A)^{5/2} \quad (7)$$

A and m_p^* have recently been calculated exactly^{14,15}: $A = -0.615$, $m_p^*/m = 1.20(2)$, and with these values inserted in equation (7) the agreement with our data is perfect. Note that our data lie slightly above the variational fixed-node Monte Carlo calculation¹⁰. We therefore conclude that interactions between polarons are not visible at this level of precision.

Alternatively, we can fit our data with m_p^*/m as a free parameter in equation (7). We obtain $m_p^*/m = 1.20(2)$. The uncertainty combines the standard error of the fit and the uncertainty on ξ_s . This value agrees with our previous measurement¹⁸ $m_p^*/m = 1.17(10)$ (with a fivefold improvement in precision), with the theoretical value^{14,15} $m_p^*/m = 1.20(2)$, and with the variational calculation¹³. It differs from the values 1.09(2) in ref. 33, 1.04(3) in ref. 10, and from the experimental value 1.06 in ref. 20.

We arrive at a simple physical picture of the $T = 0$ spin-polarized gas: the fully paired superfluid is described by an ideal gas EOS renormalized by a single coefficient ξ_s ; the normal phase is nothing but two ideal gases, one of bare majority particles and one of polaronic quasiparticles.

In conclusion, we have introduced a powerful method for the measurement of the EOS of the unitary and homogeneous Fermi gas that enables direct comparison with theoretical models and provides a set of new parameters shown in Table 1. The method

Table 1 | Table of quantities measured in this work

Parameter	b_3	b_4	$(k_B T/\mu)_c$	$(\mu/E_F)_c$	$(T/T_F)_c$
Value	$-0.35(2)$	$0.096(15)$	$0.32(3)$	$0.49(2)$	$0.157(15)$
Parameter	ξ_n	m^*/m	η_c	$(n_2/n_1)_c$	m_p^*/m
Value	$0.51(2)$	$1.13(3)$	$0.065(20)$	$0.5(1)$	$1.20(2)$

can readily be extended to any multi-component cold atom gas in three dimensions that fulfils the local density approximation (see Supplementary Discussion). We have shown that the normal phase of the unitary Fermi gas is a strongly correlated system whose thermodynamic properties are well described by Fermi liquid theory, unlike high- T_c copper oxides.

Note added in proof: Since this paper was accepted for publication, we have become aware of the measurement of a similar equation of state for the balanced unitary Fermi gas at finite temperature by different methods³⁴.

METHODS SUMMARY

Our experimental set-up is presented elsewhere¹⁸. We load into an optical dipole trap and evaporate a mixture of ^6Li in the $|1/2, \pm 1/2\rangle$ states and of ^7Li in the $|1, 1\rangle$ state at 834 G. The cloud typically contains $N_6 = (5\text{--}10) \times 10^4$ atoms of ^6Li in each spin state and $N_7 = (3\text{--}20) \times 10^3$ atoms of ^7Li at a temperature from $T = 150$ nK to 1.3 μK . The ^6Li trap frequencies are $\omega_x/2\pi = 37$ Hz, $\omega_y/2\pi$ varying from 830 Hz to 2.20 kHz, and the trap depth is 25 μK for our hottest samples, with $T \approx 2T_F$. ^6Li atoms are imaged *in situ* using absorption imaging, while ^7Li atoms are imaged after time of flight, providing the temperature in the same experimental run (Fig. 4). As the scattering length describing the interaction between ^7Li and ^6Li atoms, $a_{67} = 2$ nm, is much smaller than k_F^{-1} , the ^7Li thermometer has no influence on the ^6Li density profiles. The ^7Li – ^6Li collision rate, $\Gamma_{67} = 10\text{ s}^{-1}$, is large enough to ensure thermal equilibrium between the two species.

Full Methods and any associated references are available in the online version of the paper at www.nature.com/nature.

Received 2 November 2009; accepted 6 January 2010.

- Ho, T.-L. Universal thermodynamics of degenerate quantum gases in the unitarity limit. *Phys. Rev. Lett.* **92**, 090402 (2004).
- Inguscio, M., Ketterle, W. & Salomon, C. (eds) *Proc. Int. School of Physics Enrico Fermi* (Course CLXIV, IOS Press, Amsterdam, 2006).
- Stewart, J., Gaebler, J., Regal, C. & Jin, D. Potential energy of a ^{40}K Fermi gas in the BCS-BEC crossover. *Phys. Rev. Lett.* **97**, 220406 (2006).
- Luo, L., Clancy, B., Joseph, J., Kinast, J. & Thomas, J. Measurement of the entropy and critical temperature of a strongly interacting Fermi gas. *Phys. Rev. Lett.* **98**, 080402 (2007).
- Luo, L. & Thomas, J. Thermodynamic measurements in a strongly interacting Fermi gas. *J. Low Temp. Phys.* **154**, 1–29 (2009).
- Burovski, E., Prokofev, N., Svistunov, B. & Troyer, M. Critical temperature and thermodynamics of attractive fermions at unitarity. *Phys. Rev. Lett.* **96**, 160402 (2006).
- Bulgac, A., Drut, J. & Magierski, P. Spin 1/2 fermions in the unitary regime: a superfluid of a new type. *Phys. Rev. Lett.* **96**, 090404 (2006).
- Hausmann, R., Rantner, W., Cerrito, S. & Zwerger, W. Thermodynamics of the BCS-BEC crossover. *Phys. Rev. A* **75**, 023610 (2007).
- Combescot, R., Alzetto, F. & Leyronas, X. Particle distribution tail and related energy formula. *Phys. Rev. A* **79**, 053640 (2009).
- Lobo, C., Recati, A., Giorgini, S. & Stringari, S. Normal state of a polarized Fermi gas at unitarity. *Phys. Rev. Lett.* **97**, 200403 (2006).
- Liu, X., Hu, H. & Drummond, P. Virial expansion for a strongly correlated Fermi gas. *Phys. Rev. Lett.* **102**, 160401 (2009).
- Rupak, G. Universality in a 2-component Fermi system at finite temperature. *Phys. Rev. Lett.* **98**, 090403 (2007).
- Combescot, R., Recati, A., Lobo, C. & Chevy, F. Normal state of highly polarized Fermi gases: simple many-body approaches. *Phys. Rev. Lett.* **98**, 180402 (2007).
- Combescot, R. & Giraud, S. Normal state of highly polarized Fermi gases: full many-body treatment. *Phys. Rev. Lett.* **101**, 050404 (2008).
- Prokofev, N. & Svistunov, B. Fermi-polaron problem: diagrammatic Monte Carlo method for divergent sign-alternating series. *Phys. Rev. B* **77**, 020408 (2008).
- Shin, Y., Zwierlein, M., Schunck, C., Schirotzek, A. & Ketterle, W. Observation of phase separation in a strongly interacting imbalanced Fermi gas. *Phys. Rev. Lett.* **97**, 030401 (2006).
- Partridge, G., Li, W., Kamar, R., Liao, Y. & Hulet, R. Pairing and phase separation in a polarized Fermi gas. *Science* **311**, 503–505 (2006).
- Nascimbene, S. *et al.* Collective oscillations of an imbalanced Fermi gas: axial compression modes and polaron effective mass. *Phys. Rev. Lett.* **103**, 170402 (2009).
- Shin, Y., Schunck, C., Schirotzek, A. & Ketterle, W. Phase diagram of a two-component Fermi gas with resonant interactions. *Nature* **451**, 689–693 (2008).
- Shin, Y. Determination of the equation of state of a polarized Fermi gas at unitarity. *Phys. Rev. A* **77**, 041603 (2008).
- Chevy, F. Universal phase diagram of a strongly interacting Fermi gas with unbalanced spin populations. *Phys. Rev. A* **74**, 063628 (2006).
- Schirotzek, A., Wu, C.-H., Sommer, A. & Zwierlein, M. W. Observation of Fermi polarons in a tunable Fermi liquid of ultracold atoms. *Phys. Rev. Lett.* **102**, 230402 (2009).
- Ho, T.-L. & Zhou, Q. Obtaining phase diagram and thermodynamic quantities of bulk systems from the densities of trapped gases. *Nature Phys.* **6**, 131–134 (2010).
- Spiegelhalder, F. *et al.* Collisional stability of ^{40}K immersed in a strongly interacting Fermi gas of ^6Li . *Phys. Rev. Lett.* **103**, 223203 (2009).
- Ho, T.-L. & Mueller, E. High temperature expansion applied to fermions near Feshbach resonance. *Phys. Rev. Lett.* **92**, 160404 (2004).
- Chen, Q., Stajic, J., Tan, S. & Levin, K. BCS BEC crossover: from high temperature superconductors to ultracold superfluids. *Phys. Rep.* **412**, 1–88 (2005).
- Carlson, J., Chang, S., Pandharipande, V. & Schmidt, K. Superfluid Fermi gases with large scattering length. *Phys. Rev. Lett.* **91**, 050401 (2003).
- Bulgac, A., Drut, J. & Magierski, P. Quantum Monte Carlo simulations of the BCS-BEC crossover at finite temperature. *Phys. Rev. A* **78**, 023625 (2008).
- Gubbels, K. & Stoof, H. Renormalization group theory for the imbalanced Fermi gas. *Phys. Rev. Lett.* **100**, 140407 (2008).
- Riedl, S., Guajardo, E., Kohstall, C., Denschlag, J. & Grimm, R. Superfluid quenching of the moment of inertia in a strongly interacting Fermi gas. Preprint at (<http://arXiv.org/abs/0907.3814>) (2009).
- Greiner, M., Regal, C. & Jin, D. Emergence of a molecular Bose-Einstein condensate from a Fermi gas. *Nature* **426**, 537–540 (2003).
- Inada, Y. *et al.* Critical temperature and condensate fraction of a fermion pair condensate. *Phys. Rev. Lett.* **101**, 180406 (2008).
- Pilati, S. & Giorgini, S. Phase separation in a polarized Fermi gas at zero temperature. *Phys. Rev. Lett.* **100**, 030401 (2008).
- Horikoshi, M., Nakajima, S., Ueda, M. & Mukaiyama, T. Measurement of universal thermodynamic functions for a unitary Fermi gas. *Science* **327**, 442–445 (2010).

Supplementary Information is linked to the online version of the paper at www.nature.com/nature.

Acknowledgements We are grateful to R. Combescot, X. Leyronas, Y. Castin, A. Recati, S. Stringari, S. Giorgini, M. Zwierlein and T. Giamarchi for discussions and to C. Cohen-Tannoudji, J. Dalibard, F. Gerbier and G. Shlyapnikov for critical reading of the manuscript. We acknowledge support from ESF (Euroquam), SCALA, ANR FABIOLA, Région Ile de France (IFRAF), ERC and Institut Universitaire de France.

Author Contributions S.N. and N.N. contributed equally to this work. S.N., N.N. and K.J.J. took the experimental data, and all authors contributed to the data analysis and writing of the manuscript.

Author Information Reprints and permissions information is available at www.nature.com/reprints. The authors declare no competing financial interests. Correspondence and requests for materials should be addressed to S.N. (sylvain.nascimbene@ens.fr).

METHODS

Construction of the EOS by successive patches. A typical image at high temperature provides about 100 pixels corresponding to ζ values varying from 2 at the trap centre to 6 at the edges, with a signal-to-noise from 3 to 10. Seven such images are fitted in the wings using the second-order virial expansion and averaged to obtain a low-noise EOS up to $\zeta = 2$. Then images of clouds where the evaporation has been pushed to a slightly lower temperature are recorded. They show about 75% overlap in ζ with the previous EOS. After minimization of the distance between a new image and the previously determined EOS in the overlap region, we obtain the value of μ^0 for a single image with 3% statistical uncertainty. This process is repeated for six successive trap depths. When averaging one image with typically 10 previous images, we obtain a new EOS with an error on ζ of about $0.03/\sqrt{10} \approx 1\%$. The EOS experiences a random walk error on the 40 images of $0.01 \times \sqrt{40} \approx 5\%$ for the coldest data. An independent check of the maximum error is provided by the good agreement with the superfluid EOS for temperatures lower than T_c (refs 7, 8).

Evaluation of the systematic uncertainties. For the measurement of $h(1, \zeta)$, the combined uncertainties on the radial frequency of the trap, trap anharmonicity, magnification of our imaging system, and atom counting affect the pressure measurement given in equation (3) at $\sim 20\%$ level. However, two measurements, one at relatively high temperature and one at very low temperature, enable us to show that the overall error does not exceed 6%. In the temperature range $\zeta > 0.5$, the agreement between the experimental value $b_3 = -0.35(2)$ and the theoretical value $b_3 = -0.355$ of the third virial coefficient indicates that the global systematic error is smaller than 6%. Second, at very low temperature, theory^{7,8} predicts that the variation of $P/2P_1$ as a function of $k_B T/\mu$ in the superfluid phase remains smaller than 5%. Our value of $P/2P_1 = 3.75$ below the critical point is within 5% of the $T = 0$ prediction $\zeta_s^{-3/2} = 3.7(2)$. This confirms that systematic errors for our coldest samples are also smaller than 6%.

For the determination of the critical transition to superfluidity we fit the low-temperature data $P(\mu, T)/2P_1(\mu, 0)$ with a variable horizontal line for $T < T_c$ and

with the Fermi-liquid equation (4) for $T > T_c$. The result of the fit is the dashed black line in Fig. 3c, which intersects equation (4) at $(k_B T/\mu)_c = 0.315(8)$. This statistical error is negligible compared to the error induced by the 6% systematic uncertainty discussed above, justifying our very simplified fit procedure. Indeed a 6% error on the pressure induces a 10% error on μ for images recorded in the vicinity of the critical temperature, leading to $(k_B T/\mu)_c = 0.32(3)$.

For the measurement of $h(\eta, 0)$, the fit of the fully polarized wings of the cloud serves as a pressure calibration for the rest of the cloud, cancelling many systematic effects.

In order to estimate temperature effects in the polarized gas, let us first remark that in the superfluid phase corrections scale as T^4 for the bosonic excitations and are exponentially suppressed by the gap for the fermionic ones⁷. So in our temperature range $k_B T = 0.03\mu_1^0$ their contributions will be very small. On the other hand, in the partially polarized normal phase, we expect a typical Fermi liquid T^2 scaling. In order to obtain an estimate of the error on the EOS, we develop the following simple model. In equation (6) which describes a mixture of zero-temperature ideal gases, we replace the Fermi pressures by the finite-temperature pressures of ideal gases (see equation (1)):

$$P(\mu_1, \mu_2, T) = P_1(\mu_1, T) + \left(\frac{m_p^*}{m}\right)^{3/2} P_1(\mu_2 - A\mu_1, T)$$

and run the analysis described in the main text. At $T = 0.05\mu_1^0$, the correction on h is less than 1%, half of our current error bar.

Limit of ^7Li thermometry. As the scattering length between the ^7Li atoms, $a_{77} = -3$ nm is negative, the ^7Li cloud becomes unstable when a BEC forms. This occurs at $T \approx 150$ nK with typically 3,500 atoms. Precise thermometry with lower atom numbers becomes difficult. For the measurement of the zero-temperature EOS of the imbalanced gas, we do not use ^7Li thermometry but rather the fit of the wings of the majority spin component.

Simultaneous phase and size control of upconversion nanocrystals through lanthanide doping

Feng Wang¹, Yu Han², Chin Seong Lim³, Yunhao Lu⁴, Juan Wang¹, Jun Xu⁵, Hongyu Chen⁵, Chun Zhang^{1,4}, Minghui Hong^{3,6} & Xiaogang Liu¹

Doping is a widely applied technological process in materials science that involves incorporating atoms or ions of appropriate elements into host lattices to yield hybrid materials with desirable properties and functions. For nanocrystalline materials, doping is of fundamental importance in stabilizing a specific crystallographic phase¹, modifying electronic properties^{2–4}, modulating magnetism⁵ as well as tuning emission properties^{6–9}. Here we describe a material system in which doping influences the growth process to give simultaneous control over the crystallographic phase, size and optical emission properties of the resulting nanocrystals. We show that NaYF₄ nanocrystals can be rationally tuned in size (down to ten nanometres), phase (cubic or hexagonal) and upconversion^{10–12} emission colour (green to blue) through use of trivalent lanthanide dopant ions introduced at precisely defined concentrations. We use first-principles calculations to confirm that the influence of lanthanide doping on crystal phase and size arises from a strong dependence on the size and dipole polarizability of the substitutional dopant ion. Our results suggest that the doping-induced structural and size transition, demonstrated here in NaYF₄ upconversion nanocrystals, could be extended to other lanthanide-doped nanocrystal systems for applications ranging from luminescent biological labels¹² to volumetric three-dimensional displays¹³.

Upconversion nanocrystals are luminescent nanomaterials that convert a near-infrared excitation into a visible emission through lanthanide doping^{10,11}. Compared to organic fluorophores and semiconducting nanocrystals, upconversion nanocrystals offer high photochemical stability, sharp emission bandwidths, and large anti-Stokes shifts (up to 500 nm) that separate discrete emission peaks from the infrared excitation. Along with the remarkable light penetration depth and the absence of autofluorescence in biological specimens under infrared excitation, these upconversion nanocrystals are ideal for use as luminescent probes in biological labelling and imaging technology. Despite recent progress in nanocrystal synthesis, it has been challenging to prepare small-sized nanocrystals (sub-20 nm) that emit strong upconversion luminescence on infrared excitation¹². Conventional techniques for controlling the crystallization of nanocrystals with well-defined crystal phase and size generally impose stringent control over a set of experimental variables, such as nature of solvent, temperature, reaction time and concentration of metal precursors^{14–26}. For example, hexagonal phase NaYF₄, which offers about an order-of-magnitude enhancement of upconversion efficiency relative to its cubic phase counterpart, typically exists in bulk materials and large-sized particles²⁶. As the physical dimension of the particle is reduced, high surface tension triggers phase transformation from anisotropic (hexagonal) to isotropic (cubic)²⁷, resulting in a significant decrease of upconversion luminescence. Sufficiently high reaction temperatures

(~300 °C) and prolonged heat treatment (up to several days) can lead to the pure hexagonal form of NaYF₄, but these processes are generally associated with significant particle aggregation or enlarged crystal size. Although sub-20-nm hexagonal-phase NaYF₄ nanocrystals have been synthesized in organic solvents²⁶, the synthesis requires air-sensitive, toxic organometallic precursors and hazardous coordinating solvents, which have become matters of substantial environmental concern. Here we present direct observation and mechanistic investigation of simultaneous phase and size control of upconversion NaYF₄ nanocrystals through lanthanide doping. We find that the lanthanide doping approach results in dramatic shortening of reaction time (down to 2 h) on cubic-to-hexagonal phase transition and a substantial decrease in the reaction temperature (down to 230 °C) needed for preparing ultra-small (10 nm) hexagonal phase upconversion nanoparticles.

In cubic sodium rare earth (RE) fluoride systems (NaREF₄) containing one type of high-symmetry cation site, fluorite structures (CaF₂) are formed, with the Ca²⁺ sites randomly occupied by Na⁺ and RE³⁺ ions (Fig. 1a). In contrast, the crystal structure of hexagonal phase NaREF₄ consists of an ordered array of F[−] ions with two types of relatively low-symmetry cation sites selectively occupied by Na⁺ and RE³⁺ ions (Fig. 1b), resulting in significant electron cloud distortion of the cations to accommodate the structural change. Importantly, light lanthanides with large ionic radii exhibit a high tendency towards electron cloud distortion owing to increased dipole polarizability, and thus favour the hexagonal structures (Fig. 1c). We reasoned that doping of lanthanide ions with a size larger than Y³⁺ ($r = 1.159 \text{ \AA}$)²⁸ in NaYF₄ host lattices should dominate the formation of pure hexagonal-phase NaYF₄ nanocrystals.

To validate our hypothesis, Gd³⁺ ions ($r = 1.193 \text{ \AA}$)²⁸ at different doping levels were used to induce phase transformation in upconversion NaYF₄:Yb/Er nanocrystals. We chose NaYF₄:Yb/Er nanocrystals because of their well-established efficient upconversion luminescence and well developed synthetic methods¹⁹. All samples were first examined by X-ray powder diffraction (Fig. 1d). Without the Gd³⁺ ions added, the X-ray diffraction pattern of NaYF₄:Yb/Er (18/2 mol%) samples can be indexed as a mixture of the cubic (JCPDS file number 77-2042) and hexagonal (JCPDS file number 16-0334) phases of NaYF₄. On doping with increased Gd³⁺ concentrations, the transformation from cubic to hexagonal in these samples is evident. The pure hexagonal phase of NaYF₄ was obtained as the Gd³⁺ ion concentration reached 30 mol%. Notably, the cubic-to-hexagonal phase conversion is complete after heating at 200 °C for only 2 h, much less than the 20 h required for a complete phase transformation without the Gd³⁺ dopant. With further increase in Gd³⁺ ion concentration, no extra diffraction peaks were observed, indicating the formation of a homogeneous Y-Gd solid solution. This result can

¹Department of Chemistry, National University of Singapore, 117543, Singapore. ²Membrane Research Centre, Division of Chemical and Life Science and Engineering, King Abdullah University of Science and Technology, Thuwal 23955-6900, Saudi Arabia. ³Optical Materials and Systems Division, Data Storage Institute, A*STAR, 117608, Singapore. ⁴Department of Physics, National University of Singapore, 117543, Singapore. ⁵Division of Chemistry and Biological Chemistry, Nanyang Technological University, 637371 Singapore. ⁶Department of Electrical and Computer Engineering, National University of Singapore, 117543 Singapore.

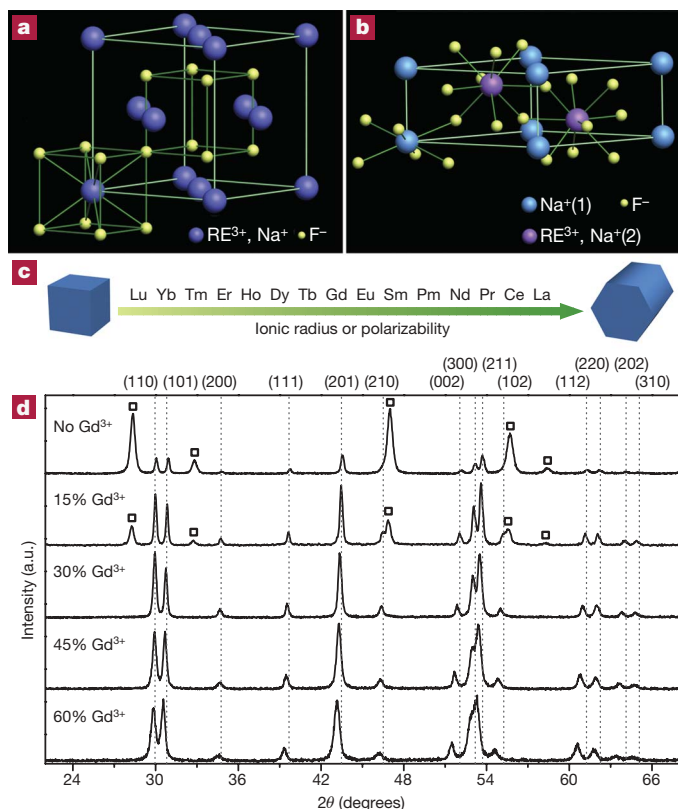


Figure 1 | Phase transformation in NaREF₄ structures by lanthanide doping. **a, b,** Schematic presentation of cubic- and hexagonal-phase NaREF₄ structures, respectively. In the cubic phase, equal numbers of F⁻ cubes contain cations and vacancies. In the hexagonal phase, an ordered array of F⁻ ions offers two types of cation sites: one occupied by Na⁺ and the other occupied randomly by RE³⁺ and Na⁺. **c,** General trend of phase transition from cubic to hexagonal as a function of ionic radius (or polarizability) of the lanthanide dopant ions. **d,** X-ray powder diffraction patterns of the NaYF₄:Yb/Er (18/2 mol%) nanocrystals obtained after heating for 2 h at 200 °C in the presence of 0, 15, 30, 45 and 60 mol% Gd³⁺ dopant ions, respectively. Diffraction peaks corresponding to cubic NaYF₄ are marked with square boxes. A gradual decrease in diffraction peak intensities for cubic phase is observed as a function of increased Gd³⁺ dopant content.

be attributed to the small structural difference between the hexagonal phase NaYF₄ and NaGdF₄. They adopt the same space group (*P6₃/m*) with similar unit-cell parameters ($a = 5.96 \text{ \AA}$, $c = 3.53 \text{ \AA}$ for NaYF₄ and $a = 6.02 \text{ \AA}$, $c = 3.60 \text{ \AA}$ for NaGdF₄). The peak shifts towards lower diffraction angles in the X-ray powder diffraction patterns as a function of the Gd³⁺ ion concentration arise as a result of expansion in unit-cell volume owing to the substitution of Y³⁺ ions by larger Gd³⁺ ions in the host lattice. Importantly, we also observed that the diffraction peaks broaden with increasing Gd³⁺ dopant content, indicating a reduction of the average crystallite size.

To shed more light on the effect of lanthanide doping, we performed first principles calculations based on density functional theory (DFT) for ground-state geometry and formation energy of NaYF₄ and NaGdF₄ nanocrystals in both cubic and hexagonal phases (Supplementary Fig. 1). The DFT calculations include the generalized gradient approximation²⁹, using a plane wave basis (kinetic energy cut-off 400 eV) and projector augmented-wave pseudo potential³⁰. The formation energy is defined as the energy difference per unit cell between the nanocrystal and isolated atoms. In cubic phase, the formation energy per atom decreases by about 0.07 eV when Y³⁺ is replaced by Gd³⁺, representing the fact that NaYF₄ is more energetically stable than NaGdF₄ in cubic phase. In contrast, the formation energy per atom in hexagonal phase increases by about 0.07 eV when Y³⁺ is replaced by Gd³⁺, indicating that NaGdF₄ is more energetically

stable than NaYF₄ in hexagonal phase. Our calculations are consistent with our experimental observations showing that an increase of the Gd³⁺ dopant content in the NaYF₄ host favours the formation of hexagonal phase nanocrystals.

We further studied the crystal structure and size of NaYF₄:Yb/Er (18/2 mol%) samples doped with Gd³⁺ ions at different concentrations (0–60 mol%) using transmission electron microscopy (TEM) (Fig. 2). Without deliberately added Gd³⁺ ions, the TEM image of the NaYF₄:Yb/Er (18/2 mol%) sample prepared in an aqueous solvent for 2 h shows two distinct particle morphologies that include small nanocubes and large nanorods (Fig. 2a), well consistent with the presence of two phases observed by X-ray powder diffraction. TEM images of samples obtained after 5 and 10 h of reactions still show the formation of mixed nanorods and nanocubes (Fig. 2b and c). High-resolution TEM analysis reveals that the small nanocubes are cubic phase NaYF₄ (Fig. 2d). We therefore concluded the large nanorods to be hexagonal-phase NaYF₄ and we further confirmed this by electron diffraction study (Fig. 2e). However, in the presence of Gd³⁺ dopant ions (30 mol%), the cubic-to-hexagonal phase conversion is clearly complete after only 2 h under identical reaction conditions (Fig. 2f). The dramatic shortening of reaction time on phase transformation was further confirmed by repeated doping experiments with 45 mol% and 60 mol% of Gd³⁺. In all cases, the complete conversion of cubic to hexagonal phase occurred after 2 h, resulting in formation of highly uniform nanorods (Fig. 2g and h). With increasing Gd³⁺ dopant concentration (30–60 mol%), nanorods with gradually decreased dimensions are formed (Fig. 2f–h), which is consistent with a previous report in the case of Eu³⁺ doping²². We determined the nanorods with a Gd³⁺ content of 60 mol% to be highly crystalline hexagonal phase using high-resolution TEM (Fig. 2i). Lattice fringes associated with (001) planes (d -spacing of 0.36 nm) appear along the nanorods, indicating that the nanorods grow along the c axis (Supplementary Fig. 2). Compositional analysis of an individual nanorod by energy-dispersive X-ray spectroscopy reveals the presence of the doped elemental Yb, Er and Gd (Supplementary Fig. 2).

The size evolution of NaYF₄:Yb/Er nanocrystals can be partly attributed to the strong effect of the Gd³⁺ dopant ion on crystal growth rate through surface charge modification. Our DFT calculation shows that the electron charge density of the crystal surface increases after a Gd³⁺ ion substitutes the Y³⁺ ion in the crystal lattice. The change of electron charge density on the surface of the small-sized nanocrystals can substantially slow the diffusion of negatively charged F⁻ ions to the surface, owing to an increase in charge repulsion, resulting in a tunable reduction of the NaYF₄ nanocrystal size (Fig. 2j).

To verify the phase and size control mechanism of this doping approach, larger lanthanide ions Sm³⁺ ($r = 1.219 \text{ \AA}$)²⁸ and Nd³⁺ ($r = 1.249 \text{ \AA}$)²⁸ were each doped into the NaYF₄:Yb/Er nanocrystals at a dopant concentration of 30 mol%. Both samples were found to crystallize in pure hexagonal phase with rod-like morphology (Supplementary Fig. 3). The larger Sm³⁺ and Nd³⁺ ions resulted in the formation of smaller nanorods than did the Gd³⁺ ion under identical reaction conditions. These results further confirm that the size and dipole polarizability of the lanthanide ion dominate the phase and size evolution of the NaYF₄ nanocrystals. We note that in the presence of a dopant ion (for example, La³⁺, $r = 1.300 \text{ \AA}$)²⁸ with a significantly larger ionic size than the Y³⁺ ion, hexagonal phase NaYF₄ nanorods were not obtained (Supplementary Fig. 3). This can be ascribed to the large disparity in size between the La³⁺ and Y³⁺ ions, which leads to the formation of stable LaF₃ phase (Supplementary Fig. 3) rather than a homogenous La–Y solid solution.

Although several lanthanide dopant ions have been shown to control the crystal phase and size of upconversion NaYF₄:Yb/Er nanocrystals, only the Gd³⁺ dopant ion is shown to favour the upconversion luminescence. Photoluminescence investigation revealed that the NaYF₄:Yb/Er nanocrystals doped with Sm³⁺ or Nd³⁺ ions (30 mol%)

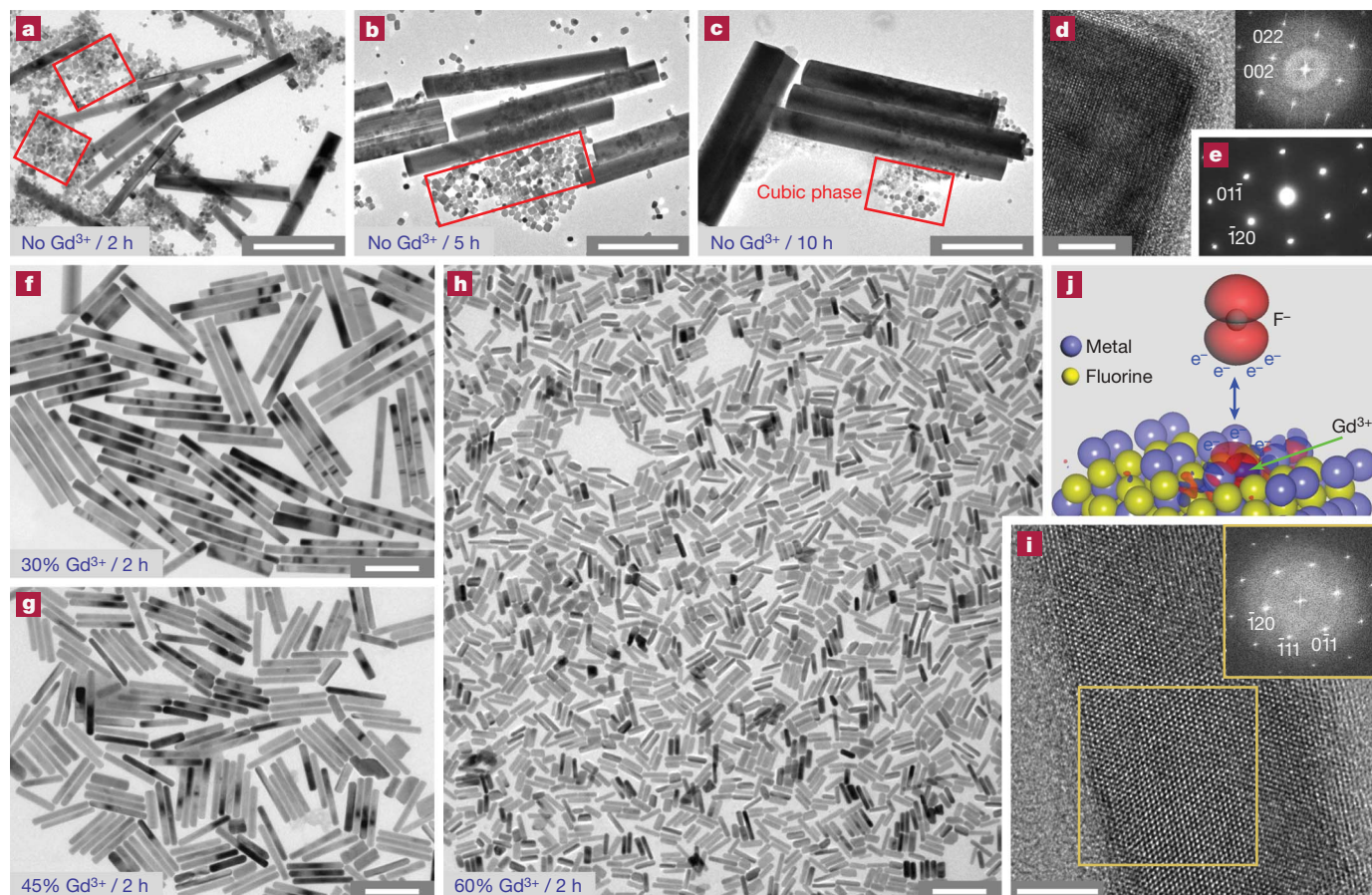


Figure 2 | TEM characterization of NaYF₄:Yb/Er (18/2 mol%) nanocrystals doped with various concentrations of Gd³⁺ ions. **a–c**, TEM images of NaYF₄:Yb/Er (18/2 mol%) products obtained after heating for 2, 5 and 10 h in the absence of Gd³⁺ dopant ions. Formation of the cubic phase products is partially marked by red squares. **d**, High-resolution TEM image taken in [100] incidence and the corresponding Fourier-transform diffractogram (inset) of a nanocube in the mixture shown in **a**, indicating the cubic phase of the nanocube. **e**, Selected area electron diffraction pattern taken in [111] incidence of a nanorod in the mixture shown in **a**, indicating formation of the hexagonal-phase nanorod. **f–h**, TEM images of the

NaYF₄:Yb/Er (18/2 mol%) products obtained after heating for 2 h in the presence of 30, 45 and 60 mol% Gd³⁺ dopant ions, respectively. **i**, High-resolution TEM image taken in [111] incidence and the corresponding Fourier-transform diffractogram (inset) of a nanorod shown in **h**, indicating the hexagonal phase of the nanorod. The yellow square on the rod indicates the area selected for Fourier transformation. **j**, DFT calculation showing the change of surface charge density caused by replacing the Y³⁺ in the host lattice with a Gd³⁺ ion. The red shading around the Gd³⁺ ion denotes the increased negative charges upon ion exchange. Scale bars are 500 nm for panels **a–c**, 200 nm for panels **f–h** and 5 nm for panels **d** and **i**.

do not emit visible upconversion luminescence. In contrast, the presence of Gd³⁺ dopant ions at a broad concentration range has no quenching effect on upconversion luminescence (Fig. 3a). This difference is probably due to quenching of the excitation energy through efficient energy transfer from Yb³⁺ and Er³⁺ to ⁶F_J manifolds of Sm³⁺ and ⁴I_J manifolds of Nd³⁺, respectively (Fig. 3b and c). In Gd³⁺ doped systems, the lowest excited level (⁶P_{7/2}) of Gd³⁺ is situated in the ultraviolet region (Fig. 3d), which is far higher than most excited levels of Yb³⁺ and Er³⁺ involved in the upconversion processes. Thus, excitation energy loss through energy transfer from Yb³⁺ and Er³⁺ to 4f levels of Gd³⁺ can be avoided. We also note that the emission intensity of NaYF₄:Yb/Er/Gd nanocrystals increases with increase in Gd³⁺ concentration to 15 mol% and then exhibits a gradual decrease upon further increase in Gd³⁺ dopant content. The initial increase in emission intensity can be associated with the increase in relative amount of hexagonal phase in the crystal structure. The subsequent decrease in emission intensity is primarily attributed to the reduction in crystal size. Smaller nanocrystals tend to have increased surface quenching sites and thus suppress upconversion luminescence by enhanced nonradiative energy transfer processes of the luminescent lanthanide ions.

To test the doping-induced crystal phase and size tuning further, we carried out the synthesis of NaYF₄:Yb/Er upconversion nanoparticles by Gd³⁺ doping in organic solvents at different temperatures.

Without the Gd³⁺ ion added, a substantially high temperature of 300 °C is needed to generate hexagonal-phase nanoparticles with an average diameter of 25 nm. On increasing Gd³⁺ dopant concentration, the size of nanoparticles can be tuned down to 10 nm (Supplementary Fig. 5). More importantly, we found that the Gd³⁺ doping can lead to a significant decrease in the reaction temperature (down to 230 °C) required for preparing hexagonal phase nanoparticles (Supplementary Fig. 6). We found that the large decrease in reaction temperature had almost no effect on the size and morphology of NaYF₄ nanoparticles. In contrast, the reaction at 230 °C in the absence of Gd³⁺ dopant ions yielded mostly polydisperse NaF crystals rather than monodisperse NaYF₄ nanoparticles. The results further confirm that the doping of Gd³⁺ promotes cubic-to-hexagonal phase transformation in NaYF₄ nanocrystals.

The successful preparation of ultra-small nanoparticles with strong upconversion luminescence by lanthanide doping suggests that it is now possible to synthesize upconversion nanocrystals with simultaneous control over crystal phase, size and emission colours through the control of different combinations of lanthanide dopants at precisely defined concentrations. For example, small-sized NaYF₄ upconversion nanoparticles that emit tunable visible colours were readily synthesized by rational doping of Yb³⁺, Er³⁺, Gd³⁺ and Tm³⁺ ions at different concentrations. The addition of a second emitter (Tm³⁺) at a trace concentration of 0.2 mol% had a negligible effect

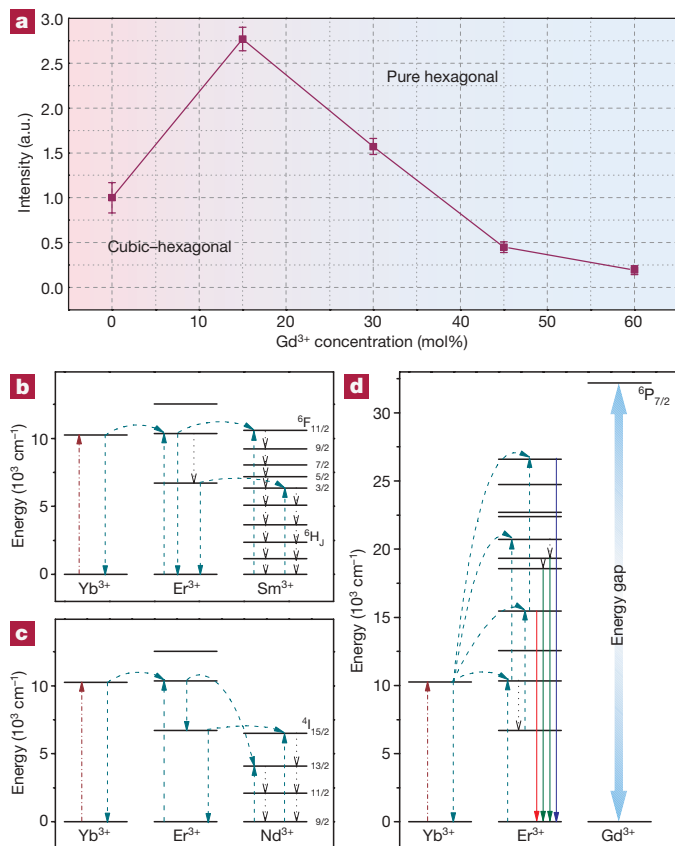


Figure 3 | Photoluminescence studies of NaYF₄:Yb/Er (18/2 mol%) nanocrystals with varying dopant concentration of Gd³⁺. **a**, Upconversion emission intensity versus dopant concentration of Gd³⁺ (0–60 mol%). The emission intensities were calculated by integrating the spectral intensity of the emission spectra over wavelength in the range 400–700 nm. Error bars shown represent the standard deviations from three repeated measurements. **b–d**, Proposed energy transfer mechanisms under 980-nm diode laser excitation in NaYF₄:Yb/Er nanocrystals doped with Sm³⁺, Nd³⁺, and Gd³⁺, respectively. The dashed-dotted, dashed, dotted, and full arrows represent photon excitation, energy transfer, multiphonon relaxation, and emission processes, respectively. The ^{2S+1}L_J notations used to label the *f* levels refer to spin (*S*), orbital (*L*) and angular (*J*) momentum quantum numbers, respectively, according to the Russel–Saunders notation.

on nanocrystal phase and size, but induced colour change markedly from green to blue (Fig. 4a and b). Owing to their small feature size and ease of dispersion, these nanoparticles can readily be incorporated in polydimethylsiloxane (PDMS) monoliths to construct volumetric three-dimensional (3D) displays (Fig. 4c and d), presenting unique interface applications for 3D image visualization. In contrast to conventional two-frequency resonant absorption techniques reliant on excitation of two near-infrared laser beams that intersect inside a glass-like matrix¹³, this single-beam design offers a simple system configuration and solves the problems of ghost voxels and alignment between beams.

In stark contrast to conventional synthetic techniques that require stringent control over several experimental variables for controlling crystallite size and phase, the lanthanide doping approach presented here requires modification of only a single variable (dopant concentration), while enabling tremendous improvements in our ability to control the formation of upconversion nanocrystals with small feature size and desirable optical properties. These findings are important not only for understanding lanthanide-doping-mediated crystal growth process, but also for providing a convenient route for facile synthesis of ultra-small hexagonal phase NaYF₄ upconversion nanocrystals without the need for toxic organometallic precursors and hazardous coordinating solvents. As an added benefit, the use of

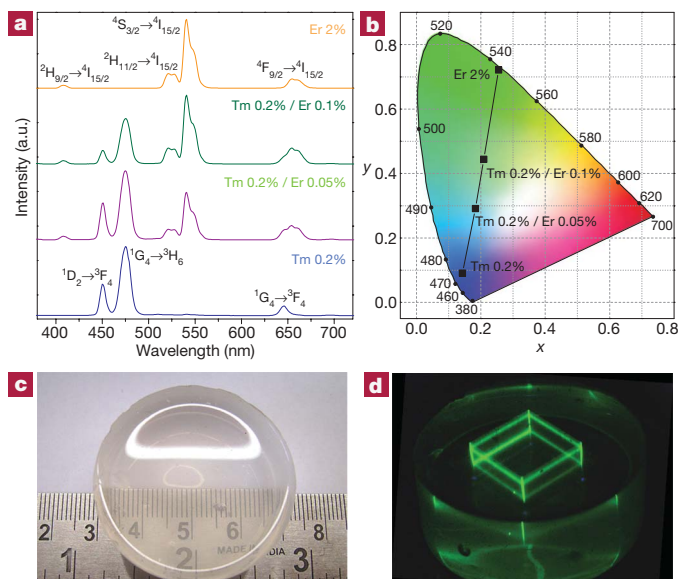


Figure 4 | Photoluminescence studies of NaYF₄ nanocrystals dispersed in solutions and embedded in PDMS composite materials. **a**, Room-temperature (25 °C) upconversion emission spectra of cyclohexane solutions comprising NaYF₄:Yb/Er/Gd (18/2/5 mol%), NaYF₄:Yb/Tm/Er/Gd (20/0.2/0.1/5 mol%), NaYF₄:Yb/Tm/Er/Gd (20/0.2/0.05/5 mol%), and NaYF₄:Yb/Tm/Gd (20/0.2/5 mol%) nanoparticles, respectively. **b**, Corresponding Commission Internationale de l'Eclairage (CIE) chromaticity coordinates of the multicolour emissions from the samples shown in **a**. **c**, Photograph showing physical dimension and transparency of a PDMS sample composed of 0.1 wt% of NaYF₄:Yb/Er/Gd (18/2/5 mol%) nanoparticles. **d**, Luminescent image of a 3D structure generated in the PDMS sample via computer-controlled near-infrared laser scanning.

paramagnetic Gd³⁺ dopant ions provides the nanocrystals with a second imaging capability as magnetic resonance imaging probes¹⁵.

METHODS SUMMARY

Nanocrystal synthesis. We synthesized lanthanide-doped NaYF₄ nanorods and nanoparticles capped with oleic acid using the methods of ref. 19 and ref. 23, respectively. Additional experimental details are provided in the Supplementary Information.

Preparation of the nanoparticle/PDMS composite materials. A 10:1:1 (vol:vol:vol) mixture of SYLGARD silicone elastomer 184, the curing agent (Dow Corning Corp.), and a cyclohexane solution containing upconversion nanoparticles (1 wt%) were thoroughly mixed in a glass container and aged overnight before heat treatment at 81 °C for 1 h. The composite materials with different types of nanoparticles can easily be cut into rectangular bars.

Volumetric 3D display. A 980-nm diode laser operating at 2,000 mW was directed into a fast scanning X-Y galvanometer with an F-theta lens (focal length of 198 mm) to focus the laser beam. A dynamic beam expander was attached to the galvanometer to control the Z position of the laser beam at a range of ±7 mm. The scanning of the laser beam was controlled through CyberLease scanning software from IDI Laser. A 3D cube structure was then drawn and imported into CyberLease to generate a 3D scanning path for the laser beam. During the writing process, the laser beam was scanned across the sample by altering the X-Y mirror of the galvanometer while the height of the laser focal point was changed by changing the expanded beam size. The laser power was attenuated to 27 mW and the scanning speed was set at 2 mm s⁻¹.

Received 25 June; accepted 15 December 2009.

- Feng, X. *et al.* Converting ceria polyhedral nanoparticles into single-crystal nanospheres. *Science* **312**, 1504–1508 (2006).
- Alivisatos, A. P. Semiconductor clusters, nanocrystals, and quantum dots. *Science* **271**, 933–937 (1996).
- Norris, D. J., Yao, N., Charnock, F. T. & Kennedy, T. A. High-quality manganese-doped ZnSe nanocrystals. *Nano Lett.* **1**, 3–7 (2001).
- Yang, Y., Chen, O., Angerhofer, A. & Cao, Y. C. Radial-position-controlled doping in CdS/ZnS core/shell nanocrystals. *J. Am. Chem. Soc.* **128**, 12428–12429 (2006).
- Wernsdorfer, W. *et al.* Macroscopic quantum tunneling of magnetization of single ferrimagnetic nanoparticles of barium ferrite. *Phys. Rev. Lett.* **79**, 4014–4017 (1997).

6. Heer, S., Kömpe, K., Güdel, H.-U. & Haase, M. Highly efficient multicolour upconversion emission in transparent colloids of lanthanide-doped NaYF₄ nanocrystals. *Adv. Mater.* **16**, 2102–2105 (2004).
7. Sivakumar, S., van Veggel, F. C. J. M. & Raudsepp, M. Bright white light through up-conversion of a single NIR source from sol-gel-derived thin film made with Ln³⁺-doped LaF₃ nanoparticles. *J. Am. Chem. Soc.* **127**, 12464–12465 (2005).
8. Ehlert, O., Thomann, R., Darbandi, M. & Nann, T. A. Four-color colloidal multiplexing nanoparticle system. *ACS Nano* **2**, 120–124 (2008).
9. Wang, F. & Liu, X. Upconversion multicolor fine-tuning: visible to near-infrared emission from lanthanide-doped NaYF₄ nanoparticles. *J. Am. Chem. Soc.* **130**, 5642–5643 (2008).
10. Auzel, F. Upconversion and anti-stokes processes with f and d ions in solids. *Chem. Rev.* **104**, 139–173 (2004).
11. Suyver, J. F. et al. Novel materials doped with trivalent lanthanides and transition metal ions showing near-infrared to visible photon upconversion. *Opt. Mater.* **27**, 1111–1130 (2005).
12. Wang, F. & Liu, X. Recent advances in the chemistry of lanthanide-doped upconversion nanocrystals. *Chem. Soc. Rev.* **38**, 976–989 (2009).
13. Downing, E., Hesselink, L., Ralston, J. & Macfarlane, R. A three-color, solid-state, three-dimensional display. *Science* **273**, 1185–1189 (1996).
14. Liu, C., Wang, H., Zhang, X. & Chen, D. Morphology- and phase-controlled synthesis of monodisperse lanthanide-doped NaGdF₄ nanocrystals with multicolor photoluminescence. *J. Mater. Chem.* **19**, 489–496 (2009).
15. Park, Y. I. et al. Nonblinking and nonbleaching upconverting nanoparticles as an optical imaging nanoprobe and T1 magnetic resonance imaging contrast agent. *Adv. Mater.* **21**, 4467–4471 (2009).
16. Lim, B. et al. Pd-Pt bimetallic nanodendrites with high activity for oxygen reduction. *Science* **324**, 1302–1305 (2009).
17. Sun, S., Murray, C. B., Weller, D., Folks, L. & Moser, A. Monodisperse FePt nanoparticles and ferromagnetic FePt nanocrystal superlattices. *Science* **287**, 1989–1992 (2000).
18. Tang, Z., Zhang, Z., Wang, Y., Glotzer, S. C. & Kotov, N. A. Self-assembly of CdTe nanocrystals into free-floating sheets. *Science* **314**, 274–278 (2006).
19. Wang, X., Zhuang, J., Peng, Q. & Li, Y. A general strategy for nanocrystal synthesis. *Nature* **437**, 121–124 (2005).
20. Cademartiri, L. et al. Multigram scale, solventless and diffusion-controlled route to highly monodisperse PbS nanocrystals. *J. Phys. Chem. B* **110**, 671–673 (2006).
21. Chen, Y., Kim, M., Lian, G., Johnson, M. B. & Peng, X. Side reactions in controlling the quality, yield, and stability of high quality colloidal nanocrystals. *J. Am. Chem. Soc.* **127**, 13331–13337 (2005).
22. Wang, L. & Li, Y. Controlled synthesis and luminescence of lanthanide doped NaYF₄ nanocrystals. *Chem. Mater.* **19**, 727–734 (2007).
23. Li, Z., Zhang, Y. & Jiang, J. Multicolor core/shell-structured upconversion fluorescent nanoparticles. *Adv. Mater.* **20**, 4765–4769 (2008).
24. Mai, H. et al. High-quality sodium rare-earth fluoride nanocrystals: controlled synthesis and optical properties. *J. Am. Chem. Soc.* **128**, 6426–6436 (2006).
25. Boyer, J. C., Vetrone, F., Cuccia, L. A. & Capobianco, J. A. Synthesis of colloidal upconverting NaYF₄ nanocrystals doped with Er³⁺, Yb³⁺ and Tm³⁺, Yb³⁺ via thermal decomposition of lanthanide trifluoroacetate precursors. *J. Am. Chem. Soc.* **128**, 7444–7445 (2006).
26. Yi, G. S. & Chow, G. M. Synthesis of hexagonal-phase NaYF₄:Yb,Er and NaYF₄:Yb,Tm nanocrystals with efficient up-conversion fluorescence. *Adv. Funct. Mater.* **16**, 2324–2329 (2006).
27. Ayyub, P., Palkar, V. R., Chattopadhyay, S. & Multani, M. Effect of crystal size reduction on lattice symmetry and cooperative properties. *Phys. Rev. B* **51**, 6135–6138 (1995).
28. Shannon, R. D. Revised effective ionic radii and systematic studies of interatomic distances in halides and chalcogenides. *Acta Crystallogr. A* **32**, 751–767 (1976).
29. Perdew, J. P., Burke, K. & Ernzerhof, M. Generalized gradient approximation made simple. *Phys. Rev. Lett.* **77**, 3865–3868 (1996).
30. Blochl, P. E. Projector augmented-wave method. *Phys. Rev. B* **50**, 17953–17979 (1994).

Supplementary Information is linked to the online version of the paper at www.nature.com/nature.

Acknowledgements We thank G. A. Ozin, X. Chen, F. Stellacci, C. Yan, Y. Xia, L. Cademartiri, T. Nann, Y. Li and Y. C. Cao for discussions. This study was supported in part by the National University of Singapore (NUS), the Ministry of Education of Singapore, the Singapore-MIT Alliance, and the Agency for Science, Technology and Research (A*STAR). X.L. is grateful to the NUS for a Young Investigator Award.

Author Contributions F.W. and X.L. conceived the experiments and wrote the paper. F.W. and J.W. were primarily responsible for the experiments. Y.H., J.X. and H.C. performed the TEM characterization. C.S.L. and M.H. contributed to the volumetric 3D display studies. Y.L. and C.Z. performed theoretical calculations. All authors contributed to the analysis of this manuscript.

Author Information Reprints and permissions information is available at www.nature.com/reprints. The authors declare no competing financial interests. Correspondence and requests for materials should be addressed to X.L. (chmlx@nus.edu.sg).

LETTERS

Tropical cyclones and permanent El Niño in the early Pliocene epoch

Alexey V. Fedorov¹, Christopher M. Brierley¹ & Kerry Emanuel²

Tropical cyclones (also known as hurricanes and typhoons) are now believed to be an important component of the Earth's climate system^{1–3}. In particular, by vigorously mixing the upper ocean, they can affect the ocean's heat uptake, poleward heat transport, and hence global temperatures. Changes in the distribution and frequency of tropical cyclones could therefore become an important element of the climate response to global warming. A potential analogue to modern greenhouse conditions, the climate of the early Pliocene epoch (approximately 5 to 3 million years ago) can provide important clues to this response. Here we describe a positive feedback between hurricanes and the upper-ocean circulation in the tropical Pacific Ocean that may have been essential for maintaining warm, El Niño-like conditions^{4–6} during the early Pliocene. This feedback is based on the ability of hurricanes to warm water parcels that travel towards the Equator at shallow depths and then resurface in the eastern equatorial Pacific as part of the ocean's wind-driven circulation^{7,8}. In the present climate, very few hurricane tracks intersect the parcel trajectories; consequently, there is little heat exchange between waters at such depths and the surface. More frequent and/or stronger hurricanes in the central Pacific imply greater heating of the parcels, warmer temperatures in the eastern equatorial Pacific, warmer tropics and, in turn, even more hurricanes. Using a downscaling hurricane model^{9,10}, we show dramatic shifts in the tropical cyclone distribution for the early Pliocene that favour this feedback. Further calculations with a coupled climate model support our conclusions. The proposed feedback should be relevant to past equable climates and potentially to contemporary climate change.

The response of tropical cyclones to global climate change, and their role in climate, has been a subject of much debate^{1,2,11}. The role of hurricanes in past climates has also been discussed, especially in relation to 'hothouse' climates such as that of the Eocene epoch^{3,12,13}. The motivation for this study originates in the climate of the early Pliocene—an epoch that many consider the closest analogue to future greenhouse conditions¹⁴. The external factors that control climate, including continental geography and the intensity of sunlight incident on the Earth, were essentially the same as at present. The atmospheric concentration of carbon dioxide was in the range 300–400 p.p.m. (ref. 15), similar to current, elevated values. Yet, the climate was significantly warmer then. Evidence from PRISM (the Pliocene research, interpretation and synoptic mapping project^{16–19}) indicates mid-Pliocene global mean temperatures 2–3 °C warmer than today. The early Pliocene was approximately 4 °C warmer than today²⁰.

The tropical climate then was also markedly different from the present-day climate. In particular, the Pacific developed a permanent El Niño-like state (for a review, see ref. 6). This term implies that the mean sea surface temperature (SST) gradient along the Equator was

very weak or absent (Fig. 1a). Similarly, the meridional temperature gradient from the Equator to the mid-latitudes was significantly reduced²¹. In fact, in the early Pliocene the SST distribution was virtually flat between the Equator and the subtropics, indicating a poleward expansion of the ocean warm pool (Fig. 1b). Cold surface waters were almost absent from upwelling zones off the western coasts of Africa and the Americas^{22,23}.

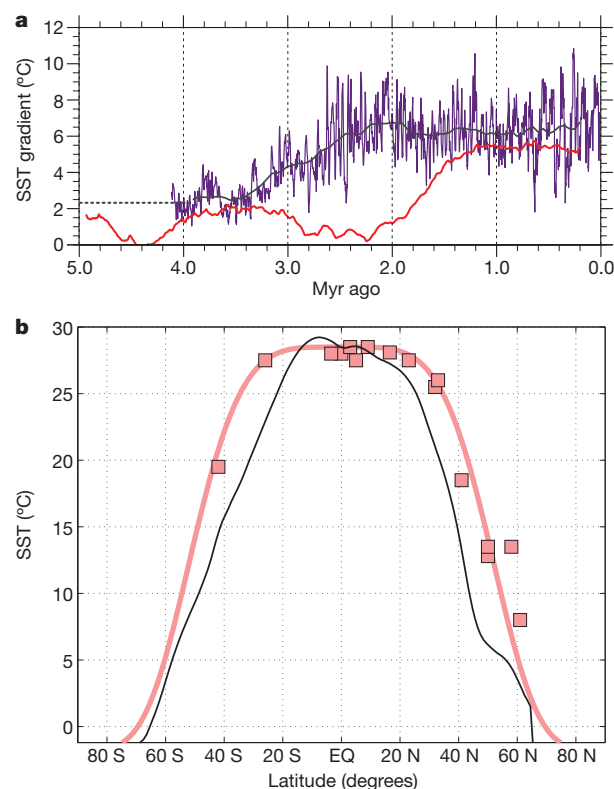


Figure 1 | Changes in SSTs in the Pacific over the past ~5 million years. **a**, The development of the meridional SST contrast in the tropical East Pacific (purple line²¹) and the zonal SST gradient along the Equator (red line³). The meridional temperature difference is estimated from alkenone records from ODP sites 846 (3° S, 91° W) and 1012 (32° N, 118° W). The zonal temperature difference is calculated from Mg/Ca temperature records from ODP sites 806 (0° N, 159° E) and 847 (0° N, 95° W). The black and the red lines are obtained using a 400,000-year running mean. **b**, A reconstruction of the latitudinal SST distribution in the early Pliocene (~4 million years ago) in the mid-Pacific roughly along the Date Line (pink squares), after ref. 21. The pink line shows the hypothetical fit of equation (1) of Methods to the proxy data. The black line shows the modern climatological SSTs along 180° E.

¹Department of Geology and Geophysics, Yale University, New Haven, Connecticut 06520, USA. ²Department of Earth, Atmospheric, and Planetary Sciences, MIT, Cambridge, Massachusetts 02139, USA.

A major unresolved issue is how the early Pliocene climate—and especially its tropical conditions—were maintained, given that CO₂ concentrations were very similar to modern values. So far, climate models have not been able to reproduce the tropical SST patterns characteristic of the early Pliocene^{18,24}. A recent study²¹ has suggested that additional mechanisms, perhaps related to ocean vertical mixing, should be considered in order to simulate a tropical climate state with weak SST contrasts. Could tropical cyclones provide such a mechanism?

Tropical storms are known to increase ocean vertical mixing—in the wake of hurricanes, the ocean mixed layer can deepen to 120–200 m (refs 13, 25, 26). As little is known about hurricanes in the past²⁷, here we reconstruct hurricane characteristics by completing several successive steps, including (1) reconstructing the SST field; (2) modelling the large-scale atmospheric circulation with a general circulation model (GCM); and (3) using the GCM data to drive a statistical downscaling model (SDSM), which computes synthetic hurricane tracks and intensity (Methods Summary; Methods).

The ocean temperature field is the starting point for our analysis, as the most reliable climatic information for the early Pliocene comes as SST data. Following ref. 21, we take the SST distribution in Fig. 1b, interpolate the data with a continuous function and, assuming very small east–west SST variations, extend the SST profile zonally. The SST profile is shifted along the meridian following the progression of the modern annual cycle. The resulting SST field is then used as boundary conditions for the atmospheric GCM (CAM3, T85 spectral resolution, see Methods).

GCM calculations show an atmospheric circulation for the early Pliocene with weaker (meridional) Hadley and (zonal) Walker cells²¹—the weakened atmospheric circulation implies reduced vertical wind shear, which is favourable for tropical cyclones. Next, we use the large-scale climatological atmospheric flow from these calculations to drive the downscaling model: weak atmospheric vortices are randomly seeded over the ocean and their evolution is followed by

the SDSM. The model predicts the tracks and calculates the intensity of the vortices—most of these disturbances die out, but some develop into mature tropical cyclones.

The results for the modern and early Pliocene climates are compared in Fig. 2 (and Supplementary Fig. 1). The SDSM adequately reproduces the observed modern distribution of tropical storms in the Pacific. The strongest modelled hurricane activity occurs east of the Philippines and Japan—a region known for frequent typhoons. Other active regions coincide with warm-water pools in the eastern North Pacific, the western South Pacific, and in the Indian Ocean. There are almost no hurricanes in the central Pacific or in the eastern South Pacific. In the North Atlantic, the tracks are shifted slightly towards the Caribbean, owing to biases in the winds simulated by the atmospheric GCM.

For the early Pliocene, the pattern of simulated tropical storm activity differs dramatically. Reduced vertical wind shear combined with warmer SSTs lead to a widespread increase in tropical cyclones (Supplementary Fig. 1). There are now two broad bands of cyclone activity both north and south of the Equator extending from the western to the eastern Pacific. Because of the warm pool's expansion, the lifespan of an average tropical cyclone is now 2–3 days longer. There are many more hurricanes in the South Pacific (and even a few in the South Atlantic). The overall number of hurricanes almost doubles (a smaller increase occurs when a lower-resolution atmospheric GCM, T42, is used). With reduced SST contrasts, the seasonal dependence of tropical cyclone activity becomes less pronounced, with cyclones occurring throughout the seasons.

How would these changes in hurricane activity influence the tropical climate? To answer this question, we first need to look at the upper ocean circulation in the tropics (Fig. 3a). This wind-driven circulation connects the regions of subduction off the coasts of California and Chile with the Equatorial Undercurrent and eventually with the eastern equatorial Pacific. The circulation is associated with a shallow ocean meridional overturning, with penetration

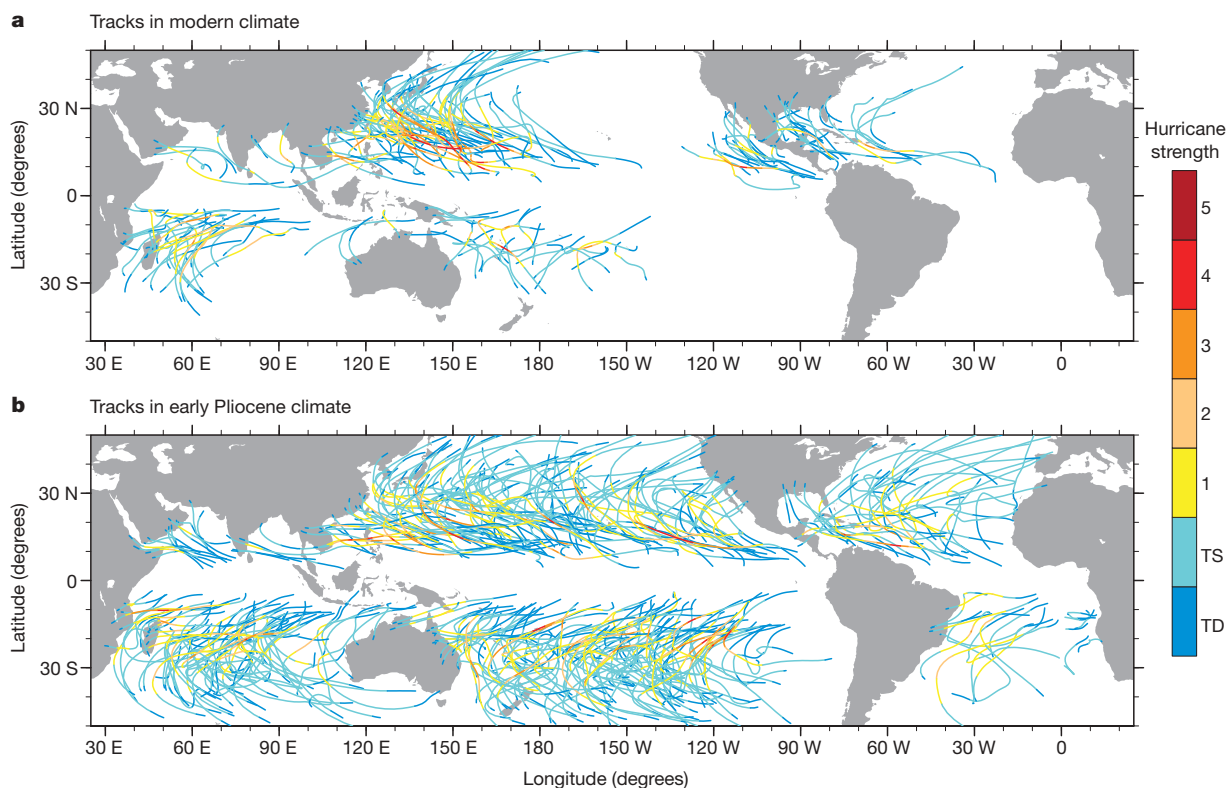


Figure 2 | The tracks of tropical cyclones simulated by the SDSM. a, In the modern climate, and **b**, in the early Pliocene climate. The colours indicate hurricane strength—from tropical depression (TD; blue) to tropical storm

(TS; cyan) to category-5 hurricanes (red). The tracks shown in each panel are a two-year subsample of 10,000 simulated tropical cyclones.

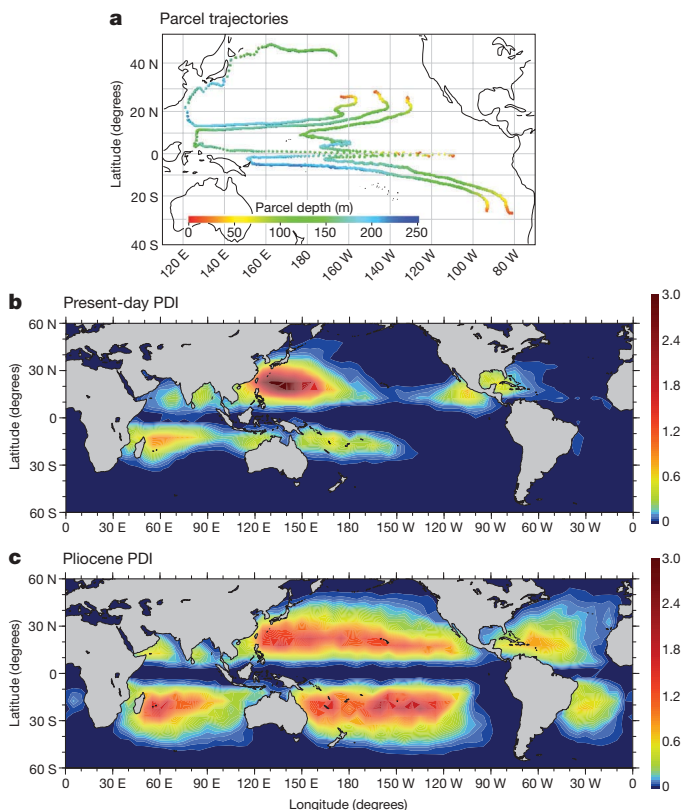


Figure 3 | Ocean wind-driven circulation and the PDI for tropical cyclones. **a**, The upper ocean circulation is shown as trajectories of water parcels over a period of 16 years after subduction off the coasts of California and Peru as simulated by an ocean GCM. The parcels move downward, westward and towards the Equator unless they start too far west off California, in which case they join the Kuroshio Current and the Pacific subtropical gyre. Along the Equator the parcels rise to the surface while being carried eastward by the Equatorial Undercurrent. The circulation remains shallow, with the parcel depth (indicated by colours) never exceeding 200–250 m. Adapted from refs 7 and 8. **b**, The PDI of the simulated tropical cyclones for modern conditions (in units of $\text{m}^3 \text{s}^{-2} \times 10^{10}$). Large values indicate regions where tropical cyclones can induce strong vertical mixing of the ocean. **c**, The same for the early Pliocene. Note the shift of the PDI towards the central Pacific, and much larger values south of the Equator during the Pliocene.

depths not greater than ~ 250 m, typically referred to as the shallow subtropical cells^{7,28}.

The effect of hurricanes on the ocean can be measured with the annual average power dissipation index (PDI), which approximates the amount of energy per unit area that tropical cyclones generate each year¹. A significant fraction of this energy is available to mix the upper ocean. In general, the PDI distribution coincides with the areas of strong hurricane activity, both in terms of frequency of occurrence and strength.

For the modern climate, the simulated mean PDI exhibits a strong maximum in the western tropical Pacific north of 10°N (Fig. 3b). Water parcels can travel towards the Equator after subduction through two ‘windows’ of the modern PDI distribution in the central Pacific without any interference from tropical storms (also see Supplementary Fig. 1). In the west Pacific, the parcels travel at the fringe of the PDI maximum, where the mixing can affect the Pacific subtropical gyre, but not the shallow subtropical cells.

For the early Pliocene, two bands of high PDI now cover the entire zonal extent of the Pacific (Fig. 3c), allowing interaction between the hurricanes and ocean circulation. With the two ‘windows’ closed, hurricane paths inevitably intersect the trajectories of water parcels, raising the parcels’ temperature. The end result is a warming of the eastern equatorial Pacific where the parcels rise to the surface. Ocean–atmosphere interactions²⁹ can amplify this warming via the

positive Bjerknes feedback—higher temperatures in the eastern equatorial Pacific imply weaker zonal winds, weaker equatorial upwelling and even higher temperatures in the east.

To test this hypothesis and replicate the effect of hurricanes for the early Pliocene, we have performed several numerical experiments with a coupled ocean–atmosphere GCM (CCSM3). In particular, we increase the ocean background vertical diffusivity tenfold to $\sim 1 \text{ cm}^2 \text{ s}^{-1}$ (consistent with ref. 3) above 200 m depth in two extra-tropical bands between 8° and 40° north and south of the Equator (similar to ref. 30). Simultaneously, CO_2 concentrations are increased from preindustrial (290 p.p.m.) to 1990 (355 p.p.m.) levels.

The tropical ocean response after 200 years of simulation includes (1) persistent El Niño-like warming in the central to eastern equatorial Pacific (Fig. 4b, Supplementary Fig. 2); (2) a small warming off the Equator indicative of a meridional expansion of the warm pool; (3) a temperature rise in most of the coastal upwelling regions; (4) a deepening of the ocean tropical thermocline; and (5) a reduction of the thermocline slope along the Equator in the Pacific (Supplementary Fig. 3). For comparison, we display SST changes in the same model (Fig. 4c) when only CO_2 concentrations are raised. In this case, the temperature increase is moderate (below 1°C) and almost uniform, indicating a near radiative-equilibrium response.

The warming of the eastern equatorial Pacific (the region typically referred to as the equatorial cold tongue) in response to increased extra-tropical mixing remains robust in a broad parameter range. Its magnitude depends on the specified diffusivity and the width of the equatorial gap between the two bands of enhanced mixing. The

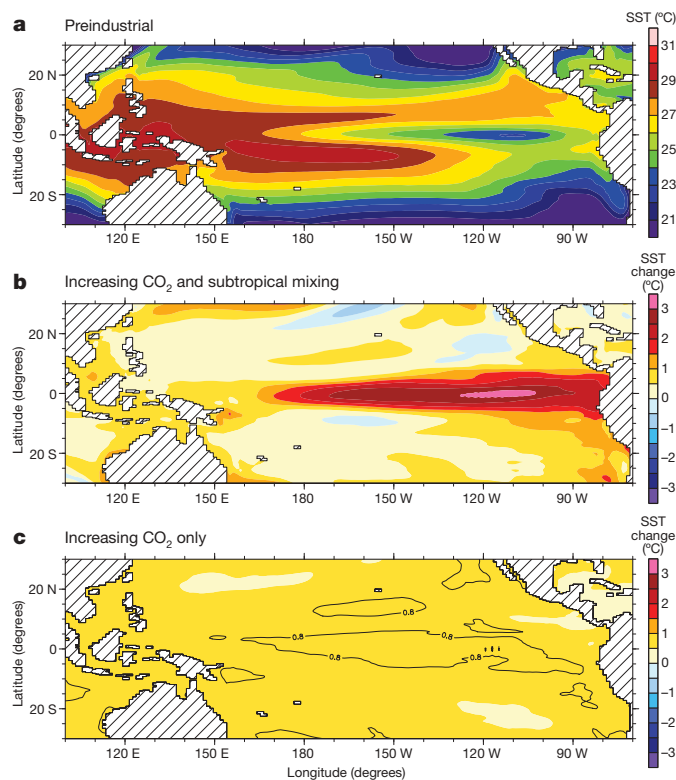


Figure 4 | SST changes in the tropical Pacific simulated by the coupled model. **a**, SSTs for preindustrial climate conditions; **b**, SST changes in response to increasing CO_2 concentration from 290 p.p.m. (preindustrial) to 355 p.p.m. (the level of 1990) and increasing vertical diffusivity in the upper ocean (0–200 m) in the extra-tropical bands (8° – 40° north and south of the Equator), after 200 years of calculations for the Pliocene scenario. The SST increase has a clear signature of permanent El Niño-like conditions, with the warming reaching 3.5°C in the eastern equatorial Pacific. **c**, SST changes in response to increasing CO_2 concentration alone. The SST increase is virtually uniform and remains below 1°C .

smaller the gap, the greater the warming that is achieved. The gap being fully closed wipes out the zonal SST gradient almost completely (Fig. 5). The depth of penetration of the mixing into the ocean is also important—the maximum warming occurs for depths of around 150–200 m.

Ocean adjustment to the imposed forcing involves different time-scales: from daily (ocean mixing from individual storms, not considered here) to seasonal, to decadal (the circulation time in the ocean's subtropical cell). The coupled model simulation takes nearly 100 years for the full impact of the imposed mixing to emerge (Fig. 5).

The results in Figs 2–5 suggest a plausible mechanism for sustaining the early Pliocene climate, based on the coupling between tropical SSTs, tropical cyclones and upper-ocean circulation. The expansion of the warm pool allows for enhanced hurricane activity throughout the subtropical Pacific. Stronger ocean vertical mixing in the two hurricane bands leads to further warming of the eastern equatorial Pacific and a deepening of the tropical thermocline. In turn, the warmer climate facilitates hurricane activity. This amounts to a positive feedback (Supplementary Fig. 4), which can potentially lead to multiple climate states—one with permanent El Niño-like conditions and strong hurricane activity, and the other corresponding to modern climate with a cold eastern equatorial Pacific.

Although promising, the proposed mechanism does not solve the early Pliocene problem completely, as the changes shown in Fig. 4b (and Supplementary Fig. 2) are not sufficient to fully bring the model to the reconstructed climate. Reduction in the meridional SST gradient is too weak compared to ref. 21, which may be related in part to biases in the coupled model (an excessively strong equatorial cold

tongue extends too far westward) or perhaps to still missing processes affecting the poleward heat transport. Numerical models able to simulate El Niño/Southern Oscillation and the mean state of the tropical Pacific more accurately are needed³¹. More work is required to improve our understanding of atmospheric dynamics in warmer climates³², and to better constrain the Pliocene SSTs^{20,21} and the contribution of tropical storms to ocean mixing^{3,12,13}. Resolving these issues will be critical both to model the early Pliocene climate and to predict future climate change, for which hurricane–ocean circulation feedbacks could become critical.

METHODS SUMMARY

The modelling of tropical storms in this study is performed using the SDSM^{9,10}. The first step of the downscaling process is to produce a global climatology for the vertical profiles of temperature, atmospheric humidity and winds. For this purpose, two experiments with an atmospheric GCM (CAM3, T85 resolution) are conducted—one forced with modern climatological SSTs, the other with an early Pliocene SST reconstruction²¹.

The next step is to create synthetic hurricane tracks. In order to increase track variations, self-consistent random realizations of the winds are created using the means, variances and covariances from the GCM simulations. Weak vortices are seeded at random throughout the tropics and their subsequent progression is computed using a model describing advection by the vertically averaged winds, corrected for a β -drift (poleward and westward motion that a hurricane would have in the absence of background winds because of the variation of Coriolis force with latitude). Over 20,000 synthetic cyclones were produced (only two years worth of tracks are shown in Fig. 2).

Once the tracks have been determined, an intensity model⁹ is integrated along each track (the Coupled Hurricane Intensity Prediction System, CHIPS). It is an axisymmetric atmosphere model with a parameterization of vertical wind shear, coupled to a simple one-dimensional ocean model, which captures the effect of the ocean mixed layer on tropical cyclones. In lieu of mixed layer depth reconstructions for the early Pliocene, we use present day values. We anticipate that the actual ocean mixed layer was deeper in the Pliocene, so that if anything we underestimate the strength of tropical storms.

The PDI in Fig. 3 is defined as an integral of v^2 over the duration of all tropical cyclones that occur on average in the course of 1 year in a $5^\circ \times 5^\circ$ gridbox (v is the maximum wind velocity associated with the cyclones in the gridbox). Further details of the SST reconstruction and numerical simulations are discussed in the Methods.

Full Methods and any associated references are available in the online version of the paper at www.nature.com/nature.

Received 8 July; accepted 29 December 2009.

1. Emanuel, K. Increasing destructiveness of tropical cyclones over the past 30 years. *Nature* **436**, 686–688 (2005).
2. Webster, P., Holland, G., Curry, J. & Chang, H. Changes in tropical cyclone number, duration, and intensity in a warming environment. *Science* **309**, 1844–1846 (2005).
3. Sriv, R. L. & Huber, M. Observational evidence for an ocean heat pump induced by tropical cyclones. *Nature* **447**, 577–580 (2007).
4. Molnar, P. & Cane, M. A. El Niño's tropical climate and teleconnections as a blueprint for pre-Ice Age climates. *Paleoceanography* **17**, 1021, doi:10.29/2001PA000663 (2002).
5. Wara, M. W., Ravelo, A. C. & Delaney, M. L. Permanent El Niño-like conditions during the Pliocene warm period. *Science* **309**, 758–761 (2005).
6. Fedorov, A. *et al.* The Pliocene paradox (mechanisms for a permanent El Niño). *Science* **312**, 1485–1489 (2006).
7. Gu, D. & Philander, S. Interdecadal climate fluctuations that depend on exchanges between the tropics and extratropics. *Science* **275**, 805–807 (1997).
8. Barreiro, M., Fedorov, A. V., Pacanowski, R. C. & Philander, S. G. Abrupt climate changes: how the freshening of the northern Atlantic affects the thermohaline and wind-driven oceanic circulations. *Annu. Rev. Earth Planet. Sci.* **36**, 33–58 (2008).
9. Emanuel, K., Ravelo, S., Vivant, E. & Risi, C. A statistical deterministic approach to hurricane risk assessment. *Bull. Am. Meteorol. Soc.* **87**, 299–314 (2006).
10. Emanuel, K., Sundararajan, R. & Williams, J. Hurricanes and global warming — results from downscaling IPCC AR4 simulations. *Bull. Am. Meteorol. Soc.* **89**, 347–367 (2008).
11. Knutson, T. R., Sirutis, J. J., Garner, S. T., Vecchi, G. A. & Held, I. M. Simulated reduction in Atlantic hurricane frequency under twenty-first-century warming conditions. *Nature Geosci.* **1**, 359–364 (2008).
12. Emanuel, K. A simple model of multiple climate regimes. *J. Geophys. Res.* **D 107**, 4077, doi:10.1029/2001JD001002 (2002).

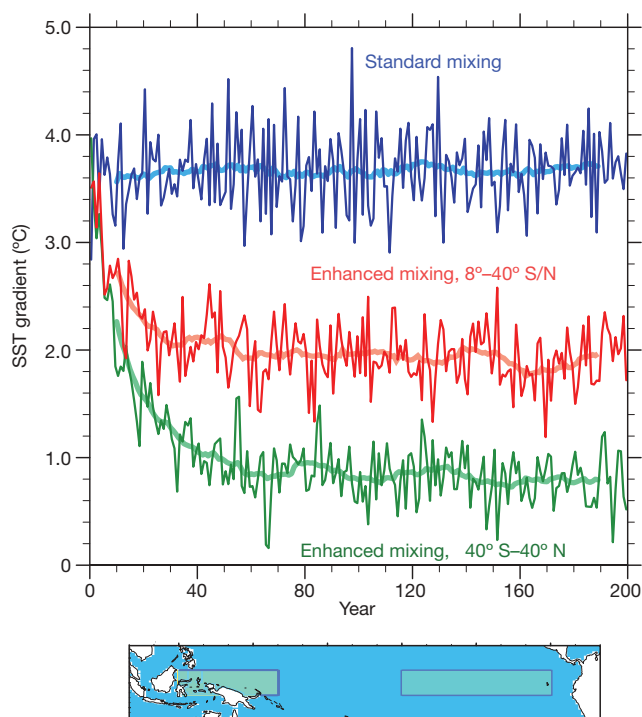


Figure 5 | Evolution of the equatorial SST gradient in three coupled experiments. The gradient is calculated as the difference in the annually averaged SSTs between the two regions in the western and eastern equatorial Pacific shown on the map at bottom. Thick lines correspond to 20-year running means. The increase in CO₂ alone from the preindustrial level to 355 p.p.m. does not change the equatorial gradient substantially (blue line). The increase in both CO₂ and ocean vertical mixing in the extra-tropical bands causes a 2 °C reduction in the equatorial gradient (red). Closing the equatorial gap reduces the SST gradient further to below 1 °C (green). The majority of these changes occur within the first 50 years of the simulations, and the adjustment of the upper ocean is almost completed by 100 years. The reduced variability in the two latter cases is indicative of a weaker El Niño/Southern Oscillation.

13. Korty, R. L., Emanuel, K. A. & Scott, J. R. Tropical cyclone-induced upper-ocean mixing and climate: application to equable climates. *J. Clim.* **21**, 638–654 (2008).
14. Robinson, M. M., Dowsett, H. J. & Chandler, M. A. Pliocene role in assessing future climate impacts. *Eos* **89**, 501–502 (2008).
15. Pagani, M., Lui, Z., LaRiviere, J. & Ravelo, A. C. High Earth-system climate sensitivity determined from Pliocene carbon dioxide concentrations. *Nature Geosci.* **3**, 27–30 (2010).
16. Thompson, R. S. & Fleming, R. F. Middle Pliocene vegetation: reconstructions, paleoclimatic inferences, and boundary conditions for climate modelling. *Mar. Micropaleontol.* **27**, 27–49 (1996).
17. Dowsett, H. J. *et al.* Middle Pliocene Paleoenvironmental Reconstruction: PRISM2 236 (Open File Rep. 99-535, USGS Geological Survey, 1999).
18. Haywood, A. & Valdes, P. Modelling Pliocene warmth: contribution of atmosphere, oceans and cryosphere. *Earth Planet. Sci. Lett.* **218**, 363–377 (2004).
19. Dowsett, H. J. & Robinson, M. M. Mid-Pliocene equatorial Pacific sea surface temperature reconstruction: a multi-proxy perspective. *Phil. Trans. R. Soc. A* **367**, 109–125 (2009).
20. Brierley, C. M. & Fedorov, A. V. The relative importance of meridional and zonal SST gradients for the onset of the Ice Ages and Pliocene-Pleistocene climate evolution. *Paleoceanography* doi:10.1029/2009PA001809 (in the press).
21. Brierley, C. M. *et al.* Greatly expanded tropical warm pool and weakened Hadley circulation in the early Pliocene. *Science* **323**, 1714–1718 (2009).
22. Dekens, P. S., Ravelo, A. C. & McCarthy, M. D. Warm upwelling regions in the Pliocene warm period. *Paleoceanography* **22**, doi:10.1029/2006PA001394 (2007).
23. Marlow, J., Lange, C., Wefer, G. & Rosell-Mele, A. Upwelling intensification as part of the Pliocene-Pleistocene climate transition. *Science* **290**, 2288–2291 (2000).
24. Haywood, A. M., Dekens, P., Ravelo, A. C. & Williams, M. Warmer tropics during the mid-Pliocene? Evidence from alkenone paleothermometry and a fully coupled ocean-atmosphere GCM. *Geochem. Geophys. Geosyst.* **6**, Q03010, doi:10.1029/2004GC000799 (2005).
25. D'Asaro, E. A. The ocean boundary layer below Hurricane Dennis. *J. Phys. Oceanogr.* **33**, 561–579 (2003).
26. Jacob, S., Shay, L., Mariano, A. & Black, P. The 3D oceanic mixed layer response to Hurricane Gilbert. *J. Phys. Oceanogr.* **30**, 1407–1429 (2000).
27. Woodruff, J. D., Donnelly, J. P., Emanuel, K. & Lane, P. Assessing sedimentary records of paleohurricane activity using modelled hurricane climatology. *Geochem. Geophys. Geosyst.* **9**, Q09V10, doi:10.1029/2008GC002043 (2008).
28. McCreary, J. & Lu, P. Interaction between the subtropical and equatorial ocean circulations — the subtropical cell. *J. Phys. Oceanogr.* **24**, 466–497 (1994).
29. Fedorov, A. & Philander, S. Is El Niño changing? *Science* **288**, 1997–2002 (2000).
30. Jansen, M. & Ferrari, R. Impact of the latitudinal distribution of tropical cyclones on ocean heat transport. *Geophys. Res. Lett.* **36**, L06604, doi:10.1029/2008GL036796 (2009).
31. Guilyardi, E. *et al.* Understanding El Niño in ocean-atmosphere general circulation models: progress and challenges. *Bull. Am. Meteorol. Soc.* **90**, 325–339 (2009).
32. Tziperman, E. & Farrell, B. Pliocene equatorial temperature: lessons from atmospheric superrotation. *Paleoceanography* **24**, PA1101, doi:10.1029/2008PA001652 (2009).

Supplementary Information is linked to the online version of the paper at www.nature.com/nature.

Acknowledgements We thank G. Philander, M. Barreiro, R. Pacanowski, C. Ravelo, P. deMenocal, T. Herbert, Y. Rosenthal, K. Lawrence, P. Dekens, A. Haywood, C. Wunsch and M. Huber for numerous discussions and encouragement. Financial support was provided by grants to A.V.F. from the NSF, the Department of Energy Office of Science, and the David and Lucile Packard Foundation. We thank B. Dobbins for help with computer simulations. This research used resources of the National Energy Research Scientific Computing Center.

Author Contributions A.V.F. and C.M.B. contributed equally to the writing and ideas in this paper. The original idea for this study belongs to A.V.F. C.M.B. conducted experiments with CAM3 and CCSM3. K.E. conducted calculations with the SDSM and provided expertise in the physics of tropical cyclones.

Author Information Reprints and permissions information is available at www.nature.com/reprints. The authors declare no competing financial interests. Correspondence and requests for materials should be addressed to A.V.F. (alexey.fedorov@yale.edu).

METHODS

The SST field used in GCM simulations for the Pliocene. The period of the SST distribution in Fig. 1b is around 4–4.2 million years ago, which coincides with the almost complete collapse of the east–west temperature gradient along the Equator in Fig. 1a. It is also after the closure of the Isthmus of Panama³³, and yet before climate cooled and large Northern Hemisphere ice sheets developed³⁴. The original temperature data are based on alkenone and Mg/Ca temperature proxies that have been adjusted to describe SSTs in the mid-Pacific approximately along the Date Line. For further details of the Pliocene SST distribution, see ref. 21. The modern SST profile shown in Fig. 1b is the average of 1961–90 from ref. 35.

The continuous SST profile used in boundary conditions for the atmospheric GCM takes the form:

$$T(\theta) = (T_{\max} - T_{\min}) \exp \left[-\frac{1}{a} \left(\frac{|\theta|}{45} \right)^N \right] + T_{\min} \quad (1)$$

where θ is the latitude in degrees, T_{\min} is the freezing temperature of sea water (set to 1.8 °C) and T_{\max} is the maximum temperature in the tropics (set to 28.5 °C). N is set to 4.5, while constant a is determined by a least-squares fit to the temperature estimates in Fig. 1b. The value of a differs in the Atlantic from the rest of globe to allow for warmer temperatures in the North Atlantic:

$$a = \begin{cases} 4.2 \Rightarrow 0 \leq \theta \leq 90, 270 \leq \phi \leq 360 \\ 2.6 \Rightarrow \text{otherwise} \end{cases} \quad (2)$$

where ϕ is the longitude in degrees east of Greenwich's prime meridian. To simulate the effect of the Peru Current along the coast of South America, which was warmer than at present but still colder than the surrounding waters²², we add a cold temperature anomaly, T_{Peru} , to our SST profile:

$$T_{\text{Peru}} = \begin{cases} -3 \cos^2 \left(\frac{\theta + 30}{30} \right) \cos^2 \left(\frac{\phi - 295}{30} \right) \Rightarrow -75 \leq \theta \leq 15, 250 \leq \phi \leq 295 \\ 0 \Rightarrow \text{otherwise} \end{cases} \quad (3)$$

Details of atmospheric GCM simulations. The atmosphere-only simulations were performed using the Community Atmosphere Model (CAM3³⁶) developed by the National Center for Atmospheric Research (NCAR). It is a three-dimensional spectral model of global extent, with 26 vertical levels and a horizontal truncation of T85. We also used CAM3 with the T42 resolution, which produced generally similar results (in particular, using data from the T42 model to drive the SDSM showed a similar shift in hurricane distribution but a smaller increase in the number of storms, ~20%).

The atmospheric model source code and the present day climatological boundary conditions are freely accessible on the Earth System Grid (<http://www.earthsystemgrid.org>). The modern simulation uses a similar set-up to that described in ref. 37. The model has been spun up for 15 months, after which it has reached dynamic equilibrium. The simulations are then integrated for another decade to create the input for the SDSM. Note that the resolution of the T42 model corresponds to ~2.8° transform grid; and the resolution of T85 to ~1.4° transform grid. The effective resolution of the downscaling model is <1 km, which is much smaller than that of the large-scale atmospheric GCMs.

For the early Pliocene run, we use the reconstructed SST profile as the surface boundary condition. The fractional sea ice cover was diagnosed from the SST. We have not included any other modifications to the boundary conditions, although changes did occur (such the extent of the Greenland ice sheet and a reduction in the height of the Rockies, Andes and Indonesia). Sensitivity studies have shown that the impact of the imposed SST profile on the Hadley circulation is an order of magnitude larger than the impact of other model modifications²¹.

Details of coupled GCM simulations. The coupled simulations are performed using the third version of NCAR's Community Climate System Model (CCSM3³⁸). This GCM incorporates the atmospheric component described above (CAM3) coupled to ocean and sea ice models (POP and CSIM, respectively). The model source code and the boundary conditions are freely accessible on the Earth System Grid (<http://www.earthsystemgrid.org>).

The two experiments discussed in this paper start from an equilibrated pre-industrial climate. The two runs are initialized with an instantaneous increase of atmospheric CO₂ concentrations to 355 p.p.m. (the level in 1990). For the first experiment (Fig. 4b), ocean background vertical diffusivity between 8° and 40° of latitude is increased by a factor of 10 in the top 200 m. This brings ocean diffusivity in the two bands on each side of the Equator to values ~1 cm² s⁻¹, which is consistent with the estimates of ref. 3.

The methodology we use here is perhaps the simplest way to treat the impact of tropical cyclones. In reality, tropical cyclones are distributed very unevenly both in space and time. This makes deriving accurately the effective vertical diffusivity from a tropical cyclone distribution a non-trivial task with many uncertainties. A comprehensive study of these issues is now under way.

Our coupled experiments are similar to the recent work using an ocean-only simulation³⁰. Whereas those authors found a reduction in the ocean poleward heat transport in response to the subtropical mixing, we find an increase. This difference could arise from their use of restoring boundary conditions, which prevents significant SST and salinity variations and does not allow the atmosphere to respond to ocean circulation changes.

Our second experiment (Fig. 4c) utilizes the standard model set-up, used for instance in the IPCC Fourth Assessment Report³⁹. Both runs have been spun-up for 200 years, and an average of the last 20 years is chosen to make the comparison in Fig. 4.

33. Haug, G., Tiedemann, R., Zahn, R. & Ravelo, A. Role of Panama uplift on oceanic freshwater balance. *Geology* **29**, 207–210 (2001).
34. Zachos, J., Pagani, M., Sloan, L., Thomas, E. & Billups, K. Trends, rhythms, and aberrations in global climate 65 Ma to present. *Science* **292**, 686–693 (2001).
35. Rayner, N. A. *et al.* Global analyses of sea surface temperature, sea ice, and night marine air temperature since the late nineteenth century. *J. Geophys. Res.* **D 108**, 4407, doi:10.1029/2002JD002670 (2003).
36. Collins, W. D. *et al.* The formulation and atmospheric simulation of the Community Atmosphere Model: CAM3. *J. Clim.* **19**, 2144–2161 (2006).
37. Hack, J. J. *et al.* CCSM-CAM3 climate simulation sensitivity to changes in horizontal resolution. *J. Clim.* **19**, 2267–2289 (2006).
38. Collins, W. D. *et al.* The Community Climate System Model version 3 (CCSM3). *J. Clim.* **19**, 2122–2143 (2006).
39. Randall, D. A. *et al.* in *Climate Change 2007: The Physical Science Basis* (eds Susan, S. *et al.*) 589–662 (Cambridge Univ. Press, 2007).

Electric currents couple spatially separated biogeochemical processes in marine sediment

Lars Peter Nielsen¹, Nils Risgaard-Petersen², Henrik Fossing³, Peter Bondo Christensen³ & Mikio Sayama⁴

Some bacteria are capable of extracellular electron transfer, thereby enabling them to use electron acceptors and donors without direct cell contact^{1–4}. Beyond the micrometre scale, however, no firm evidence has previously existed that spatially segregated biogeochemical processes can be coupled by electric currents in nature. Here we provide evidence that electric currents running through defaunated sediment couple oxygen consumption at the sediment surface to oxidation of hydrogen sulphide and organic carbon deep within the sediment. Altering the oxygen concentration in the sea water overlying the sediment resulted in a rapid (<1-h) change in the hydrogen sulphide concentration within the sediment more than 12 mm below the oxic zone, a change explicable by transmission of electrons but not by diffusion of molecules. Mass balances indicated that more than 40% of total oxygen consumption in the sediment was driven by electrons conducted from the anoxic zone. A distinct pH peak in the oxic zone could be explained by electrochemical oxygen reduction, but not by any conventional sets of aerobic sediment processes. We suggest that the electric current was conducted by bacterial nanowires combined with pyrite, soluble electron shuttles and outer-membrane cytochromes. Electrical communication between distant chemical and biological processes in nature adds a new dimension to our understanding of biogeochemistry and microbial ecology.

Biogeochemistry is generally dominated by reduction–oxidation chemistry, with the electron donors and acceptors reacting either directly or through electron transport chains inside living cells. An exception is that some prokaryotes are able to use solid-phase electron acceptors such as ferric oxides through extracellular electron transport mediated by outer-membrane cytochromes, soluble electron shuttles and possibly also microbial nanowires^{1–3}. This capability is essential in engineered bioelectrochemical systems such as microbial fuel cells⁴. Aquatic sediments are known to be capable of generating electric current when electrodes mounted in the sediment and the overlying water phase are connected^{5,6}. The abundance of sediment bacteria able to exchange electrons with the surroundings and use almost any available electron donor and acceptor has led to speculation that extracellular electrochemical interactions might have an important, yet overlooked, role in global biogeochemical cycles⁴.

When we incubated defaunated sulphidic marine sediment in the presence of oxic seawater, hydrogen sulphide (that is, $\Sigma\text{H}_2\text{S} = [\text{H}_2\text{S}] + [\text{HS}^-] + [\text{S}^{2-}]$, where square brackets denote concentration) gradually disappeared from the pore water in the surface sediment. After one month, the oxic and sulphidic zones became separated by a 12–19-mm deep suboxic zone devoid of both O_2 and $\Sigma\text{H}_2\text{S}$ (Fig. 1). In contrast, control sediment cores incubated in the presence of anoxic sea water remained sulphidic from the sediment surface downwards. We conclude that the remote coupling between oxygen reduction and sulphide depletion is due to the presence of natural electric currents

(Fig. 2) as evidenced by the exclusion of other biogeochemical reactions known to support the formation of a suboxic zone; the presence of a distinct electrochemical pH signature; and the rapidity of the interaction between the two spatially separated processes. We consider these three factors separately in the following three paragraphs.

Iron and manganese are oxidized to insoluble minerals in the presence of oxygen. When these oxides become buried in anoxic sediment by bioturbation or sedimentation, they are able to oxidize or precipitate the $\Sigma\text{H}_2\text{S}$ in the sediment, thus creating a suboxic zone⁷. In the present study, bioturbating fauna was eliminated by sieving the sediment (0.5-mm mesh size). Moreover, the seawater column was gently mixed during incubation to prevent non-biological transport of sediment particles. Any iron and manganese oxides that may have been present in the sediment at the start of incubation had no impact on sulphide oxidation, as evidenced by the fact that no sulphide depletion occurred in the control cores (Fig. 1c, g). Oxidation of sulphide by free nitrate can have had only minor impact because the $\Sigma\text{H}_2\text{S}$ and pH profiles remained unchanged in the presence or absence in the overlying sea water of both NO_3^- (>50 μM) and the nitrification inhibitor thiourea (300 μM) (data not shown). Large sulphur bacteria of genus *Beggiatoa* are able to transport nitrate from the sediment surface and use it to oxidize the $\Sigma\text{H}_2\text{S}$, with the resultant formation of a suboxic zone in the sediment⁸. Our careful microscopic inspection of the sediment cores did not reveal the presence of any sulphur bacteria of this sort, however. Neither did the sediment contain any foraminifera, another organism able to transport nitrate into sediment⁹. Bioadvective flow of pore water was excluded as macrofauna were absent and the few meiofauna specimens (<15 ciliates and nematodes per cubic centimetre) should not increase transport coefficients by more than 1% (ref. 10). The permeability of the sediment was too low ($3.6 \times 10^{-12} \text{ m}^2$) to support pressure-driven advection in the experimental set-up used (which featured narrow cores and low current speeds)¹¹.

The pH profiles exhibited a sharp peak (up to pH 8.9) in the oxic zone (Fig. 1b, f) consistent with proton consumption by electrochemical oxygen reduction: $\text{O}_2 + 4\text{e}^- + 4\text{H}^+ \rightarrow 2\text{H}_2\text{O}$ (Fig. 2). All other aerobic processes in the sediment, that is, oxidation of organic carbon, ammonium and reduced species of iron, manganese and sulphur, result in net generation of protons in the pH range observed here¹². An exception is partial aerobic oxidation of $\Sigma\text{H}_2\text{S}$ to elemental sulphur (that is, $2\text{HS}^- + 2\text{H}^+ + \text{O}_2 \rightarrow 2\text{S} + 2\text{H}_2\text{O}$). This process can be excluded here, however, as no hydrogen sulphide reached the oxic zone (Fig. 1). The distinctive pH peak thus constitutes an important and independent indication of electric currents across the oxic–anoxic interface in the sediment.

When the oxygen content of the overlying sea water was altered, the depth of the suboxic zone rapidly changed. Every time the overlying sea water was depleted of oxygen, the sulphidic zone in the

¹Department of Biological Sciences, ²Center for Geomicrobiology, Aarhus University, Ny Munkegade 114, DK-8000 Aarhus C, Denmark. ³Department of Marine Ecology, National Environmental Research Institute, Aarhus University, Vejlsøvej 25, DK-8600 Silkeborg, Denmark. ⁴National Institute of Advanced Industrial Science and Technology, 16-1 Onogawa, Tsukuba 305-8569, Japan.

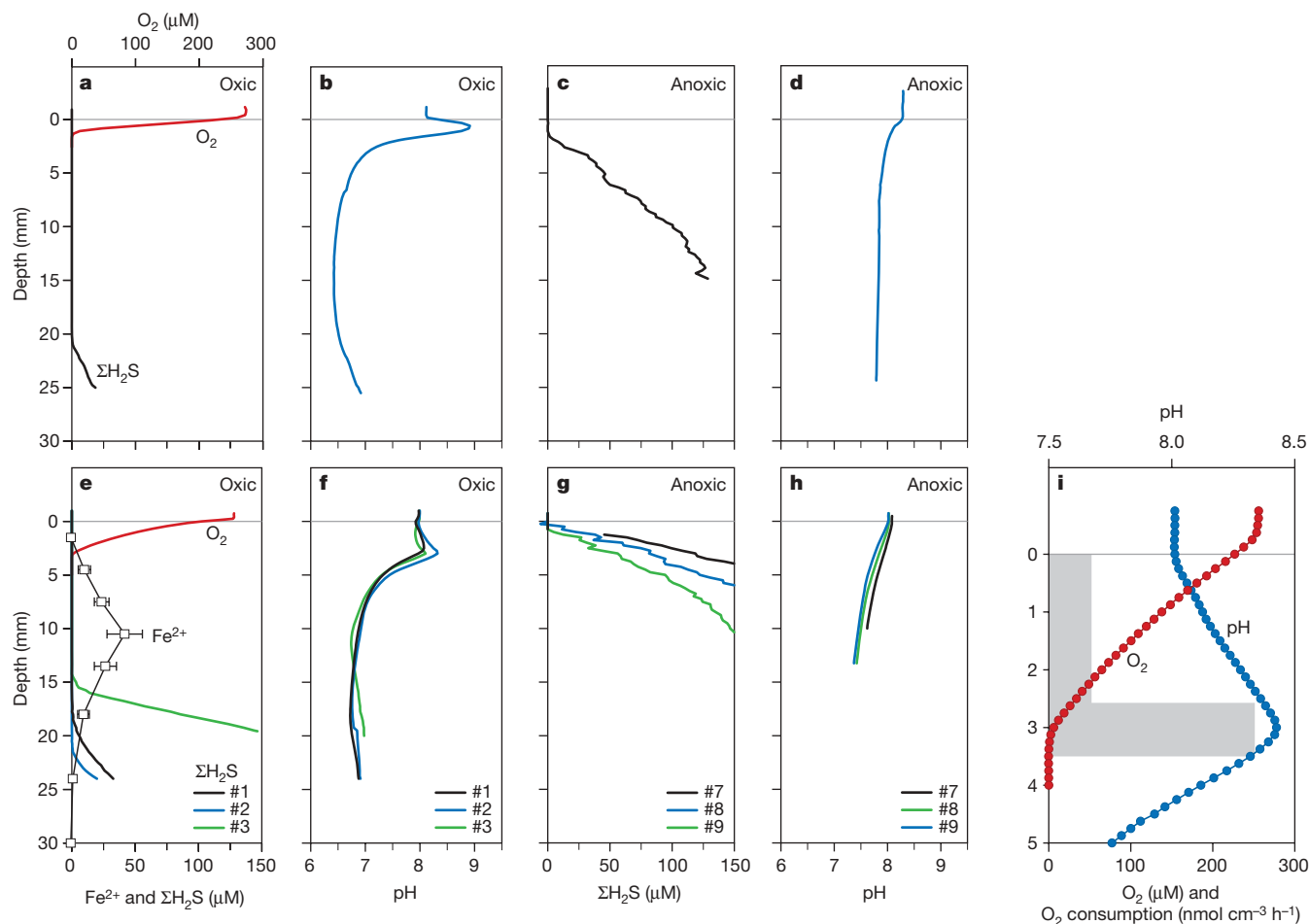


Figure 1 | Sediment O_2 , ΣH_2S , Fe^{2+} and pH microprofiles.

a–d, Sediment with shallow oxygen penetration (Aarhus Harbour). **e–i**, Sediment with deeper oxygen penetration (Aarhus Bay). The sediment was incubated for one month in the presence (**a**, **b**, **e**, **f**, **i**) or absence (**c**, **d**, **g**, **h**) of oxygen in the overlying sea water. **i**, pH (blue), O_2 (red) and O_2 consumption (grey) profiles in the upper 5 mm of the Aarhus Bay sediment. Hydrogen sulphide and pH were measured with a depth resolution of 250 μm , and O_2 was measured in steps of 150 μm . The

replicates of each of the various profiles ($n = 3–6$) obtained with the Aarhus Harbour sediment (**a–d**) and the O_2 profiles obtained with the Aarhus Bay sediment (**e**, **i**) were visually indistinguishable and are therefore represented here by average profiles. The replicate pairs of ΣH_2S and pH profiles obtained with the Aarhus Bay sediment (**e–f**) differed more and are therefore shown individually. The pore-water Fe^{2+} concentration is shown as mean \pm s.e.m. ($n = 3$).

sediment started to rise within 1 h (Fig. 3). When oxygen was re-introduced, the opposite occurred. The rapidity of the chemical response over distances exceeding 10 mm cannot be explained by diffusion of any known or hypothetical compound linking oxygen and ΣH_2S consumption: even if all the oxygen were used to generate a compound that subsequently diffused towards the sulphidic zone, the concentration at a depth of 10 mm after 1 h would be no more than 0.1% of the concentration at the sediment–water interface, assuming a molecular diffusion coefficient as high as $2 \times 10^{-5} \text{ cm}^2 \text{ s}^{-1}$ (refs 13, 14, 15).

Our data are in agreement with observations made using sediment batteries, such as those in a study⁶ of the chemistry in the vicinity of planar graphite electrodes that had functioned for seven months as sediment anodes delivering electrons to cathodes in the water phase. In line with our observations at the oxic–anoxic interface (Fig. 1e), it reported the development of a 3-cm suboxic zone with Fe^{2+} accumulation and suggested that conductance in the sediment could explain the distant impact of the electrode. It attributed the liberation of Fe^{2+} to oxidation of iron sulphide and possibly pyrite at an anode potential sufficient for sulphur oxidation but not for iron oxidation. These processes are indeed what seem to occur naturally in sediment devoid of inserted electrodes and external wires.

A conservative estimate of electrochemical oxygen consumption and current density can be obtained from proton–electron–oxygen

mass balance calculations. For each O_2 molecule reduced electrochemically, four electrons and four protons are consumed (Fig. 2). Non-electrochemical O_2 consumption generates a minimum of one proton per O_2 molecule reduced at $pH > 8$ (ref. 12). The minimum proton consumption rate, U_{H+} , in a zone can therefore be expressed as a function of total oxygen consumption rate, U_{O_2} , in the zone and the percentage, p , of oxygen consumed electrochemically:

$$U_{H+} = \frac{(4p - (100 - p))U_{O_2}}{100}$$

This can be reformulated as follows: $p = 20(1 + U_{H+}/U_{O_2})$.

We calculated U_{O_2} from the diffusive flux determined from the oxygen profile and found that it varied from 46 $\text{mmol } O_2 \text{ m}^{-2} \text{ d}^{-1}$ (Aarhus Harbour sediment) to 9.7 $\text{mmol } O_2 \text{ m}^{-2} \text{ d}^{-1}$ (Aarhus Bay sediment). Assuming that the carbonate system is the only important pH buffer in the sediment in the observed pH range, net proton consumption in a given zone is primarily balanced by H_2CO_3 and HCO_3^- diffusing in and being de-protonized to form CO_3^{2-} . To calculate the minimum proton consumption, U_{H+} , the concentration and flux of the carbonate species were determined from the pH profiles assuming the same concentration of total dissolved inorganic carbon at all depths, equilibrium between dissolved and atmospheric CO_2 in the water column and no precipitation of carbonate. Incorporation of additional inorganic carbon from mineralization

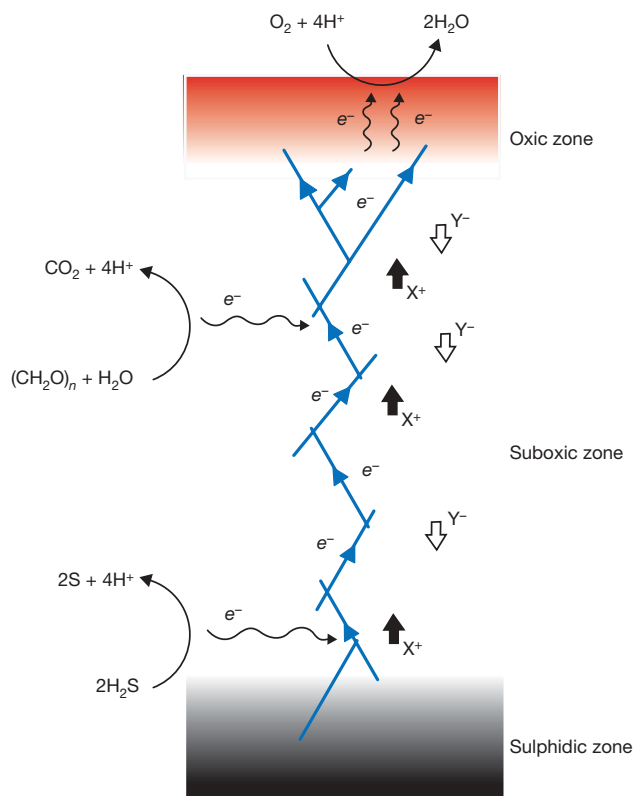


Figure 2 | Electric currents in sediment. Conceptual illustration of the electric communication between oxygen reduction in the oxic zone and oxidation of hydrogen sulphide and organic carbon in the suboxic and sulphidic zones. Electrons (e^-) are transmitted in a conductive network (blue arrows), and the circuit is completed by migration of ions (X^+ and Y^-) in the pore water.

or occurrence of precipitation would have enhanced the estimated proton consumption. The proportion of oxygen consumption driven by electric current, p , was thus found to be at least 42% using sediment from Aarhus Harbour and at least 31% using sediment from Aarhus Bay (Fig. 1a, b, i). In the zone of increased oxygen consumption at the oxic–anoxic interface of the Aarhus Bay sediment (Fig. 1i), the proportion was at least 42%.

The high proportion of oxygen consumption driven by electric current highlights the importance of this hitherto overlooked process as the major link between aerobic and anaerobic processes in the present sediment system. The current densities calculated from oxygen fluxes and p values (obtained using conversion factors of $4e^-$ per O_2 molecule reduced and $1A = 1.036 \times 10^{-5} \text{ mol } e^- \text{ s}^{-1}$) were 86 and 14 mA m^{-2} in the Aarhus Harbour and Aarhus Bay sediments, respectively. These values compare well with typical current densities of 40 mA m^{-2} for sediment electrodes⁶.

Electrochemical oxidation prevented the escape of sulphide from the sediment when oxygen was present in the overlying sea water. In this case, the maximum sulphide oxidation rate was assumed to be equivalent to the recorded upwards sulphide flux in sediment incubated in the absence of oxygen (Fig. 1), that is, $0.60 \text{ mmol S m}^{-2} \text{ d}^{-1}$ for the Aarhus Harbour sediment and $1.34 \text{ mmol S m}^{-2} \text{ d}^{-1}$ for the Aarhus Bay sediment. Even if the sulphide was completely oxidized to sulphate, the resultant electron flux would not account for more than 6% of the estimated minimum current in the Aarhus Harbour sediment and 87% of it in the Aarhus Bay sediment. This suggests that processes other than oxidation of sulphide donated electrons to the electric pathway, probably oxidation of organic carbon.

The existence of similar large-scale, natural electric currents was first proposed in 1960¹⁶ in connection with conductive pyrite ores, and further elaborated later^{17–19}. The existence of these so-called geobatteries has so far remained controversial, however, owing to the

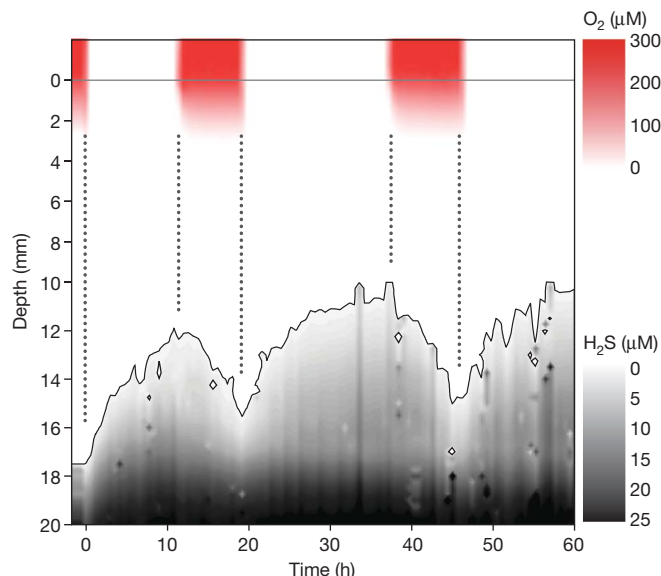


Figure 3 | Time series of O_2 and H_2S distribution in the sediment during oxic–anoxic cycles. The oscillating upper boundary of the sulphidic zone (solid line) equals $1 \mu\text{M } H_2S$ (the detection limit of the H_2S microsensor). The oxic–anoxic transitions are indicated by vertical lines. At time zero, the sediment had been incubated for 45 d with overlying air-saturated sea water. Three periods of oxygen depletion in the overlying sea water were introduced by gentle aeration with an $Ar\text{--}CO_2$ mixture in place of air. Vertical profiles of H_2S and O_2 were recorded continuously in steps of $250 \mu\text{m}$ over the depth intervals 10–20 mm, for H_2S , and $\sim 5\text{--}5 \text{ mm}$, for O_2 .

lack of theoretical consensus on the geoelectric implications and absence of evidence of spatially separated electrochemical reactions or direct measurements of such electric currents^{20–22}.

Bacterial nanowires¹ are suggested to comprise the main conductors of the electrons, possibly assisted by pyrite grains¹⁶ in the sediment ($30 \mu\text{mol}$ of pyrite per gram (wet weight) in the Aarhus Bay sediment). Highly efficient electron conductance has been measured in microbial fuel-cell biofilm²³, and observations in gradient cultures of bacterial strains that do and do not construct nanowires suggest that crosslinking of nanowires can facilitate conduction of electrons between distantly located cells¹⁹. Establishment of the conductive network in our sediment was probably the result of microbial activity as the initial development of the suboxic zone took a period of weeks, whereafter oscillations in the depth of the sulphidic zone could be induced on the scale of hours (Fig. 3). Humic and biogenic electron shuttles and outer-membrane cytochromes^{2–4} could facilitate local electron transfer to the network, although diffusion limitations make these mechanisms unsuitable for rapid, long-distance transmission²³.

This study adds a new dimension to the understanding of biogeochemical interactions, in that natural electric currents allow oxidation and reduction processes to be spatially separated yet instantly and intimately coupled. Oxygen-respiring microorganisms in sediment have hitherto been considered to depend on organic and inorganic electron donors mobilized within the oxic zone or transported up from the anoxic zone²⁴. Our study shows that electrons conducted from microbial oxidation processes deep within the sediment may make a considerable contribution to supporting aerobic life in the surface sediment. For the connected organisms, this electric pathway seems to allow mutually favourable subdivision of metabolism, in that those organisms with access to oxygen perform the oxygen reduction steps for all the connected organisms, whereas those with access to electron donors perform the oxidation steps for all the organisms.

The presence of benthic fauna should, on the one hand, suppress the electric current as bioturbation and bioadvection facilitate oxygen transport and iron–manganese cycling and possibly also interrupt the conductive network. On the other hand, the lining of

ventilated, stabilized burrows could provide an additional site for electric coupling. The electric currents described here are likely to be most prominent in sediment that has been abandoned by macrofauna owing to temporary oxygen depletion of the overlying sea water. When oxygen returns to the bottom water, the electric currents in the sediment may promote rapid oxidation of hydrogen sulphide and thereby detoxify the benthic environment. Recent measurements with *in situ* microsenors indicate such seasonal electric sulphide depletion in Tokyo Bay (M. Sayama, manuscript in preparation).

More generally, the spatial separation of electrochemical processes and the associated pH extremes might interfere with precipitation and dissolution of minerals, thus leaving a persistent signature in the geological record. Bioelectrochemical systems are rapidly being developed in many laboratories for studies of bacterial networking, interaction and energy sharing, and as new technologies for energy production, waste treatment and biosynthesis⁴. With our discovery of natural electric currents, such systems might become highly relevant for the study of microbial communities and biogeochemical processes in nature.

METHODS SUMMARY

We sampled sediment from Aarhus Harbour, Denmark (56.1388° N, 10.2240° E; depth, 4 m), using a Kajak sampler (KC Denmark) and sediment from Aarhus Bay (56.1034° N, 10.4579° E; depth, 22 m) using a box corer. To eliminate macrofauna, sediment from the upper 4 cm (Aarhus Harbour) or 11 cm (Aarhus Bay) was discarded and the underlying sulphidic sediment passed through a 0.5-mm sieve, homogenized and repacked in glass core liners sealed at the bottom (height, 100 mm; inner diameter, 57 mm). Care was taken to minimize exposure to air during handling. We incubated the cores in aquaria with circulating, nitrate-free artificial seawater (Aarhus Harbour sediment: 20‰, 20 °C; Aarhus Bay sediment: 30‰, 15 °C) gently aerated with either compressed air (oxic incubations) or an Ar–CO₂ mixture (anoxic incubations; 400 p.p.m. CO₂). A minimum of three sediment cores were incubated in each aquarium, and water was renewed weekly.

We determined porosity (vol./vol.) from the density and water content of 3-mm or 6-mm sediment slices, and determined permeability from percolation through 30 mm of sediment with a constant head of 1,400 Pa (ref. 11).

Micropores for O₂, H₂S and pH were measured with microsenors as previously described⁸. The total hydrogen sulphide ($\Sigma\text{H}_2\text{S} = [\text{H}_2\text{S}] + [\text{HS}^-] + [\text{S}^{2-}]$) profile was calculated from parallel H₂S and pH profiles²⁵, and the profiles of dissolved carbonate species were calculated from pH profiles using standard equilibrium constants²⁶. Subcores for measurement of dissolved Fe²⁺ were collected using severed 20-ml syringes and transferred into an O₂-free glove box, where 3-mm or 6-mm slices were cut and centrifuged in tubes containing filter units (Whatman). Pore-water samples (100 µl) were immediately mixed with 1,250 µl of ferrozine reagent and the Fe²⁺ content determined spectrophotometrically²⁷. Pyrite was measured as chrome-reducible sulphur²⁸.

We calculated diffusion fluxes from the pore-water profiles, diffusion coefficients^{8,29} and porosity¹⁵. The distribution of oxygen consumption rates was determined by numerical modelling³⁰.

Received 11 September; accepted 18 December 2009.

- Reguera, G. *et al.* Extracellular electron transfer via microbial nanowires. *Nature* **435**, 1098–1101 (2005).
- Lovley, D. R. & Coates, J. D. Blunt-Harris, E. L., Phillips, E. J. P. & Woodward, J. C. Humic substances as electron acceptors for microbial respiration. *Nature* **382**, 445–448 (1996).
- Leang, C., Coppi, M. V. & Lovley, D. R. OmcB, a c-type polyheme cytochrome, involved in Fe(III) reduction in *Geobacter sulfurreducens*. *J. Bacteriol.* **185**, 2096–2103 (2003).
- Rabaey, K. *et al.* Microbial ecology meets electrochemistry: electricity-driven and driving communities. *ISME J.* **1**, 9–18 (2007).

- Reimers, C. E., Tender, L. M., Fertig, S. & Wang, W. Harvesting energy from the marine sediment-water interface. *Environ. Sci. Technol.* **35**, 192–195 (2001).
- Ryckelynck, N., Stecher, H. A. III & Reimers, C. E. Understanding the anodic mechanism of a seafloor fuel cell: interactions between geochemistry and microbial activity. *Biogeochemistry* **76**, 113–139 (2005).
- Canfield, D. E. *et al.* Pathways of organic carbon oxidation in three continental margin sediments. *Mar. Geol.* **113**, 27–40 (1993).
- Sayama, M., Risgaard-Petersen, N., Nielsen, L. P., Fossing, H. & Christensen, P. B. Impact of bacterial NO₃[−] transport on sediment biogeochemistry. *Appl. Environ. Microbiol.* **71**, 7575–7577 (2005).
- Risgaard-Petersen, N. *et al.* Evidence for complete denitrification in a benthic foraminifer. *Nature* **443**, 93–96 (2006).
- Glud, R. N. & Fenchel, T. The importance of ciliates for interstitial solute transport in benthic communities. *Mar. Ecol. Prog. Ser.* **186**, 87–93 (1999).
- Glud, R. N., Forster, S. & Huettel, M. Influence of radial pressure gradients on solute exchange in stirred benthic chambers. *Mar. Ecol. Prog. Ser.* **141**, 303–311 (1996).
- Soetaert, K., Hofmann, A. F., Middelburg, J. J., Meysman, F. J. R. & Greenwood, J. The effect of biogeochemical processes on pH. *Mar. Chem.* **105**, 30–51 (2007).
- Crank, J. *The Mathematics of Diffusion* 1st edn, 18–19 (Clarendon, 1967).
- Li, Y.-H. & Gregory, S. Diffusion of ions in sea water and in deep-sea sediments. *Geochim. Cosmochim. Acta* **38**, 703–714 (1974).
- Ullman, W. J. & Aller, R. C. Diffusion coefficients in nearshore marine sediments. *Limnol. Oceanogr.* **27**, 552–556 (1982).
- Sato, M. & Mooney, H. M. The electrochemical mechanism of sulfide self-potentials. *Geophysics* **25**, 226–249 (1960).
- Bigalke, J. & Grabner, E. W. The geobattery model: a contribution to large scale electrochemistry. *Electrochim. Acta* **42**, 3443–3452 (1997).
- Naudet, V. & Revil, A. A sandbox experiment to investigate bacteria-mediated redox processes on self-potential signals. *Geophys. Res. Lett.* **32**, L11405 (2005).
- Ntarlagiannis, D., Atekwana, E. A., Hill, E. A. & Gorby, Y. Microbial nanowires: is the subsurface “hardwired”? *Geophys. Res. Lett.* **34**, L17305 (2007).
- Corry, C. E. Spontaneous polarization associated with porphyry sulfide mineralization. *Geophysics* **50**, 1020–1034 (1985).
- Leney, G. W. On: “Spontaneous polarization associated with porphyry sulfide mineralization” by C. E. Corry (GEOPHYSICS, 50, 1020–1034, June 1985). *Geophysics* **51**, 1153–1154 (1986).
- Williams, K. H., Hubbard, S. S. & Banfield, J. F. Galvanic interpretation of self-potential signals associated with microbial sulfate-reduction. *J. Geophys. Res.* **112**, G03019 (2007).
- Torres, C. I., Marcus, A. K., Parameswaran, P. & Rittmann, B. E. Kinetic experiments for evaluating the Nernst-Monod model for anode-respiring bacteria (ARB) in a biofilm anode. *Environ. Sci. Technol.* **42**, 6593–6597 (2008).
- Glud, R. N. Oxygen dynamics of marine sediments. *Mar. Biol. Res.* **4**, 243–289 (2008).
- Jeroschewski, P., Steuckart, C. & Kuhl, M. An amperometric microsensor for the determination of H₂S in aquatic environments. *Anal. Chem.* **68**, 4351–4357 (1996).
- Stumm, W. & Morgan, J. J. *Aquatic Chemistry* 2nd edn, 179–206 (Wiley, 1981).
- Stookey, L. L. Ferrozine - a new spectrophotometric reagent for iron. *Anal. Chem.* **42**, 779–781 (1970).
- Fossing, H. & Jørgensen, B. B. Measurement of bacterial sulfate reduction in sediments - evaluation of a single-step chromium reduction method. *Biogeochemistry* **8**, 205–222 (1989).
- Tromp, T. K., Van Cappellen, P. & Key, R. M. A global model for the early diagenesis of organic carbon and organic phosphorous in marine sediments. *Geochim. Cosmochim. Acta* **59**, 1259–1284 (1995).
- Berg, P., Risgaard-Petersen, N. & Rysgaard, S. Interpretation of measured concentration profiles in sediment pore water. *Limnol. Oceanogr.* **43**, 1500–1510 (1998).

Acknowledgements This research was financially supported by the Aarhus University Research Foundation, the Danish National Research Foundation (N.R.-P.), the Max Planck Society (N.R.-P.) and the Japan Society for the Promotion of Science (M.S.).

Author Contributions The study was conceived by L.P.N. All authors contributed to the design and execution of the study, interpretation of the results and preparation of the manuscript.

Author Information Reprints and permissions information is available at www.nature.com/reprints. The authors declare no competing financial interests. Correspondence and requests for materials should be addressed to L.P.N. (biolpn@biology.au.dk).

Fossilized melanosomes and the colour of Cretaceous dinosaurs and birds

Fucheng Zhang¹, Stuart L. Kearns², Patrick J. Orr³, Michael J. Benton², Zhonghe Zhou¹, Diane Johnson⁴, Xing Xu¹ & Xiaolin Wang¹

Spectacular fossils from the Early Cretaceous Jehol Group^{1,2} of northeastern China have greatly expanded our knowledge of the diversity and palaeobiology of dinosaurs and early birds, and contributed to our understanding of the origin of birds, of flight, and of feathers. Pennaceous (vaned) feathers and integumentary filaments are preserved in birds^{3–5} and non-avian theropod dinosaurs^{6–12}, but little is known of their microstructure. Here we report that melanosomes (colour-bearing organelles) are not only preserved in the pennaceous feathers of early birds, but also in an identical manner in integumentary filaments of non-avian dinosaurs, thus refuting recent claims^{13–16} that the filaments are partially decayed dermal collagen fibres. Examples of both eumelanosomes and phaeomelanosomes have been identified, and they are often preserved in life position within the structure of partially degraded feathers and filaments. Furthermore, the data here provide empirical evidence for reconstructing the colours and colour patterning of these extinct birds and theropod dinosaurs: for example, the dark-coloured stripes on the tail of the theropod dinosaur *Sinosauropteryx* can reasonably be inferred to have exhibited chestnut to reddish-brown tones.

Ever since they were first announced^{6,7}, the ‘feathered’ dinosaurs from the lacustrine sediments of the Jehol Group (Early Cretaceous, 131–120 Myr ago¹) of China have been controversial. Pennaceous feathers—those with a central shaft and lateral vanes, such as the contour and flight feathers of modern birds—occur both in Jehol birds^{3–5} and in non-avian theropods, primarily Maniraptora such as the oviraptorosaur *Caudipteryx*⁷, the dromaeosaurid *Microraptor gui*⁹, and the unclassified maniraptorans *Protarchaeopteryx*⁷, *Pedopenna*¹⁰ and *Yixianosaurus*¹¹.

Integumentary filaments occur both in non-avian theropods that possessed true pennaceous feathers (for example, *Caudipteryx*) and in those in which the latter are absent, such as *Sinosauropteryx*⁶, *Sinornithosaurus*⁸ and *Beipiaosaurus*¹². The report of superficially similar unbranched filaments in the ornithischian dinosaurs *Psittacosaurus* and *Tianyulong*¹⁷ suggests that such structures might be common to all dinosaurs. Many investigators have accepted that these various filamentous to feather-like structures are epidermal in origin and represent feathers^{6–12,17,18}; others^{13–16} have disputed this view, arguing, for example, that in the theropod dinosaur *Sinosauropteryx* they represent degraded dermal collagen fibres, part of the original strengthening materials of the animal’s skin¹⁶. Resolving this fundamental difference in interpretation is important for our understanding of the biology of the taxa in which they occur, but also has wider implications; if epidermal in origin, these structures will inform models of the evolutionary origin of modern feathers^{19,20}, and the timing of steps in the acquisition of this evolutionary novelty.

Here we demonstrate, using scanning electron microscopy (SEM), that both the integumentary filaments of *Sinosauropteryx* and *Sinornithosaurus* and the pennaceous feathers of the Jehol birds contain sub-micrometre-sized bodies that are either highly elongate with rounded termini, or oblate to sub-spherical, in shape. We eliminate the possibility that these bodies represent fossilized bacteria or diagenetic minerals, and interpret them as fossilized melanosomes. Their morphology is identical to that of melanosomes in the feathers of extant birds. Melanosomes are lysosome-related organelles of pigment cells in which melanins are stored, and are responsible, in part, for the colours exhibited by the feathers of modern birds. The two most common types of melanin are the reddish-brown to yellow pigment phaeomelanin and the black-grey pigment eumelanin²¹. These melanosomes, the first examples reported from the Jehol Group, and the first fossil examples of phaeomelanosomes, are preserved in life position. Representative examples are shown from an isolated feather (Fig. 1), feathers from the bird *Confuciusornis* (Fig. 2), and integumentary filaments of the theropod dinosaurs *Sinosauropteryx* (Fig. 3) and *Sinornithosaurus* (Fig. 4).

The outline of fossil feathers is often defined by layers of closely spaced, aligned, micrometre-sized, oblate bodies that have been

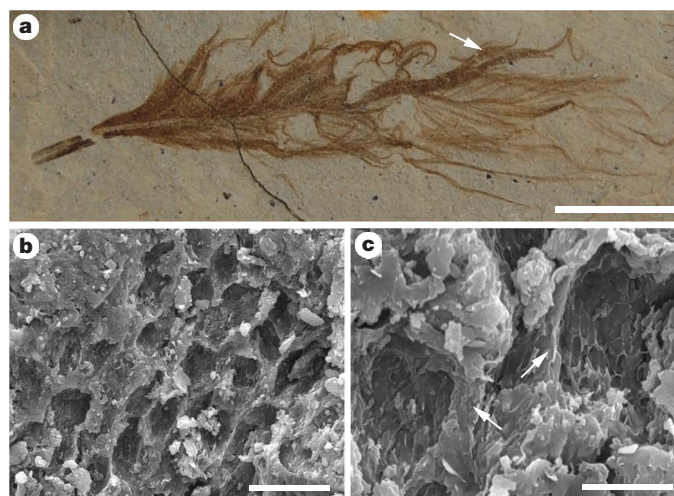


Figure 1 | Melanosomes in an isolated pennaceous feather (IVPP V15388B). **a**, Optical photograph; position of area analysed by SEM indicated by arrow. **b**, **c**, SEM images (at lower and higher magnification, respectively) of eumelanosomes preserved as moulds inside small areas that are separated from each other by anastomosing ridges of degraded feather (at arrows in **c**). Scale bars: **a**, 5 mm; **b**, 20 μ m; **c**, 5 μ m.

¹Key Laboratory of Evolutionary Systematics of Vertebrates, Institute of Vertebrate Paleontology and Paleoanthropology, Chinese Academy of Sciences, PO Box 643, Beijing 100044, China. ²Department of Earth Sciences, University of Bristol, Bristol BS8 1RJ, UK. ³UCD School of Geological Sciences, University College Dublin, Belfield, Dublin 4, Ireland. ⁴Planetary and Space Sciences Research Institute, The Open University, Walton Hall, Milton Keynes MK7 6AA, UK.

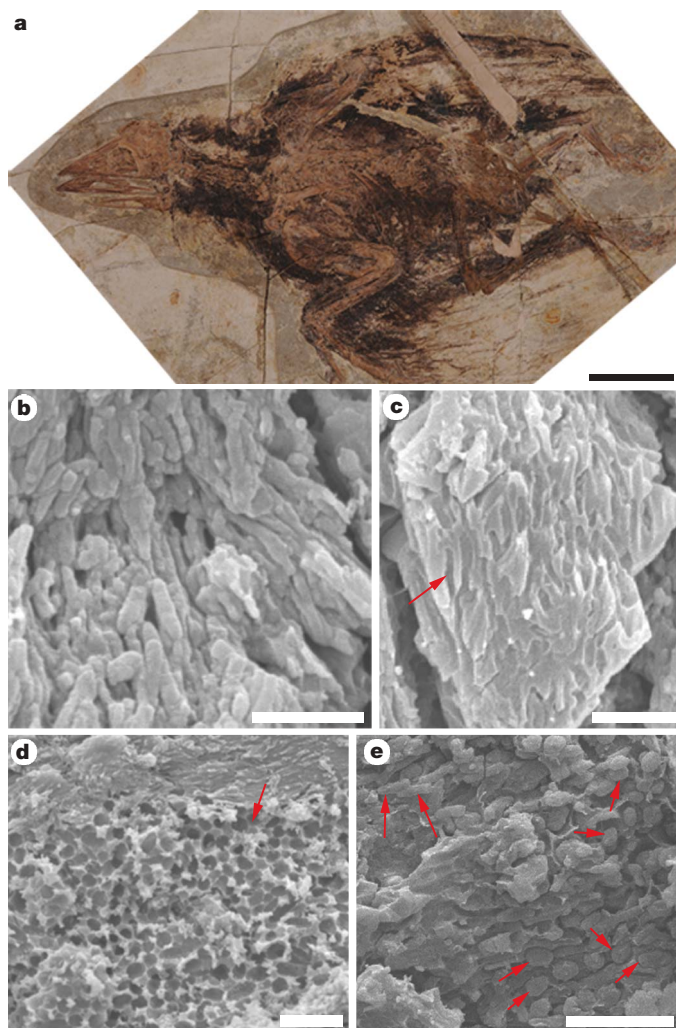


Figure 2 | Melanosomes in feathers of the bird *Confuciusornis* (IVPP V13171). **a**, Optical photograph. **b**, Strongly aligned, closely spaced, eumelanosomes preserved as solid bodies. **c**, Mouldic (that is, preserved as moulds) eumelanosomes (at arrow) a short distance above a layer in which the eumelanosomes are preserved as aligned solid bodies. **d**, Area (at arrow) comprising more widely spaced mouldic phaeomelanosomes surrounded by less distinct, aligned eumelanosomes (top of image). **e**, Gradational boundary between areas dominated by eumelanosomes (longer arrows) and phaeomelanosomes (shorter arrows), both preserved as solid bodies. Scale bars: **a**, 50 mm; **b–e**, 2 μ m.

interpreted either as a film of keratinophilic bacteria that coated the surface of the feather during early diagenesis²², or, more recently, as melanosomes^{23,24}. Both melanosomes and bacteria are generally similar in size (one micrometre or less) and shape (spherical, oblate or elongate), so it is essential to distinguish the two.

One objection to our interpretation could be that melanosomes are unlikely to survive the fossilization process. However, as argued elsewhere^{23,24} there is extensive evidence that melanosomes are highly resistant to chemical and physical degradation and have higher resistance to decay than the keratin substrate of feathers and hairs in a variety of physical environments (see also Supplementary Information).

There are three pieces of evidence that confirm that the microstructures in the Jehol fossils are melanosomes, not replacement bacteria. First, the bodies occur embedded inside the feathers, and in those feather parts that exhibit melanosomes in modern birds^{21,25}. In extant birds, melanosomes in the feather barbules are arranged in complex arrays²⁵. The typical configuration is one or more layers of regularly oriented melanosomes suspended in a β -keratin matrix below a superficial layer of β -keratin; melanosomes can also occur,

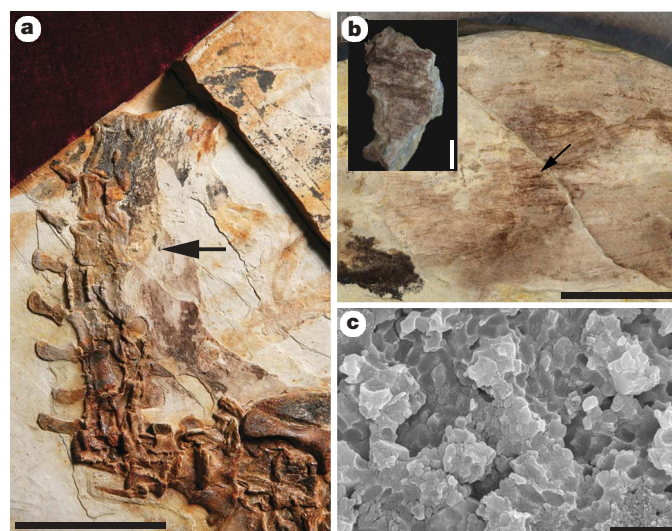


Figure 3 | Melanosomes in the integumentary filaments of the dinosaur *Sinosauropteryx* (IVPP V14202). **a**, Optical photograph of the proximal part of the tail. Arrow indicates position of sample removed previously. **b**, Optical photograph of sample of integumentary filaments; position of SEM sample (inset) indicated by arrow. **c**, Mouldic phaeomelanosomes within a filament. Scale bars: **a**, 50 mm; **b**, main panel, 20 mm, and inset, 1 mm; **c**, 2 μ m.

usually arranged less regularly, medial to such layers²⁵. Preservation (presumably as primarily an organic remain) of the degraded keratinous matrix occurs locally in some of the Jehol feathers, most obviously where the fossil bodies are exposed as moulds (Fig. 2c, d); the fossil bodies are, like melanosomes, clearly embedded within this matrix (Fig. 2e), and are not a superficial coating. The integumentary filaments also exhibit this feature (Figs 3c, 4b–d). Second, it has been shown²³ that eumelanosomes occur only in dark bands of banded feathers, and not in light bands: a fossilized biofilm of keratinophilic bacteria would be likely to occur throughout a uniformly preserved structure, and not stop suddenly along an apparent feather stripe. Notably, those parts of a feather that lack melanosomes, the calamus and proximal part of the rachis, are repeatedly absent in Jehol materials (for example, Fig. 1a) unless preserved in calcium phosphate². There is no reason to suppose that a film of keratinophilic bacteria would have developed elsewhere over the surface of the feather, but not on these parts, nor could their absence imply that these portions were buried in the skin and so escaped bacterial replacement because most of the rachis would have been exposed. The third line of evidence for fossil melanosomes comes from ref. 24, which showed packing and layering of melanosomes in fossil feathers, identical to ultrastructures seen in modern feathers and in the Jehol feathers, but incompatible with a bacterial origin.

The chemistry of the fossils² confirms that the melanosomes are not diagenetic minerals, especially not inorganic pyrite framboids. The phaeomelanosomes superficially resemble framboidal pyrite in shape, but are more than an order of magnitude smaller. Further, the fossils are primarily preserved as carbon, that is, they are organically preserved, consistent with their being melanosomes²¹. Framboids and microcrysts of pyrite occur associated with Jehol fossils, but the pyrite microcrystals are typically well faceted, not well-rounded, and their diameters range from about 1 to 5 μ m. Energy-dispersive X-ray (EDX) microanalyses confirm that the composition of the pyrite (now iron oxides) is different from that of the fossil bodies.

The two distinct morphologies of fossil body are interpreted as eumelanosomes and phaeomelanosomes based on their having 'rod-like' and 'globular' geometries, respectively, in the feathers of modern birds²¹ (see also Supplementary Information). The fossilized eumelanosomes are elongate (~ 0.8 –1 μ m long, and 200–400 nm wide)

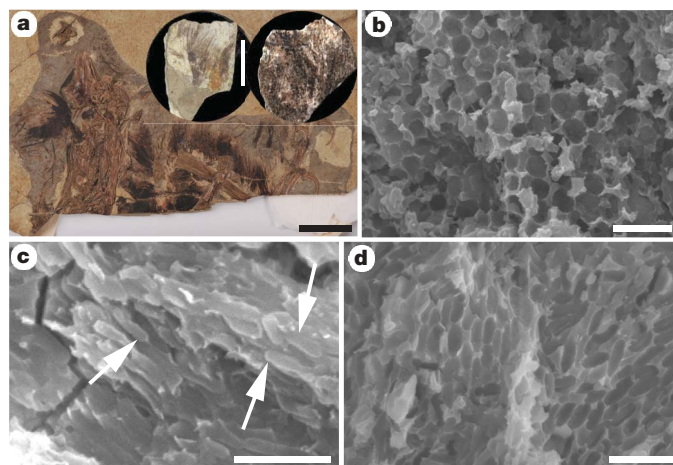


Figure 4 | Melanosomes in the integumentary filaments of the dinosaur *Sinornithosaurus* (IVPP V12811). **a**, Optical photographs of part of the holotype and SEM samples (insets). **b**, Mouldic phaeomelanosomes. **c**, Aligned eumelanosomes preserved as solid bodies (at arrows). **d**, Strongly aligned mouldic eumelanosomes. Scale bars: **a**, main panel, 50 mm and inset, 5 mm; **b–d**, 2 µm.

with rounded termini. The phaeomelanosomes are ovoid to sub-spherical and vary more in size; most are between 500 and 700 nm long (occasionally up to 900 nm) and 300 and 600 nm wide. The variation in size falls well within that of melanosomes in modern birds, even within a single feather (Supplementary Fig. 1f–i). Eumelanosomes often occur closely packed, strongly aligned and forming a discrete layer (Fig. 2b, d), as in other fossil birds^{23,24}, and the arrays of melanosomes in extant birds²⁵. This fabric is most obvious when the remainder of the feather has decayed completely. In isolated feathers, the eumelanosomes occur in well-defined areas (each ~20 µm long and 6–8 µm wide) that are separated by narrow (~2 µm wide), anastomosing, ridges of degraded feather (Fig. 1b, c). The eumelanosomes are strongly aligned, parallel to the long axis of each area (Fig. 1c). Phaeomelanosomes only may be present, as in *Sinosauropteryx* (Fig. 3c), or occur as areas surrounded by eumelanosomes, as in *Confuciusornis* (Fig. 2d); in the latter case the boundary between the two types of melanosome can be sharp (Fig. 2d) or more gradational (Fig. 2e).

The Jehol melanosomes are in life position, exposed on the plane of splitting as both solid bodies and moulds. Solid bodies can occur embedded inside, and moulds are always defined by, the variably degraded, organically preserved, feather matrix, never the host sediment. Areas where the degraded, originally keratinous, matrix has decayed completely are characterized by a fabric of densely packed, strongly aligned, eumelanosomes preserved as solid bodies; the regularity shows that this fabric could not have originated post-mortem.

Our results demonstrate conclusively that the integumentary filaments of non-avian theropod dinosaurs are epidermal structures. In birds, melanin is synthesized endogenously in specialized pigment-producing cells, melanocytes, that occur primarily in the dermis²¹; the melanocytes migrate into the dermal pulp of the developing feather germ, where the melanin is packaged into melanosomes and then those melanosomes are transferred to keratinocytes for deposition into developing feathers²⁶. In various avian species melanin granules also form, and are apparently retained, in dermal melanocytes²⁷; melanin granules can form a discrete layer in the dermis, but below, and not as part of, the collagen layer²⁸. The occurrence of melanosomes embedded inside the filaments of Jehol non-avian dinosaurs thus confirms that these structures are unequivocally epidermal structures, not the degraded remains of dermal collagen fibres, as has been argued recently^{13–16}. Our work confirms that these filaments are probably the evolutionary precursors of true feathers^{18–20}, and it will be interesting to determine whether any fossil

filaments might relate to other kinds of epidermal outgrowths in modern birds²⁹.

The occurrence of melanosomes in fossil birds^{23,24} and non-avian dinosaurs allows the first opportunity to reconstruct certain aspects of the external coloration of these organisms. The colours, and their hues and shades, of modern bird feathers derive from a variety of pigments, including melanin, as well as the microstructural arrangement of the tissues^{28,30}. Our identification of both eumelanosomes and phaeomelanosomes implies that some basal birds and non-avian theropods had black and russet coloration. In *Sinornithosaurus* the filaments are locally dominated either by eumelanosomes or phaeomelanosomes, indicating significantly different colour tones. In *Confuciusornis*, variation in colour within a single feather is indicated by changes in the relative abundance of phaeomelanosomes and eumelanosomes over short distances (Fig. 2e). Only phaeomelanosomes have been identified so far in filaments from the tail of *Sinosauropteryx*, and this suggests that the dark-coloured stripes along the tail in the fossil, and possibly also the filamentous crest along the back, exhibited chestnut to rufous (reddish-brown) tones. As the melanosomes are preserved in life position in the Jehol fossils, detailed study of differences in their spatial distribution, including orientation and density, and the relative abundance of each type, will reveal greater detail regarding both colour and colour patterning. Reconstruction of colour patterns will also inform debates on the functions of feathers in non-avian dinosaurs, whether primarily for thermoregulation, camouflage or communication.

METHODS SUMMARY

All materials used in this study are in the collections of the Institute of Vertebrate Paleontology and Paleoanthropology, Chinese Academy of Sciences, Beijing, China (IVPP). As well as material illustrated herein (Figs 1–4), samples from *Beipiaosaurus*, *Pedopenna* and *Yixianosaurus* also show fossilized melanosomes. **Isolated feather.** IVPP V15388B (Fig. 1); Ningcheng County, Inner Mongolia, China.

Confuciusornis. IVPP V13171 (Fig. 2); Sihetun, Beipiao City, Liaoning Province, China. About 300 samples, primarily from the periphery of the specimen, were removed during preparation with needles. Sizes range from 3 to 300 mm².

The relative rarity in the Jehol biota of examples of the non-avian theropod dinosaurs precluded extensive destructive sampling of existing specimens; for each taxon, samples were removed from the surface of unlacquered specimens that had been prepared previously.

Sinosauropteryx. IVPP V14202 (Fig. 3); Dawangzhangzhi, Lingyuan City, Liaoning Province, China. This is a new, as yet undescribed, specimen. A large flake was removed from the dorsal side close to the base of the tail (Fig. 3a). The integumentary filaments were better preserved on the reverse side of this flake; small samples of these were picked off with a scalpel (Fig. 3b).

Sinornithosaurus. IVPP V12811 (Fig. 4); Sihetun, Beipiao City, Liaoning Province, China. The holotype is accessioned with several other small pieces, the remains of the counterpart. Samples were taken from the surface of those pieces that correspond to parts of the area shown in Fig. 4a.

SEM. Samples were mounted on pin stubs using double-sided carbon tape and examined using a Hitachi S-3500N variable pressure SEM equipped with an EDAX Genesis energy dispersive spectrometer, at the University of Bristol. Initial screening was performed on uncoated specimens, and composition was determined via energy-dispersive X-ray microanalysis (EDX). All images herein are of specimens that were gold-coated subsequently.

Received 21 September; accepted 10 December 2009.

Published online 27 January 2010.

1. Zhou, Z.-H., Barrett, P. M. & Hilton, J. An exceptionally preserved Lower Cretaceous ecosystem. *Nature* **421**, 807–814 (2003).
2. Benton, M. J., Zhou, Z.-H., Orr, P. J., Zhang, F.-C. & Kearns, S. L. The remarkable fossils from the Early Cretaceous Jehol Biota of China and how they have changed our knowledge of Mesozoic life. *Proc. Geol. Assoc.* **119**, 209–228 (2008).
3. Zhang, F.-C. & Zhou, Z.-H. A primitive enantiornithine bird and the origin of feathers. *Science* **290**, 1955–1959 (2000).
4. Zhang, F.-C. & Zhou, Z.-H. Leg feathers in an Early Cretaceous bird. *Nature* **431**, 925 (2004).
5. Zhang, F.-C., Zhou, Z.-H. & Benton, M. J. A primitive confuciusornithid bird from China and its implications for early avian flight. *Sci. China D* **51**, 625–639 (2008).
6. Chen, P.-J., Dong, Z.-M. & Zhen, S.-N. An exceptionally well-preserved theropod dinosaur from the Yixian Formation of China. *Nature* **391**, 147–152 (1998).

7. Ji, Q., Currie, P. J., Norell, M. A. & Ji, S.-A. Two feathered dinosaurs from northeastern China. *Nature* **393**, 753–761 (1998).
8. Xu, X., Wang, X.-L. & Wu, X.-C. A dromaeosaurid dinosaur with filamentous integument from the Yixian Formation of China. *Nature* **401**, 262–266 (1999).
9. Xu, X. *et al.* Four-winged dinosaurs from China. *Nature* **421**, 335–340 (2003).
10. Xu, X. & Wang, X. A. A new maniraptoran from the Early Cretaceous Yixian Formation of western Liaoning. *Vertebr. Palasiat.* **41**, 195–202 (2003).
11. Xu, X. & Zhang, F.-C. A new maniraptoran dinosaur from China with long feathers on the metatarsus. *Naturwissenschaften* **92**, 173–177 (2005).
12. Xu, X., Zheng, X. & You, H. A new feather type in a nonavian theropod and the early evolution of feathers. *Proc. Natl Acad. Sci. USA* **106**, 832–834 (2009).
13. Lingham-Soliar, T. Evolution of birds: ichthyosaur integumental fibers conform to dromaeosaur protofeathers. *Naturwissenschaften* **90**, 428–432 (2003).
14. Lingham-Soliar, T. The dinosaurian origin of feathers: perspectives from dolphin (Cetacea) collagen fibres. *Naturwissenschaften* **90**, 563–567 (2003).
15. Feduccia, A., Lingham-Soliar, T. & Hinchliffe, J. R. Do feathered dinosaurs exist? Testing the hypothesis on neontological and paleontological evidence. *J. Morphol.* **266**, 125–166 (2005).
16. Lingham-Soliar, T., Feduccia, A. & Wang, X. A new Chinese specimen indicates that 'protofeathers' in the Early Cretaceous theropod dinosaur *Sinosauropteryx* are degraded collagen fibres. *Proc. R. Soc. Lond. B* **274**, 1823–1829 (2007).
17. Zheng, X.-T., You, H.-L., Xu, X. & Dong, Z.-M. An Early Cretaceous heterodontosaurid dinosaur with filamentous integumentary structures. *Nature* **458**, 333–336 (2009).
18. Zhang, F.-C., Zhou, Z.-H. & Dyke, G. J. Feathers and 'feather-like' integumentary structures in Liaoning birds and dinosaurs. *Geol. J.* **41**, 395–404 (2006).
19. Prum, R. O. & Brush, A. H. The evolutionary origin and diversification of feathers. *Q. Rev. Biol.* **77**, 261–295 (2002).
20. Prum, R. O. Evolution of the morphological innovations of feathers. *J. Exp. Zool. B* **304**, 570–579 (2005).
21. McGraw, K. J. in *Bird Coloration. 1. Mechanisms and Measurements* (eds Hill, G. E. & McGraw, K. J.) 243–294 (Harvard Univ. Press, 2006).
22. Wuttke, M. "Weichteil-Erhaltung" durch lithifizierte Mikroorganismen bei mittel-eozänen Vetebraten aus den Ölschiefern der "Grube Messel" bei Darmstadt. *Senck. Leth.* **64**, 509–527 (1983).
23. Vinther, J., Briggs, D. E. G., Prum, R. O. & Saranathan, V. The colour of fossil feathers. *Biol. Lett.* **4**, 522–525 (2008).
24. Vinther, J., Briggs, D. E. G., Clarke, J., Mayr, G. & Prum, R. O. Structural coloration in a fossil feather. *Biol. Lett.* doi:10.1098/rsbl.2009.0524 (published online 26 August 2009).
25. Durrer, H. in *Biology of the Integument 2, Vertebrates* (eds Bereiter-Hahn, J., Matolsky, A. G. & Richards, K. S.) 239–247 (Springer, 1986).
26. Prum, R. O. & Williamson, S. Reaction-diffusion models of within-feather pigmentation patterning. *Proc. R. Soc. Lond. B* **269**, 781–792 (2002).
27. Ortolani-Machado, C. F., Freitas, P. F. & Faraco, C. D. Melanogenesis in dermal melanocytes of Japanese Silky chicken embryos. *Tissue Cell* **41**, 239–248 (2009).
28. Prum, R. & Torres, R. Structural coloration of avian skin: convergent evolution of coherently scattering dermal collagen arrays. *J. Exp. Biol.* **206**, 2409–2429 (2003).
29. Sawyer, R. H., Washington, L. D., Salvatore, B. A., Glenn, T. C. & Knapp, L. W. Origin of archosaurian integumentary appendages: the bristles of the wild turkey beard express feather-type β keratins. *J. Exp. Zool. B* **297**, 27–34 (2003).
30. Prum, R. O. in *Bird Coloration Vol. 1* (eds Hill, G. E. & McGraw, K. J.) 295–353 (Harvard Univ. Press, 2006).

Supplementary Information is linked to the online version of the paper at www.nature.com/nature.

Acknowledgements We thank M. McNamara (University College Dublin), R. Prum (Yale University) and J. Simon (Duke University) for comments, and L. Leonard and N. Monaghan (National Museum of Ireland) for materials. This work was supported by the NERC, the Major Basic Research Projects of MST of China, and the National Natural Science Foundation of China.

Author Contributions F.Z., S.L.K., P.J.O., M.J.B., Z.Z. and D.J. designed the research, performed the research, analysed data and wrote the paper. X.W. and X.X. provided field assistance, discussion and materials for analysis.

Author Information Reprints and permissions information is available at www.nature.com/reprints. The authors declare no competing financial interests. Correspondence and requests for materials should be addressed to M.J.B. (mike.benton@bristol.ac.uk) and Z.Z. (zhonghe@yeah.net).

Arthropod relationships revealed by phylogenomic analysis of nuclear protein-coding sequences

Jerome C. Regier¹, Jeffrey W. Shultz^{1,2,3}, Andreas Zwick¹, April Hussey¹, Bernard Ball⁴, Regina Wetzer⁵, Joel W. Martin⁵ & Clifford W. Cunningham⁴

The remarkable antiquity, diversity and ecological significance of arthropods have inspired numerous attempts to resolve their deep phylogenetic history, but the results of two decades of intensive molecular phylogenetics have been mixed^{1–7}. The discovery that terrestrial insects (Hexapoda) are more closely related to aquatic Crustacea than to the terrestrial centipedes and millipedes^{2,8} (Myriapoda) was an early, if exceptional, success. More typically, analyses based on limited samples of taxa and genes have generated results that are inconsistent, weakly supported and highly sensitive to analytical conditions^{7,9,10}. Here we present strongly supported results from likelihood, Bayesian and parsimony analyses of over 41 kilobases of aligned DNA sequence from 62 single-copy nuclear protein-coding genes from 75 arthropod species. These species represent every major arthropod lineage, plus five species of tardigrades and onychophorans as outgroups. Our results strongly support Pancrustacea (Hexapoda plus Crustacea) but also strongly favour the traditional morphology-based Mandibulata¹¹ (Myriapoda plus Pancrustacea) over the molecule-based Paradoxopoda (Myriapoda plus Chelicerata)^{2,5,12}. In addition to Hexapoda, Pancrustacea includes three major extant lineages of ‘crustaceans’, each spanning a significant range of morphological disparity. These are Oligostraca (ostracods, mystacocarids, branchiurans and pentastomids), Vericrustacea (malacostracans, thecostracans, copepods and branchiopods) and Xenocarida (cephalocarids and remipedes). Finally, within Pancrustacea we identify Xenocarida as the long-sought sister group to the Hexapoda, a result confirming that ‘crustaceans’ are not monophyletic. These results provide a statistically well-supported phylogenetic framework for the largest animal phylum and represent a step towards ending the often-heated, century-long debate on arthropod relationships.

The molecular phylogeny of Arthropoda has proven difficult to resolve. In an attempt to overcome this, we increased both taxon and gene sampling relative to earlier studies. Our broad taxon sample includes the basal lineages of Hexapoda, every class of traditional ‘Crustacea’, every class in Myriapoda, every order in Arachnida and multiple representatives from Xiphosura, Pycnogonida and the outgroups Onychophora and Tardigrada.

Until recently, arthropod molecular phylogenetics relied mainly upon nuclear ribosomal DNA and mitochondrial sequences. Our data come from the complementary DNA of single-copy nuclear protein-coding genes, which represent the largest source of data for phylogenetics. Three phylogenomic studies of single-copy nuclear genes in the past year included 9 (ref. 13), 32 (ref. 14) and 6 (ref. 15) arthropod taxa, respectively (165 kilobases (kb), 319 kb and 432 kb of DNA sequences, not including missing data). The present study of 75 arthropods brings to bear 2.6 megabases of aligned arthropod DNA from 62 single-copy

protein-coding genes (not including 18% missing data). This data set builds on a previous study that sequenced the same gene regions for 12 arthropods and one tardigrade outgroup (446 kb)¹⁶. With the exception of three nodes, that study showed unconvincing bootstrap support, which improved only modestly when we added 44 arthropods previously sequenced for only three genes (an additional 227 kb)¹⁶. The present study enlarges our earlier data set nearly fourfold, greatly improving support throughout the entire phylogeny.

Sequences for each of the 62 genes from 80 taxa were obtained using PCR primers designed to amplify genes determined a priori to be single-copy orthologues in *Drosophila melanogaster* when compared with *Caenorhabditis elegans* and *Homo sapiens*¹⁶. Alignment of these orthologues was based on translated amino-acid sequences, which are highly conserved. For example, the most divergent pair of protein sequences in the entire data set is still identical at 73% of their amino-acid sites. Uncertainty about homology at sites bracketing small insertion–deletion (indel) regions resulted in exclusion of approximately 6.5% of all sites¹⁶.

The phylogeny shown in Figs 1 and 2 has largely robust bootstrap support from four methods of analysis that are well suited to inferring deep-level phylogenies (Fig. 1). Additional likelihood, Bayesian and parsimony analyses shown in Supplementary Figs 1–6 also support all major conclusions described here. With the major exception of ordinal relationships within Arachnida, bootstrap values above 80% and posterior probabilities of 1.0 pertain in Fig. 1 and Supplementary Figs 3–5. With few exceptions, we also recovered clades widely accepted by morphologists, which is an informal criterion that supports our conclusions based on bootstrap analyses. Furthermore, there was little evidence of strong conflict among 68 gene regions from 62 nuclear protein-coding genes. Single-gene analyses showed that 95% of all relationships with >70% bootstrap support agreed with the phylogeny from the concatenated genes shown in Fig. 1 (Supplementary Table 3). This paucity of strong conflict is consistent with the orthology of these sequences. Of the six newly named groups shown in bold in Fig. 1, only two had more than 70% bootstrap support in single-gene analyses (one gene each; Supplementary Table 3). This suggests that the strong support in Fig. 1 is the result of the cumulative phylogenetic signal across numerous gene regions. Bootstrap values derived for amino acids were sometimes lower than those derived from nucleotides. This result is due, at least in part, to the failure of amino-acid models to distinguish between serine residues encoded by TCN and AGY codons (A.Z. and J.C.R., manuscript in preparation), and is consistent with recent work questioning the performance of widely implemented amino-acid models in comparison with nucleotide and codon models^{17,18}.

At the deepest level, our phylogeny strongly supports Mandibulata¹¹ (Pancrustacea plus Myriapoda), a controversial result that

¹Center for Biosystems Research, University of Maryland Biotechnology Institute, ²Department of Entomology, ³Institute for Bioscience and Biotechnology Research, University of Maryland, College Park, Maryland 20742, USA. ⁴Department of Biology, Duke University, Durham, North Carolina 27708, USA. ⁵Natural History Museum of Los Angeles County, Los Angeles, California 90007, USA.

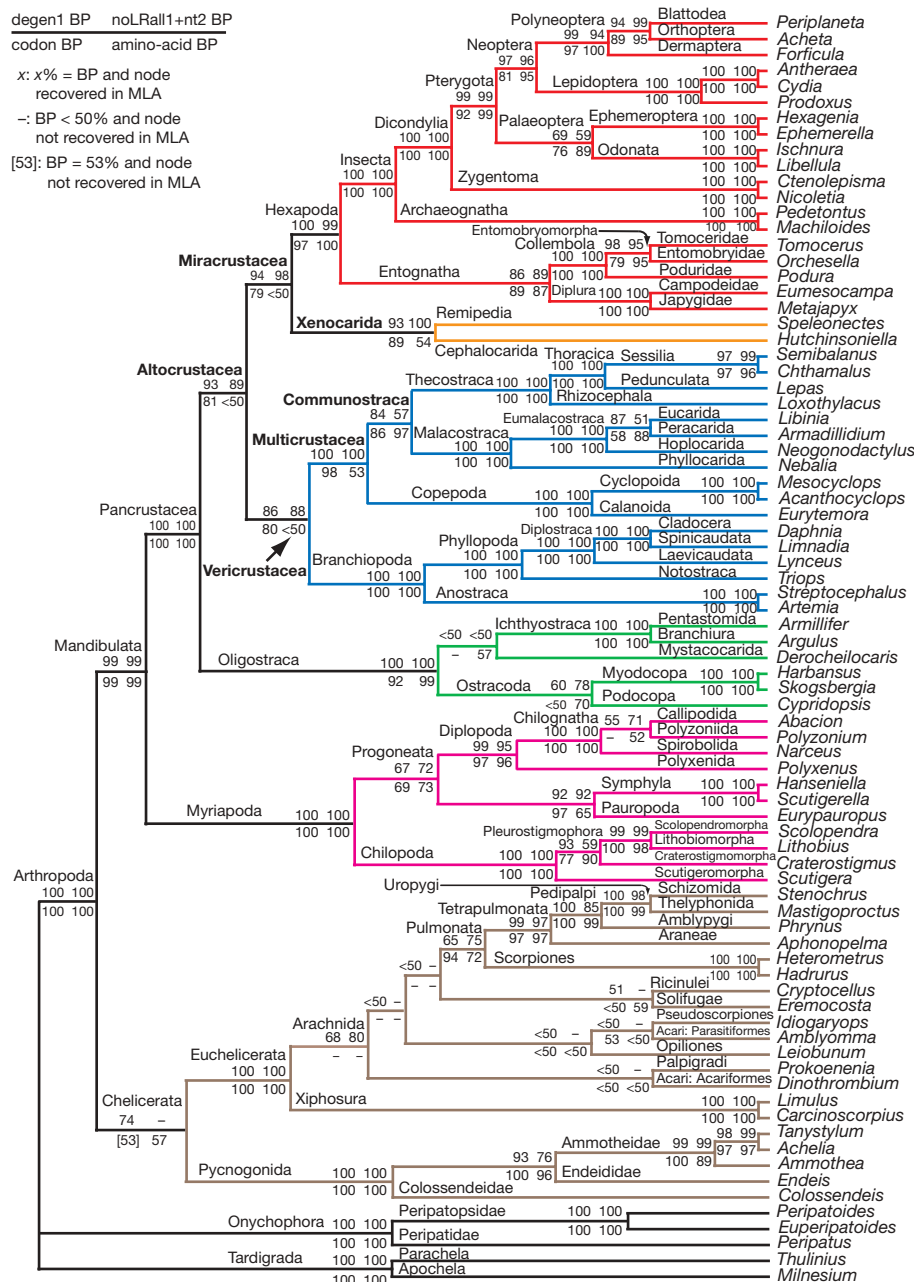


Figure 1 | Phylogenetic relationships of 75 arthropod and five outgroup species. Aligned sequences for 62 nuclear protein-coding genes were analysed under the likelihood criterion²⁹ using four strategies. Each strategy is designed to minimize deleterious effects of rapid sequence evolution and heterogeneous base composition: degen1, which fully degenerates all codons encoding the same amino acid; noLRall1 + nt2, which excludes all third-codon positions and those first-codon positions encoding one or more

leucine or arginine codons¹⁶; codon model, by which in-frame triplets of nucleotides are analysed directly under a model of codon change³⁰; and amino acid. The degen1 maximum-likelihood topology is shown. Each group of four numbers shows the respective bootstrap percentages calculated using (clockwise from top left) degen1, noLRall1 + nt2, amino acid and codon model (see figure key). MLA, maximum-likelihood analysis.

is robust to expanded outgroup sampling. Specifically, the addition of five more outgroup taxa (two nematodes, one priapulid, one mollusc and *H. sapiens*) to an amino-acid analysis had virtually no effect on the support for Mandibulata (reducing bootstrap support from 99% to 93%) and very little effect elsewhere in the phylogeny (Supplementary Fig. 7). Our strong support for Mandibulata contradicts several molecular studies that have placed Myriapoda as sister group to the Chelicerata (Euchelicerata plus Pycnogonida), a grouping so contrary to morphology that it was recently dubbed Paradoxopoda^{2,5,12}. Broadly speaking, Paradoxopoda has received its strongest support from nuclear ribosomal genes^{2,6,12} and mitochondrial genome sequences^{5,19}. Recent phylogenomic studies have disagreed on support for¹⁶ and against^{13,15} the Mandibulata. Given

our broad taxon and gene sampling, and stability with regard to outgroup choice, we now consider this issue to be resolved in favour of Mandibulata.

Although our phylogeny resolves many problems within Mandibulata, it does not resolve the status of Chelicerata, the group including Pycnogonida (sea spiders) and Euchelicerata (horseshoe crabs, scorpions and spiders). Of the four methods described in Fig. 1, only degen1 recovered Chelicerata with modest support (bootstrap percentage, BP = 74%), whereas amino acid (BP = 57%), noLRall1 + nt2 (BP = 49%) and codon model (BP = 53%) only marginally favoured Chelicerata over the alternative of a more basal placement of Pycnogonida (BP = 41%, 48% and 43%, respectively). Monophyly of Euchelicerata (Xiphosura plus Arachnida) is strongly recovered, as

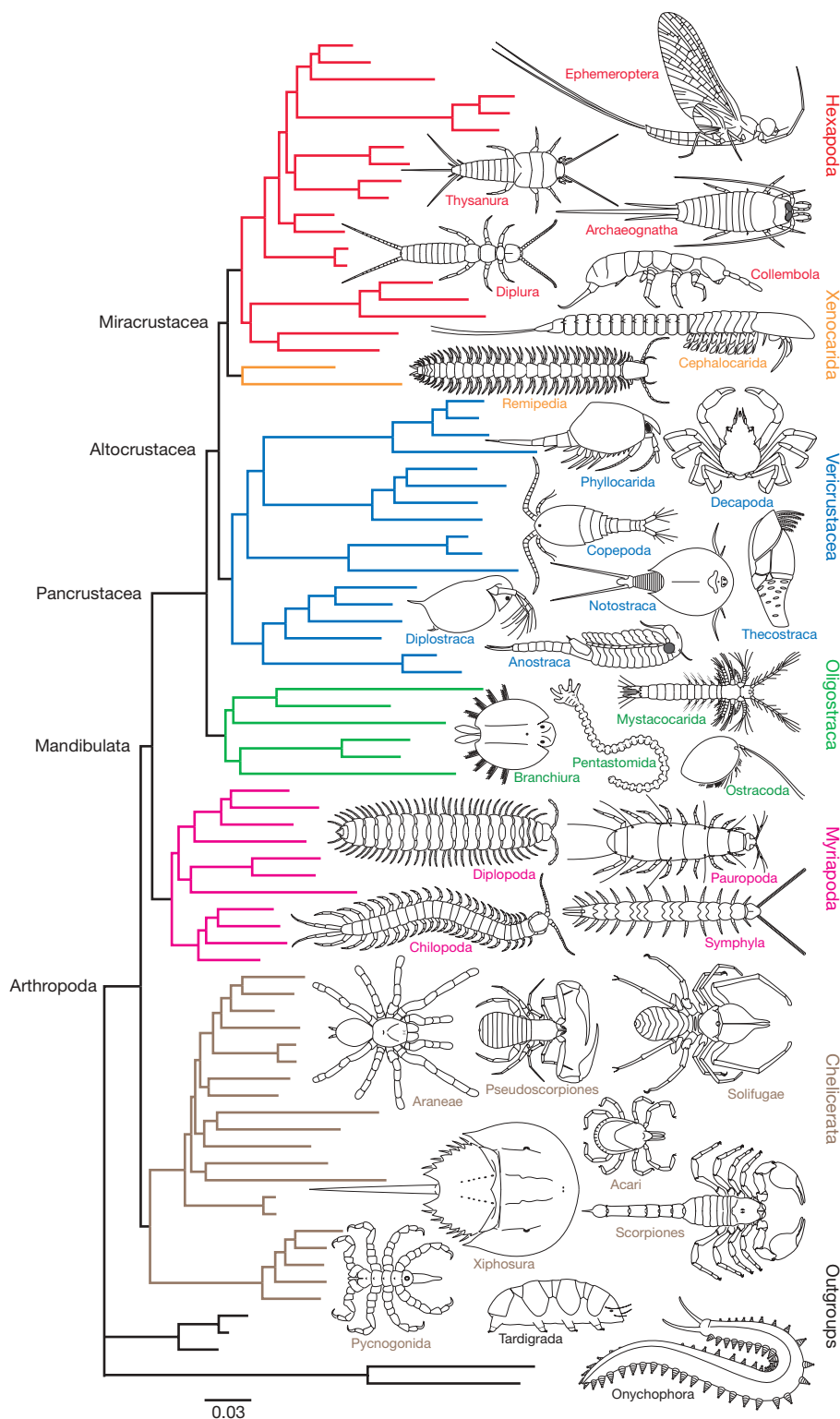


Figure 2 | Phylogram of relationships for 75 arthropod and five outgroup species. Based on likelihood analyses of 62 nuclear protein-coding genes. Branch lengths are proportional to the amount of inferred sequence change, with the topology and analytical conditions identical to the degen1 analysis

in Fig. 1. Line drawings of representatives of the major taxonomic groups show the morphological disparity across Arthropoda. Scale bar, nucleotide changes per site.

is that of Arachnida. Among arachnids, our results strongly support the relationships among tetrapulmonate orders recovered in recent morphology-based studies²⁰, although our additional, strong placement of scorpions as the sister group to tetrapulmonates does not. Otherwise, there is a notable lack of robust resolution within Arachnida owing to a lack of phylogenetic information rather than intergene conflict (Supplementary Table 3).

Our phylogeny resolves the internal structure of Pancrustacea. Until now, it was unknown whether hexapods were the sister group to a monophyletic Crustacea or to some subset of crustaceans. Our phylogeny identifies Xenocarida ('strange shrimp') as the sister group to Hexapoda, thereby confirming the paraphyly of the Crustacea. Xenocarida includes two unusual and morphologically dissimilar classes of crustacean, Remipedia and Cephalocarida. We

place the xenocarids and hexapods in the newly named clade Miracrustacea ('surprising crustaceans'). Both Xenocarida and Miracrustacea are found in the maximum-likelihood trees for all four methods of analysis, although support varies. Bootstrap support for both Xenocarida and Miracrustacea is strong for noLRall1 + nt2 and degen1 analyses (93–100%), moderately strong for codon analysis (79–89%) and weak for amino-acid analysis (17–54%).

The two classes of Xenocarida were discovered in the second half of the twentieth century, and for several decades each was viewed as the morphological model of the ancestral 'urcrustacean'²¹. Apart from the absence of eyes and the possible compensatory enhancement of olfactory nerve centres^{22–24}, Remipedia and Cephalocarida share few obvious synapomorphies. On the other hand, neurobiological studies have rejected the hypothesis that xenocarid brains are 'primitive'^{22,23}, and have proposed either Malacostraca or—as in our study—Hexapoda as possible relatives. Remipedes are relatively large predators with a long series of biramous swimming legs and are the only extant pancrustaceans that lack significant postcephalic tagmosis (Fig. 2). Cephalocarids are tiny particle feeders with large cephalic shields, distinct pereons (thoraxes) with foliaceous swimming legs, and long, legless pleons (abdomens). Despite these differences, a close relationship between remipedes and cephalocarids has been suggested before^{4,21}; Fig. 1 provides robust likelihood bootstrap support for this proposal.

Our results strongly support the monophyly of Hexapoda, in contrast to mitochondrial studies that place Collembola (springtails) among 'crustaceans' rather than other hexapods²⁵. Within Hexapoda, our results agree with long-standing, morphology-based hypotheses of the basal lineages²⁶. Specifically, we recover Entognatha (non-insectan hexapods) as the sister group to Insecta, Archaeognatha (jumping bristletails) as the sister group to all other insects and Zygentoma (silverfish, firebrats and so on) as the sister group to Pterygota (winged insects). Relationships among pterygotes recovered here are largely non-controversial, although relationships between the extant paleopterous orders Ephemeroptera (mayflies) and Odonata (dragonflies and damselflies) have been a subject of persistent debate. We recover them as a monophyletic group.

The sister group to Miracrustacea is another unanticipated group, Vericrustacea ('true crustaceans'), which joins Malacostraca (crabs, shrimp and so on), Branchiopoda (fairy shrimp, water fleas and so on) and some members of the polyphyletic 'Maxillopoda', namely Thecostraca (barnacles) and Copepoda. The Vericrustacea encompass the most familiar and diverse groups from the traditional 'crustaceans', including species of economic significance and model organisms. Within the Vericrustacea are two other groupings not anticipated by morphology: the Multicrustacea ('numerous crustaceans': Malacostraca plus Thecostraca plus Copepoda) and the Communostraca ('common shelled ones': Malacostraca plus Thecostraca).

Our results agree with a recent ribosomal study⁶ supporting both the monophyly of Oligostraca and its position as the sister group to all other pancrustaceans (the same study also identifies Communostraca). As originally proposed²⁷, Oligostraca included Ostracoda (seed shrimp) and Ichthyostraca, which encompass the highly derived, endoparasitic Pentastomida (tongue worms) and ectoparasitic Branchiura (fish lice). Significantly, our analysis adds Mystacocarida to Oligostraca. The mystacocarids are small, enigmatic crustaceans that live between sand grains along marine shores. Oligostracans are a disparate, ancient clade, and there is little in their gross morphology other than reduction in the number of body segments that would suggest a close relationship among them.

The fully terrestrial Myriapoda is the sister group to Pancrustacea. The basic internal phylogenetic structure of Myriapoda recovered here is consistent with that favoured by morphology, including monophyly of its constituent classes, namely Diplopoda (millipedes), Symphyla and Chilopoda (centipedes), and Pauropoda (only one species sampled). It also recovers Progoneata (Diplopoda plus Pauropoda plus Symphyla), the members of which each have an

anteriorly placed gonopore. Our results differ from morphology-inspired hypotheses in uniting Pauropoda with Symphyla rather than with Diplopoda, a result that is also seen in recent analyses of nuclear ribosomal sequences^{6,28}.

In conclusion, our phylogenomic study provides a strongly supported phylogenetic framework for the arthropods, but the problem of reconstructing and interpreting morphological evolution within this diverse group remains. Our phylogeny highlights the large gaps in the morphological spectrum of extant arthropods that have complicated the task of morphology-based systematists. Our result has significant implications, as it requires taxonomists to acknowledge crustaceans as a paraphyletic grade of primitively aquatic mandibulates and to classify hexapods as a terrestrial clade within Pancrustacea. In particular, the position of Xenocarida (Remipedia plus Cephalocarida) as the sister group to Hexapoda, and the relatively derived placement of supposedly 'primitive' groups such as Branchiopoda, promises to alter views on the evolution of morphology and morphogenesis in Arthropoda.

METHODS SUMMARY

A flow chart of activities leading to the phylogenetic trees shown in Figs 1 and 2 can be found in Supplementary Fig. 1. Laboratory procedures are described in Methods. Supplementary Tables 1–3 respectively include a list of taxa, tests of nucleotide homogeneity and bootstrap support for taxonomic groups recovered in single-gene analyses. Supplementary Tables 4 and 5 include GenBank accession numbers. Likelihood analyses of DNA and amino acids for the 80 taxa can be found in Figs 1 and 2 and Supplementary Fig. 2. Bayesian analyses can be found in Supplementary Figs 3–5 and parsimony analysis can be found in Supplementary Fig. 6. Likelihood analysis of 85 taxa with expanded outgroup sampling can be found in Supplementary Fig. 7. Separate supplementary files include the 80-taxon nucleotide data matrix, the 80-taxon degen1 data matrix, and the 85-taxon amino-acid data matrix. Also available as supplementary files are the PERL script and instructions to produce degenerated nucleotide matrices (Degen1_v1_2.pl, Degen1_README.txt; <http://www.phylotools.com>).

Full Methods and any associated references are available in the online version of the paper at www.nature.com/nature.

Received 1 September; accepted 10 December 2009.

Published online 10 February 2010.

1. Abele, L. G., Kim, W. & Felgenhauer, B. E. Molecular evidence for inclusion of the phylum Pentastomida in the Crustacea. *Mol. Biol. Evol.* **6**, 685–691 (1989).
2. Friedrich, M. & Tautz, D. Ribosomal DNA phylogeny of the major extant arthropod classes and the evolution of myriapods. *Nature* **376**, 165–167 (1995).
3. Regier, J. C. & Shultz, J. W. Molecular phylogeny of the major arthropod groups indicates polyphyly of crustaceans and a new hypothesis for the origin of hexapods. *Mol. Biol. Evol.* **14**, 902–913 (1997).
4. Giribet, G., Edgecombe, G. D. & Wheeler, W. C. Arthropod phylogeny based on eight molecular loci and morphology. *Nature* **413**, 157–161 (2001).
5. Hwang, U. W., Friedrich, M., Tautz, D., Park, C. J. & Kim, W. Mitochondrial protein phylogeny joins myriapods with chelicerates. *Nature* **413**, 154–157 (2001).
6. Mallatt, J. & Giribet, G. Further use of nearly complete 28S and 18S rRNA genes to classify Ecdysozoa: 37 more arthropods and a kinorhynch. *Mol. Phylogenet. Evol.* **40**, 772–794 (2006).
7. Budd, G. E. & Telford, M. J. The origin and evolution of arthropods. *Nature* **457**, 812–817 (2009).
8. Boore, J. L., Lavrov, D. V. & Brown, W. M. Gene translocation links insects and crustaceans. *Nature* **392**, 667–668 (1998).
9. Phillips, M. J., Delsuc, F. & Penny, D. Genome-scale phylogeny and the detection of systematic biases. *Mol. Biol. Evol.* **21**, 1455–1458 (2004).
10. Rota-Stabelli, O. & Telford, M. J. A multi criterion approach for the selection of optimal outgroups in phylogeny: recovering some support for Mandibulata over Myriochelata using mitogenomics. *Mol. Phylogenet. Evol.* **48**, 103–111 (2008).
11. Snodgrass, R. E. *Evolution of the Annelida, Onychophora and Arthropoda* (Smithsonian Inst. Press, 1938).
12. Mallatt, J. M., Garey, J. R. & Shultz, J. W. Ecdysozoan phylogeny and Bayesian inference: first use of nearly complete 28S and 18S rRNA gene sequences to classify the arthropods and their kin. *Mol. Phylogenet. Evol.* **31**, 178–191 (2004).
13. Dunn, C. W. *et al.* Broad phylogenomic sampling improves resolution of the animal tree of life. *Nature* **452**, 745–749 (2008).
14. Timmermans, M. J. T. N., Roelofs, D., Mariën, J. & Van Straalen, N. M. Revealing pancrustacean relationships: phylogenetic analysis of ribosomal protein genes places Collembola (springtails) in a monophyletic Hexapoda and reinforces the discrepancy between mitochondrial and nuclear DNA markers. *BMC Evol. Biol.* **8**, 83 (2008).
15. Philippe, H. *et al.* Phylogenomics revives traditional views on deep animal relationships. *Curr. Biol.* **19**, 706–712 (2009).

16. Regier, J. C. *et al.* Resolving arthropod phylogeny: exploring phylogenetic signal within 41 kb of protein-coding nuclear gene sequence. *Syst. Biol.* **57**, 920–938 (2008).
17. Holder, M. T., Zwickl, D. J. & Dessimoz, C. Evaluating the robustness of phylogenetic methods to among-site variability in substitution processes. *Phil. Trans. R. Soc. B* **363**, 4013–4021 (2008).
18. Seo, T. & Kishino, H. Statistical comparison of nucleotide, amino acid, and codon substitution models for evolutionary analysis of protein-coding sequences. *Syst. Biol.* **58**, 199–210 (2009).
19. Podsiadlowski, L., Braband, A. & Mayer, G. The complete mitochondrial genome of the onychophoran *Epiperipatus biolleyi* reveals a unique transfer RNA set and provides further support for the Ecdysozoa hypothesis. *Mol. Biol. Evol.* **25**, 42–51 (2008).
20. Shultz, J. W. A phylogenetic analysis of the arachnid orders based on morphological characters. *Zool. J. Linn. Soc.* **150**, 221–265 (2007).
21. Schram, F. R. (ed.) *Crustacean Phylogeny* (Balkema, 1983).
22. Fanenbruck, M., Harzsch, S. & Wagele, J. The brain of the Remipedia (Crustacea) and an alternative hypothesis on their phylogenetic relationships. *Proc. Natl Acad. Sci. USA* **101**, 3868–3873 (2004).
23. Harzsch, S. Neurophylogeny: architecture of the nervous system and a fresh view on arthropod phylogeny. *Integr. Comp. Biol.* **46**, 162–194 (2006).
24. Boxshall, G. A. Crustacean classification: on-going controversies and unresolved problems. *Zootaxa* **1668**, 313–325 (2007).
25. Carapelli, A., Liò, P., Nardi, F., van der Wath, E. & Frati, F. Phylogenetic analysis of mitochondrial protein coding genes confirms the reciprocal paraphyly of Hexapoda and Crustacea. *BMC Evol. Biol.* **7** (suppl. 2), S8 (2007).
26. Hennig, W. *Insect Phylogeny* (Wiley, 1981).
27. Zrzavy, J., Hypsa, V. & Vlaskova, M. in *Arthropod Relationships* (eds Fortey, R. A. & Thomas, R. H.) 97–107 (Chapman and Hall, 1997).
28. Gai, Y.-H., Song, D., Sun, H. & Zhou, K. Myriapod monophyly and relationships among myriapod classes based on nearly complete 28S and 18S rDNA sequences. *Zool. Sci.* **23**, 1101–1108 (2006).
29. Zwickl, D. J. *Genetic Algorithm Approaches for the Phylogenetic Analysis of Large Biological Sequence Datasets under the Maximum Likelihood Criterion*. PhD thesis, Univ. Texas Austin (2006).
30. Goldman, N., Thorne, J. L. & Jones, D. T. Using evolutionary trees in protein secondary structure prediction and other comparative sequence analyses. *J. Mol. Biol.* **263**, 196–208 (1996).

Supplementary Information is linked to the online version of the paper at www.nature.com/nature.

Acknowledgements C.W.C. thanks W. Hartman for early insight into questions of arthropod phylogeny and D. Percy for sequencing. J.W.M. and R.W. thank N. Tait, G. Hampson and R. Hessler for help collecting samples. J.C.R. and A.Z. thank M. Cummings and A. Bazinet for making available grid computing, and the DNA Sequencing Facility at the Center for Biosystems Research, University of Maryland Biotechnology Institute. J.W.S. was supported by the Maryland Agricultural Experiment Station. C.W.C. was supported by the Whiteley Center. This work was funded by two programmes at the US National Science Foundation, namely Biocomplexity in the Environment: Genome-Enabled Environmental Science and Engineering, and Assembling the Tree of Life.

Author Contributions C.W.C., J.C.R., J.W.S., A.Z. and J.W.M. designed the project. J.W.S., J.W.M., R.W. and J.C.R. designed and carried out taxon sampling and collection. J.C.R. and C.W.C. supervised DNA sequencing and editing, with PCR templates generated by J.C.R., B.B. and others. J.C.R., A.Z., C.W.C. and J.W.S. decided on the strategy for data analysis and its implementation, with the degen1 coding method developed and implemented by J.C.R., A.H. and A.Z. J.C.R. and A.Z. assembled the Supplementary Information and submitted sequences to GenBank. J.W.S. and J.W.M. proposed the names for the new, strongly supported clades in the Pancrustacea. C.W.C. wrote the first draft of the manuscript, with major additions by J.C.R. and J.W.S. and additional contributions by J.W.M. and A.Z. All authors commented on the manuscript.

Author Information All sequences generated for this publication have been deposited in GenBank under the accession numbers given in Supplementary Tables 4 and 5. Full data matrices are available in Supplementary Information. Reprints and permissions information is available at www.nature.com/reprints. The authors declare no competing financial interests. Correspondence and requests for materials should be addressed to C.W.C. (cliff@duke.edu).

METHODS

Specimen storage. Typically, live specimens were placed in at least 15 volume equivalents of 100% ethanol and stored at -85°C . Sometimes, reaching a temperature of -85°C took several weeks, in which case temporary storage at -20°C or 0°C proved satisfactory. For smaller specimens, storage in 100% ethanol at room temperature ($\sim 22^{\circ}\text{C}$) was satisfactory, even for as long as one year.

Nucleic-acid extraction. We extracted total RNA from specimens using the SV Total RNA Isolation System (catalogue no. Z3100; Promega) with the DNase-digestion steps omitted and with intentional vortexing to fragment the genomic DNA.

PCR primers and amplification strategies. This study differs from most animal phylogenomic studies because the gene regions were screened a priori for orthology and for an intermediate rate of substitution¹⁶. Instead of screening EST libraries for genes that are most consistently expressed, our study amplified genes using reverse-transcription PCR (RT-PCR) of mRNA extractions. All PCR primers and amplification strategies have been published (see Appendix 1 of ref. 16, available at <http://systbio.org/?q=node/295>). To summarize, primers were designed from single-copy, orthologous protein-coding nuclear genes as described in ref. 16. We made pairwise alignments for 5,274 putative orthologues from *D. melanogaster* and *H. sapiens* identified using the InParanoid method³¹, and further reduced them to 595 genes with $>55\%$ sequence identity between *D. melanogaster* and *H. sapiens* (sequences from *C. elegans* were added to the alignments when suitable¹⁶). Our primers amplified messenger RNAs encoded by 62 distinct genes from most of the 80 taxa in this study (Supplementary Table 1) and many Bilateria (C.W.C., unpublished results). The primers were completely degenerate with respect to the amino-acid code. All forward and reverse primers had 18-nucleotide-long M13REV or M13(-21) sequences appended to facilitate amplification³² and automated sequencing.

Preparation of DNA fragments for automated sequencing. Laboratory methods have been described in detail (see Appendix 2 of ref. 16; <http://systbio.org/?q=node/295>). To summarize, we reverse transcribed total RNA and amplified the resulting cDNA using PCR (RT-PCR). This approach avoided problems with introns. These problems include lack of phylogenetic informativeness at the taxonomic level of this study and the difficulty of identifying the correctly sized amplicon due to variation in intron length and location. This strategy also kept our fragments within the size range for convenient sequencing. Without introns, expected amplicon lengths could be accurately inferred from orthologues of other species (for example *Drosophila* and other test taxa) and gel isolated. A problem with the RT-PCR approach is that amplification is probably limited to genes that are expressed in moderate to abundant amounts and in a relatively non-cell-specific manner, but we were still able to amplify 62 distinct genes.

Following gel isolation, the RT-PCR amplicon was typically re-amplified using one nested primer and one of primers used for RT-PCR (hemi-nested re-amplification), again followed by gel isolation. If the template concentration was insufficient for sequencing, we re-amplified the amplicon a second time using only M13REV and M13(-21) primers, and again followed this with gel isolation. Templates were sequenced using a 3730 DNA Analyser (Applied Biosystems).

Construction of data matrices. Sequencer chromatograms were edited and individual-gene, individual-taxon sequences were assembled using the PREGAP4 and GAP4 programs in the Staden package³³ (version staden_solaris-1-5-3) or SEQUENCHER (version 4.5; GeneCodes). Multi-sequence alignments were performed manually using the sequence editor Genetic Data Environment³⁴ (version 2.2) and with MAFFT³⁵ (version 6.716b). Sequences from individual gene regions were concatenated into the final nt123 nucleotide data matrix (39,261 sites with 6.5% unalignable sites removed using criteria described in ref. 16), and character sets were defined.

Phylogenetic analysis. Phylogenetic analyses were performed using PAUP* 4.0b10 (parsimony; ref. 36), GARLI0.96b8 (likelihood; ref. 29) and MRBAYES 3.2 (Bayesian; refs 37–39) with the best-fit models as determined in

MRMODELTEST 2.3 (ref. 40). The nt123 data matrix was analysed under a codon model (13,087 sites). The codon model incorporated four discrete dN/dS categories, where dN/dS refers to the ratio of nonsynonymous to synonymous change, and a GTR-gamma model to describe underlying nucleotide change. From the nt123 matrix, three other matrices were derived and analysed, as follows. In the matrix used for degen1 analyses (39,261 sites), codons for each amino acid were fully degenerated for the first and third codon positions using ambiguity coding, an extension of RY coding⁹. The resulting partially polymorphic nucleotide data matrix was analysed under the best-fit GTR-gamma-invariant model. In the matrix used for noLall1+nt2 analyses (21,823 sites), nucleotide characters were excluded at all third-codon positions and at Lall1 sites (that is, first-codon positions that encoded one or more leucine or arginine codons^{16,41}). Removing Lall1 eliminated significant heterogeneity in base composition (Supplementary Table 2). The resulting nucleotide data matrix was analysed under the best-fit GTR-gamma-invariant model. In the matrix used for amino acid analyses (13,087 sites), amino acids were first automatically generated using GARLI0.96b8 and then analysed under the best-fit model of amino-acid change (JTT-gamma-F). For each strategy, multiple search replicates were performed to find the maximum-likelihood topology, and involved 11, 600, 675 and 574 search replicates for the strategies codon model, degen1, noLall1+nt2 and amino acid, respectively. The non-parametric bootstrap analyses in Fig. 1 involved one search replicate for each of 105, 1065, 1005, and 1024 pseudoreplicates for the respective strategies. Scripts written in PERL for identifying Lall1 sites (LeuArg1_v1_2.pl) are available from files supplementary to ref. 16 (<http://systbio.org/?q=node/295>) and for the degen1 method in Supplementary Information (Methods Summary). The latest versions of both scripts will be available at <http://www.phylotools.com>.

Computational resources. To make thorough maximum-likelihood and bootstrap searches (involving, for example, hundreds of maximum-likelihood search replicates per data matrix) possible under a GTR model, we performed analyses in parallel using grid computing^{38,42}, through The Lattice Project⁴³. Additionally, a dedicated cluster of Linux servers with 40 cores at 2.5 GHz each and 80 GB RAM was set up to allow the computationally very demanding codon-model analyses. Additional analyses were carried out using the CIPRES cluster at the San Diego Supercomputing Center, and on the Duke Shared Resource Cluster.

1. Remm, M., Storm, C. E. & Sonnhammer, E. L. Automatic clustering of orthologs and in-paralogs from pairwise species comparisons. *J. Mol. Biol.* **314**, 1041–1052 (2001).
2. Regier, J. C. & Shi, D. Increased yield of PCR product from degenerate primers with nondegenerate, nonhomologous 5' tails. *Biotechniques* **38**, 34–38 (2005).
3. Staden, R., Judge, D. & Bonfield, J. Sequence assembly and finishing methods. *Methods Biochem. Anal.* **43**, 303–322 (2001).
4. Smith, S. W., Overbeck, R., Woese, C. R., Gilbert, W. & Gillevet, P. M. The genetic data environment and expandable GUI for multiple sequence analysis. *Comp. Appl. Biosci.* **10**, 671–675 (1994).
5. Katoh, K., Kuma, K., Toh, H. & Miyata, T. MAFFT version 5: improvement in accuracy of multiple sequence alignment. *Nucleic Acids Res.* **33**, 511–518 (2005).
6. PAUP*. v.4.0 (Sinauer Associates, Sunderland, Massachusetts, 2002).
7. Huelsenbeck, J. P. & Ronquist, F. MRBAYES: Bayesian inference of phylogeny. *Bioinformatics* **17**, 754–755 (2001).
8. Ronquist, F. & Huelsenbeck, J. P. MRBAYES 3: Bayesian phylogenetic inference under mixed models. *Bioinformatics* **19**, 1572–1574 (2003).
9. Altekar, G., Dwarkadas, S., Huelsenbeck, J. P. & Ronquist, F. Parallel Metropolis-coupled Markov chain Monte Carlo for Bayesian phylogenetic inference. *Bioinformatics* **20**, 407–415 (2004).
10. MRMODELTEST. v.2 (Evolutionary Biology Centre, Uppsala University, 2004).
11. Regier, J. C. & Shultz, J. W. Elongation factor-2: a useful gene for arthropod phylogenetics. *Mol. Phylogenet. Evol.* **20**, 136–148 (2001).
12. Cummings, M. & Huskamp, J. Grid computing. *EDUCAUSE Rev.* **40**, 116–117 (2005).
13. Bazinet, A. L. & Cummings, M. C. in *Distributed & Grid Computing—Science Made Transparent for Everyone. Principles, Applications and Supporting Communities* (ed. Weber, M. H. W.) 2–13 (Tectum, 2009).

LETTERS

Ancient animal microRNAs and the evolution of tissue identity

Foteini Christodoulou¹, Florian Raible^{1,2,†}, Raju Tomer¹, Oleg Simakov¹, Kalliopi Trachana², Sebastian Klaus^{1,†}, Heidi Snyman¹, Gregory J. Hannon³, Peer Bork² & Detlev Arendt¹

The spectacular escalation in complexity in early bilaterian evolution correlates with a strong increase in the number of microRNAs^{1,2}. To explore the link between the birth of ancient microRNAs and body plan evolution, we set out to determine the ancient sites of activity of conserved bilaterian microRNA families in a comparative approach. We reason that any specific localization shared between protostomes and deuterostomes (the two major superphyla of bilaterian animals) should probably reflect an ancient specificity of that microRNA in their last common ancestor. Here, we investigate the expression of conserved bilaterian microRNAs in *Platynereis dumerilii*, a protostome retaining ancestral bilaterian features^{3,4}, in *Capitella*, another marine annelid, in the sea urchin *Strongylocentrotus*, a deuterostome, and in sea anemone *Nematostella*, representing an outgroup to the bilaterians. Our comparative data indicate that the oldest known animal microRNA, miR-100, and the related miR-125 and let-7 were initially active in neurosecretory cells located around the mouth. Other sets of ancient microRNAs were first present in locomotor ciliated cells, specific brain centres, or, more broadly, one of four major organ systems: central nervous system, sensory tissue, musculature and gut. These findings reveal that microRNA evolution and the establishment of tissue identities were closely coupled in bilaterian evolution. Also, they outline a minimum set of cell types and tissues that existed in the protostome–deuterostome ancestor.

Deep sequencing of *Platynereis* small RNAs identified 34 microRNA families common to protostomes and deuterostomes (Supplementary Fig. 1, Supplementary Table 1), in accordance with recent studies². To investigate the temporal and spatial localization profile of these conserved bilaterian microRNAs, whole mount *in situ* hybridization (WMISH) was conducted using locked nucleic acids as probes. In all cases, localization of mature *Platynereis* microRNAs was spatially restricted and almost exclusively occurred in actively differentiating tissues (Supplementary Fig. 2). We also analysed tissue-specific expression of predicted targets (Supplementary Fig. 3 a, b and Supplementary Table 2) and identified a subset of tissues in which microRNAs were less frequently co-expressed with their predicted targets than expected to occur by chance, whereas other tissues showed the opposite trend (Supplementary Table 3 a, b and Supplementary Data), indicating different modes of involvement of the conserved bilaterian microRNAs in regulating the establishment and/or maintenance of tissue identity⁵.

We found the oldest conserved microRNA, miR-100, shared by cnidarians and bilaterians^{1,2}, highly specifically localized in two small groups of cells of the larval foregut (Fig. 1a, e). These cells also expressed let-7 (Fig. 1b, f) and miR-125 (Fig. 1c), which play a conserved role in developmental timing^{6–8}, and miR-375 (Fig. 1d), demarcating foregut-related, neurosecretory/endocrine cell populations of vertebrate pituitary and pancreas⁹. Marker gene analysis revealed that these cells are

differentiated secretory neurons (Supplementary Fig. 4c). As in fly^{7,8}, *Platynereis* miR-100 and let-7 are processed from a single polycistronic transcript (Supplementary Table 4) that in many bilaterians also includes miR-125 (refs 7,8). Since miR-100, miR-125 and let-7 are expressed much more broadly in fly⁸ and vertebrate¹⁰ (Supplementary Table 5), we challenged evolutionary conservation of the highly specific *Platynereis* pattern by investigating the expression of miR-100 in a cnidarian, the sea anemone *Nematostella*. miR-100 was exclusively detected in single cells located around the pharynx anlage (Fig. 1g and Supplementary Fig. 5a, b), demarcated by *brachyury*¹¹ and *foxa* expression (blue, red and yellow in Fig. 1h). Intriguingly, miR-100, *brachyury*¹² and *foxa2* also colocalize in the *Platynereis* foregut (Fig. 1i; blue, red and yellow in Fig. 1j). These findings indicate that early in animal evolution miR-100 was active in a small population of cells located around a digestive opening. This expression was inherited by let-7 and by miR-125 once they evolved in the bilaterian stem line, to expand into other tissues only later in evolution. Corroborating this, expression of miR-100, miR-125 and let-7 was similarly restricted to foregut tissue in *Capitella* (Fig. 1k, data not shown) and in the sea urchin *Strongylocentrotus* (Fig. 1l and Supplementary Fig. 5c, e).

Locomotor ciliary bands are characteristic for the swimming larvae of marine protostomes and deuterostomes¹³. In *Platynereis*, miR-29, miR-34 and miR-92 demarcated the ciliary bands from early larval stages onwards (Fig. 2a–f) and were also detected in motile ciliated cells of the apical organ and later in the medial head region (Fig. 2a–e). While expression was similar for all ‘ciliary’ microRNAs at early larval stages, partly complementary patterns were observed in the developing young worm (arrowheads in Fig. 2d, e). *Capitella* showed a similar localization of these microRNAs to ciliary bands (Fig. 2h and Supplementary Fig. 6a, b). We also investigated the sea urchin pluteus larva and indeed found miR-92 expressed in the ciliary bands (Fig. 2i) and miR-92 and miR-34 in motile ciliated cells lining the foregut and stomach (Supplementary Fig. 5g, h). The similar specific affiliation of these microRNAs to motile ciliated cells in both protostome and deuterostome larvae is best explained by evolutionary conservation.

Two sets of conserved bilaterian microRNAs showed localized expression in distinct parts of the brain. For miR-7 (ref. 4), miR-137 and miR-153 we observed very similar expression in the dorso-medial neurosecretory tissue of the *Platynereis* brain (Fig. 3a–d) comprising differentiated vasotocinergic and FMRFamide⁴ as well as serotonergic neurons (Fig. 3e). The same microRNAs showed brain-restricted expression in *Capitella* (Supplementary Fig. 6c–e) and have also been reported to show spatially localized expression in the zebrafish brain, including neurosecretory brain parts of the hypothalamus¹⁴ (Supplementary Table 5). Our comparative data thus indicate that these three microRNAs co-evolved in neurosecretory brain tissue. A

¹Developmental Biology Unit, ²Computational Biology Unit, European Molecular Biology Laboratory, D-69117 Heidelberg, Germany. ³Cold Spring Harbor Laboratory, 1 Bungtown Road, Cold Spring Harbor, New York 11724, USA. [†]Present addresses: Max F. Perutz Laboratories, Campus Vienna Biocenter, Dr. Bohr-Gasse 9/4, A-1030 Vienna, Austria (F.R.); J. W. Goethe - Universität Frankfurt Biologie-Campus, Siesmayerstrasse 70-72, D-60323 Frankfurt, Germany (S.K.).

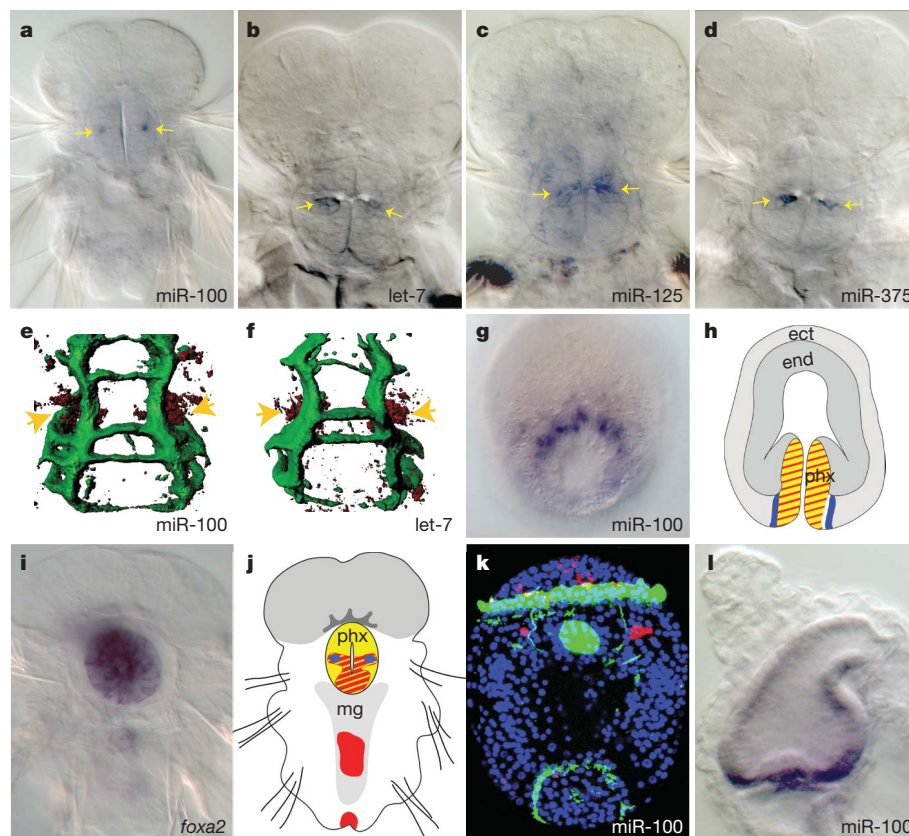
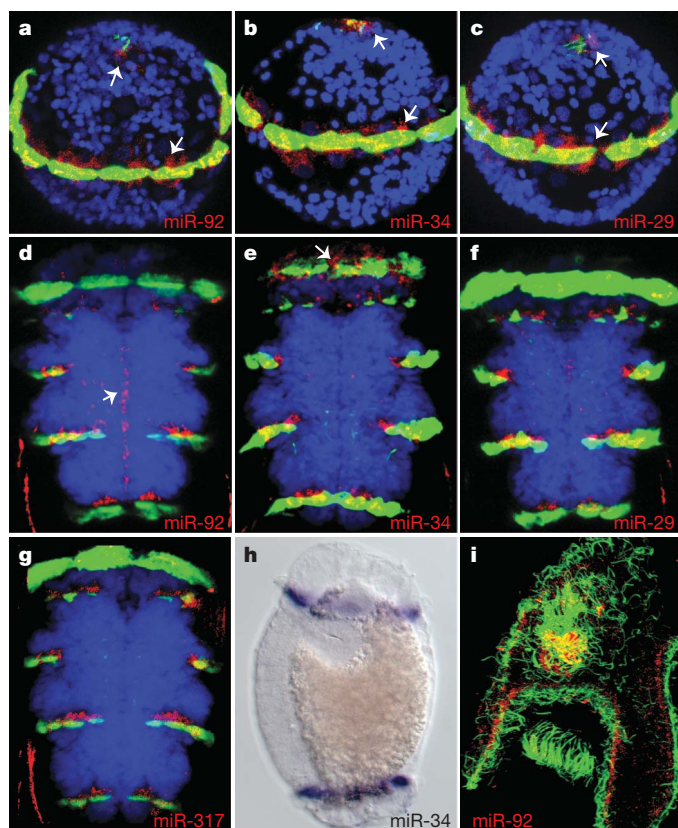


Figure 1 | Foregut-related expression of conserved microRNAs. **a**, Ventral view of 72 hours post fertilization (h.p.f.) *Platynereis*. **b–d**, dorsal view of 5 d.p.f. *Platynereis*. **e**, **f**, Three-dimensional reconstructions of 5 d.p.f. foregut (acTub green, miR-100 and let-7 red). **g**, Oral view of *Nematostella* planula. **h**, Scheme of *Nematostella* planula with pharynx showing *brachyury*¹¹ (red) *foxa*¹¹ (yellow) and miR-100 (blue) expression (phx,

pharynx; end, endoderm; ect, ectoderm). **i**, Ventral view of 72 h.p.f. *Platynereis*. **j**, scheme of 72 h.p.f. *Platynereis* foregut expressing *foxa* (yellow), *brachyury*¹² (red) and miR-100 (blue). **k**, Ventral view of *Capitella* stage 4 larva with expression lateral to stomodaeum and in brain. **l**, Lateral view of *Strongylocentrotus* with expression in sphincter between oesophagus/ stomach.



conserved pair of complementary microRNAs, miR-9 and miR-9*/miR-131 (ref. 15) also showed highly restricted expression in the annelid brain, in two ventro-lateral sets of differentiated neurons (Fig. 3f–h and Supplementary Fig. 6f). In mouse, miR-9 and miR-9*/miR-131 are detected broadly in neuronal precursors but among all differentiated neurons are expressed only in the telencephalon¹⁵, comprising olfactory brain centres. In *Platynereis*, the most apical cells expressing mature miR-9 and miR-9* were located at the base of the antennae, a pair of head appendages considered to be chemosensory sense organs (Fig. 3h). This indicates that miR-9 and miR-9* may ancestrally locate to neurons involved in olfactory/chemosensory information processing. As in vertebrates, both miR-9 and miR-9* are detected in relatively high abundance in *Platynereis* and thus represent a pair of complementary microRNAs conserved in bilaterians².

Other conserved bilaterian microRNAs were expressed more broadly in one of four major organ systems, representing the central nervous system, peripheral sensory tissue, musculature or gut. For each of these groups, expression of individual microRNAs was largely overlapping, but at the same time complementary to those of other groups.

Figure 2 | MicroRNAs expressed in locomotor ciliated cells. **a–c**, Ventral-anterior views of 24 h.p.f. *Platynereis* trochophora larvae with microRNA expression (red) in prototroch cells and apical organ (arrowheads) (blue, DAPI; green, acTub). **d**, Ventral view of 72 h.p.f. *Platynereis* with expression in ciliated cells and midline (arrow). **e**, 72 h.p.f. *Platynereis*; expression in ciliated cells of trunk and prototroch (arrow). **f**, **g**, 72 h.p.f. *Platynereis*; expression in ciliated cells of the trunk. **h**, Lateral view of *Capitella* stage 6 larva; expression in ciliated bands. **i**, Ventral-lateral view of *Strongylocentrotus* pluteus larva with expression in ciliated cells lining the foregut and arms.

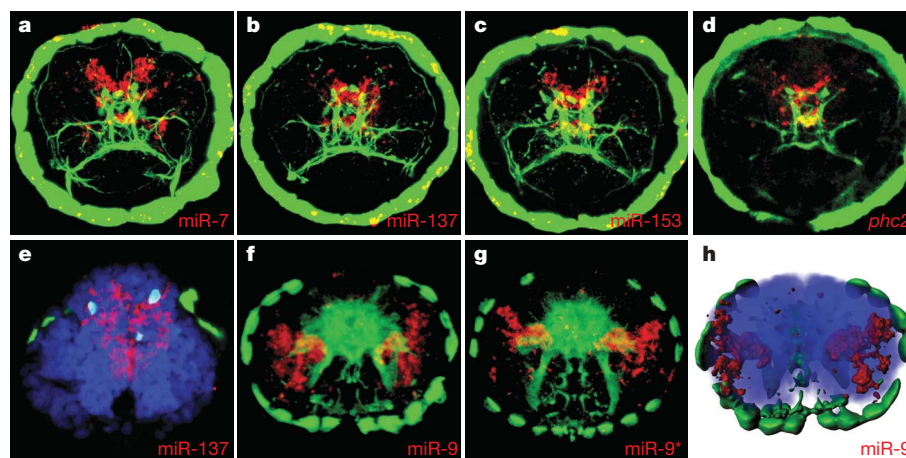


Figure 3 | Expression of brain-specific microRNAs. **a–d**, Apical view of 48 h.p.f. *Platynereis* with expression in dorso-medial brain (green, acTub; red, microRNAs). **e**, Apical view of 72 h.p.f. *Platynereis* brain section showing colocalization of microRNA (red) with serotonin (cyan) (blue,

DAPI, green, acTub). **f, g**, Apical views of 5 d.p.f. *Platynereis* brain. **h**, 3D reconstruction of 5 d.p.f. apical brain with superficial expression at the base of antennae.

miR-124 (Fig. 4a, d), known to maintain neuronal identity in the vertebrates^{14,16} and expressed in developing central nervous system (CNS) in fly¹⁷ and planarian¹⁸, was found in differentiating neurons in the brain and ventral nerve cord in *Platynereis*. miR-71, lost in vertebrates and insects² and restricted to CNS and parenchyma in planarians¹⁸, is also nervous system-specific in *Platynereis* (Fig. 4b, c and Supplementary Fig. 6h). miR-8 proved to be an excellent marker for differentiating sensory organs, including eyes, antennae, palps and sensory organs of the parapodia¹⁹, covering both neural and non-neural tissue (Fig. 4e and Supplementary Fig. 6j). A sensory tissue affiliation is likely to be evolutionarily ancient for this microRNA since the related miR-200a, miR-200b and miR-141 likewise show restricted expression in sensory organs such as nose and lateral line

in the vertebrates¹⁰ (Supplementary Table 5). miR-183 and miR-263, clustered in the *Lottia* genome and processed from the same transcript in *Platynereis* (Supplementary Table 4), also showed a conserved affiliation with sensory organ differentiation (Fig. 4f, g and Supplementary Fig. 6i), as previously reported for other bilaterians^{14,17}. Notably, the expression of the sensory tissue-specific miR-183 and of the CNS-specific miR-124 was mutually exclusive (compare Fig. 4d, h). In fly and vertebrate, miR-1 is active during muscular differentiation^{10,17}. In *Platynereis*, miR-1 and miR-133, clustered in vertebrates and in molluscs (Supplementary Table 4), showed almost identical expression in the differentiating musculature (Fig. 4i, k, l). In vertebrates, these microRNAs are robustly induced upon myotube differentiation concomitant with reduced expression of their target messengers^{16,20,21}.

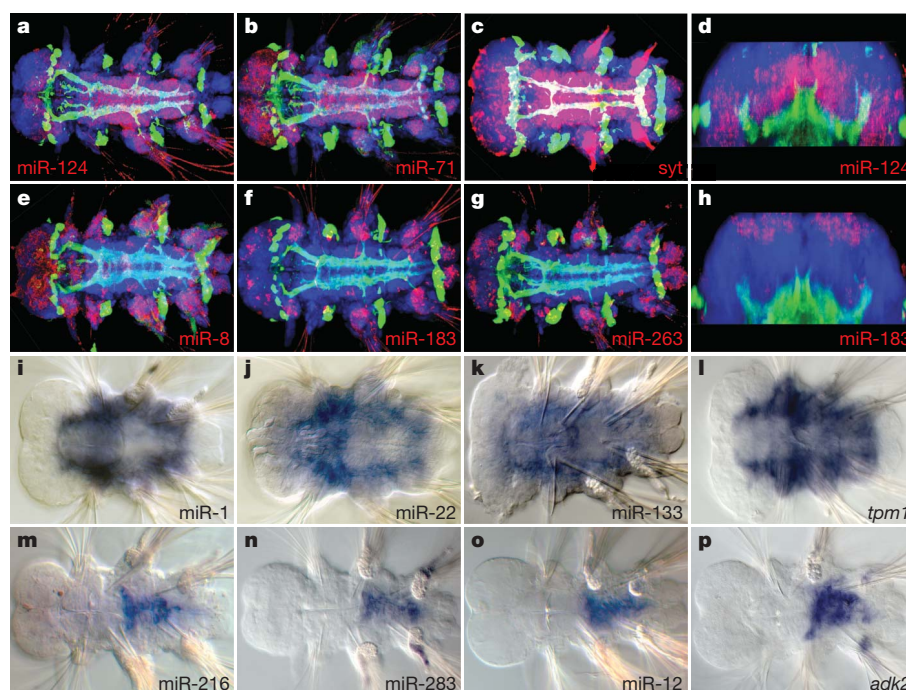


Figure 4 | MicroRNAs demarcating organ systems. **a, b**, Ventral views of 5 d.p.f. *Platynereis* with expression in CNS (blue, DAPI; green, acTub; red, microRNA). **c**, *synaptotagmin* (*syt*) expression at 5 d.p.f. ventral view. **d**, Virtual section of 5 d.p.f. *Platynereis* brain exemplifying the basal expression of CNS-specific microRNAs. **e–g**, Ventral views of 5 d.p.f. worms with expression in peripheral nervous system. **h**, Section of 5 d.p.f.

Platynereis brain exemplifying the apical expression of peripheral nervous system-specific microRNAs. **i–l**, Ventral views of 72 h.p.f. *Platynereis* with expression in differentiated musculature. *tpm*, Tropomyosin. **m–p**, dorsal views of 5 d.p.f. *Platynereis* with expression in differentiating midgut. *adk*, Adenosine kinase.

Similar musculature-specific expression was observed for miR-22 (Fig. 4j) that together with miR-1 and miR-133 has been reported to have myoD and myogenin upstream binding sites in the vertebrates²⁰. Finally, miR-12, miR-216 and miR-283 showed identical expression in the differentiating midgut at 5 days post fertilization (d.p.f.) (Fig. 4m–p). miR-12 clusters with miR-216 in *Platynereis* and in *Lottia*²² and with miR-283 in *Drosophila*¹⁷ (Supplementary Table 4), indicating that these three microRNAs evolved from the same precursor gene. In the vertebrates, expression of miR-216 is characteristic of pancreatic tissue²³ and targets of *miR-216* are expressed at lower levels in pancreatic than in other tissue²¹, indicating that the ancient site of activity of the miR-12/-216/-283 precursor had indeed been the gut.

Our results indicate that the conserved bilaterian microRNAs evolved in a strictly tissue-specific context. Corroborating this, brain- or musculature-specific microRNAs that we found in *Platynereis* show similar specificity in fish, human and mouse expression profiling, with high confidence (Supplementary Table 5). Although we cannot exclude that other expression sites initially existed for some of these microRNAs, these would have been lost in subsequent evolution in multiple lineages. At the present state of analysis, we can only speculate about the tissue-specific ancient roles of these microRNAs, by extrapolating from observations in other animal models. For example, miR-100 and the related miR-125 and let-7 may have acquired an ancient role in developmental timing: The very late onset of *let-7* expression at 5 d.p.f. in *Platynereis* (before settlement) is consistent with earlier observations in nematode⁶, fly^{7,8}, mollusc²⁴, zebrafish²⁴ and in another annelid²⁴, indicative of a role in the control of late developmental transitions^{6–8,24}. With time, such role may then have spread to other tissues, such as target tissue differentiating in the course of metamorphosis, as observed in fly^{7,8} and nematode^{6,24}. Similarly, the affinity of miR-29, miR-34 and miR-92 to motile ciliated cells sheds new light on the evolution of ventricular neuron types expressing these microRNAs in the vertebrate CNS¹⁴ (Supplementary Table 5), some of which are known to bear motile cilia²⁵. A comparison of targets in slow-evolving species should reveal the functional evolution of the conserved bilaterian microRNAs and also allow understanding why in many cases these microRNAs were co-opted by new tissues that did not express them before.

The identification of ancient expression sites for conserved bilaterian microRNAs implies that these microRNA-defined tissues existed in the protostome-deuterostome ancestor (Supplementary Fig. 1). Our data indicate that it possessed a miR-124+ central nervous tissue as opposed to miR-8/-183/-263+ peripheral sensory nervous tissue¹⁹, consistent with the notion that nervous system centralization predated the protostome/deuterostome ancestor¹⁹. The ancient brain comprised miR-7+, miR-137+ and miR-153+ neurosecretory parts, as recently suggested⁴ and miR-9/9*+ parts that may relate to sensory information processing. Our data also indicate the existence of miR-1/-22/-133+ body musculature, in line with the proposed conservation of somatic muscle cell types¹⁹, and of a miR-12/-216/-283+ gut. Finally, the protostome/deuterostome ancestors possessed miR-100/-125/let-7/+ neurosecretory cells along the mouth and miR-29, miR-34, miR-92+ motile ciliated cells, possibly forming part of *otx*+ larval ciliary bands^{12,26}. We have thus established microRNAs as an important new tool for reconstructing ancient animal body plans at important evolutionary nodes, focusing here on the protostome-deuterostome divergence. More complete inventories of microRNAs—yielding a refined picture of gains (and losses) of microRNAs in the diverging lineages—and concomitant expression analysis will allow expanding this approach to other key events of animal evolution.

METHODS SUMMARY

***Platynereis* and *Capitella* whole mount *in situ* hybridization with locked nucleic acids probes.** Whole mount *in situ* hybridizations (WMISH) were performed by modifying fish and *Platynereis* established protocols^{10,27}. Use of a more stringent hybridization mix with 70% formamide allowed lowering the hybridization temperature down to 37 °C to successfully visualize the expression of any microRNA

tested (regardless of the locked nucleic acids' T_m). The same *in situ* protocol was used for the hybridization of long DIG-11-UTP-labelled RNA probes.

***Nematostella* and sea urchin whole mount *in situ* hybridization with locked nucleic acids probes.** Fixations and hybridizations of *Nematostella* carried out as described in ref. 28 and for sea urchin larvae done as described in ref. 29 with the following adaptations: content of formamide in hybridization mix increased to 70% instead of 50%. Pre-hybridization and hybridization carried out at 37 °C instead of 60 °C.

Microscopy. Nitroblue tetrazolium chloride (NBT)/5-Bromo-4-chloro-3-indolyl-phosphate (BCIP) stained embryos were imaged using a Leica TCS SPE confocal microscope through reflection imaging as described in ref. 27. White light pictures were taken under Nomarski optics using a Zeiss Axiophot microscope.

microRNA cloning and sequencing. Small RNA cloning was performed as described in ref. 30. Small RNA libraries were sequenced using the Illumina platform. We only analysed sequence reads with quality score higher than 35 in Solexa/Illumina files. Reads were clustered according to sequence similarity and of these, dominant reads were analysed by BLAST search against miRBase v10.0. Comparison required $\geq 80\%$ identity of the query with the target and ≥ 7 out of 8 nucleotides in the 5' end and yielded a list of conserved microRNAs (Supplementary Table 1).

Full Methods and any associated references are available in the online version of the paper at www.nature.com/nature.

Received 31 July; accepted 4 December 2009.

Published online 31 January 2010.

- Grimson, A. *et al.* Early origins and evolution of microRNAs and Piwi-interacting RNAs in animals. *Nature* **455**, 1193–1197 (2008).
- Wheeler, B. M. *et al.* The deep evolution of metazoan microRNAs. *Evol. Dev.* **11**, 50–68 (2009).
- Raible, F. *et al.* Vertebrate-type intron-rich genes in the marine annelid *Platynereis dumerilii*. *Science* **310**, 1325–1326 (2005).
- Tessmar-Raible, K. *et al.* Conserved sensory-neurosecretory cell types in annelid and fish forebrain: insights into hypothalamus evolution. *Cell* **129**, 1389–1400 (2007).
- Shkumatava, A., Stark, A., Sive, H. & Bartel, D. P. Coherent but overlapping expression of microRNAs and their targets during vertebrate development. *Genes Dev.* **23**, 466–481 (2009).
- Reinhart, B. J. *et al.* The 21-nucleotide *let-7* RNA regulates developmental timing in *Caenorhabditis elegans*. *Nature* **403**, 901–906 (2000).
- Caygill, E. E. & Johnston, L. A. Temporal regulation of metamorphic processes in *Drosophila* by the *let-7* and *miR-125* heterochronic microRNAs. *Curr. Biol.* **18**, 943–950 (2008).
- Sokol, N. S., Xu, P., Jan, Y. N. & Ambros, V. *Drosophila let-7* microRNA is required for remodeling of the neuromusculature during metamorphosis. *Genes Dev.* **22**, 1591–1596 (2008).
- Poy, M. N. *et al.* A pancreatic islet-specific microRNA regulates insulin secretion. *Nature* **432**, 226–230 (2004).
- Wienholds, E. *et al.* MicroRNA expression in zebrafish embryonic development. *Science* **309**, 310–311 (2005).
- Scholz, C. B. & Technau, U. The ancestral role of *Brachyury*: expression of *NemBra1* in the basal cnidarian *Nematostella vectensis* (Anthozoa). *Dev. Genes Evol.* **212**, 563–570 (2003).
- Arendt, D., Technau, U. & Wittbrodt, J. Evolution of the bilaterian larval foregut. *Nature* **409**, 81–85 (2001).
- Nielsen, C. *Animal Evolution: Interrelationships of the Living Phyla*, 2nd edn (Oxford Univ. press, 2001).
- Kapsimali, M. *et al.* MicroRNAs show a wide diversity of expression profiles in the developing and mature central nervous system. *Genome Biol.* **8**, R173 (2007).
- Deo, M. *et al.* Detection of mammalian microRNA expression by *in situ* hybridization with RNA oligonucleotides. *Dev. Dyn.* **235**, 2538–2548 (2006).
- Farh, K. K. *et al.* The widespread impact of mammalian microRNAs on mRNA repression and evolution. *Science* **310**, 1817–1821 (2005).
- Aboobaker, A. A. *et al.* *Drosophila* microRNAs exhibit diverse spatial expression patterns during embryonic development. *Proc. Natl Acad. Sci. USA* **102**, 18017–18022 (2005).
- González-Estévez, C. *et al.* Diverse miRNA spatial expression patterns suggest important roles in homeostasis and regeneration in planarians. *Int. J. Dev. Biol.* (in press) (2009).
- Denes, A. S. *et al.* Molecular architecture of annelid nerve cord supports common origin of nervous system centralization in bilateria. *Cell* **129**, 277–288 (2007).
- Rao, P. K. *et al.* Myogenic factors that regulate expression of muscle-specific microRNAs. *Proc. Natl Acad. Sci. USA* **103**, 8721–8726 (2006).
- Sood, P. *et al.* Cell-type-specific signatures of microRNAs on target mRNA expression. *Proc. Natl Acad. Sci. USA* **103**, 2746–2751 (2006).
- Prochnik, S. E., Rokhsar, D. S. & Aboobaker, A. A. Evidence for a microRNA expansion in the bilaterian ancestor. *Dev. Genes Evol.* **217**, 73–77 (2007).

23. Szafranska, A. E. *et al.* MicroRNA expression alterations are linked to tumorigenesis and non-neoplastic processes in pancreatic ductal adenocarcinoma. *Oncogene* **26**, 4442–4452 (2007).
24. Pasquinelli, A. E. *et al.* Conservation of the sequence and temporal expression of *let-7* heterochronic regulatory RNA. *Nature* **408**, 86–89 (2000).
25. Vigh, B. *et al.* The system of cerebrospinal fluid-contacting neurons. Its supposed role in the nonsynaptic signal transmission of the brain. *Histol. Histopathol.* **19**, 607–628 (2004).
26. Harada, Y. *et al.* Developmental expression of the hemichordate *otx* ortholog. *Mech. Dev.* **91**, 337–339 (2000).
27. Jékely, G. & Arendt, D. Cellular resolution expression profiling using confocal detection of NBT/BCIP precipitate by reflection microscopy. *Biotechniques* **42**, 751–755 (2007).
28. Rentzsch, F. *et al.* Asymmetric expression of the BMP antagonists *chordin* and *gremlin* in the sea anemone *Nematostella vectensis*: implications for the evolution of axial patterning. *Dev. Biol.* **296**, 375–387 (2006).
29. Arenas-Mena, C., Cameron, A. R. & Davidson, E. H. Spatial expression of *Hox* cluster genes in the ontogeny of a sea urchin. *Development* **127**, 4631–4643 (2000).
30. Pfeffer, S. *et al.* Identification of microRNAs of the herpesvirus family. *Nature Methods* **2**, 269–276 (2005).

Supplementary Information is linked to the online version of the paper at www.nature.com/nature.

Acknowledgements We thank A. Fischer for drawing schematic illustrations and providing probes for *tropomyosin 1*, A. Boutla for advice when initiating the project,

J. Brennecke for help with small RNA cloning and discussions, M. Hentze for critical reading of the manuscript, P. Steinmetz and U. Technau for *Nematostella* embryos and discussions, E. Arboleda and I. Arnone for sea urchin plutei and discussions, V. Benes and the EMBL-Genecore facility for expert technical advice, W. R. McCombie, M. Rooks and E. Hodges for help with sequencing and M. Arumugam, V. Van Noort, J. Muller and C. Creevey for advice in target analysis.

Author Contributions F.C. initiated the project, cloned *Platynereis* small RNAs, characterized the temporal and spatial expression of ancient miRNAs and their targets, coordinated the collaborations and wrote the paper. F.R. analysed and evaluated the Solexa sequencing data. R.T. assembled the 3'UTRs of targets from *Platynereis* ESTs and provided riboprobes. O.S. did the SNP and miRNA::target co-expression analysis. K.T. performed target predictions under the supervision of P.B., and S.K. characterized *foxa2* expression. H.S. generated probes for targets *in situ* screen. G.J.H. hosted the small RNA cloning and sequencing. D.A. analysed comparative miRNA expression, provided ideas and strategies and wrote the paper. All authors discussed the results and commented on the manuscript.

Author Information Sequences for *Platynereis* miRNA primary transcripts pri-miR-100/let-7, pri-miR-12/216 and pri-miR-183/263 were deposited in the GenBank database with accession numbers FJ838789.1, FJ838790.1 and GU224283, respectively. Reprints and permissions information is available at www.nature.com/reprints. The authors declare no competing financial interests. Correspondence and requests for materials should be addressed to D.A. (arendt@embl.de).

METHODS

Platynereis and Capitella whole-mount *in situ* hybridization with LNA probes. Custom miRCURY LNA³¹ (locked nucleic acid) Detection Probes (Exiqon) for *Platynereis* were labelled with digoxigenin (DIG) 3'-end labeling kit 2nd generation (Roche) and then purified with Sephadex G25 Micro Spin columns (GE Healthcare) as described in ref. 32.

Platynereis and *Capitella* embryos were fixed at room temperature in 4% paraformaldehyde in 2× PBS + 0.1% Tween-20 for 2 h and stored in methanol at -20 °C. *In situ* hybridizations were performed by fusing and modifying fish and *Platynereis* whole mount *in situ* (WMISH) protocols^{27,32} as follows:

Stepwise 5 min rehydration of fixed embryos in PBS + 0.1% Tween (PTW) to dilute methanol from 100%, 75%, 50%, 25% to 0%.

Digestion times of embryos in 10 µg ml⁻¹ proteinase K PTW: *Capitella* larvae (stage 3–7), 5 min; *Platynereis* embryos 24 h.p.f., 7 min; 48 h.p.f., 30 min; 72 h.p.f., 60 min; 5 d.p.f., 75 min. Two 5 min washes in 2 mg ml⁻¹ glycine PTW followed by 20 min post-fixation in 4% paraformaldehyde PTW. Five 5 min washes in PTW. Pre-hybridization in high stringency hybridization mix (HM) for 1 h at 37 °C (70% formamide, 5× SSC, 50 µg ml⁻¹ heparin, 5 mg ml⁻¹ tRNA, 0.1% Tween 20) followed by overnight hybridization at 37 °C in 200 µl of high stringency HM + 4 pmol labelled LNA probe.

Post-hybridization washes were done in standard HM (50% formamide, 5× SSC, 50 µg ml⁻¹ heparin, 5 mg ml⁻¹ tRNA, 0.1% Tween 20) at 37 °C stepwise: 15 min 75% HM/25% 2× SSC, 15 min 50% HM/2× SSC, 15 min 25% HM/2× SSC followed by two 15 min 2× SSC and two 30 min 0.2× SSC washes. Then at room temperature: 10 min 75% 0.2× SSC/25% PTW, 10 min 50% 0.2× SSC/50% PTW, 10 min 25% 0.2× SSC/25% PTW, 10 min PTW and blocking for 90 min in 2% sheep serum in PTW. Alkaline phosphatase-coupled anti-DIG-Fab' fragments (Roche) were diluted 1:2,000, mouse anti-acetylated tubulin (Sigma) 1:500 and rabbit anti-serotonin (5HT) 1:250 (ImmunoStar) in PTW for overnight incubation at 4 °C. Embryos were washed six times 15 min in PTW, twice in staining buffer (100 mM Tris, pH 9.5, 100 mM NaCl, 50 mM MgCl₂, 0.1% Tween-20), and stained with 337.5 µg ml⁻¹ nitroblue tetrazolium (NBT) and 175 µg ml⁻¹ 5-bromo-4-chloro-3-indolyl phosphate (BCIP) in staining buffer for several hours. After staining, embryos were rinsed in 100% ethanol for 15 min, washed in PTW and immunostaining proceeded as in ref. 27 to be finally mounted in glycerol containing 2.5 mg ml⁻¹ 1,4-diazabicyclo[2.2.2]octane (DABCO). The same *in situ* protocol was used for the hybridization of long DIG-11-UTP-labelled RNA probes.

Nematostella and sea urchin whole mount *in situ* hybridization with LNA probes. Fixations and hybridizations of *Nematostella* were carried out as described in ref. 28 and for sea urchin larvae as described in ref. 29 with the following adaptations: content of formamide in hybridization mix increased to 70% instead of 50%, and pre-hybridization and hybridization carried out at 37 °C instead of 60 °C.

Microscopy. NBT/BCIP stained embryos were imaged using a Leica TCS SPE confocal microscope through reflection imaging as described previously²⁷. A ×40 oil-immersion objective was used. White light pictures were taken under Nomarski optics using a Zeiss Axiophot microscope equipped with a Leica DC500 camera.

Image processing. Most confocal stacks images were acquired with voxel size 0.537 × 0.537 × 1 microns, 8-bit image depth and were processed using ImageJ 1.40g. All confocal images displayed are products of z-projections of stacks. Image reconstructions and sections were generated using Imaris 6.2.1. Contrast was adjusted uniformly across the entire image.

Northern blot analysis. Total RNA was isolated from *Platynereis* embryos at 6 h.p.f., 12 h.p.f., 18 h.p.f., 24 h.p.f., 48 h.p.f. and 5 d.p.f. using peqGOLD TriFast reagent (peqlab Biotechnologie). Total RNA (15 µg) was separated on 15% denaturing polyacrylamide gel and blotted via chemical cross-linking as in ref. 33. For detection, oligonucleotide probes were designed for each miRNA and end-labelled with [³²P]-ATP using T4 polynucleotide kinase (NEB).

miRNA cloning and sequencing. Small RNA cloning was performed separately for three different developmental stages of *Platynereis*: 20 min post fertilization, swimming larvae and young worms. For each stage four batches were pooled. RNA extraction and cloning of the small RNA fraction (19–24 nucleotides) was performed as described in ref. 30. The resulting small RNA libraries were sequenced using the Illumina platform.

Sequence processing and analysis. For each of the three libraries, raw Illumina reads were processed as follows: first, adaptor sequences (5'-CTGTAGGCAC CATCAAT-3') were clipped off by searching for the motif CTGTAGGC (allowing one degenerate position). Subsequently, sequences were selected for length (16 ≤ x ≤ 29) and quality (base scores ≥ 35 out of a maximum of 40). Sequences of the individual libraries were then pooled into one non-redundant data set. Finally, around 4% of these sequences were excluded, as database searches revealed significant similarity to known mitochondrial or ribosomal sequences.

The resulting non-redundant sequence data set comprised 111,575 sequences, representing 1,259,482 individual sequence reads. Known miRNA sequences were identified from this set by sequence searches with sequences retrieved from the miRBase repository v10.1 from ref. 34). Comparisons required 80% overall identity of the query with the target and 7 out of 8 nucleotides in the 5' end. The *Platynereis* correlates of conserved animal miRNAs are listed in Supplementary Table 1.

Sequence variants. We note that 3,735 sequences of our data set represent ~89% (1,114,984) of all the reads, whereas the remaining reads occur less than ten times. We assume that this general disproportion in distribution reflects a combination of (1) methodological artefacts, (2) original heterogeneity of alleles present in the batches pooled for the sampling, and (3) differences in miRNA processing, as previously observed in large miRNA data sets generated by massive parallel sequencing^{35,36}.

As we lack information about the complete *Platynereis* genome, we can presently not reliably distinguish between these possibilities. However, we note that in several cases, sequence variants account for significant fractions of a given miRNA family. This is illustrated for the case of miR-9 (Supplementary Fig. 8). 71% of the respective RNAs represent the canonical sequence, whereas the remainder includes length variants and point mutations, including a 5' variant that would be predicted to shift the seed region involved in target recognition. For miR-22/-745, we find a similar case of seed shifting (Supplementary Fig. 8). In this case, a recent study⁷ indeed supports the notion that the respective sub-classes of miRNAs reflect genetic divergence of the family.

Primer sequences for miRNA cluster cloning. Gene specific cDNA libraries were prepared using the 3'-most miRNA sequence of mir-100-let-7 cluster, mir-12-mir-216 cluster and mir-183-mir-263 cluster.

Pdu-mir-100-let-7 cluster (FJ838789) resulted from a PCR reaction using the forward primer AACCCGTACAACCGAAGCTTGTG and the reverse primer ACTATACAACCTACTACCTCA.

Pdu-mir-12-mir-216 cluster (FJ838790) resulted from a PCR reaction using the forward primer UGAGTATTACATCAGGTACTGA and the reverse primer CTCACCTTTGCCAGCTGAGATTA.

Pdu-mir-183-mir-263 (GU224283) cluster resulted from a PCR reaction using the forward primer AATGGCACTGGTAGAATTCACGG and the reverse primer CTTGGCACTGGTAGAATTCACCTGA.

The RNAfold program³⁷ was used to find the hairpin structure within the cluster. **miRNA target prediction analysis.** Several (92) 3'-UTRs were surveyed for octamer, heptamer-A1 and heptamer-m8 binding sites using TargetScan³⁸ and for octamer, heptamer and hexamer perfect seed binding sites using PITA³⁹ with default settings. TargetScan yielded 433 and PITA 741 binding sites. The intersection between the two data sets contains 293 binding sites. A sliding window of either 1 or 2 nucleotides was allowed in order to capture binding sites that were predicted as a hexamer in PITA but as heptamer or octamer in TargetScan.

Calculation of significance for co-expression of miRNAs and target transcripts. For tissues, the co-expression ratio is defined as the number of miRNA:target pairs that show overlap in the given tissue divided by the total number of miRNA:target pairs. Iterative randomization was done by reshuffling the predicted targets of miRNAs. Bootstrap for depletions and enrichment shows total count of iterations when the observed coexpression ratio for a particular tissue was below or above the randomly obtained value, respectively.

3'-UTR retrieval. The majority of the EST sequences used to find 3' UTRs were 3' Sanger reads of a full-length cDNA library. We used BLAST to search the sequences against swissprot protein database to identify the correct open reading frame, and thus the 3' UTR. In few cases where there was no significant BLAST hit, we assumed it to be mostly composed of UTR, as they contained frequent stop codons in all the reading frames.

Single nucleotide polymorphism (SNP) assessment in the 3'UTRs. Total RNA extracted from heads of adult animals and different developmental stages was sequenced with the Solexa platform at EMBL yielding 15 million 76 bp reads, 21,000 of which could be mapped to 3' UTRs by BLASTN. Reads were truncated to the first 40 bp in order to reduce sequencing errors. Every position in the 3' UTR was analysed for the presence of a mismatch and a SNP was called when less than 90% of nucleotides assigned to the position showed conservation. Whereas on average we observed SNP rate of 1/45 bp in the non-coding regions, the predicted miRNA binding sites showed a rate of 1/60 bp. Still, the overall SNP frequency was too low in order to distinguish between conserved and non-conserved miRNA binding sites for the entire set of predicted targets.

31. Válczy, A. *et al.* Sensitive and specific detection of microRNAs by northern blot analysis using LNA-modified oligonucleotide probes. *Nucleic Acids Res.* **32**, e175 (2004).

32. Wienholds, E. *et al.* MicroRNA expression in zebrafish embryonic development. *Science* **309**, 310–311 (2005).

33. Pall, G. S. & Hamilton, A. J. Improved northern blot method for enhanced detection of small RNA. *Nature Protocols* **3**, 1077–1084 (2008).

34. Griffiths-Jones, S., Saini, H. K., van Dongen, S. & Enright, A. J. miRBase: tools for microRNA genomics. *Nucleic Acids Res.* **36** (Database issue), D154–D158 (2008).
35. Lu, J. *et al.* The birth and death of microRNA genes in *Drosophila*. *Nature Genet.* **40**, 351–355 (2008).
36. Morin, R. D. *et al.* Application of massively parallel sequencing to microRNA profiling and discovery in human embryonic stem cells. *Genome Res.* **18**, 610–621 (2008).
37. Hofacker, I. L. Vienna RNA secondary structure server. *Nucleic Acids Res.* **31**, 3429–3431 (2003).
38. Lewis, B. P., Burge, C. B. & Bartel, D. P. Conserved seed pairing, often flanked by adenosines, indicates that thousands of human genes are microRNA targets. *Cell* **120**, 15–20 (2005).
39. Kertesz, M. *et al.* The role of site accessibility in microRNA target recognition. *Nature Genet.* **39**, 1278–1284 (2007).

Neural evidence for inequality-averse social preferences

Elizabeth Tricomi¹, Antonio Rangel^{2,3}, Colin F. Camerer^{2,3} & John P. O'Doherty^{2,3,4}

A popular hypothesis in the social sciences is that humans have social preferences to reduce inequality in outcome distributions because it has a negative impact on their experienced reward^{1–3}. Although there is a large body of behavioural and anthropological evidence consistent with the predictions of these theories^{1,4–6}, there is no direct neural evidence for the existence of inequality-averse preferences. Such evidence would be especially useful because some behaviours that are consistent with a dislike for unequal outcomes could also be explained by concerns for social image⁷ or reciprocity^{8,9}, which do not require a direct aversion towards inequality. Here we use functional MRI to test directly for the existence of inequality-averse social preferences in the human brain. Inequality was created by recruiting pairs of subjects and giving one of them a large monetary endowment. While both subjects evaluated further monetary transfers from the experimenter to themselves and to the other participant, we measured neural responses in the ventral striatum and ventromedial prefrontal cortex, two areas that have been shown to be involved in the valuation of monetary and primary rewards in both social and non-social contexts^{10–14}. Consistent with inequality-averse models of social preferences, we find that activity in these areas was more responsive to transfers to others than to self in the 'high-pay' subject, whereas the activity of the 'low-pay' subject showed the opposite pattern. These results provide direct evidence for the validity of this class of models, and also show that the brain's reward circuitry is sensitive to both advantageous and disadvantageous inequality.

A pervasive notion in social science is that human preferences and behaviour are sensitive to inequality considerations^{1–3}. This suggestion is based on considerable experimental and field evidence. Small-scale societies often share through norms of informal social insurance¹⁵, and large-scale societies share through governmental welfare transfers and progressive taxation¹⁶. In corporations, wages are typically secret and vary less than productivity does, as though workers have a strong aversion for earning less than others do¹⁷. Workers also seem to reciprocate when they feel companies have treated them well¹⁸, but withdraw effort when they feel wronged¹⁹. These social patterns have been replicated under controlled conditions in many behavioural economics experiments: participants regularly share wealth with strangers²⁰, punish non-cooperators at a cost to themselves^{4,20,21}, and reject unfair divisions of a pool of money²².

Subjective ratings, and preferences inferred from choices, provide evidence that subjects like transfers that reduce inequality⁵. However, it is unknown whether reward structures in the brain respond to self–other monetary gains in ways that reflect a preference for reducing inequality. The missing neural evidence is important because most of the behavioural observations consistent with a dislike for unequal distributions can also be explained by concerns for social image⁷ or

reciprocity^{8,9}, rather than an aversion to inequality. Furthermore, the behavioural evidence is mixed about people's dislike of advantageous inequality (that is, a willingness to decrease their own payoff to improve those of people who are worse off). Some studies indicate that the better-off will pay to reduce an outcome gap, but other studies suggest they will pay only to maintain or to increase their relative status^{23,24}.

We used functional magnetic resonance imaging (fMRI) to test directly for the presence of inequality-averse social preferences in the human brain, for both positive and negative inequality. A stark and salient inequality in overall pay for experimental participation was created by recruiting 20 pairs of unacquainted male participants. They each received \$30 base pay, and then drew balls labelled 'rich' or 'poor.' The 'rich' (high-pay) participant received a \$50 bonus to the base pay and the 'poor' (low-pay) participant received no bonus. We then scanned the participants as they each rated their subjective valuations for further positive potential monetary transfers from the experimenter to themselves and to the other player (Fig. 1). Each transfer ranged from \$0 to \$50 and the set of transfers was symmetrical over the two participants. At the end of the experiment the transfers from a randomly chosen trial were paid to the subjects.

Our test focused on the response of the ventral striatum and ventromedial prefrontal cortex (vmPFC), areas known to be involved in the valuation of stimuli at the time of decision making^{25,26} and with processing the experienced subjective value of receiving monetary reward and other rewards¹¹. We characterized the pattern of stated inequality preferences by regressing each subject's ratings on the transfer amount to themselves and to the other person. Both groups rated transfers to themselves positively, indicating that they valued having higher earnings to themselves, although the value was lower for the high-pay group than for the low-pay group (Fig. 1b; $t_{(38)} = -3.8$, $P = 0.0005$). Consistent with previous studies⁵, the low-pay group disliked falling farther behind the high-pay group ('disadvantageous inequality aversion'), because they rated positive transfers to the high-pay participants negatively, even though these transfers had no effect on their own earnings ($t = 3.4$, $P = 0.003$). Conversely, the high-pay group seemed to value transfers that closed the gap between their earnings and those of the low-pay group ('advantageous inequality aversion'), because they rated transfers to the low-pay participants positively ($t = 2.8$, $P = 0.01$). This difference in whether transfers to others are valued negatively (by the low-pay group) or positively (by the high-pay group) resulted in a significant group-by-recipient interaction ($F_{(1,20)} = 9.4$, $P < 0.01$).

In the fMRI data, on trials in which there was a transfer only to oneself, activation in the ventral striatum (coordinates $-9, 12, -6$; $t_{(19)} = 3.6$, $P < 0.05$, small-volume-corrected) and vmPFC correlated significantly with the magnitude of the monetary transfer (coordinates $-9, 39, -9$; $t_{(19)} = 3.75$, $P < 0.05$, small-volume-corrected),

¹Psychology Department, Rutgers University, Newark, New Jersey 07102, USA. ²Division of the Humanities and Social Sciences, ³Computational and Neural Systems, California Institute of Technology, Pasadena, California 91125, USA. ⁴School of Psychology and Trinity College Institute of Neuroscience, Trinity College, Dublin 2, Ireland.

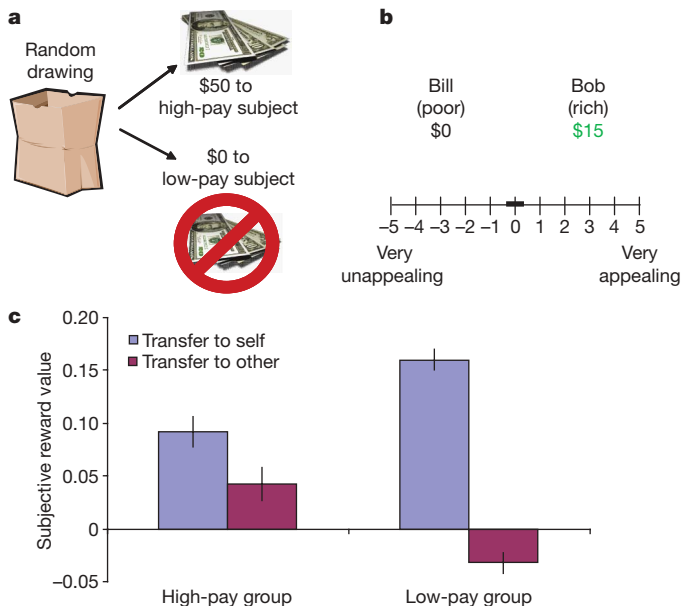


Figure 1 | Effect of inequality manipulation on behaviour. **a**, Two participants each drew a ball from hat. One, labelled 'rich', led to a bonus payment of \$50. The other, labelled 'poor', entailed no bonus. **b**, Each participant was then scanned while they rated further potential monetary transfers to themselves and the other player on a scale from -5 to 5. **c**, Estimated coefficients from a linear regression of the behavioural ratings on the transfers to self and other. The high-pay group rated transfers to themselves less highly than the low-pay group did, while rating transfers to the other player more highly. Error bars represent s.e.m.

confirming previous findings implicating these regions in reward-related processing^{11,25,26}. Next we tested for effects of our inequality manipulation on activity in these areas by computing a contrast of the difference in fMRI responses for transfers to self minus transfers to other in each of the two groups. In both regions this contrast was significantly greater for the low-pay group than for the high-pay group (Figs 2a and 3a; see also Supplementary Table 1; $t_{(38)} > 3.3$, $P < 0.05$, small-volume-corrected). This is further illustrated in Figs 2b and 3b, which show that both the ventral striatum and mPFC of low-pay subjects responded more strongly to transfers to self than other, whereas the opposite pattern was observed for high-pay subjects.

We conducted further analyses to address two potential concerns about our results. First, because high-pay and low-pay subjects had different initial wealth levels, the differences in their ratings and neural activity might have been due to 'wealth effects' and not to equity considerations. To address this we ran two behavioural versions of the experiment in which both subjects had the same initial wealth, so

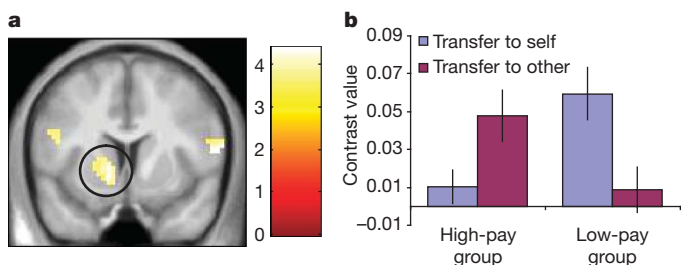


Figure 2 | Effect of inequality manipulation on activity in the ventral striatum. **a**, In the ventral striatum (circled), the summary statistic, '(transfer to self) minus (transfer to other)', was significantly greater for the low-pay group than the high-pay group ($P < 0.05$, small-volume-corrected). The image is shown at $P < 0.001$, uncorrected. **b**, Parameter estimates for each of the parametric regressors in the general linear model. Error bars represent s.e.m.

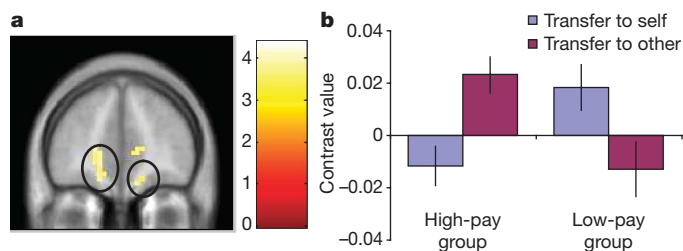


Figure 3 | Effect of inequality manipulation on activity in the vmPFC. **a**, In the vmPFC, bilaterally (circled regions), activity in the '(transfer to self) minus (transfer to other)' contrast was also significantly greater for the low-pay group than high-pay group ($P < 0.05$, small-volume-corrected). The image is shown at $P < 0.001$, uncorrected. **b**, Parameter estimates for each of the parametric regressors in the general linear model. Error bars represent s.e.m.

they were either both high-pay or both low-pay. As shown in Supplementary Fig. 1, there were no significant differences in the ratings of the two groups, which rules out this alternative explanation.

Second, because activity in ventral striatum and vmPFC has been associated with prediction errors measuring the degree of surprise in receiving rewards¹⁰, there is a concern that some of the difference in activity between rich and poor might be explained by differences in expectations, which have nothing to do with social preferences. To address this we estimated another model in which neural activity was assumed to be modulated by prediction errors for the transfers to oneself, using an initial expected value of 50 for the high-pay subjects and 0 for the low-pay subjects, but not by the transfers to the other subject (see Methods for details). We then performed a Bayesian model comparison of the two models. The results indicate that the original model provides a better fit to the data in our regions of interest. In the left vmPFC the probability that our valuation model was a better explanation of the BOLD (blood oxygen level dependent) response profile than the prediction error model (exceedance probability; EP) was 0.92, whereas for the right vmPFC the EP was 0.9998 and for the left ventral striatum the EP was 0.76.

Although we found that both behavioural ratings and neural activity in vmPFC and striatum showed significant effects of advantageous and disadvantageous inequality aversion, the pattern of advantageous inequality aversion measured in the brain data was discernibly different from that expressed in the behavioural ratings. For high-pay subjects, neural responses associated with transfers to themselves were lower than those associated with transfers to the other, whereas the low-pay subjects showed the opposite pattern. In contrast, the stated preferences of the high-pay subjects showed a greater valuation for their own transfers than for transfers to the other. This apparent incongruity between stated behavioural ratings and brain data indicates that basic reward structures in the brain may reflect even stronger equity considerations than is necessarily expressed or acted on at the behavioural level. These findings raise the possibility that even when basic reward responses reflect strong equity considerations, in some cases additional factors may intercede to moderate the influence of such equity judgements on behaviour, such as strategizing¹⁵ (under situations in which a competition is perceived between individuals), or the engagement of self-serving biases such as judgements of deservingness or need.

Our results provide direct neurobiological evidence in support of the existence of inequality-averse social preferences in the human brain. Although the objective values of the transfers shown to the high-pay and low-pay subjects was equivalent, the subjective value of the transfers was influenced by who received the initial \$50 endowment, and activity in the striatum and vmPFC reflected this influence. This builds on a growing body of research showing that experienced subjective reward signals in the striatum and vmPFC are modulated by a variety of other social factors^{13,14,27-30}. Furthermore, given that the initial wealth manipulation was small relative to the subjects' overall income, our results also underscore the strong sensitivity of

how the brain's reward circuitry responds to equity considerations. This provides insight into why equity concerns seem to be such a pervasive and fundamental feature of human social exchange.

METHODS SUMMARY

Twenty pairs of healthy, previously unacquainted male participants participated in the experiment. They were each paid a base \$30 fee; each then drew a ball from a hat, labelled 'rich' or 'poor'. The 'rich' (high-pay) subject received an immediate payment of \$50, whereas the 'poor' (low-pay) player received no bonus payment. They then performed an identical task in consecutive fMRI scanning sessions. In each trial subjects viewed possible monetary transfers from the experimenter to themselves and to the other player, ranging from \$0 to \$50 (Fig. 1). Participants rated how appealing they found the possible transfers on a scale of -5 (very unappealing) to 5 (very appealing). After both players' scans, a single trial was randomly picked from the set, and the transfers for that trial were paid out.

For each participant, the behavioural ratings were regressed on the transfers to self and other. The resulting coefficients were pooled into a mixed-effects group analysis using two-sided t -tests to determine whether the high-pay and low-pay groups differed in their social preferences. We estimated the parameters of a general linear model of the fMRI data that included parametric effects of the transfer amounts on the BOLD signal. A random (between-subject) effects analysis was then used to identify regions that responded differentially to transfers to self versus transfers to the other player in the two groups. Images are displayed with a voxel-wise significance threshold of $P < 0.001$. Results are reported with a corrected significance threshold of $P < 0.05$, based on a small-volume correction within an 8-mm sphere centred on coordinates in the striatum and vmPFC taken from previous studies.

Full Methods and any associated references are available in the online version of the paper at www.nature.com/nature.

Received 29 June; accepted 22 December 2009.

- Fehr, E. & Schmidt, K. A theory of fairness, competition, and cooperation. *Q. J. Econ.* **114**, 817–868 (1999).
- Adams, J. in *Advances in Experimental Social Psychology* (ed. Berkowitz, L.) 267–299 (Academic, 1965).
- Bolton, D. & Ockenfels, A. ERC: A theory of equity, reciprocity, and competition. *Am. Econ. Rev.* **82**, 166–193 (2000).
- Dawes, C. T., Fowler, J. H., Johnson, T., McElreath, R. & Smirnov, O. Egalitarian motives in humans. *Nature* **446**, 794–796 (2007).
- Loewenstein, G. F., Thompson, L. & Baserman, M. H. Social utility and decision making in interpersonal contexts. *J. Pers. Soc. Psychol.* **57**, 426–441 (1989).
- Henrich, J. et al. 'Economic man' in cross-cultural perspective: behavioral experiments in 15 small-scale societies. *Behav. Brain Sci.* **28**, 795–815 (2005).
- Andreoni, J. & Bernheim, B. Social image and the 50–50 norm: a theoretical and experimental analysis of audience effects. *Econometrica* **77**, 1607–1636 (2009).
- Falk, A., Fehr, E. & Fischbacher, U. Testing theories of fairness—intentions matter. *Games Econ. Behav.* **62**, 287–303 (2008).
- Rabin, M. Incorporating fairness into game theory and economics. *Am. Econ. Rev.* **83**, 1281–1302 (1993).
- Schultz, W., Dayan, P. & Montague, P. R. A neural substrate of prediction and reward. *Science* **275**, 1593–1599 (1997).
- O'Doherty, J. P. Reward representations and reward-related learning in the human brain: insights from neuroimaging. *Curr. Opin. Neurobiol.* **14**, 769–776 (2004).
- Fliessbach, K. et al. Social comparison affects reward-related brain activity in the human ventral striatum. *Science* **318**, 1305–1308 (2007).
- Harbaugh, W. T., Mayr, U. & Burghart, D. R. Neural responses to taxation and voluntary giving reveal motives for charitable donations. *Science* **316**, 1622–1625 (2007).
- Tabibnia, G., Satpute, A. B. & Lieberman, M. D. The sunny side of fairness: preference for fairness activates reward circuitry (and disregarding unfairness activates self-control circuitry). *Psychol. Sci.* **19**, 339–347 (2008).
- Gurven, M. The evolution of contingent cooperation. *Curr. Anthropol.* **47**, 185–192 (2006).
- Kakwani, N. C. Measurement of tax progressivity: an international comparison. *Econ. J.* **87**, 71–80 (1977).
- Frank, R. H. Are workers paid their marginal products. *Am. Econ. Rev.* **74**, 549–571 (1984).
- Akerlof, G. A. & Yellen, J. L. The fair wage-effort hypothesis and unemployment. *Q. J. Econ.* **105**, 255–283 (1990).
- Krueger, A. B. & Mas, A. Strikes, scabs, and tread separations: labor strife and the production of defective Bridgestone/Firestone tires. *J. Polit. Econ.* **112**, 253–289 (2004).
- Fehr, E. & Fischbacher, U. The nature of human altruism. *Nature* **425**, 785–791 (2003).
- Fehr, E. & Gächter, S. Altruistic punishment in humans. *Nature* **415**, 137–140 (2002).
- Sanfey, A. G., Rilling, J. K., Aronson, J. A., Nystrom, L. E. & Cohen, J. D. The neural basis of economic decision-making in the Ultimatum Game. *Science* **300**, 1755–1758 (2003).
- Frank, R. H. *Choosing the Right Pond: Human Behavior and the Quest for Status* (Oxford Univ. Press, 1985).
- Herrmann, B., Thoni, C. & Gächter, S. Antisocial punishment across societies. *Science* **319**, 1362–1367 (2008).
- Hare, T. A., O'Doherty, J., Camerer, C. F., Schultz, W. & Rangel, A. Dissociating the role of the orbitofrontal cortex and the striatum in the computation of goal values and prediction errors. *J. Neurosci.* **28**, 5623–5630 (2008).
- Plassmann, H., O'Doherty, J. & Rangel, A. Orbitofrontal cortex encodes willingness to pay in everyday economic transactions. *J. Neurosci.* **27**, 9984–9988 (2007).
- Rilling, J. et al. A neural basis for social cooperation. *Neuron* **35**, 395–405 (2002).
- Moll, J. et al. Human fronto-mesolimbic networks guide decisions about charitable donation. *Proc. Natl Acad. Sci. USA* **103**, 15623–15628 (2006).
- Singer, T. et al. Empathic neural responses are modulated by the perceived fairness of others. *Nature* **439**, 466–469 (2006).
- Krajchich, I., Adolphs, R., Tranel, D., Denburg, N. L. & Camerer, C. F. Economic games quantify diminished sense of guilt in patients with damage to the prefrontal cortex. *J. Neurosci.* **29**, 2188–2192 (2009).

Supplementary Information is linked to the online version of the paper at www.nature.com/nature.

Acknowledgements We thank B. Bushong, N. Tetrault, S. Bray, J. Gläscher and R. Lee for their assistance. This work was supported by grants from the US National Science Foundation to J.O.D. (0617174), from the Human Frontiers of Science Program to C.F.C., and from the Gordon and Betty Moore Foundation to J.O.D., A.R., C.F.C. and the Caltech Brain Imaging Center.

Author Contributions E.T., A.R., C.F.C. and J.O.D. designed the experiment, E.T. conducted the experiment and analysed the data, and E.T., A.R., C.F.C. and J.O.D. discussed the results and wrote the paper.

Author Information Reprints and permissions information is available at www.nature.com/reprints. The authors declare no competing financial interests. Correspondence and requests for materials should be addressed to J.O.D. (johnpodoherty@gmail.com).

METHODS

Participants. Forty-two healthy, right-handed participants participated in the experiment; two were excluded for excessive head movement, leaving 40 subjects in the analysis (age 21.9 ± 3.6 years (mean \pm s.d.); range 18–34 years). Because of potential gender differences in social behaviour^{29,31}, the study included males only. Participants were pre-screened to ensure that they were within one standard deviation from the mean on the altruism subscore of the NEO PI-R personality questionnaire³². All participants gave informed consent, and the Institutional Review Board at the California Institute of Technology approved the study.

Experimental procedure. Pairs of participants who did not know each other performed the experiment. They were each paid a base \$30 fee at the beginning of the experiment, and then each drew a ball from a hat, labelled 'rich' or 'poor'. The 'rich' (high-pay) player received an immediate payment of \$50, whereas the 'poor' (low-pay) player received no bonus payment. They then performed an identical task, in consecutive fMRI scanning sessions (with scan order determined by another random draw).

In addition, two other behavioural versions of the experiment were performed with high-pay/high-pay and low-pay/low-pay pairs. The purpose of these experiments was to see whether any behavioural effects observed in the main experiment could be due to windfall gains rather than due to the inequality manipulation.

Stimulus presentation and behavioural data acquisition were implemented in Matlab (The Mathworks Inc.) with the Cogent 2000 toolbox (Wellcome Department of Imaging Neuroscience). For each trial of the experimental task, the participant viewed possible monetary transfers from the experimenter to himself and to the other player (Fig. 1). There were three trial types: transfer to high-pay player only, transfer to low-pay player only, and transfer to both players. Positive transfers varied randomly between \$1 and \$50. After 2 s, a rating scale appeared on the screen, and the participants rated how appealing they found the transfer on a scale of -5 (very unappealing) to 5 (very appealing) by moving a cursor along the scale with button presses. The rating period lasted 4 s and was followed by a jittered intertrial interval of 1–7 s.

Additional control trials were included in which X's were shown in place of the transfers. For these trials, a second, grey cursor was shown at a random value on the rating scale. Participants were asked to match the main cursor with the grey cursor and enter the response. The trials were randomly interspersed, with 120 experimental trials (40 of each type) and 60 control trials. The trials were broken up into four sessions of about 8 min each. After both players' scans, a single trial was randomly picked from the set, and the transfers for that trial were paid out.

fMRI data acquisition. A 3-T Trio scanner (Siemens) and an eight-channel phased array coil was used to acquire high-resolution T1-weighted structural images ($1 \text{ mm} \times 1 \text{ mm} \times 1 \text{ mm}$) for anatomical localization and T2*-weighted echo planar images (45 slices, $3 \text{ mm} \times 3 \text{ mm} \times 3 \text{ mm}$ voxels, $\text{TR} = 2.65 \text{ s}$, $\text{TE} = 30 \text{ ms}$, flip angle = 80° , $\text{FoV} = 192 \text{ mm} \times 192 \text{ mm}$, slice gap = 0 mm). Each image was acquired in an oblique orientation of 30° to the anterior-commissure-posterior-commissure (AC-PC) axis, which reduces signal drop-out in the vmPFC relative to AC-PC-aligned images³³.

Behavioural data analysis. For each participant, the behavioural ratings were regressed on the transfers to self and other. The resulting parameter estimates were used as summary statistics for between-subject random effects inference; the parameter estimates were pooled into a mixed-effects group analysis with the use of two-sided t -tests to determine whether the high-pay and low-pay groups differed in their social preferences. A two-way analysis of variance with experimental group (high-pay, low-pay) as a between-subjects factor and recipient (self, other) as a within-subjects factor was used to examine whether these parameter estimates differed between the experimental conditions. Post-hoc t -tests were used to determine whether the parameter estimates differed significantly between the high-pay and low-pay players for transfers to oneself and transfers to the other player.

fMRI preprocessing. We used SPM5 (Wellcome Department of Imaging Neuroscience) for fMRI data analysis. The images were slice-time corrected, realigned to the first volume to correct for subject motion, spatially transformed to match the Montreal Neurological Institute EPI template, and spatially smoothed with a Gaussian kernel (8 mm , full-width at half-maximum). We also applied intensity normalization and high-pass filtering (filter width 128 s) to the imaging data.

fMRI analysis 1. We estimated the parameters of a general linear model for each participant to generate voxel-wise statistical parametric maps of brain activation. For each participant we constructed an fMRI design matrix by modelling the following regressors for each session: 'task' (modelled as a 0-s duration event at the onset of each trial of the experimental task), 'transfer to self' (a parametric

modulator of the task regressor indicating the transfer amount to oneself), 'transfer to other' (a parametric modulator of the task regressor indicating the transfer amount to the other player) and 'control' (a 0-s duration event at the onset of each control trial). The regressors were convolved with a canonical haemodynamic response function. Regressors of no interest were also generated by using the realignment parameters from the image preprocessing to further correct for residual subject motion. The parameter estimates from this first-level analysis were then entered into a random (between-subject) effects group analysis, and linear contrasts were used to identify regions that responded differentially to transfers to self versus transfers to the other player, for the high-pay versus low-pay players.

Because of previous studies indicating a role for the ventral striatum and vmPFC in processing reward value, we had an a priori hypothesis that these regions would be involved in our study. A small-volume correction was performed based on the averaged MNI coordinates from previous studies^{12–14,27–29,34–38} (right vmPFC: $x = 9$, $y = 45$, $z = -13$; left vmPFC: $x = -8$, $y = 40$, $z = -13$; left striatum: $x = -10$, $y = 9$, $z = 0$), with a corrected significance threshold of $P < 0.05$. For anatomical localization, the statistical maps were rendered on the average of all subjects' structural images. For completeness, Supplementary Tables 1 and 2 list all regions displaying an effect with a voxel-wise significance threshold of $P < 0.001$, uncorrected. However, we cannot make strong conclusions about the regions outside our regions of interest, because we did not have a priori hypotheses regarding them, and no regions survived a whole-brain correction at a threshold of $P < 0.05$.

To quantify the effects we found to be significant, the underlying parameter estimates were plotted for each region of interest, by extracting the average parameter estimates from each activated cluster from each subject separately and plotting the average of those across subjects.

fMRI analysis 2. We estimated an additional related general model in which prediction error measures of the transfer to self were used as the sole parametric modulator. The prediction error measure was calculated from the following equations: $B(1) = 0$ for the low-pay group, $B(1) = 50$ for the high-pay group; and for all $t > 1$: $E_p(t) = V(t) - B(t)$; $B(t+1) = B(t) + \lambda \times E_p(t)$, where E_p is the prediction error, t the trial number, $V(t)$ is the value of the transfer to oneself on trial t , $\lambda = 0.5$ and B is the expected value. The data were modelled separately with λ values ranging from 0.1 to 0.7; $\lambda = 0.5$ was found to provide the best fit for the current data, and this value was used in the subsequent Bayesian model comparison.

Bayesian model comparison. We performed a Bayesian model comparison of the fit of the two general linear models at the random effects level, comparing the model in which we tested for a significant interaction in the responses to transfers of self compared with others between high-pay and low-pay subjects with the alternative prediction error account³⁹. This analysis outputs an exceedance probability that assigns a probability to the event that one model accounts better than the other model for neural activity in a given voxel. We report the results of the Bayesian model comparison at the a priori coordinates used for the small-volume corrections, so as not to bias the results by using regions or coordinates from our voxel-wise analysis.

- Andreoni, J. & Vesterlund, L. Which is the fair sex? Gender differences in altruism. *Q. J. Econ.* **116**, 293–312 (2001).
- Costa, P. T. Jr & McCrae, R. R. *Revised NEO Personality Inventory (NEO PI-R) and NEO Five-Factor Inventory (NEO-FFI) Professional Manual* (Psychological Assessment Resources, Inc., 1992).
- Deichmann, R., Gottfried, J. A., Hutton, C. & Turner, R. Optimized EPI for fMRI studies of the orbitofrontal cortex. *Neuroimage* **19**, 430–441 (2003).
- de Quervain, D. J. et al. The neural basis of altruistic punishment. *Science* **305**, 1254–1258 (2004).
- Nieuwenhuis, S. et al. Activity in human reward-sensitive brain areas is strongly context dependent. *Neuroimage* **25**, 1302–1309 (2005).
- Breiter, H. C., Aharon, I., Kahneman, D., Dale, A. & Shizgal, P. Functional imaging of neural responses to expectancy and experience of monetary gains and losses. *Neuron* **30**, 619–639 (2001).
- O'Doherty, J., Critchley, H., Deichmann, R. & Dolan, R. J. Dissociating valence of outcome from behavioral control in human orbital and ventral prefrontal cortices. *J. Neurosci.* **23**, 7931–7939 (2003).
- Lohrenz, T., McCabe, K., Camerer, C. F. & Montague, P. R. Neural signature of fictive learning signals in a sequential investment task. *Proc. Natl Acad. Sci. USA* **104**, 9493–9498 (2007).
- Stephan, K. E., Penny, W. D., Daunizeau, J., Moran, R. J. & Friston, K. J. Bayesian model selection for group studies. *Neuroimage* **46**, 1004–1017 (2009).

LETTERS

An essential role for XBP-1 in host protection against immune activation in *C. elegans*

Claire E. Richardson¹, Tristan Kooistra¹ & Dennis H. Kim¹

The detection and compensatory response to the accumulation of unfolded proteins in the endoplasmic reticulum (ER), termed the unfolded protein response (UPR), represents a conserved cellular homeostatic mechanism with important roles in normal development and in the pathogenesis of disease¹. The IRE1–XBP1/Hac1 pathway is a major branch of the UPR that has been conserved from yeast to human^{2–6}. X-box binding protein 1 (XBP1) is required for the differentiation of the highly secretory plasma cells of the mammalian adaptive immune system^{7,8}, but recent work also points to reciprocal interactions between the UPR and other aspects of immunity and inflammation^{9–11}. We have been studying innate immunity in the nematode *Caenorhabditis elegans*, having established a principal role for a conserved PMK-1 p38 mitogen-activated protein kinase (MAPK) pathway in mediating resistance to microbial pathogens¹². Here we show that during *C. elegans* development, XBP-1 has an essential role in protecting the host during activation of innate immunity. Activation of the PMK-1-mediated response to infection with *Pseudomonas aeruginosa* induces the XBP-1-dependent UPR. Whereas a loss-of-function *xbp-1* mutant develops normally in the presence of relatively non-pathogenic bacteria, infection of the *xbp-1* mutant with *P. aeruginosa* leads to disruption of ER morphology and larval lethality. Unexpectedly, the larval lethality phenotype on pathogenic *P. aeruginosa* is suppressed by loss of PMK-1-mediated immunity. Furthermore, hyperactivation of PMK-1 causes larval lethality in the *xbp-1* mutant even in the absence of pathogenic bacteria. Our data establish innate immunity as a physiologically relevant inducer of ER stress during *C. elegans* development and indicate that an ancient, conserved role for XBP-1 may be to protect the host organism from the detrimental effects of mounting an innate immune response to microbes.

We began our analysis of the role of the UPR in *C. elegans* immunity by asking if the UPR is activated upon exposure of *C. elegans* larvae to *P. aeruginosa* strain PA14, a human opportunistic pathogen that can also infect and kill *C. elegans*¹³. First, we assessed expression of the transgenic transcriptional reporter *Phsp-4::GFP(zIs4)* (the *C. elegans* *hsp-4* gene encodes a homologue of mammalian BiP/GRP78), which reflects activation of the IRE1–XBP-1 branch of the UPR⁵. After exposure of *C. elegans* larvae to *P. aeruginosa*, green fluorescent protein (GFP) expression was induced in the intestine, the site of infection (Fig. 1a). We confirmed the pathogen-induced activation of the endogenous *hsp-4* gene by quantitative polymerase chain reaction with reverse transcription (qRT–PCR) (Fig. 1b).

The mechanism by which IRE-1 activates XBP-1 in response to ER stress is conserved from yeast to mammals^{2,4–6}. Upon accumulation of unfolded proteins in the ER, the integral ER-membrane protein IRE-1 activates XBP-1 by alternative splicing of the *xbp-1* mRNA, thereby changing the reading frame. The activated ‘spliced form’ of XBP-1 regulates expression of genes involved in ER homeostasis,

such as those encoding chaperones. Using qRT–PCR to quantify the IRE-1-mediated splicing of *xbp-1* messenger RNA after exposure to *P. aeruginosa*, we found that there was a marked induction of IRE-1-spliced *xbp-1* transcript within 4 h of exposure to pathogen (Fig. 1c).

We hypothesized that the rapid activation of the IRE-1–XBP-1 pathway after *P. aeruginosa* exposure might be caused by induction of the host immune response. A conserved p38 MAPK pathway mediates innate immunity in organisms ranging from *C. elegans* to

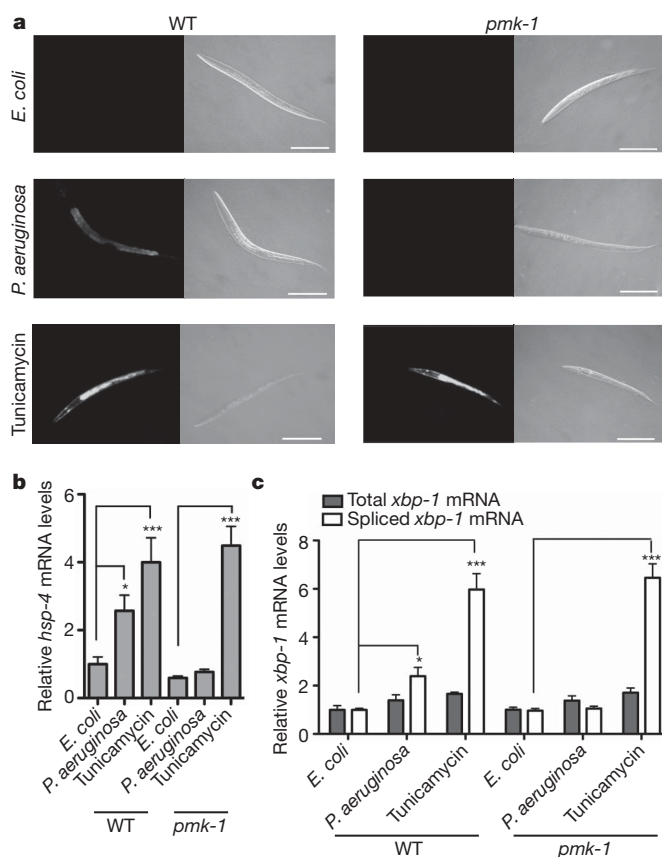


Figure 1 | PMK-1 p38 MAPK-dependent activation of the IRE1–XBP-1-dependent UPR by *P. aeruginosa* infection. **a**, Fluorescence and differential interference contrast (DIC) microscopy of wild-type (WT) and mutant larvae carrying the *Phsp-4::GFP(zIs4)* transgene 24 h after egg laying on indicated treatments. Scale bars, 100 μ m. **b**, qRT–PCR of endogenous *hsp-4* mRNA levels. **c**, qRT–PCR analysis of total and spliced *xbp-1* mRNA levels. Values represent fold change relative to wild type on OP50 \pm s.e.m. ($n = 4$ independent experiments, * $P < 0.05$ and *** $P < 0.001$, two-way ANOVA with Bonferroni post test).

¹Department of Biology, Massachusetts Institute of Technology, Cambridge, Massachusetts 02139, USA.

humans^{12,14}. We have previously shown that loss-of-function of the p38 MAPK orthologue PMK-1 results in markedly enhanced susceptibility to killing of *C. elegans* by *P. aeruginosa*. In the *pmk-1(km25)* mutant, we found no increase in IRE-1-spliced *xbp-1* mRNA and no induction of the *Phsp-4::GFP* reporter in response to *P. aeruginosa* (Fig. 1). RNA interference (RNAi) of *sek-1*, encoding a MAPKK required for PMK-1 activation¹², also abrogated induction of *Phsp-4::GFP* expression in response to *P. aeruginosa* infection (Supplementary Fig. 1a).

Consistent with the induction of XBP-1 splicing arising as a consequence of a transcriptional response to infection, we found that a mutant, *atf-7(qd22 qd130)*, carrying a mutation in a conserved transcription factor that abrogates the pathogen-induced expression of genes regulated by the PMK-1 pathway (R. Shivers *et al.*, manuscript submitted) also blocked induction of the *Phsp-4::GFP* reporter in response to *P. aeruginosa* PA14 (Supplementary Fig. 1b). Activation of the IRE-1–XBP-1 pathway in response to tunicamycin (an *N*-glycosylation inhibitor), however, occurred in the *pmk-1* mutant as in the wild-type strain N2 (hereafter referred to as wild type), as reported in a study of PMK-1-dependent activation of the IRE-1–XBP-1 pathway in the *C. elegans* response to a pore-forming toxin from *Bacillus thuringiensis*¹⁵. Whereas our data show that activation of the IRE-1–XBP-1 pathway by *P. aeruginosa* infection is dependent on the PMK-1 pathway, we did not observe a reciprocal dependence of activation of the PMK-1 pathway on XBP-1 (Supplementary Fig. 2).

We next asked if XBP-1 is required for resistance to *P. aeruginosa*, focusing on its role during larval development. Synchronized eggs of wild-type and mutants deficient in each of the three branches of the UPR were propagated on plates with *P. aeruginosa* PA14 as the only food source and development was monitored over time. Nearly all the eggs of the wild-type strain developed to at least the fourth larval stage (L4) in this assay, comparable to their growth and development on the relatively non-pathogenic bacterial strain and standard laboratory food source *Escherichia coli* OP50 (Fig. 2a). In contrast, the *xbp-1(zc12)* mutant on *P. aeruginosa* exhibited severely attenuated larval development and growth, as measured by the rate of progression between moults, size of larvae, and ability of larvae to reach the L4 stage by 72 h (Fig. 2a), eventually resulting in larval lethality. Loss-of-function mutations in each of the other two major branches of the UPR, *atf-6(ok551)* and *pek-1(ok275)*^{4,16}, did not affect larval development in the presence of *P. aeruginosa* (Fig. 2a). These data implicate a specific and essential role for the IRE-1–XBP-1 branch of the UPR in *C. elegans* development in the presence of *P. aeruginosa*.

The *xbp-1* developmental phenotype was alleviated in the presence of the *gacA* mutant of *P. aeruginosa* PA14 (Supplementary Fig. 3a), which has diminished pathogenicity in *C. elegans* and mammals^{13,17}. On a lawn of wild-type *P. aeruginosa* PA14 mixed with relatively non-pathogenic *E. coli*, the *xbp-1* mutant again exhibited the severely attenuated developmental phenotype that was observed in the presence of *P. aeruginosa* alone, indicating that the pathogenicity of *P. aeruginosa*, not a nutritional deficiency, caused the *xbp-1* developmental phenotype (Fig. 2b and Supplementary Fig. 3b). Behavioural avoidance of pathogenic bacteria^{18,19} can influence survival^{20–22}, but we found that the development of wild type was unaffected by experimental conditions in which the *P. aeruginosa* could not be avoided, demonstrating that the inability of the *xbp-1* mutant to develop on *P. aeruginosa* was not due to a defect in behavioural avoidance (C.E.R. and D.H.K., unpublished data). In addition, the attenuated development and death of the *xbp-1* mutant on *P. aeruginosa* was also unaffected by the blocking of cell necrosis (Supplementary Table 1).

Wild-type and *xbp-1* mutant larvae show characteristic ribosome-studded tubular structures of the ER by transmission electron microscopy when propagated on relatively non-pathogenic *E. coli* OP50 (Fig. 2c). The ER architecture of wild-type worms was not markedly perturbed upon exposure to *P. aeruginosa* (Fig. 2c). In contrast, *xbp-1(zc12)* larvae propagated on *P. aeruginosa* PA14 revealed disruption in ER morphology of *xbp-1* mutant worms upon pathogen exposure

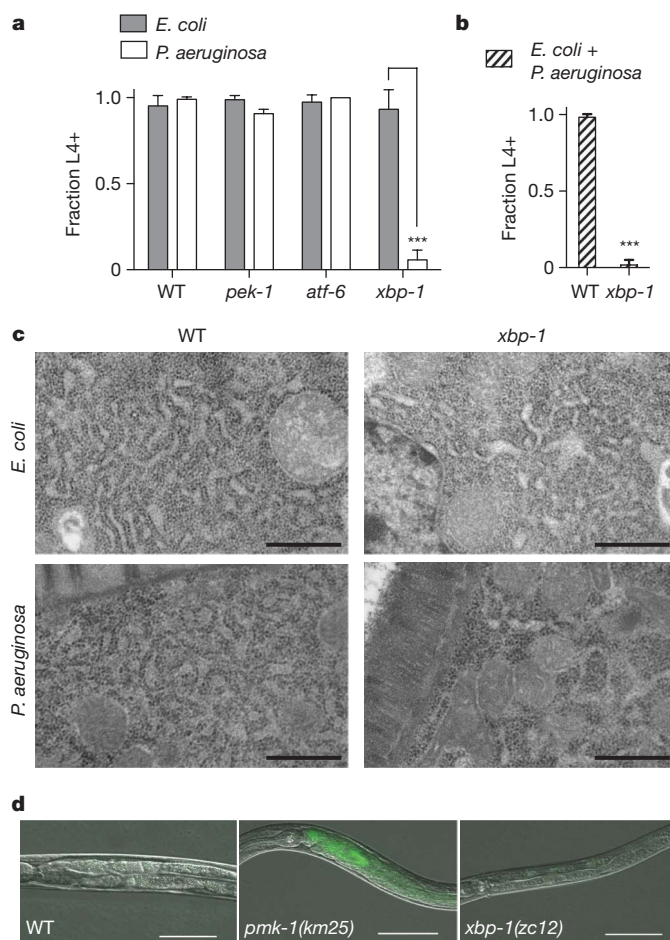


Figure 2 | XBP-1 is required for *C. elegans* development and survival on *P. aeruginosa*. **a**, **b**, Development of indicated mutants to the L4 larval stage or older after 3 days at 25 °C on either *P. aeruginosa* PA14 or *E. coli* OP50 (**a**), or a mixture of PA14 and *E. coli* HB101 (**b**). Plotted is mean \pm s.d. ($n = 3$ –4 plates, *** $P < 0.001$, two-way ANOVA with Bonferroni post test in **a**; $n = 4$ plates, *** $P < 0.001$ two-tailed t -test in **b**). Results in **a** and **b** are representative of three independent experiments. **c**, Transmission electron microscopy of L3 larvae at $\times 60,000$ magnification. Scale bars, 500 nm. **d**, Fluorescence and DIC microscopy overlay of larvae 40 h after egg laying on *P. aeruginosa* PA14 expressing GFP.

(Fig. 2c), with localized regions of dilated ER lumen, comparable to that induced by tunicamycin treatment of *xbp-1(zc12)* worms (Supplementary Fig. 4). Such changes in ER morphology are consistent with ER stress and perturbation²³, and indicate that a disruption in ER homeostasis is induced by *P. aeruginosa* PA14 infection in the *xbp-1* mutant.

We considered whether the developmental lethality of the *xbp-1* mutant might be attributable to the toxicity of PA14 arising from accelerated infection due to diminished resistance to *P. aeruginosa* in the *xbp-1* mutant. Because activation of the PMK-1 pathway results in the splicing of XBP-1 upon *P. aeruginosa* exposure, we first asked whether XBP-1 confers a survival benefit against *P. aeruginosa* by facilitating resistance to intestinal infection. Diminished activation of PMK-1-dependent innate immunity is accompanied by an increased rate of *P. aeruginosa* accumulation in the intestine¹² (Fig. 2d). If XBP-1 functioned downstream of PMK-1 to promote the immune response to *P. aeruginosa*, we would anticipate that *xbp-1* deficiency would lead to an increased rate of *P. aeruginosa* accumulation relative to wild type. Interestingly, in spite of the severely attenuated development and survival of the *xbp-1* mutant larvae on *P. aeruginosa*, the kinetics of accumulation of a PA14-derived strain of *P. aeruginosa* expressing GFP in the *xbp-1(zc12)* mutant were comparable to that observed for wild type (Fig. 2d). Although the *pmk-1(km25)* mutant exhibited an increased

rate of accumulation of *P. aeruginosa* (Fig. 2d), larval development and survival was markedly greater than that observed for the *xbp-1* mutant (Fig. 3a, b and Supplementary Fig. 5). These data decouple enhanced susceptibility to *P. aeruginosa* infection from the attenuated larval development phenotype of the *xbp-1* mutant and indicate that although activation of XBP-1 by *P. aeruginosa* infection is PMK-1-dependent, the primary protective role of XBP-1 is not to facilitate the killing of *P. aeruginosa*.

In view of these data, we considered whether the XBP-1-dependent UPR functions in this setting to protect against the ER stress induced by the immune response itself. If this were the case, then diminishing the immune response might actually improve the survival of the *xbp-1* mutant on *P. aeruginosa*. To test this hypothesis, we examined the larval development of a *xbp-1(zc12);pmk-1(km25)* double mutant. Notably, the *xbp-1;pmk-1* double mutant showed markedly increased development and survival relative to the *xbp-1* mutant, to a degree that was comparable to the development and survival of the *pmk-1* mutant (Fig. 3a, b). RNAi of *sek-1* and RNAi of *atf-7* in the *xbp-1(zc12)* mutant each alleviated the attenuated development phenotype in the presence of *P. aeruginosa* (Supplementary Fig. 6a, b). These data indicate that activation of the PMK-1-dependent transcriptional innate immune response to pathogen is indeed detrimental to survival during development in the absence of the IRE-1–XBP-1 pathway, and that the principal mechanism by which XBP-1 promotes development and survival during infection with *P. aeruginosa* is by protecting against the innate immune response.

To separate further the effect of toxicity caused by pathogenic *P. aeruginosa* from that caused specifically by immune activation on the *xbp-1* developmental phenotype, we next asked if the *xbp-1* mutant would be compromised in the setting of hyperactivation of the PMK-1-mediated immune response in the absence of *P. aeruginosa*. RNAi against *vhp-1*, which encodes a MAPK phosphatase that negatively

regulates PMK-1, results in hyperactivation of PMK-1 (ref. 24). We observed that RNAi of *vhp-1* resulted in sustained induction of the *Phsp-4::GFP(zcIs4)* reporter with the relatively non-pathogenic, standard laboratory food source *E. coli* OP50 as the only bacterium present in the assay (Fig. 4a). RNAi-mediated knockdown of *vhp-1* had little effect on development of wild-type worms (Fig. 4b). In contrast, RNAi of *vhp-1* severely impaired development of the *xbp-1(zc12)* mutant in the absence of pathogenic bacteria (Fig. 4b) in a manner similar to that observed for the *xbp-1* mutant when propagated on *P. aeruginosa* (Fig. 2a). Both the induction of *hsp-4* and the larval developmental phenotype of the *xbp-1* mutant resulting from RNAi of *vhp-1* were suppressed by *pmk-1* (Fig. 4a, b), demonstrating that the observed effects of RNAi of *vhp-1* were mediated by the PMK-1-dependent immune response.

Our data indicate that the XBP-1-mediated UPR has an essential role during *C. elegans* larval development by protecting against the activation of innate immunity. Transcriptional profiling of the *C. elegans* response to infection with *P. aeruginosa*^{25,26} has revealed the induction of at least 300 genes²⁵, nearly half of which are predicted to be trafficked through the ER. Although this innate immune response promotes pathogen resistance, retarding the intestinal accumulation of *P. aeruginosa* and substantially increasing the fraction of the population that survives through larval development (as shown by the survival of wild type relative to the *pmk-1(km25)* mutant (Fig. 3 and Supplementary Fig. 5)), our data suggest that innate immunity also constitutes a physiologically relevant source of ER stress that

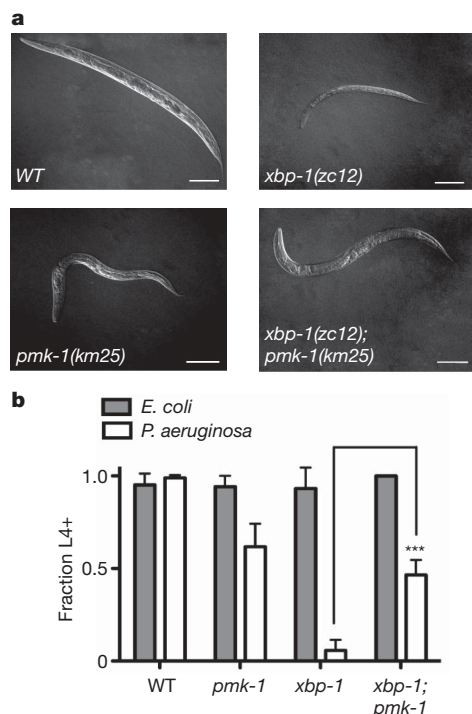


Figure 3 | Suppression of the *P. aeruginosa*-induced larval lethality phenotype of *xbp-1(zc12)* by *pmk-1(km25)*. **a**, DIC microscopy of representative worms of each genotype 3 days after egg laying on *P. aeruginosa* PA14. Scale bars, 100 μ m. **b**, Development of indicated mutants to the L4 larval stage or older after 3 days at 25 °C on either *P. aeruginosa* PA14 or *E. coli* OP50. Plotted is the mean \pm s.d. ($n = 3$ –4 plates, *** $P < 0.001$, two-way ANOVA with Bonferroni post test). Representative results of three independent experiments are shown.

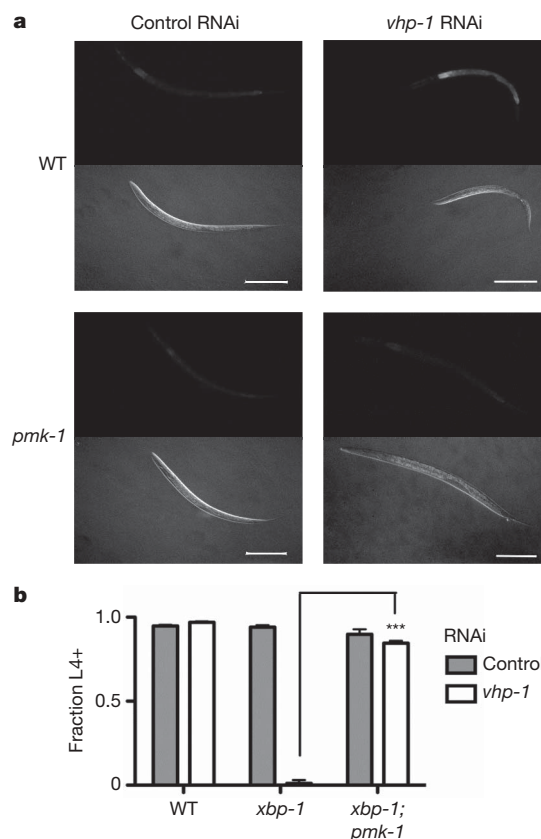


Figure 4 | XBP-1 is required for development and survival during pathogen-independent constitutive activation of PMK-1. **a**, Fluorescence and DIC microscopy of wild-type and *xbp-1* larvae carrying the *Phsp-4::GFP(zcIs4)* transgene, which have been treated with control (empty vector) or *vhp-1* RNAi, 24 h after egg laying. Scale bars, 100 μ m. **b**, Development to the L4 larval stage or older after 3 days at 25 °C of wild-type, *xbp-1(zc12)* and *xbp-1(zc12);pmk-1(km25)* mutants that have been subjected to RNAi of *vhp-1* and propagated on *E. coli* OP50. Plotted is mean \pm s.e.m. ($n = 3$ independent experiments, *** $P < 0.001$, two-way ANOVA with Bonferroni post test).

necessitates the compensatory activity of the UPR in *C. elegans* larval growth and development. An ancient role for the UPR may be to facilitate the development and survival of metazoan cell types that are exposed to the environment and mount a defensive, secretory response to microbial pathogens and abiotic toxins^{4,27}. Our data not only support this hypothesis, but more specifically indicate that in fact the essential role of XBP-1 lies not in the neutralization of these environmental insults, but instead in conferring protection against the potentially lethal ER stress that is induced by this response. Our findings support the idea that the microbiota of multicellular organisms may represent the most commonly encountered and physiologically relevant inducer of such ER stress. Consistent with this hypothesis is the Paneth cell death observed in *Xbp1* intestinal knockout mice¹⁰. Evolutionary conservation of the function of XBP-1 that we have defined in *C. elegans* would implicate the UPR in protection against ER toxicity caused by activation of immune and inflammatory pathways in mammals, where the UPR may have a critical role in the pathogenesis of infectious and inflammatory autoimmune diseases.

METHODS SUMMARY

Caenorhabditis elegans strains were maintained as described²⁸. Strains used in this study were N2 Bristol wild-type strain, SJ4005 *Phsp-4::GFP(zcls4)*, ZD305 *pmk-1(km25);Phsp-4::GFP(zcls4)*, ZD441 *atf-7(qd22 qd130);Phsp-4::GFP(zcls4)*, ZD361 *xbp-1(zc12)*, RB545 *pek-1(ok275)*, RB772 *atf-6(ok551)*, ZD363 *xbp-1(zc12);pmk-1(km25)*, ZD416 *xbp-1(tm2457)*, ZD417 *xbp-1(tm2457);pmk-1(km25)*, ZD418 *xbp-1(tm2482)* and ZD419 *xbp-1(tm2482);pmk-1(km25)*. Strain construction is detailed in Methods. All *P. aeruginosa* (strain PA14) plates were prepared as described¹³; exceptions are detailed in Methods. For tunicamycin treatments, tunicamycin was added to *E. coli* plates at 5 µg ml⁻¹ final concentration. Images were acquired with an Axioimager Z1 microscope using worms anaesthetized in 0.1% sodium azide. Transmission electron microscopy was performed as described in Methods. For RNA analysis, L1 larvae were synchronized by hypochlorite treatment, washed onto OP50 plates and grown at 20 °C for 23 h on OP50, then washed in M9 onto treatment plates. After 4 h, worms were washed off plates and frozen in liquid nitrogen. RNA and qRT-PCR methods are detailed in Methods. For development assays, *E. coli* OP50 plates were prepared in parallel with PA14 plates. Strains were egg laid in parallel onto four plates each of PA14 and OP50 (at least 80 eggs for each strain and treatment), and the fraction of worms growing to at least the L4 larval stage (L4+) between the plates was averaged. The L4 stage of development was chosen owing to the ease of scoring vulval development. RNAi by feeding of bacteria²⁹ was performed as described by propagating stains on *E. coli* HT115 carrying the RNAi clones as indicated at 20 °C, and adult progeny were used to lay eggs in experiments, which were performed at 25 °C. Details regarding RNAi clones are in Methods. Statistical analysis was performed using GraphPad Prism (GraphPad Software).

Full Methods and any associated references are available in the online version of the paper at www.nature.com/nature.

Received 2 June; accepted 15 December 2009.

- Schröder, M. & Kaufman, R. J. The mammalian Unfolded Protein Response. *Annu. Rev. Biochem.* **74**, 739–789 (2005).
- Cox, J. S. & Walter, P. A novel mechanism for regulating activity of a transcription factor that controls the Unfolded Protein Response. *Cell* **87**, 391–404 (1996).
- Mori, K., Kawahara, T., Yoshida, H., Yanagi, H. & Yura, T. Signalling from endoplasmic reticulum to nucleus: transcription factor with a basic-leucine zipper motif is required for the Unfolded Protein Response pathway. *Genes Cells* **1**, 803–817 (1996).
- Shen, X. *et al.* Complementary signaling pathways regulate the Unfolded Protein Response and are required for *C. elegans* development. *Cell* **107**, 893–903 (2001).
- Calfon, M. *et al.* IRE1 couples endoplasmic reticulum load to secretory capacity by processing the *xbp-1* mRNA. *Nature* **415**, 92–96 (2002).
- Yoshida, H., Matsui, T., Yamamoto, A., Okada, T. & Mori, K. XBP1 mRNA is induced by ATF6 and spliced by IRE1 in response to ER stress to produce a highly active transcription factor. *Cell* **107**, 881–891 (2001).
- Reimold, A. M. *et al.* Plasma cell differentiation requires the transcription factor XBP-1. *Nature* **412**, 300–307 (2001).

- Iwakoshi, N. N. *et al.* Plasma cell differentiation and the Unfolded Protein Response intersect at the transcription factor XBP-1. *Nature Immunol.* **4**, 321–329 (2003).
- Todd, D. J., Lee, A.-H. & Glimcher, L. H. The endoplasmic reticulum stress response in immunity and autoimmunity. *Nature Rev. Immunol.* **8**, 663–674 (2008).
- Zhang, K. *et al.* Endoplasmic reticulum stress activates cleavage of CREBH to induce a systemic inflammatory response. *Cell* **124**, 587–599 (2006).
- Kaser, A. *et al.* XBP1 links ER stress to intestinal inflammation and confers genetic risk for human inflammatory bowel disease. *Cell* **134**, 743–756 (2008).
- Kim, D. H. *et al.* A conserved p38 MAP kinase pathway in *Caenorhabditis elegans* innate immunity. *Science* **297**, 623–626 (2002).
- Tan, M.-W., Mahajan-Miklos, S. & Ausubel, F. M. Killing of *Caenorhabditis elegans* by *Pseudomonas aeruginosa* used to model mammalian bacterial pathogenesis. *Proc. Natl Acad. Sci. USA* **96**, 715–720 (1999).
- Dong, C., Davis, R. J. & Flavell, R. A. MAP kinases in the immune response. *Annu. Rev. Immunol.* **20**, 55–72 (2002).
- Bischof, L. J. *et al.* Activation of the Unfolded Protein Response is required for defenses against bacterial pore-forming toxin *in vivo*. *PLoS Pathog.* **4**, e1000176 (2008).
- Shen, X., Ellis, R. E., Sakaki, K. & Kaufman, R. J. Genetic interactions due to constitutive and inducible gene regulation mediated by the Unfolded Protein Response in *C. elegans*. *PLoS Genet.* **1**, e37 (2005).
- Rahme, L. G. *et al.* Common virulence factors for bacterial pathogenicity in plants and animals. *Science* **268**, 1899–1902 (1995).
- Zhang, Y., Lu, H. & Bargmann, C. I. Pathogenic bacteria induce aversive olfactory learning in *Caenorhabditis elegans*. *Nature* **438**, 179–184 (2005).
- Pujol, N. *et al.* A reverse genetic analysis of components of the Toll signaling pathway in *Caenorhabditis elegans*. *Curr. Biol.* **11**, 809–821 (2001).
- Reddy, K. C., Anderson, E. C., Kruglyak, L. & Kim, D. H. A polymorphism in *npr-1* is a behavioral determinant of pathogen susceptibility in *C. elegans*. *Science* **323**, 382–384 (2009).
- Shivers, R. P., Kooistra, T., Chu, S. W., Pagano, D. J. & Kim, D. H. Tissue-specific activities of an immune signaling pathway regulate physiological responses to pathogenic and nutritional bacteria in *C. elegans*. *Cell Host Microbe* **6**, 321–330 (2009).
- Styer, K. L. *et al.* Innate immunity in *Caenorhabditis elegans* is regulated by neurons expressing NPR-1/GPCR. *Science* **322**, 460–464 (2008).
- Rutkowski, D. T. *et al.* Adaptation to ER stress is mediated by differential stabilities of pro-survival and pro-apoptotic mRNAs and proteins. *PLoS Biol.* **4**, e374 (2006).
- Kim, D. H. *et al.* Integration of *Caenorhabditis elegans* MAPK pathways mediating immunity and stress resistance by MEK-1 MAPK kinase and VHP-1 MAPK phosphatase. *Proc. Natl Acad. Sci. USA* **101**, 10990–10994 (2004).
- Troemel, E. R. *et al.* p38 MAPK regulates expression of immune response genes and contributes to longevity in *C. elegans*. *PLoS Genet.* **2**, e183, doi:10.1371/journal.pgen.0020183 (2006).
- Shapira, M. *et al.* A conserved role for a GATA transcription factor in regulating epithelial innate immune responses. *Proc. Natl Acad. Sci. USA* **103**, 14086–14091 (2006).
- Kaufman, R. J. *et al.* The Unfolded Protein Response in nutrient sensing and differentiation. *Nature Rev. Mol. Cell Biol.* **3**, 411–421 (2002).
- Brenner, S. The genetics of *Caenorhabditis elegans*. *Genetics* **77**, 71–94 (1974).
- Timmons, L. & Fire, A. Specific interference by ingested dsRNA. *Nature* **395**, 854 (1998).

Supplementary Information is linked to the online version of the paper at www.nature.com/nature.

Acknowledgements Electron microscopy was performed by M. McKee in the Microscopy Core of the Center for Systems Biology/Program in Membrane Biology at Massachusetts General Hospital (supported by NIH grants DK43351 and DK57521). We thank E. Hartwig and G. Voeltz for discussions regarding the interpretation of electron microscopy images. We thank T. Stiernagle and the *Caenorhabditis* Genetics Center (supported by the NIH), and S. Mitani and the National Bioresource Project of Japan for strains. T.K. was supported by summer research fellowships from the Howard Hughes Medical Institute. This work was supported by NIH grant R01-GM084477, a Career Award in the Biomedical Sciences from the Burroughs Wellcome Fund, and an Ellison Medical Foundation New Scholar Award (to D.H.K.).

Author Contributions C.E.R. and D.H.K. conceived and planned experiments. C.E.R. and T.K. performed experiments. C.E.R. and D.H.K. analysed the data and wrote the paper.

Author Information Reprints and permissions information is available at www.nature.com/reprints. The authors declare no competing financial interests. Correspondence and requests for materials should be addressed to D.H.K. (dhkim@mit.edu).

METHODS

Strain construction. To make ZD361 and ZD363, SJ17 *xbp-1(zc12)* was outcrossed twice, removing *Phsp-4::GFP (zcls4)*, then crossed to ZD39 *pT24B8.5::GFP(agIs9)III;pmk-1(km25)* to isolate a *xbp1(zc12);pmk-1(km25)* double mutant. This *xbp-1(zc12);pmk-1(km25)* double mutant was backcrossed to ZD39 to isolate 4× backcrossed *xbp-1(zc12);pmk-1(km25)* and *xbp-1(zc12)*. To make ZD416, ZD417, ZD418 and ZD419, strains carrying the *xbp-1(tm2457)* and *xbp-1(tm2482)* alleles were outcrossed four times, then crossed to ZD39 *pT24B8.5::GFP(agIs9)III;pmk1(km25)*, from which single *xbp-1* and double *xbp-1;pmk-1* strains were isolated.

Preparation of *P. aeruginosa* treatment plates. *P. aeruginosa* PA14 was grown in Luria Broth (LB). For RNA preparation and electron microscopy, 25 µl overnight culture was seeded onto 10-cm plates. To make plates with lawns of mixed bacteria, *E. coli* HB101 containing an ampicillin-resistant plasmid encoding GFP was grown in LB with 50 µg ml⁻¹ ampicillin in parallel to *P. aeruginosa*, and the two cultures were mixed in equal parts before seeding 10 µl of the mix onto plates containing 25 µg ml⁻¹ carbenicillin. The presence of *E. coli* in the lawns at the end of assays was confirmed by the expression of GFP. To visualize intestinal accumulation of *P. aeruginosa*, *P. aeruginosa* PA14 containing an ampicillin-resistant plasmid encoding GFP was grown in LB with 50 µg ml⁻¹ ampicillin, and 10 µl of the culture was seeded onto plates containing 25 µg ml⁻¹ carbenicillin and spread to cover the surface of the plate (to prevent the growth of patches of the lawn from which the GFP plasmid had been lost).

Transmission electron microscopy. Synchronized L1 larvae were grown on *E. coli* (OP50) or *P. aeruginosa* (PA14) at 25 °C to the L3 stage (Fig. 2c), or as described in the figure legend (Supplementary Fig. 4), then fixed as described³⁰. The wild-type and *xbp-1(zc12)* strains were grown in parallel on *P. aeruginosa* and fixed twice in independent experiments with similar results.

RNA extraction, cDNA preparation and quantitative RT-PCR. Total RNA was isolated using Tri Reagent (Ambion), DNA contamination was removed with

DNA-free treatment (Ambion). cDNA was synthesized with RETROscript kit (Ambion) using oligo(dT) primers. Quantitative real-time PCR reactions were performed in triplicate using FastStart SYBR green master mix (Roche) with a Realplex mastercycler (Eppendorf). Relative mRNA was determined with the $\Delta\Delta C_t$ method using expression of *snb-1* (Fig. 1b) or the mean expression of *snb-1*, *act-1* and *tba-1* as a normalization control (Fig. 1c and Supplementary Fig. 2)^{25,31,32}. Biological replicates were compared as described³³. Primer efficiencies were tested with dilution series, and primer sequences are provided in Supplementary Table 2.

RNAi methodology. The *vhp-1* RNAi clone and clones of genes required for necrosis were from the Ahringer library, and the *sek-1* RNAi clone was from the Vidal library^{34,35}. A segment of the *atf-7* coding region, 771-bp region of *atf-7* corresponding to bases 11,532 to 12,303 with respect to cosmid C07G2, was amplified by PCR and subcloned into the Fire vector L4440 (R. Shivers *et al.*, manuscript submitted). The sequences of all clones were confirmed before use.

30. Troemel, E. R., Félix, M.-A., Whiteman, N. K., Barrière, A. & Ausubel, F. M. Microsporidia are natural intracellular parasites of the nematode *Caenorhabditis elegans*. *PLoS Biol.* **6**, e309 (2008).
31. Pocock, R. & Hobert, O. Oxygen levels affect axon guidance and neuronal migration in *Caenorhabditis elegans*. *Nature Neurosci.* **11**, 894–900 (2008).
32. Hoogewijs, D., Houthoofd, K., Matthijssens, F., Vandesompele, J. & Vanfleteren, J. R. Selection and validation of a set of reliable reference genes for quantitative *sod* gene expression analysis in *C. elegans*. *BMC Mol. Biol.* **9**, doi:10.1186/1471-2199-9-9 (2008).
33. Willems, E., Leyns, L. & Vandesompele, J. Standardization of real-time PCR gene expression data from independent biological replicates. *Anal. Biochem.* **379**, 127–129 (2008).
34. Kamath, R. S. *et al.* Systematic functional analysis of the *Caenorhabditis elegans* genome using RNAi. *Nature* **421**, 231–237 (2003).
35. Rual, J. F. *et al.* Toward improving *Caenorhabditis elegans* phenome mapping with an orfeome-based RNAi library. *Genome Res.* **14**, 2162–2168 (2004).

LETTERS

Tbx3 improves the germ-line competency of induced pluripotent stem cells

Jianyong Han^{1,3}, Ping Yuan¹, Henry Yang⁴, Jinqiu Zhang¹, Boon Seng Soh¹, Pin Li¹, Siew Lan Lim¹, Suying Cao¹, Junliang Tay¹, Yuriy L. Orlov², Thomas Lufkin¹, Huck-Hui Ng^{1,5}, Wai-Leong Tam^{1†} & Bing Lim^{1,6}

Induced pluripotent stem (iPS) cells can be obtained by the introduction of defined factors into somatic cells¹. The combination of Oct4 (also known as Pou5f1), Sox2 and Klf4 (which we term OSK) constitutes the minimal requirement for generating iPS cells from mouse embryonic fibroblasts. These cells are thought to resemble embryonic stem cells (ESCs) on the basis of global gene expression analyses; however, few studies have tested the ability and efficiency of iPS cells to contribute to chimaerism, colonization of germ tissues, and most importantly, germ-line transmission and live birth from iPS cells produced by tetraploid complementation. Using genomic analyses of ESC genes that have roles in pluripotency and fusion-mediated somatic cell reprogramming, here we show that the transcription factor Tbx3 significantly improves the quality of iPS cells. iPS cells generated with OSK and Tbx3 (OSKT) are superior in both germ-cell contribution to the gonads and germ-line transmission frequency. However, global gene expression profiling could not distinguish between OSK and OSKT iPS cells. Genome-wide chromatin immunoprecipitation sequencing analysis of Tbx3-binding sites in ESCs suggests that Tbx3 regulates pluripotency-associated and reprogramming factors, in addition to sharing many common downstream regulatory targets with Oct4, Sox2, Nanog and Smad1. This study underscores the intrinsic qualitative differences between iPS cells generated by different methods, and highlights the need to rigorously characterize iPS cells beyond *in vitro* studies.

The pluripotency and self-renewing properties of ESCs are conferred by a set of core factors that helps determine their unique identity. Adult somatic cells can be reprogrammed to resemble ESCs when some of these key transcription factors are introduced¹. iPS cells can be obtained by the viral transduction of a few genes in both mouse and human cells, albeit at low efficiency. Supplementations with chemical compounds such as inhibitors to DNA methyltransferase, histone deacetylase, histone methyltransferase, mitogen-activated protein kinase (MAPK) and glycogen synthase kinase-3 (GSK3) have been reported to improve the reprogramming efficiency^{2–4}. Recently, iPS cells have been generated without the use of viral vectors⁵. Although ESC-like iPS cells are routinely obtained with these methods, very few studies have carefully examined their germ-line contribution and transmission frequency⁶. Although iPS cells have a distinct morphology and express molecular markers similar to ESCs, their ability and degree of contribution to the chimaerism seem highly varied^{3,7–9}. This suggests that iPS cells do not completely resemble ESCs¹⁰, and there is marked disparity in the quality of different iPS cell lines. Hence, we postulated that other factors in addition to the basal requirements of OSK may improve the quality of iPS cells as defined by their capacity for high germ-line competency.

We speculated that iPS-cell-reprogramming factors may share common characteristics with pluripotency-associated genes whose perturbed levels in ESCs confer resistance to differentiation. Previous studies have shown that mouse ESCs that overexpress *Nanog* are resistant to differentiation¹¹, express higher levels of pluripotency-associated genes, and are more effective at reprogramming somatic cells by cell fusion¹². Depletion of another transcription factor, *Tcf3*, in ESCs limits their differentiation ability and upregulates the expression of pluripotency markers such as *Oct4*, *Sox2*, *Nanog* and *Sall4* (ref. 13). As both *Nanog* and *Tcf3* regulate each other and are core features of the ESC transcriptional network, we speculated that similar to *Nanog*-overexpressing ESCs, the loss of *Tcf3* may enhance fusion-mediated reprogramming of somatic hybrid cells. To test this, we used polyethyleneglycol to generate duo drug-resistant fusion hybrids between *Nanog* overexpressing or *Tcf3* RNA interference (RNAi) ESCs that were neomycin-resistant (Neo^r) and primary mouse embryonic fibroblasts (MEFs) that were puromycin-resistant (Puro^r) (Fig. 1a). Consistent with previous observations, *Nanog*-overexpressing ESCs showed enhanced reprogramming efficiency (Fig. 1b, c). Using *Tcf3*-deficient ESC lines, a significant increase in the number of hybrid clones was also observed (Fig. 1b, c). Karyotype analysis confirmed that these were tetraploid (Supplementary Fig. 1). The hybrids possess similar properties to the parental modified ESC lines, including their response to the lack of leukaemia inhibitory factor (LIF) and epigenetic reprogramming of the *Nanog* promoter (Supplementary Figs 2 and 3). We eliminated the possibility that improvements in reprogramming frequency were attributed to increased cell fusion events¹² (Supplementary Fig. 4).

To dissect the commonalities between *Nanog* and *Tcf3* pathways, we examined the repertoire of genes increased in *Nanog* overexpressing and *Tcf3* RNAi ESCs that could suggest shared downstream mediators. The intersected expression profiles revealed a handful of genes such as *Dazl*, *Fzd10*, *Hal*, *4930502E18Rik* and *Erf1* that were upregulated in both conditions (Supplementary Tables 1 and 2). Notably, *Tbx3*, a transcription factor previously reported to sustain pluripotency¹⁴, was strongly increased (Fig. 1d and Supplementary Fig. 5A). RNAi knock-down of *Tbx3* in ESCs induced differentiation (Fig. 1e), with concomitant downregulation of pluripotency-associated genes (Supplementary Table 3). *Tbx3* is also directly bound by both *Nanog* and *Tcf3* (Fig. 1f). In reprogrammed ESC-MEF hybrids, *Tbx3* levels remained greatly increased (Supplementary Fig. 5B and Supplementary Tables 4 and 5). To test the role of *Tbx3* in cell fusion-mediated reprogramming, we fused Neo^r *Tbx3* overexpressing ESC lines with MEFs (Supplementary Fig. 6). Indeed, there was an increase in the number of hybrids (Fig. 1b, c), which was not due to enhanced cell fusion (Supplementary Fig. 4).

¹Stem Cell and Developmental Biology, ²Systems Biology, Genome Institute of Singapore, 138672, Singapore. ³State Key Laboratory for Agrobiotechnology, College of Biological Sciences, China Agricultural University, Beijing 100193, China. ⁴Singapore Immunology Network, 138648, Singapore. ⁵Department of Biological Sciences, National University of Singapore, 117543, Singapore. ⁶Center for Life Sciences, Beth Israel Deaconess Medical Center, Harvard Medical School, Boston, Massachusetts 02115, USA. †Present address: Whitehead Institute for Biomedical Research, 9 Cambridge Center, Cambridge, Massachusetts 02142, USA.

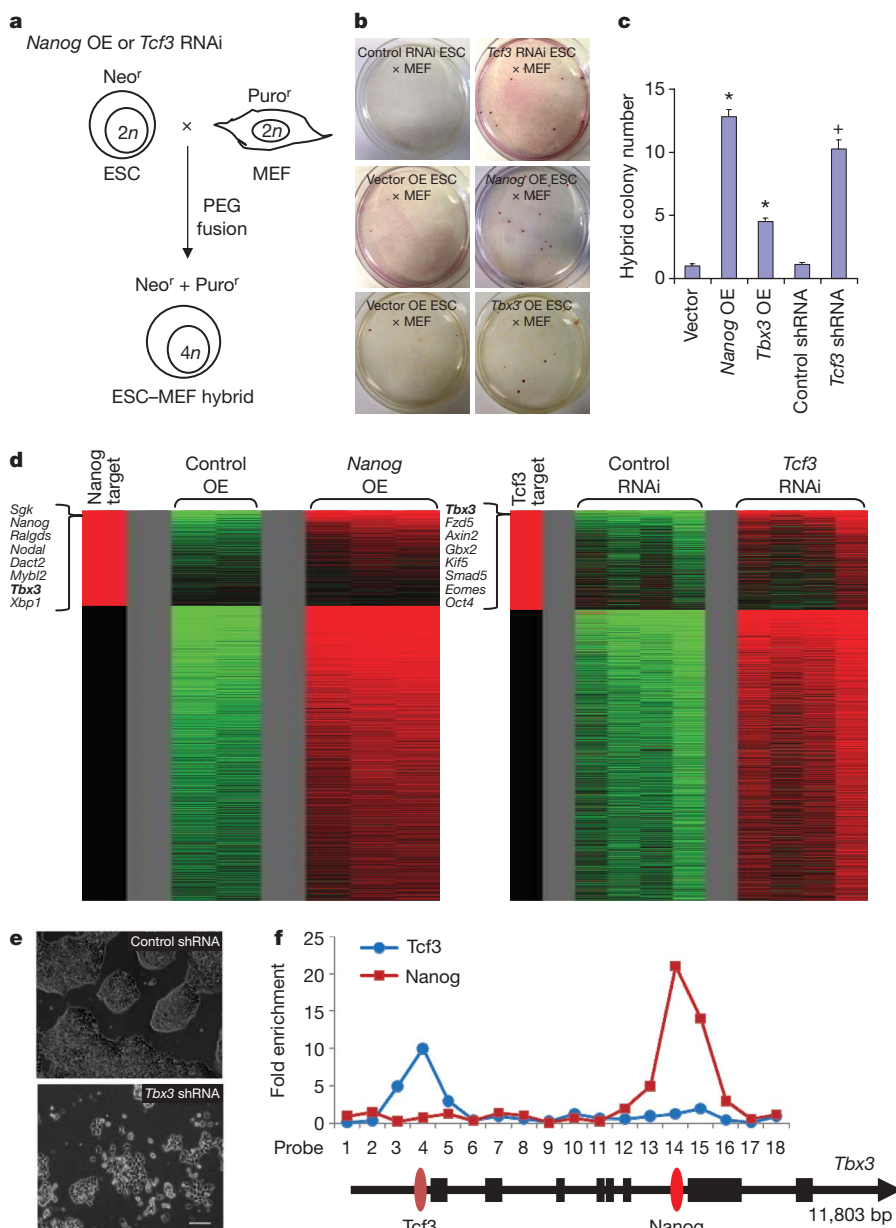


Figure 1 | Global gene expression profiling reveals *Tbx3* aids cell fusion-mediated reprogramming. **a**, Modified ESCs with *Nanog* overexpression (OE) or *Tcf3* RNAi were fused with MEFs to generate tetraploid ESC-MEF hybrids resistant to neomycin and puromycin. **b**, *Nanog* overexpression, *Tbx3* overexpression and *Tcf3* RNAi enhanced cell-fusion-mediated reprogramming of MEFs. Representative examples illustrate the emergence of ESC-MEF hybrid colonies. Control ESC fusion with MEFs resulted in an average of one per experiment, whereas *Tcf3* RNAi, *Nanog* overexpression or *Tbx3* overexpression ESCs produced several hybrid clones. **c**, *Nanog* overexpressing ESCs were efficient in reprogramming MEFs, generating 13 colonies, followed by *Tcf3* RNAi (10) and *Tbx3* overexpression (4.5). Numbers represent the average of four independent fusion experiments. Asterisk denotes significant difference from vector, plus symbol denotes significant difference from control short hairpin RNA (shRNA); error bars represent s.e.m. **d**, The heat-map shows all genes that were increased in treated ESCs compared to controls. *Tbx3* was among the most highly upregulated genes in *Nanog* overexpressing and *Tcf3* RNAi ESCs. The left-most column in red indicates direct gene targets of *Nanog* or *Tcf3* on the basis of the ChIP-PET²¹ and ChIP-chip¹³ databases, respectively. **e**, RNAi knockdown of *Tbx3* in ESCs led to a loss of self-renewal and induced differentiation. Scale bar, 100 μ m. **f**, Enrichment of *Tcf3* and *Nanog* occupancy on the *Tbx3* gene, as measured by ChIP-qPCR.

We postulated that *Tbx3* may also improve the reprogramming efficiency or the quality of iPS cells. Retroviral infection of MEFs bearing the *Oct4-GFP* transgene with OSKC induced ~ 300 ESC-like colonies per 5×10^4 starting cells (Fig. 2a). However, only $\sim 10\%$ of these showed activation of the transgene. The addition of *Tbx3* (OSKCT) did not increase the frequency of green fluorescent protein (GFP)⁺ colony numbers (Fig. 2a). With three factors (OSK), the total number of ESC-like colonies was markedly reduced but 74% of OSK colonies expressed GFP (Fig. 2a). The addition of *Tbx3* (OSKT) improved the colony count (~ 38 on average) when compared with OSK (~ 26), and the percentage of GFP⁺ colonies also significantly increased to 89% (Fig. 2a). Other qualitative differences between iPS cells obtained with different factor combinations were observed. OSKC iPS cell colonies were difficult to distinguish among transformed and partially reprogrammed cells that did not show GFP expression. OSK and OSKT iPS cell colonies were morphologically similar, with uniform GFP expression within individual colonies (Fig. 2b). However, although the activation of *Oct4* typically required 14 days after infection with OSK and OSKC, the use of OSKT took 9–10 days, suggesting that *Tbx3* accelerated the reprogramming process (Fig. 2c). The efficiency of isolating stable iPS cell lines from GFP⁺ colonies was similar between OSK and OSKT transduction,

but almost twofold higher than OSKC and OSKCT (Supplementary Fig. 7). For all the iPS cell lines obtained, we performed PCR analyses and confirmed genomic integration of the respective transduced genes (Supplementary Fig. 8). Molecular characterization of iPS cells from OSKT confirmed that these were alkaline-phosphatase-positive and expressed *Nanog*, *Sox2* and *SSEA1* (Supplementary Fig. 9). They also form teratomas comprised of several differentiated cell types when xenografted into severe combined immunodeficient (SCID) mice (Supplementary Fig. 10).

Next we sought to examine the differences in global transcriptome profiles between iPS cells generated using different factor combinations. To eliminate variations that could have arisen from handling techniques, and to ensure the reproducibility of properties inherent to iPS cell lines generated with different combinations, clones were isolated from two or more independent transduction experiments. Hierarchical clustering showed that the recently reported iPS cells generated with *Oct4*, *Sox2* and *Esrrb* (OSE)⁷ were most dissimilar to wild-type R1 and D3 ESCs with a correlation coefficient (R^2) of 0.92 (Fig. 3a). Both OSK and OSKT iPS cells bore closer resemblance to ESCs but were indistinguishable from each other; $R^2 = 0.94$. Hence, global expression profiling was not sufficiently sensitive to detect differences between these clones. Closer examination of specific gene level

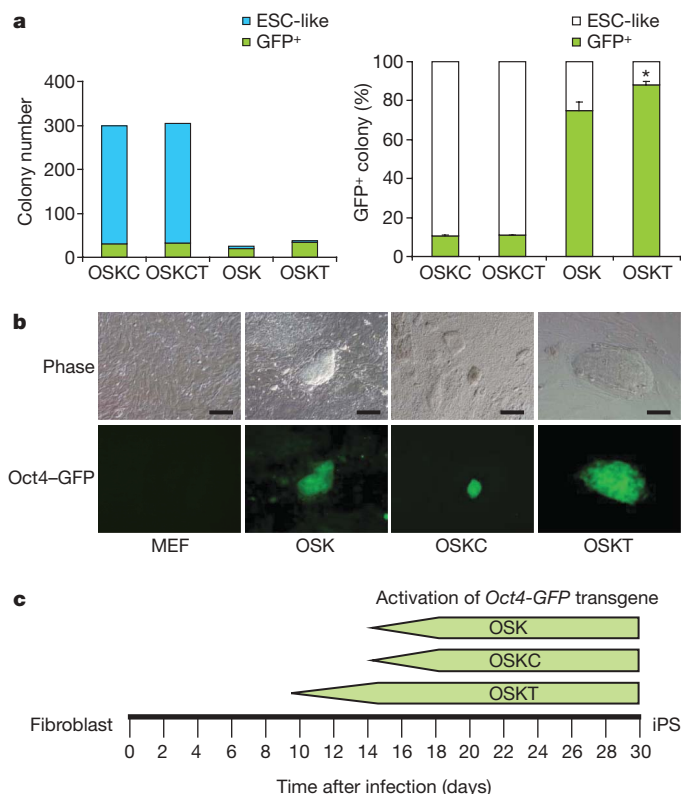


Figure 2 | Generation of iPS cells with Oct4, Sox2, Klf4 and Tbx3 retroviral transduction. **a**, OSKCT and OSKCT induced ~300 ESC-like colonies, with ~10% expressing GFP, whereas OSKT and OSK induced an average of 38 and 26 ESC-like colonies, with 89% and 74% GFP activation, respectively. Colonies were assessed and counted on day 16. Data represents the average of three independent transduction experiments. * $P < 0.05$, compared to OSK; error bars represent s.e.m. **b**, OSK and OSKT iPS cell clones showed tight, domed-shaped ESC-like morphology and uniform GFP expression throughout the colony, whereas OSKCT clones appeared as flattened, transformed cells with sparse GFP expression. Scale bars, 100 μ m. **c**, OSKT induced the activation of Oct4-GFP transgene in iPS derived from primary MEFs at days 9–10 after infection, whereas OSK and OSKCT combinations required 14 days, observed in four independent transduction experiment.

alterations, however, showed key differences (Fig. 3b and Supplementary Fig. 11). We compared the pluripotency-associated gene levels among OSK, OSKT iPS and ES cells. Most of these genes, such as *Sall4*, *Tcf3*, *Sox2*, *Zfx*, *Lin28*, *Utf1* and *Zic3*, were non-distinguishing between OSKT and OSK cells as their levels were similar. Surprisingly, a small subset of distinguishing features seemed to define OSKT from OSK cells. *Oct4*, *Nanog*, *Gdf3*, *Dppa4* and *Tbx3* levels in OSKT cells were equivalent to ESCs, but significantly reduced in OSK cells. This suggests that exogenous *Tbx3* may be crucial for assisting in re-establishing proper levels of certain ESC factors critical for the induction of pluripotency that cannot be completely achieved with OSK alone.

We then investigated whether OSKT cells were of higher quality than OSK and OSE cells (Supplementary Fig. 12; summarized in Supplementary Table 7). We selected numerous iPS cell lines generated from each combination that showed homogeneous activation of Oct4-GFP within each colony: OSKT 1, 2, 4, 6, 11–22; OSK 1–3, 12–14, 16–22; OSE 1, 2, 9. These lines were derived from four independent transduction experiments performed at different times to eliminate any bias in clonal selection that may arise from the stochastic behaviour of individual clones. iPS cells were then injected into 4–8-cell embryos and cultured *in vitro* to blastocysts (Supplementary Fig. 13). There was no difference in the maturation efficiency (~95%) between the three iPS cell types (data not shown). All blastocysts transplanted into the surrogate female mice had initially shown robust contribution of GFP⁺ cells to the inner cell mass (Supplementary Fig. 13) and live

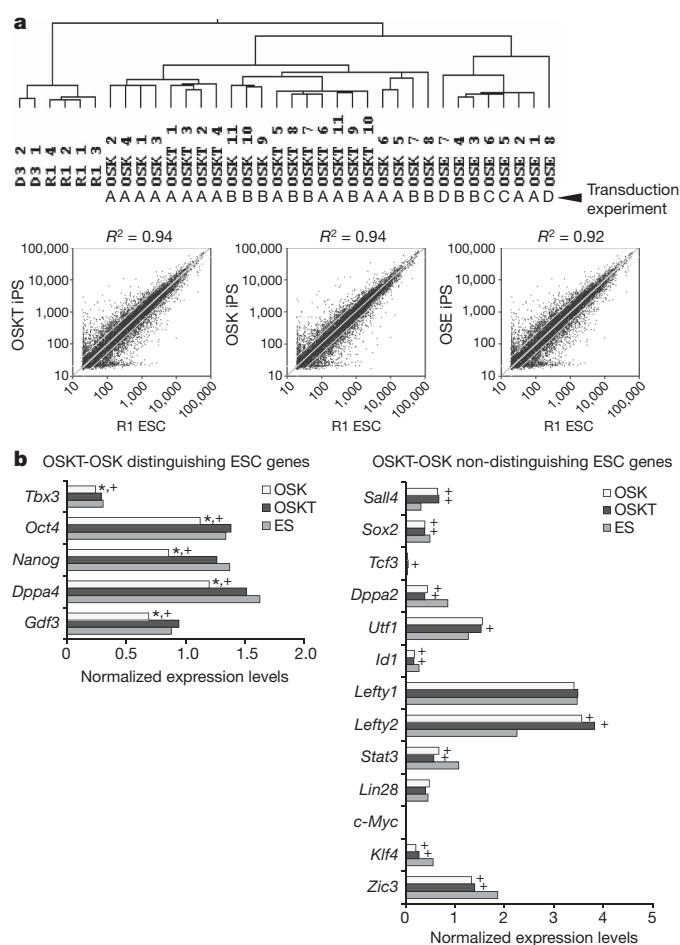


Figure 3 | Transcriptome of iPS cell clones generated with different combinations of reprogramming factors. **a**, Hierarchical clustering of global expression profiling showed that OSKT and OSK clones are more similar to wild-type ESCs than OSE, but indistinguishable from each other based on correlation coefficient. The R^2 value was obtained from the average individual gene signal intensity of all iPS clones in each combination and compared with R1 ESCs. The independent transduction experiments where the clones were isolated are denoted as A, B, C and D. **b**, Analysis of individual ESC-associated gene profiles showed a subset that could distinguish OSKT- from OSK-derived iPS cells. 'Distinguishing' ESC genes were expressed at similar levels between OSKT and ESCs, but at significantly lower levels in OSK. Most other ESC-associated genes were 'non-distinguishing' and present at similar levels in OSKT and OSK. Asterisk denotes significantly different from OSKT; plus symbol denotes significantly different from ESC; $P < 0.05$. Changes in gene expression based on microarray were confirmed with quantitative PCR (Supplementary Fig. 11).

chimaeras were obtained. As evaluated by coat colour, all OSKT and OSK chimaeras showed coats with varying density of black fur, signifying iPS cell contribution; whereas OSE chimaeras clearly had lesser black coats (Fig. 4c, top), indicating that OSE cells tend to contribute poorly to chimaerism.

More interestingly, obvious differences were discerned between OSKT and OSK cells in their ability to colonize the germ tissues. At embryonic day (E)13.5, gonads were obtained from the F₁ chimaeric embryos. 34.9% of the gonads from OSKT embryos showed contribution of iPS cells with GFP expression contrasting with 23.6% from OSK and 12.5% from OSE embryos (Fig. 4a, b and Supplementary Fig. 14; $P < 0.01$). Further assessment on the basis of GFP distribution within these gonads showed extensive contribution by OSKT cells, as 57.5% of the chimaeric gonads were >90% GFP⁺, compared to 26.2% of those from OSK embryos (Fig. 4b; $P < 0.01$). This indicates that OSKT cells were more efficient in colonizing the germ tissues. Using one of the most stringent criteria for demonstrating the quality of iPS cell clones, we tested their

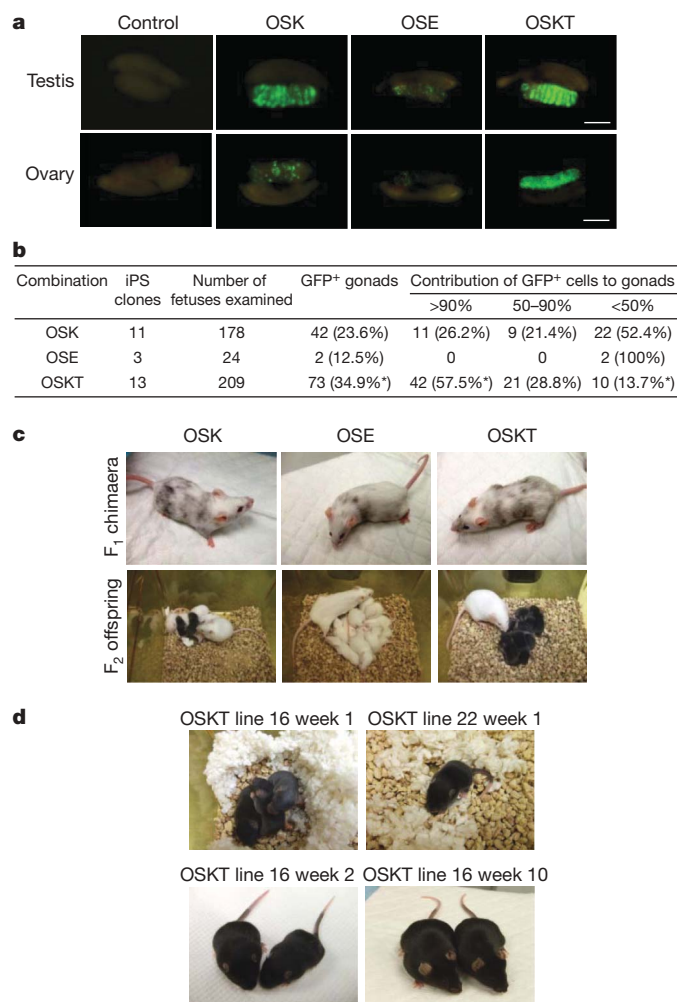


Figure 4 | OSKT iPS cells show enhanced germ-line contribution and transmission. The iPS clone number and the types of analyses that were performed are summarized in Supplementary Table 7. **a**, Representative photos of the quantitative contribution and spatial distribution of GFP⁺ cells generated with different reprogramming factor combinations in the gonads of chimaeric embryos. **b**, Tabulation comparing the contribution of GFP⁺ iPS-cell-derived germ cells to the gonads of chimaeric fetuses and their spatial distribution with different combinations of factors. OSKT iPS cells were most effective at colonizing the gonads, compared to OSK and OSE iPS cells. Asterisk denotes significantly different from OSK; $P < 0.01$. At least 11 independent sets of microinjections were performed for OSK versus OSKT comparison. **c**, Representative photos showing the contribution of iPS cells to chimaeric coat and the production of F₂ offspring after crossing with albino mice. Black offspring indicates germ-line transmission of iPS cells. **d**, Live birth animals obtained from two OSKT iPS cell lines tested by tetraploid complementation.

frequency for germ-line transmission and production of viable F₂ offspring. Once again, we used several iPS cell lines from each combination. iPS cells generated with OSE had very poor capacity for germ-line transmission (Fig. 4c, bottom and Table 1). Using five chimaeras from two lines that were bred with albino mice, a total of seven litters were obtained. Only one litter contained two out of ten offspring that had iPS cell-derived black coat. With OSK, nine chimaeras from five lines were used for breeding. Thirteen litters were produced, of which only two had 100% black offspring, and another four had an average of ~33%. Notably, with the nine OSKT chimaeras obtained from six lines, nine of 14 litters had 100% black offspring, three had 41%, 50% and 28% each, and there were only two with none (Table 1; $P < 0.005$).

Previous reports had implicated improper retroviral silencing and the frequency of retroviral integrations in altering the efficiency of

Table 1 | The germ-line transmission frequency of iPS cells

	iPS line	Chimaera	Total offspring per litter	Percentage
OSK	1	1	11 (11); 4 (4)	100.0
		2	10 (0)	0
	2	3	6 (2); 10 (4)	37.5
		4	12 (0)	0
		5	8 (0)	0
	12	8	8 (0); 10 (0)	0
	13	6	11 (3); 3 (1)	28.5
		7	5 (0)	0
	14	9	9 (0)	0
OSE	1	1	10 (2)	20.0
	2	2	13 (0); 9 (0)	0
		3	9 (0)	0
		4	10 (0)	0
OSKT*	6	5	8 (0); 10 (0)	0
		1	13 (13); 10 (10)	100.0
		2	7 (7)	100.0
		3	8 (4); 12 (5)	45.0
		4	6 (6); 9 (9); 10 (0)	100.0
	11	5	10 (0)	0
		6	6 (6)	100.0
		7	7 (2)	28.6
	13	7	7 (0)	0
	14	8	7 (0)	0
	15	9	4 (4); 7 (7)	100.0

The germ-line transmission frequency of iPS cells generated with different combinations of factors is shown. For each combination, between two and six iPS cell lines were used to obtain live chimaeras, of which at least one male from each combination was crossed with an albino female to determine the frequency of black F₂. Values in parentheses denote the frequency of black offspring.

* Significantly different from OSK and OSE, $P < 0.005$ and $P < 0.001$, respectively.

generating iPS cells and their resultant properties¹⁵. To exclude these possibilities, we confirmed that exogenous expression from the retroviral plasmids was silenced (Supplementary Fig. 15). Southern blot analyses showed that retroviral integration of *Oct4*, *Sox2* and *Klf4* transgenes into either OSK or OSKT cells was comparable (Supplementary Fig. 16). Notably, even with the additional integration of exogenous *Tbx3*, these cells were consistently of higher quality, thus ruling out the effects of DNA damage. We then speculated that the higher quality OSKT iPS cells could be used to generate viable mice composed entirely of the engineered cells through tetraploid complementation^{16,17}. This has not been shown previously, perhaps owing to the difficulty in generating high-quality iPS cells. Five lines of each OSK and OSKT were tested. In two lines of each, surrogate females were sacrificed at E19 to check for embryos. Only one embryo was obtained out of 66 implanted tetraploid aggregates for OSK cells, whereas four embryos were obtained out of 59 implants for OSKT cells. With the remaining three lines from each, implanted females were followed to term. With OSK lines, only one produced live birth, with a cumulative yield of three births from 105 implants, whereas two of the OSKT lines yielded 11 live births out of 107 implants, and two animals continued to thrive beyond ten weeks (Fig. 4d).

To understand better how *Tbx3* may contribute to improving iPS cell quality, we performed Solexa chromatin immunoprecipitation (ChIP)-sequencing to uncover the direct regulatory targets of *Tbx3* in ESCs (Supplementary Table 6). Hierarchical clustering of *Tbx3* with the previously mapped ESC factors¹⁸ showed that it shares a large number of common binding sites with the classic pluripotency-associated transcription factors *Oct4*, *Sox2*, *Nanog* and *Smad1* (Supplementary Fig. 17). *Tbx3* is also found to target ESC factors *Oct4*, *Sox2*, *Sall4*, *Lefty1*, *Lefty2* and *Zfp42*, as well as reprogramming factors *Klf2*, *Klf4*, *Klf5*, *N-myc* (also known as *Mycn*) and *c-myc* (*Myc*) (Supplementary Fig. 18).

Taken altogether, our study highlights the success of OSKT combination in generating high-quality iPS cells capable of germ-line transmission at high efficiency. Previous studies have primarily used morphological assessments and global gene expression analyses as indicators of iPS cell pluripotency. However, *in vitro* analyses are not sufficient to distinguish bona fide iPS cells with true ESC properties from poor-quality iPS cells that do not possess germ-line competency. The ability of OSKT cells to generate high frequency live-birth mice by

tetraploid complementation further strengthens the qualitative effect of *Tbx3*. Although *Tbx3* retroviral transduction in conjunction with OSK significantly improves iPS cell quality, we noted that not all OSK clones would manifest robust germ-line transmission. Two reports of more uniform platforms for reprogramming could help address this issue further. First, an inducible system in homogenous starting fibroblast population¹⁹ that includes *Tbx3* for reprogramming may allow for derivation and evaluation of iPS clones with more consistent biological properties. Second, the dual inhibition of MAPK signalling pathway and GSK3, which greatly enhances the conversion of pre-iPS to fully pluripotent iPS cells⁴ may also lead to the production of iPS clones with more uniform properties.

With the emergence of modified genetic and chemical methods, and an emphasis on the use of minimal reprogramming factors to derive iPS cells, some benchmark as exemplified here by OSK-derived iPS cells should be used to evaluate their qualitative and biological properties (Supplementary Fig. 19). The precise mechanistic role for *Tbx3* in vastly improving iPS cell quality needs more clarification. The initial ChIP-sequencing data suggests that *Tbx3* may be important for the effective re-establishment of the ESC circuitry during the onset of reprogramming, and its subsequent maintenance. The presence of exogenous *Tbx3* during the initiation of reprogramming may ensure proper titration of pluripotency-associated and reprogramming factors that are reactivated by OSK to the optimal level. We propose a model in which the re-establishment of pluripotency from a somatic state is achieved in an increasing probabilistic step-wise manner (Supplementary Fig. 19). The use of different factor combinations results in the generation of iPS cell populations and clones with markedly varied developmental potentials centred on attaining progressive 'landmarks' of pluripotency. The addition of *Tbx3* to a particular combination increases the probabilistic frequency of iPS cells that attain a pluripotent state equivalent or closest to ESCs within the entire population of reprogrammed cells.

METHODS SUMMARY

Tbx3 was cloned into pLenti6-UBC and pMXs vectors; *Oct4*, *Sox2*, *Klf4*, *c-Myc* plasmids were obtained from Addgene; *Esrrb* was obtained from ref. 7. Retrovirus and lentivirus were generated as previously described^{1,20}. Equal amounts of virus encoding different combination of factors were applied to 5×10^4 plated *Oct4*-GFP transgenic MEFs in 10-cm² dishes. After 24 h, inactivated feeder cells were added, and the culture was then maintained for up to 21 days. To generate chimaeras, albino embryos were isolated at the 2-cell stage, matured to the 4–8-cell stage and microinjected with iPS cells using the Piezo Micro Manipulator. Injected embryos were cultured to the blastocyst stage and transferred to the uterine horns of E2.5 pseudopregnant F₁ (CBA \times C57BL/6J) females. Chimaeric embryos were collected at E13.5 for analyses of GFP expression in the gonads. For tetraploid complementation, tetraploid (4*n*) embryos were generated using 2-cell electrofusion and incubated in KSOM until the 4–8-cell stage before aggregation with iPS cells. The zona pellucida of the tetraploid 4–8-cell stage embryos were removed by brief exposure to acid Tyrode's solution. Three tetraploid embryos and ~40 iPS cells were aggregated in a single well, and incubated in medium for 24 h to form a morula or blastocyst^{16,17}. Approximately 10–14 embryos were transferred into the uterus or oviducts of pseudopregnant mice.

Full Methods and any associated references are available in the online version of the paper at www.nature.com/nature.

Received 14 February; accepted 9 December 2009.

Published online 7 February 2010.

1. Takahashi, K. & Yamanaka, S. Induction of pluripotent stem cells from mouse embryonic and adult fibroblast cultures by defined factors. *Cell* **126**, 663–676 (2006).

2. Huangfu, D. *et al.* Induction of pluripotent stem cells by defined factors is greatly improved by small-molecule compounds. *Nature Biotechnol.* **26**, 795–797 (2008).
3. Shi, Y. *et al.* Induction of pluripotent stem cells from mouse embryonic fibroblasts by *Oct4* and *Klf4* with small-molecule compounds. *Cell Stem Cell* **3**, 568–574 (2008).
4. Silva, J. *et al.* Promotion of reprogramming to ground state pluripotency by signal inhibition. *PLoS Biol.* **6**, e253 (2008).
5. Okita, K., Nakagawa, M., Hyenjong, H., Ichisaka, T. & Yamanaka, S. Generation of mouse induced pluripotent stem cells without viral vectors. *Science* **322**, 949–953 (2008).
6. Daley, G. Q. *et al.* Broader implications of defining standards for the pluripotency of iPS cells. *Cell Stem Cell* **4**, 200–201 (2009).
7. Feng, B. *et al.* Reprogramming of fibroblasts into induced pluripotent stem cells with orphan nuclear receptor *Esrrb*. *Nature Cell Biol.* **11**, 197–203 (2009).
8. Marson, A. *et al.* Wnt signaling promotes reprogramming of somatic cells to pluripotency. *Cell Stem Cell* **3**, 132–135 (2008).
9. Wernig, M. *et al.* *In vitro* reprogramming of fibroblasts into a pluripotent ES-cell-like state. *Nature* **448**, 318–324 (2007).
10. Chin, M. H. *et al.* Induced pluripotent stem cells and embryonic stem cells are distinguished by gene expression signatures. *Cell Stem Cell* **5**, 111–123 (2009).
11. Mitsui, K. *et al.* The homeoprotein *Nanog* is required for maintenance of pluripotency in mouse epiblast and ES cells. *Cell* **113**, 631–642 (2003).
12. Silva, J., Chambers, I., Pollard, S. & Smith, A. *Nanog* promotes transfer of pluripotency after cell fusion. *Nature* **441**, 997–1001 (2006).
13. Tam, W. L. *et al.* T-cell factor 3 regulates embryonic stem cell pluripotency and self-renewal by the transcriptional control of multiple lineage pathways. *Stem Cells* **26**, 2019–2031 (2008).
14. Ivanova, N. *et al.* Dissecting self-renewal in stem cells with RNA interference. *Nature* **442**, 533–538 (2006).
15. Hotta, A. & Ellis, J. Retroviral vector silencing during iPS cell induction: an epigenetic beacon that signals distinct pluripotent states. *J. Cell. Biochem.* **105**, 940–948 (2008).
16. Eakin, G. S. & Hadjantonakis, A. K. Production of chimeras by aggregation of embryonic stem cells with diploid or tetraploid mouse embryos. *Nature Protocols* **1**, 1145–1153 (2006).
17. Ohta, H., Sakaide, Y., Yamagata, K. & Wakayama, T. Increasing the cell number of host tetraploid embryos can improve the production of mice derived from embryonic stem cells. *Biol. Reprod.* **79**, 486–492 (2008).
18. Chen, X. *et al.* Integration of external signaling pathways with the core transcriptional network in embryonic stem cells. *Cell* **133**, 1106–1117 (2008).
19. Wernig, M. *et al.* A drug-inducible transgenic system for direct reprogramming of multiple somatic cell types. *Nature Biotechnol.* **26**, 916–924 (2008).
20. Yu, J. *et al.* Induced pluripotent stem cell lines derived from human somatic cells. *Science* **318**, 1917–1920 (2007).
21. Loh, Y. H. *et al.* The *Oct4* and *Nanog* transcription network regulates pluripotency in mouse embryonic stem cells. *Nature Genet.* **38**, 431–440 (2006).

Supplementary Information is linked to the online version of the paper at www.nature.com/nature.

Acknowledgements This work is supported by the Agency for Science, Technology and Research (Singapore) and the Singapore Stem Cell Consortium grant (SSCC-06-003). The work is also partially supported by National Institutes of Health (NIH) grants to B.L. (DK047636 and AI54973). W.-L.T. is supported by the A*STAR Post-doctoral Fellowship. We acknowledge the Genome Technology and Biology group for technical support. We are grateful to T. Huber, P. Robson and L. Stanton for critical comments, V. Cacheux-Rataboul for karyotype analyses, Y. Loon Lee, P. Gaughwin and colleagues from the Stem Cell and Developmental Biology group for technical assistance. We also thank T. Wakayama and N. Li for imparting mouse embryo manipulation techniques.

Author Contributions J.H., W.-L.T. and B.L. conceptualized and designed the experiments; J.H. and W.L.T. performed most of the experiments and analysed the data; P.Y. and J.Z. performed molecular cloning and ChIP experiments; S.L.L. performed Southern hybridizations; J.T., P.L. and S.C. assisted with cell culture and mouse embryo manipulation; B.S.S. performed microarray and quantitative PCR measurements; H.Y. and Y.L.O. performed bioinformatics analyses; T.L. and H.-H.N. analysed the data and commented on the manuscript. W.L.T. and B.L. conceived the study and wrote the manuscript.

Author Information All microarray and sequencing data are available from the Gene Expression Omnibus database (<http://www.ncbi.nlm.nih.gov/geo>) under accession codes GSE19164 and GSE19219. Reprints and permissions information is available at www.nature.com/reprints. The authors declare no competing financial interests. Correspondence and requests for materials should be addressed to W.-L.T. (tamwli@wi.mit.edu) or B.L. (limb1@gis.a-star.edu.sg).

METHODS

Cell culture and transfection. All cell cultures were maintained at 37 °C with 5% CO₂. The culture of mouse R1 and D3 ESCs was described previously²². HEK293T cells were maintained in DMEM supplemented with 10% FBS and penicillin/streptomycin. Transfection of plasmids into mouse ESCs and HEK293 cells was performed using Lipofectamine 2000 (Invitrogen). Plat-E packaging cells (Cell Biolabs), which were used to produce retrovirus, were maintained according to the manufacturer's guide.

Plasmid construction, viral packaging and infection. Coding sequences of *Tbx3* were amplified from mouse ESCs by RT-PCR and cloned into pLenti6-UBC (Invitrogen) and pMXs vectors; *Oct4*, *Sox2*, *Klf4* and *c-Myc* in pMXs were obtained from Addgene; *Esrrb* was obtained from ref. 7. The retrovirus and lentivirus were generated as previously described^{1,20}. For the generation of iPS cells, equal amounts of virus encoding different combination of factors were applied to 5×10^4 plated MEFs in 10-cm² dishes in 10% FBS DMEM media containing 8 ng ml⁻¹ polybrene. After 24 h, inactivated feeder cells and fresh media were added, and the culture was then maintained for up to 21 days. For RNAi design and construction of plasmids for shRNA synthesis, 19 base-pair gene-specific regions were designed based on the algorithm described previously²³. Oligonucleotides were cloned into pSuper.puro (Oligoengine). All sequences were analysed by BLAST to ensure specificity. *Tbx3* RNAi sequence: 5'-GAGCCAACGATATCCTGAA-3'; control RNAi sequence: 5'-GATGAAATGGGTAAGTACA-3'.

Cell fusion. For polyethyleneglycol-mediated fusions, cells of each type ($\sim 1 \times 10^6$) were mixed in serum-free DMEM, pelleted, and the supernatant was removed. The pellet was resuspended in 300 µl of 50% (w/v) PEG1500 and left for 3 min with occasional tapping to mix. Then 2 ml of medium was added and the cells were spun down, and the supernatant discarded. The pellet was resuspended in ESC medium and plated on 10-cm² dishes. Puromycin (1 µg ml⁻¹) and neomycin (300 mg ml⁻¹) were added after 24 h.

Gene expression microarray and analysis. Cells were rinsed twice in ice-cold PBS. Total RNA was extracted using Trizol (Invitrogen) and column-purified with RNeasy kits (Qiagen). Expression profiling of coding genes was carried out using Illumina MouseRef-8v1.1 BeadArrays as per manufacturer's instructions. Array data are deposited for public access with GEO repository accession number GSE19164. All data were subtracted from background intensities and normalized across chips using the cross-correlation method²⁴. The normalized data were first log₂ transformed and then subtracted from the mean of the median intensities of the two groups (that is, *Nanog* overexpression with control vector, *Tcf3* RNAi with control RNAi). Before clustering, the data were further sorted based on direct targets of *Nanog* or *Tcf3*, and subsequently arranged in descending order of the fold change. The clustering tree was generated using hierarchical clustering with average linkage.

ChIP sequencing analysis. ChIP assay was carried out as described previously²⁵. In brief, cells were cross-linked with 1% (w/v) formaldehyde for 10 min at room

temperature, and formaldehyde was then inactivated by the addition of 125 mM glycine. Chromatin extracts containing DNA fragments with an average size of 500 bp were immunoprecipitated using anti-Tbx3 antibody (sc-31657; Santa Cruz Biotechnology). The ChIP-enriched DNA was then de-crosslinked and analysed by real-time PCR using the ABI PRISM 7900 sequence detection system and SYBR green master mix. For ChIP-seq assay, 10 ng of ChIP DNA was end polished with T4 DNA polymerase and kinase. An A base was added to the polished DNA fragments followed by the Qiaquick column clean up. Solexa adaptors were ligated to the ChIP DNA fragments and enriched by 15 cycles of PCR amplification. 150–300-bp size fractions were selectively cut out from the gel and eluted using the Qiagen gel extraction kit. The extracted DNA was quantified by picogreen assay and subjected to Solexa sequencing according to the manufacturer's instructions. Tbx3-binding sites peak calling was done by MACS program using specific ChIP and control input sequencing data from the same cells as described in the Supplementary Information. Colocalization of ChIP-seq transcription-factor-binding sites in the mouse genome was done as described previously¹⁸. The ChIP-seq data are deposited in GEO under accession number GSE19219.

Mouse molecular genetics. *Oct4-GFP* transgenic mice (Jackson's Laboratory, stock no. 004654) were used for MEF isolation at E13.5. Albino embryos were isolated at the 2-cell stage, matured to the 4–8-cell stage and microinjected with iPS cells using the Piezo Micro Manipulator (PMAS-CT150, PMM) under the fluorescent microscope (Olympus) to generate chimaeras. Injected embryos were cultured in KSOM media (Speciality Media) to the blastocyst stage and then transferred to the uterine horns of E2.5 pseudopregnant F₁ (CBA × C57BL/6J) females. Chimaeric embryos were collected at E13.5 for analysis of GFP expression in the gonads.

Tetraploid complementation. Tetraploid (4n) embryos were generated using 2-cell fusion by Electro cell manipulator (ECM 2001, BTX Harvard Apparatus) and incubated in KSOM until the 4–8-cell stage before aggregation with iPS cells. The zona pellucida of the tetraploid 4–8-cell stage embryos were removed by brief exposure to acid Tyrode's solution. Three tetraploid embryos and ~40 iPS cells were aggregated in a single well, and incubated in KSOM medium for 24 h to form a morula or blastocyst^{16,17}. Approximately 10–14 embryos were transferred into the uterus (for blastocysts) or oviducts (for morulas) of CBAB6 (CBA × C57BL/6J) F₁ pseudopregnant mice.

22. Zhang, J. et al. Sall4 modulates embryonic stem cell pluripotency and early embryonic development by the transcriptional regulation of Pou5f1. *Nature Cell Biol.* **8**, 1114–1123 (2006).
23. Reynolds, A. et al. Rational siRNA design for RNA interference. *Nature Biotechnol.* **22**, 326–330 (2004).
24. Chua, S. W. et al. A novel normalization method for effective removal of systematic variation in microarray data. *Nucleic Acids Res.* **34**, e38 (2006).
25. Jiang, J. et al. A core Klf circuitry regulates self-renewal of embryonic stem cells. *Nature Cell Biol.* **10**, 353–360 (2008).

Genome-wide erasure of DNA methylation in mouse primordial germ cells is affected by AID deficiency

Christian Popp^{1*}, Wendy Dean^{1*}, Suhua Feng^{2*}, Shawn J. Cokus², Simon Andrews³, Matteo Pellegrini², Steven E. Jacobsen^{2,4} & Wolf Reik¹

Epigenetic reprogramming including demethylation of DNA occurs in mammalian primordial germ cells (PGCs) and in early embryos, and is important for the erasure of imprints and epimutations, and the return to pluripotency^{1–9}. The extent of this reprogramming and its molecular mechanisms are poorly understood. We previously showed that the cytidine deaminases AID and APOBEC1 can deaminate 5-methylcytosine *in vitro* and in *Escherichia coli*, and in the mouse are expressed in tissues in which demethylation occurs¹⁰. Here we profiled DNA methylation throughout the genome by unbiased bisulphite next generation sequencing^{11–13} in wild-type and AID-deficient mouse PGCs at embryonic day (E)13.5. Wild-type PGCs revealed marked genome-wide erasure of methylation to a level below that of methylation deficient (*Np95*^{−/−}, also called *Uhrf1*^{−/−}) embryonic stem cells, with female PGCs being less methylated than male ones. By contrast, AID-deficient PGCs were up to three times more methylated than wild-type ones; this substantial difference occurred throughout the genome, with introns, intergenic regions and transposons being relatively more methylated than exons. Relative hypermethylation in AID-deficient PGCs was confirmed by analysis of individual loci in the genome. Our results reveal that erasure of DNA methylation in the germ line is a global process, hence limiting the potential for transgenerational epigenetic inheritance. AID deficiency interferes with genome-wide erasure of DNA methylation patterns, indicating that AID has a critical function in epigenetic reprogramming and potentially in restricting the inheritance of epimutations in mammals.

In plants, active demethylation occurs widely (including in imprinted genes) and is carried out by 5-methylcytosine (5meC) glycosylases such as Demeter and Demeter-like proteins^{14–16}. This class of enzymes does not seem to exist in mammalian genomes, but instead we found that the cytosine deaminases AID and APOBEC1 can deaminate 5meC both *in vitro* and in *E. coli*¹⁰, indicating that deamination of 5meC followed by T:G base excision repair by glycosylases such as TDG or MBD4 might be an equivalent pathway for demethylation of DNA. Recently it has been shown that co-expression of AID and MBD4 in zebrafish embryos can lead to demethylation of DNA, lending support to the idea that demethylation in animals might proceed by deamination followed by base excision repair¹⁷. These results raise the question of whether naturally occurring demethylation in PGCs or early embryos involves deaminases or base excision repair.

We previously found that AID is expressed in PGCs and in early embryos at a time when demethylation occurs¹⁰. Methylation in some single-copy genes, differentially methylated regions in imprinted genes, and long interspersed nuclear element (LINE) 1 repeats has been shown to be substantially erased in PGCs between E11.5 and

E13.5, whereas methylation of intracisternal A particles (IAPs) was significantly more resistant to erasure^{6–9,18}. The extent of demethylation of the genome as a whole in PGCs is unknown. To understand the dynamics of erasure on a genome-wide scale we carried out unbiased sequencing of bisulphite-treated DNA by next generation sequencing (bisulphite next generation sequencing; BS-Seq), which accurately quantifies whole-genome methylation levels^{11,13}. We were able to scale down by 20-fold the construction and analysis of Illumina Solexa libraries to as little as 150 ng of genomic DNA, enabling for the first time a genome-wide view of methylation in fully reprogrammed PGCs at E13.5, isolated by cell sorting of *Oct4-Gfp*-positive germ cells (Fig. 1). Both male and female PGCs were strikingly hypomethylated, with a median methylation level of 16.3% and 7.8%, respectively (for comparison, methylation-deficient *Np95*^{−/−} embryonic stem (ES) cells had a methylation level of 22%). It is interesting to note that female PGCs had a lower methylation level than male PGCs; this is consistent with female ES cells having less methylation than male ones¹⁹, indicating that the proposed effects of two active X chromosomes on decreasing genome methylation might operate *in vivo* as well as in pluripotent cell lines derived from inner cell mass (ICM) cells or PGCs. Methylation levels in fetus, ES cells and sperm were high (73.2–85%), whereas those in placenta were intermediate (42.3%), consistent with results of previous experiments in which individual gene sequences or transposons were analysed. Notably, genome-wide hypomethylation has recently been reported in *Arabidopsis* endosperm in comparison to the embryo (although the difference, 6%, is considerably smaller than the one that we found here in the mammalian system), a tissue that supports embryo development and nutrition in seed plants in analogy to the function of the placenta in mammals^{15,16}.

We next carried out a more detailed analysis of the patterns of methylation erasure in PGCs in various genomic elements (Figs 2 and 3). We assessed levels of methylation of promoters, exons, introns and intergenic regions (Fig. 2), as well as those of various transposon families (Fig. 3 and Supplementary Fig. 1; BS-Seq reads of transposons and repeats with identical sequence are eliminated bioinformatically, but BS-Seq reads of transposon family members that map uniquely, owing to unique sequence variation, can be assessed). In highly methylated tissues (ES, sperm, fetus), methylation was similarly high in exons (above 70%), and was considerably lower in promoters (35–40%), consistent with a recent whole-genome BS-Seq analysis in human ES cells¹³. Introns and retrotransposons were particularly highly methylated in sperm (approximately 10% higher than in the fetus or ES cells), supporting the notion that *de novo* methylation in male germ cells, before resumption of mitosis after birth, is important for suppressing transposon mobility in the germ line. In comparison

¹Laboratory of Developmental Genetics and Imprinting, The Babraham Institute, Cambridge CB22 3AT, and Centre for Trophoblast Research, University of Cambridge, Cambridge CB2 3EG, UK. ²Department of Molecular Cell and Developmental Biology, University of California at Los Angeles, Los Angeles, California 90095, USA. ³Bioinformatics Group, The Babraham Institute, Cambridge CB22 3AT, UK. ⁴Howard Hughes Medical Institute, University of California at Los Angeles, Los Angeles, California 90095, USA.

*These authors contributed equally to this work.

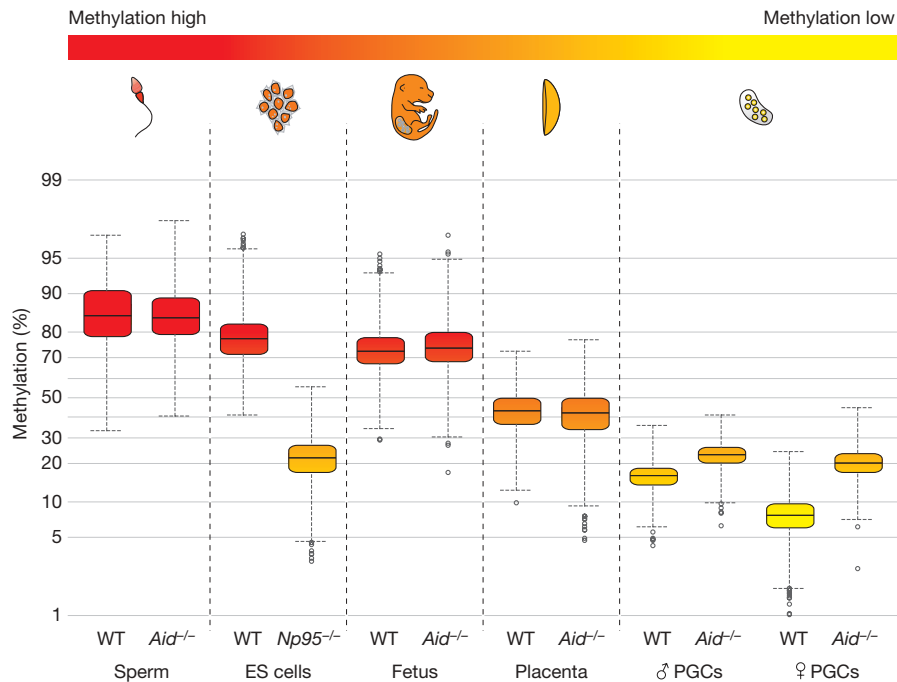


Figure 1 | Genome-wide BS-Seq reveals global hypomethylation in PGCs dependent on AID. Tissues and cells analysed by BS-Seq are shown in a gradient from red to yellow illustrating methylation levels from high to low, respectively. BS-Seq reads were analysed using windows of 250 kb across the whole genome. Boxes show the range of the 25–75th quartiles of the data; the

line in the middle the median value. Whiskers show either highest and lowest values (if there are no outliers) or upper and lower confidence intervals. Outliers are shown as circles. Placenta, fetal carcass and PGCs were collected at E13.5. Note the global hypomethylation in PGCs, and the substantially higher levels of methylation in *Aid*^{-/-} PGCs. WT, wild type.

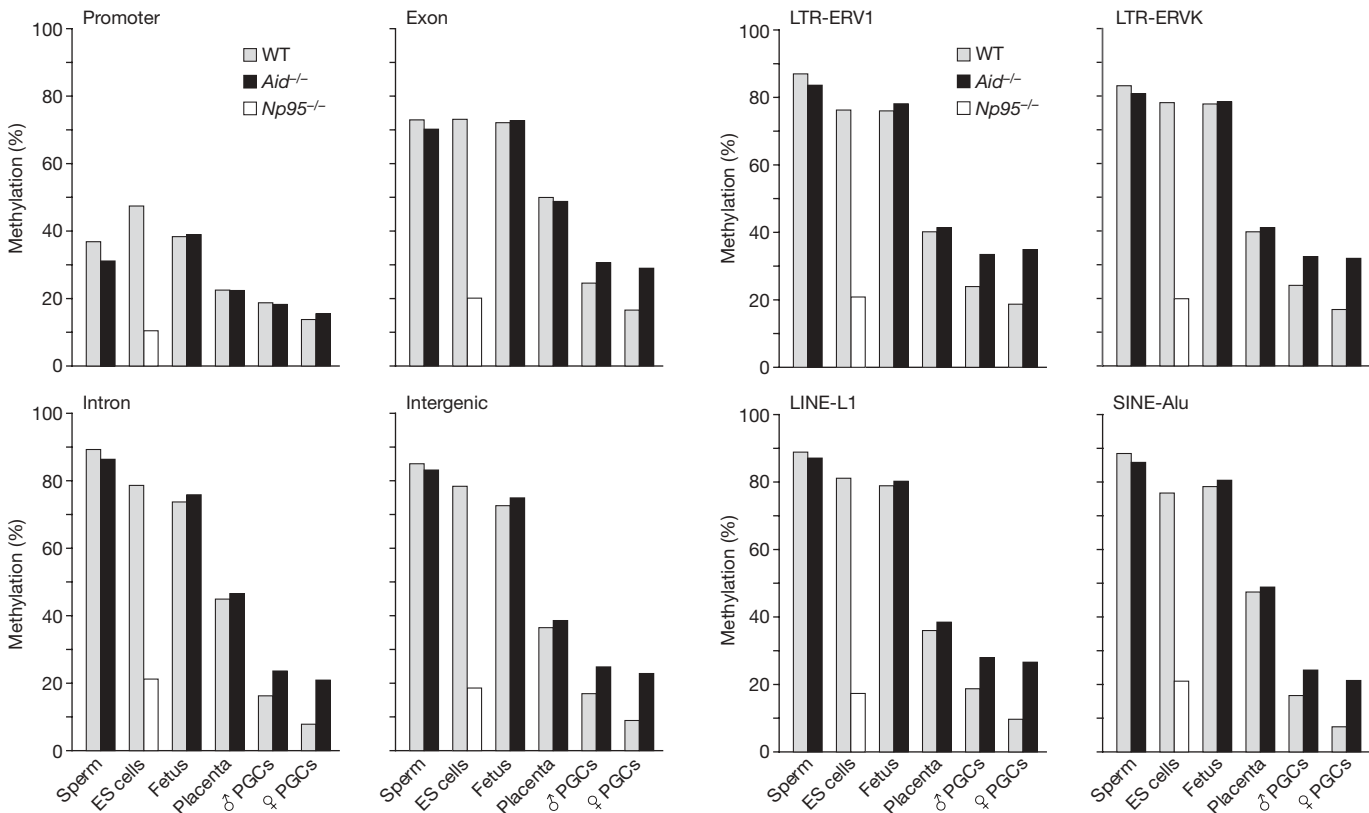


Figure 2 | Erasure of DNA methylation in different genomic elements in PGCs. Methylation levels in promoters, exons, introns and intergenic regions in ES cells, *Np95*^{-/-} ES cells and various tissues of C57BL/6J and *Aid*^{-/-} knockout mice are shown based on ratios of methylated to unmethylated BS-Seq reads. Placenta, fetal carcass and PGCs were all collected at E13.5. Note the particularly pronounced effect of AID deficiency on methylation of introns and intergenic regions.

Figure 3 | Erasure of DNA methylation in different classes of transposable elements in PGCs. Methylation levels of different classes of transposons in ES cells, *Np95*^{-/-} ES cells, and various tissues of C57BL/6J and *Aid*^{-/-} knockout mice are shown based on ratios of methylated to unmethylated BS-Seq reads. Placenta, fetal carcass and PGCs were all collected at E13.5. Note that LTR-ERV1 and LTR-ERVK elements retain more methylation in PGCs than any other repeat family.

to the highly methylated tissues, the greatest loss of methylation in PGCs (and in placenta) was observed within introns, intergenic regions and repeats, followed by exons, and then promoters. Hence, demethylation in PGCs is indeed global and encompasses genic, intergenic and transposon sequences. Sequences that retained the highest levels of methylation in the face of reprogramming were long terminal repeat (LTR)-ERV1 and LTR-ERVK elements (approximately 10% of the latter are IAPs). PGCs at the endpoint of reprogramming have therefore attained a unique epigenetic state, with genome-wide demethylation of DNA, and loss of the repressive histone marks H3K9me2 and H2A/H4R3me2 together with H2AZ, as well as loss of the active histone mark H3K9ac^{9,20}. Thus, an epigenetic ground state that is depleted both of key activating and repressive epigenetic marks seems to be uniquely characteristic of reprogrammed PGCs. We carried out a biological replicate of the BS-Seq experiment on E13.5 PGCs isolated by a different method (see Supplementary Methods), which indeed replicated qualitatively all conclusions with the *Oct4-Gfp* fluorescence-activated cell sorted (FACS) PGCs, whereas the baseline was shifted to higher levels of methylation, reflecting either a greater contamination with somatic gonadal cells or epigenetic heterogeneity within germ cells that are not *Oct4-Gfp* positive (Supplementary Fig. 2).

We next examined the effects of AID deficiency on erasure of methylation in PGCs. We introgressed the *Oct4-Gfp* transgene into *Aid*^{-/-} (also called *Aicda*^{-/-}) knockout mice²¹ (both on a C57BL/6J inbred genetic background). PGCs from *Aid*^{-/-} knockout mice showed substantially higher levels of methylation than wild type ones; this difference was more pronounced in female than in male mice (Figs 1–3), in which the mean methylation level was more than 2.5-fold higher in the *Aid*^{-/-} knockout than the wild type. AID-deficient PGCs were particularly more methylated than wild-type PGCs in introns and transposons (more than a 3-fold difference in LINE-L2 and in short interspersed nuclear element (SINE)-B4 elements; Supplementary Fig. 1), followed by exons, whereas no differences were found in promoters. We were unable to analyse PGCs by BS-Seq before genome-wide erasure (E10.5, 11.5) because the numbers of cells that can be obtained are not currently sufficient for this technique. Previous analyses of individual gene loci and transposons found that the methylation profile of PGCs before erasure is similar to that of embryonic somatic cells^{6–9,18}, whereas another study suggested that the overall levels are slightly lower²⁰. Hence, whereas *Aid*^{-/-} PGCs are hypermethylated in comparison to wild type ones, a significant level of demethylation also occurs in *Aid*^{-/-} PGCs, the extent of which depends on the precise genomic levels before erasure. Notably, an effect of AID deficiency on genome-wide methylation levels was only found in primordial germ cells, and not in the fetus, the placenta, or in sperm (Figs 1–3). These observations were again qualitatively replicated in an independent set of BS-Seq experiments using an alternative method of isolation of *Aid*^{-/-} PGCs (Supplementary Fig. 2). Indeed, the ratios of the percentages of methylation between wild-type and *Aid*^{-/-} PGCs were very similar when comparing the data sets obtained with the two different methods of isolation (Figs 2 and 3 and Supplementary Fig. 2).

The depth of sequencing in our experiments does not currently allow the comparison of methylation levels of individual gene loci between the various tissues analysed. However, given the global differences observed between wild-type and *Aid*^{-/-} PGCs we compared methylation levels in randomly selected genomic loci (R1 and R2 are located in intergenic regions, R3 in the first intron of *Foxo1*, and R4 in the seventh exon of *Xirp2*), promoters or differentially methylated regions of genes including imprinted ones that are known to become demethylated during PGC development (*Dazl*, *H19*, *Lit1* (also called *Kcnq1ot1*)) and retrotransposons by Sequenom bisulphite assay (Fig. 4 and Supplementary Fig. 3). Where methylation differences were observed it was always the *Aid*^{-/-} PGCs that were more highly methylated, confirming in an independent assay that *Aid*^{-/-} PGCs remained relatively hypermethylated. This assay also confirmed that

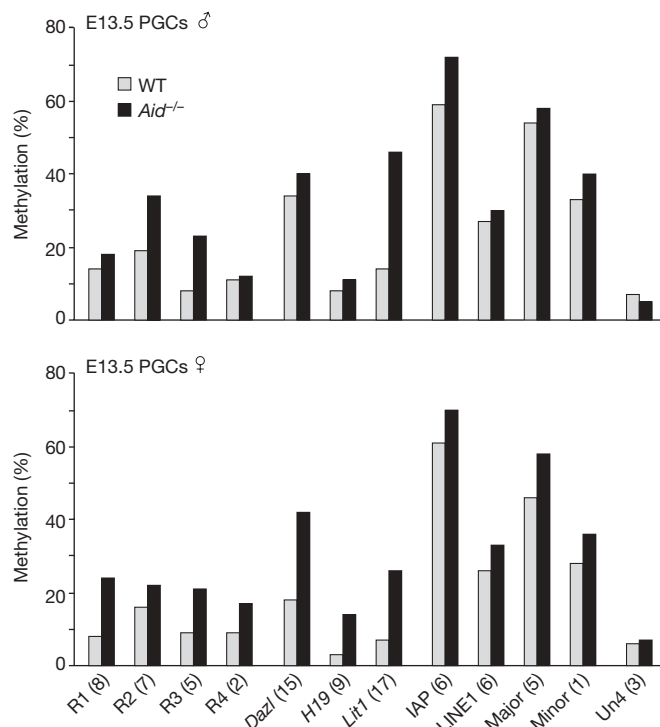


Figure 4 | Analysis of DNA methylation of individual genomic loci in E13.5 PGCs by Sequenom MassArray. Methylation levels of individual genomic loci (R1–4, randomly selected sequences, located in intergenic regions (R1, R2), the first intron of *Foxo1* (R3) and the seventh exon of *Xirp2* (R4); the *Dazl* amplicon is located in the promoter region and the *H19* and *Lit1* amplicons are located in the differentially methylated regions) and of transposons and major and minor satellite repeats in wild-type and *Aid*^{-/-} E13.5 PGCs are shown based on Sequenom MassArray analysis. The number of CpGs analysed for each region is stated in brackets. Un4, unmethylated control located in the *Hoxc* cluster. Note substantially increased levels of methylation in many genomic loci in *Aid*^{-/-} PGCs.

IAPs retained relatively high levels of methylation in PGCs (note that IAPs are a subfamily of LTR-ERV elements and that the absolute values of methylation cannot therefore be compared between the Sequenom and BS-Seq assays). We also analysed methylation by Sequenom bisulphite assay in E12.5 PGCs, and again found relative hypermethylation of several loci in *Aid*^{-/-} in comparison to wild-type PGCs (data not shown).

More detailed analyses at single CpG resolution of regions that were found to be hypermethylated in *Aid*^{-/-} PGCs (Fig. 4) revealed that predominantly there was a homogeneous increase in methylation across the whole of the regions analysed (Supplementary Fig. 3).

Our results show that the vast majority of genomic DNA methylation is erased during normal development of PGCs. In mammals, this limits the scope for inheritance of epigenetic marks (based on methylation) across generations, which if it occurred would be of potential evolutionary significance as well as affecting disease risk in humans²². Indeed, in the mouse the only two well-documented examples of transgenerational inheritance involve alleles of genes with an insertion of an IAP element whose DNA methylation alters the expression of the neighbouring gene²², consistent with our observation that LTR retrotransposons, including IAPs, are the genomic elements that are most resistant to erasure. This is in marked contrast to seed plants in which reprogramming of DNA methylation does not seem to occur in germ cells themselves²³, and in which stable inheritance of epialleles across generations is more common²⁴. Our observation that erasure of DNA methylation is less efficient in *Aid*^{-/-} PGCs (especially in the female germ line) indicates that the extent to which epigenetic information is heritable in mammals might be under regulation by genetic factors. In crosses between AID-deficient and wild-type parents, we observed

significant effects on growth of offspring at birth as well as on litter size. Notably, AID-deficient mothers did not regulate the size of their offspring in an inverse relationship to litter size, as wild-type mothers do (Supplementary Fig. 4). Second, litter sizes from both AID-deficient mothers and fathers in crosses with wild-type animals were significantly larger than in wild-type or homozygous *Aid*^{-/-} crosses (Supplementary Fig. 4). Detailed epigenetic analyses need to be carried out on mature AID-deficient germ cells (particularly oocytes) and offspring to examine if heritable epimutations are indeed the basis for these significant reproductive phenotypes in *Aid*^{-/-} knockout mice. It cannot be excluded that kinetics of methylation reprogramming are shifted in AID-deficient animals or that further reprogramming steps occur after E13.5 in *Aid*^{-/-} knockout PGCs, which could further modify the differences observed here. This requires a substantially increased depth of sequencing on much reduced numbers of cells, which awaits further technical improvements and cost savings in BS-Seq technology.

Together with work just published in which it was shown that AID is required in ES cells to demethylate pluripotency genes during reprogramming of a somatic genome by cell fusion²⁵, our study shows that AID has a role in epigenetic reprogramming in mammals. Off-target effects of AID have recently been described in the immune system²⁶; in this respect it is perhaps not surprising that AID has also evolved roles outside of the immune system. AID might exert its substantial effect on genome-wide demethylation of DNA in PGCs through its established function as a cytosine²⁷ or 5meC (refs 10, 28) deaminase. This can be tested genetically by examining the base excision repair pathways that are expected to be downstream of AID, including TDG and MBD4. Of particular interest is a recent report in zebrafish indicating that AID and MBD4 are involved cooperatively in demethylation of DNA¹⁷; this link might also involve GADD45, which has been implicated previously in demethylation of DNA. Notably, the effect of AID deficiency on methylation in PGCs was considerably more pronounced than that of deficiency of the 5meC glycosylase Demeter in the *Arabidopsis* endosperm^{15,16}. Alternatively, AID might be required more indirectly as an essential component in the pathway that regulates erasure of methylation in PGCs. Other deaminases such as APOBEC1–3 might also have roles in demethylation of DNA, especially as our results show that AID deficiency does interfere with, but does not abrogate, erasure of methylation in PGCs. It is interesting to note that in plants Demeter is specifically required for erasure of methylation in imprinted genes, whereas Demeter-like genes are responsible for more general reprogramming of methylation patterns¹⁴. Other pathways to deamination of 5meC, such as one involving the *de novo* methyltransferases DNMT3A and DNMT3B, are less likely to operate in PGCs, as DNMT3A is not expressed and DNMT3B is excluded from the nucleus at the time of erasure of methylation⁶. Finally, our results do not exclude the existence of other pathways to demethylation of DNA in mammals, including oxidation of 5meC by the recently described TET family of 5meC hydroxylases^{29,30}, or removal of 5meC by glycosylases.

METHODS SUMMARY

Mouse tissues, including male and female PGCs at E13.5, were isolated from C57BL/6J mice, C57BL/6J mice transgenic for *Oct4-Gfp*, or *Aid*^{-/-} knockout mice bred into a C57BL/6J background for seven generations during this study. The *Oct4-Gfp* transgene was subsequently bred into *Aid*^{-/-} knockout mice. PGCs were isolated on a FACS-Aria cell sorter by sorting for green fluorescence; the isolated cell populations were >98% pure. DNA was isolated, bisulphite converted, and prepared for Illumina Solexa libraries. Each Illumina Solexa library was sequenced in a single end read, except for *Oct4-Gfp* isolated PGC libraries which were sequenced in two single end reads each; subsequently, a published highly customized software package was used to carry out Gaussian base-calling and sequence alignment for bisulphite-converted reads against the mouse genome¹¹. On average, around 1.5 million aligned 27-bp reads (5.4 million 50-bp reads for the PGC libraries) were obtained for each library. For methylation analysis, bases 6 to 22 in the 27-bp reads (bases 15 to 41 in the 50-bp reads) were

used, and CpGs were base called as methylated or unmethylated, respectively. Genome-wide averages of DNA methylation of individual samples, or averages of methylation in promoters, exons, introns, intergenic regions, and different classes of transposons, were bioinformatically determined. For Sequenom MassArray, bisulphite-converted DNA was amplified and subjected to quantitative analysis of methylation by mass spectrometry.

Full Methods and any associated references are available in the online version of the paper at www.nature.com/nature.

Received 24 November 2009; accepted 15 January 2010.

Published online 22 January 2010.

- Reik, W., Dean, W. & Walter, J. Epigenetic reprogramming in mammalian development. *Science* **293**, 1089–1093 (2001).
- Sasaki, H. & Matsui, Y. Epigenetic events in mammalian germ-cell development: reprogramming and beyond. *Nature Rev. Genet.* **9**, 129–140 (2008).
- Oswald, J. *et al.* Active demethylation of the paternal genome in the mouse zygote. *Curr. Biol.* **10**, 475–478 (2000).
- Mayer, W., Niveleau, A., Walter, J., Fundele, R. & Haaf, T. Demethylation of the zygotic paternal genome. *Nature* **403**, 501–502 (2000).
- Dean, W. *et al.* Conservation of methylation reprogramming in mammalian development: aberrant reprogramming in cloned embryos. *Proc. Natl Acad. Sci. USA* **98**, 13734–13738 (2001).
- Hajkova, P. *et al.* Epigenetic reprogramming in mouse primordial germ cells. *Mech. Dev.* **117**, 15–23 (2002).
- Lee, J. *et al.* Erasing genomic imprinting memory in mouse clone embryos produced from day 11.5 primordial germ cells. *Development* **129**, 1807–1817 (2002).
- Yamazaki, Y. *et al.* Reprogramming of primordial germ cells begins before migration into the genital ridge, making these cells inadequate donors for reproductive cloning. *Proc. Natl Acad. Sci. USA* **100**, 12207–12212 (2003).
- Hajkova, P. *et al.* Chromatin dynamics during epigenetic reprogramming in the mouse germ line. *Nature* **452**, 877–881 (2008).
- Morgan, H. D., Dean, W., Coker, H. A., Reik, W. & Petersen-Mahrt, S. K. Activation-induced cytidine deaminase deaminates 5-methylcytosine in DNA and is expressed in pluripotent tissues: implications for epigenetic reprogramming. *J. Biol. Chem.* **279**, 52353–52360 (2004).
- Cokus, S. J. *et al.* Shotgun bisulfite sequencing of the *Arabidopsis* genome reveals DNA methylation patterning. *Nature* **452**, 215–219 (2008).
- Meissner, A. *et al.* Genome-scale DNA methylation maps of pluripotent and differentiated cells. *Nature* **454**, 766–770 (2008).
- Lister, R. *et al.* Human DNA methylomes at base resolution show widespread epigenomic differences. *Nature* **462**, 315–322 (2009).
- Gehring, M., Reik, W. & Henikoff, S. DNA demethylation by DNA repair. *Trends Genet.* **25**, 82–90 (2009).
- Gehring, M., Bubb, K. L. & Henikoff, S. Extensive demethylation of repetitive elements during seed development underlies gene imprinting. *Science* **324**, 1447–1451 (2009).
- Hsieh, T. F. *et al.* Genome-wide demethylation of *Arabidopsis* endosperm. *Science* **324**, 1451–1454 (2009).
- Rai, K. *et al.* DNA demethylation in zebrafish involves the coupling of a deaminase, a glycosylase and gadd45. *Cell* **135**, 1201–1212 (2008).
- Lane, N. *et al.* Resistance of IAPs to methylation reprogramming may provide a mechanism for epigenetic inheritance in the mouse. *Genesis* **35**, 88–93 (2003).
- Zvetkova, I. *et al.* Global hypomethylation of the genome in XX embryonic stem cells. *Nature Genet.* **37**, 1274–1279 (2005).
- Seki, T. *et al.* Cellular dynamics associated with the genome-wide epigenetic reprogramming in migrating primordial germ cells in mice. *Development* **134**, 2627–2638 (2007).
- Muramatsu, M. *et al.* Class switch recombination and hypermutation require activation-induced cytidine deaminase (AID), a potent RNA editing enzyme. *Cell* **102**, 553–563 (2000).
- Whitelaw, N. C. & Whitelaw, E. Transgenerational epigenetic inheritance in health and disease. *Curr. Opin. Genet. Dev.* **18**, 273–279 (2008).
- Slotkin, R. K. *et al.* Epigenetic reprogramming and small RNA silencing of transposable elements in pollen. *Cell* **136**, 461–472 (2009).
- Teixeira, F. K. *et al.* A role for RNAi in the selective correction of DNA methylation defects. *Science* **323**, 1600–1604 (2009).
- Bhutani, N. *et al.* Reprogramming towards pluripotency requires AID-dependent DNA demethylation. *Nature* doi:10.1038/nature08752 (21 December 2009).
- Robbiani, D. F. *et al.* AID produces DNA double-strand breaks in non-Ig genes and mature B cell lymphomas with reciprocal chromosome translocations. *Mol. Cell* **36**, 631–641 (2009).
- Neuberger, M. S., Harris, R. S., Di Noia, J. & Petersen-Mahrt, S. K. Immunity through DNA deamination. *Trends Biochem. Sci.* **28**, 305–312 (2003).
- Larijani, M. *et al.* Methylation protects cytidines from AID-mediated deamination. *Mol. Immunol.* **42**, 599–604 (2005).
- Kriaucionis, S. & Heintz, N. The nuclear DNA base 5-hydroxymethylcytosine is present in Purkinje neurons and the brain. *Science* **324**, 929–930 (2009).

30. Tahiliani, M. *et al.* Conversion of 5-methylcytosine to 5-hydroxymethylcytosine in mammalian DNA by MLL partner TET1. *Science* **324**, 930–935 (2009).

Supplementary Information is linked to the online version of the paper at www.nature.com/nature.

Acknowledgements We thank H. Morgan for his contributions to some of the early analysis of *Aid*^{-/-} mice, A. Segonds-Pichon for help with statistical evaluation, and J. Hetzel for assisting in preparing the Illumina Solexa libraries and their sequencing. We also thank S. Petersen-Mahrt, C. Rada and F. Santos for advice and discussions. C.P. was a Boehringer-Ingelheim predoctoral Fellow. S.F. is a Howard Hughes Medical Institute Fellow of the Life Science Research Foundation. S.E.J. is an investigator of the Howard Hughes Medical Institute. This work was supported by BBSRC, MRC, EU NoE The Epigenome, and CellCentric (to W.R.), and by HHMI, NSF Plant Genome Research Programme, and NIH (to S.E.J.).

Author Contributions C.P. and W.D. isolated tissue samples and PGCs, assessed the purity of the samples and prepared DNA. C.P. undertook genetic crosses, determined weights of mouse pups and carried out Sequenom EpiTYPER analysis. S.F. constructed bisulphite libraries and did Illumina Solexa sequencing. S.J.C., S.A. and M.P. carried out mapping, base-calling and computational analyses. C.P., W.D., S.F., S.J.C., S.A., M.P., S.E.J. and W.R. analysed data. C.P., W.D., S.F., S.E.J. and W.R. designed experiments; S.E.J. and W.R. designed and directed the study. C.P. and W.R. wrote the manuscript.

Author Information All sequencing files have been deposited in GEO under accession code GSE19960. Reprints and permissions information is available at www.nature.com/reprints. The authors declare no competing financial interests. Correspondence and requests for materials should be addressed to S.E.J. (jacobsen@ucla.edu) or W.R. (wolf.reik@bbsrc.ac.uk).

METHODS

Mice and isolation of tissue and DNA samples. Mice deficient for AID have been described previously²¹ and were provided by T. Honjo. These were backcrossed for seven generations into the C57BL/6J strain during the course of this study. C57BL/6J mice or C57BL/6J mice carrying an *Oct4-Gfp* transgene were used as controls throughout. The *Oct4-Gfp* transgene was bred into the *Aid*^{-/-} knockout following backcrossing into the C57BL/6J background. Epididymal sperm was collected from fertile adult males. PGCs were isolated on a FACS-Aria cell sorter by sorting for green fluorescence; the isolated cell populations were >98% pure. Placentas and carcasses were taken from fetuses used for PGC collection. Genomic DNA from wild-type (E14) and *Np95*^{-/-} mouse ES cells was provided by A. Clarke.

Shotgun bisulphite sequencing and computational analysis of data. Genomic DNA extracted from various mouse tissues with the Qiagen blood and tissue kit were treated with sodium bisulphite and then used to generate Illumina/Solexa sequencing libraries as described previously¹¹, except that fewer cycles of PCR amplification were used (15 cycles instead of 18 cycles) to optimize the base composition of the libraries. For PGC samples, owing to the limited sources of tissue, the input DNA amount for libraries had to be reduced to as low as 150 ng. Therefore, the enzymatic reaction steps used for library construction (including reagents and adapters for PCR) were scaled down to accommodate the reduced input amount. On the other hand, more DNA template (in volume) was used in each PCR reaction and more duplicate PCR reactions were performed in parallel to obtain equivalent amounts of product as for the other libraries. The libraries were sequenced on an Ultra-high-throughput Illumina/Solexa 1G Genome Analyser following manufacturer's instructions. Initial sequencing data analysis was performed using version 0.3 of the Illumina/Solexa Analysis Pipeline; subsequently, a previously published highly customized software package was used to carry out Gaussian base-calling and sequence alignment for bisulphite-converted reads against the mouse genome¹¹. Around 5.4 million aligned 50-bp reads were obtained for PGC libraries isolated by *Oct4-Gfp* FACS sorting, whereas sequencing of all other libraries yielded on average 1.5 million aligned 27-bp reads. For methylation status analysis, bases 15 to 41 in the 50-bp reads and bases 6 to 22 in the 27-bp reads were used, equalling a coverage of around 5.8% and 1%, respectively. Methylated cytosines were identified as cytosines (or guanines as appropriate) in sequencing reads aligned to genomic cytosines, whereas unmethylated cytosines were identified as thymines (or adenines as appropriate) in sequencing reads aligned to genomic cytosines. Bisulphite conversion efficiency was always above 95% as judged by conversion of cytosines in CHG and CHH contexts (data not shown). The mapped bisulphite sequences

were split into three groups. Sequences not spanning a CpG were discarded, and separate lists were made for sequences showing complete methylation or complete demethylation. In the very small number of cases where the same sequence showed both methylation and demethylation it was added to both lists. Where there were multiple data sets for the same sample the methylated and unmethylated lists were merged. Analysis of the data was performed using SeqMonk (<http://www.bioinformatics.bbsrc.ac.uk/projects/seqmonk>). The methylated and unmethylated lists were merged together with the methylation status being encoded in the strand of the read (methylated = forward; unmethylated = reverse). A tile of 250-kb regions was overlaid on the genome and the methylation status of each tile was calculated. Tiles containing fewer than ten reads were discarded, as were tiles where there were five or more reads with exactly the same mapped position. The methylation status was calculated as the log₂ ratio of the methylated:unmethylated counts. The distribution of values showed a normal distribution and a comparison between tissues was made using a boxwhisker plot which showed the median, upper and lower quartiles and extremities (median $\pm 2 \times$ interquartile range). Any values outside this range were plotted individually as outliers. To calculate the methylation levels in specific genomic regions (promoters, genes, introns, exons, transposon families) SeqMonk was used to generate probe regions using the Ensembl features from the annotated NCBI37 genome as a template. Total counts of overlapping reads in all of these regions across the genome were made and a single methylated:unmethylated ratio was produced. The positions of all repeats in the NCBI37 mouse genome were extracted from Ensembl and classified into families based on their annotation. A count was made of reads which overlapped with all of these repeat regions and these counts were combined across all members of each family. A single measure per family was then made of the log₂ ratio of methylated:unmethylated reads. All repeat families shown are represented by more than 1,000 CpG containing reads in each data set.

Methylation analysis by Sequenom MassArray. DNA from FACS-sorted PGCs was extracted using the AllPrep DNA/RNA Micro Kit (Qiagen). The DNA was then treated with bisulphite reagent using the two-step modification procedure outlined in the Imprint DNA modification kit (Sigma). Primer pairs were designed using the MethPrimer program (<http://www.uogene.org/methprimer/index1.html>). A complete list of primers used for analysis is available on request (primers for IAPs were based on the consensus sequence of IAPLTR1a repeats which represent approximately 1.5% of the ERVK family). Amplification of the bisulphite-converted DNA and preparation of PCR products for quantitative analysis of methylation as detected by the MassArray system was according to the protocol provided by the manufacturer.

CORRIGENDUM

doi:10.1038/nature08846

The sequence and *de novo* assembly of the giant panda genome

Ruiqiang Li, Wei Fan, Geng Tian, Hongmei Zhu, Lin He, Jing Cai, Quanfei Huang, Qingle Cai, Bo Li, Yinqi Bai, Zhihe Zhang, Yaping Zhang, Wen Wang, Jun Li, Fuwen Wei, Heng Li, Min Jian, Jianwen Li, Zhaolei Zhang, Rasmus Nielsen, Dawei Li, Wanjuan Gu, Zhentao Yang, Zhaoling Xuan, Oliver A. Ryder, Frederick Chi-Ching Leung, Yan Zhou, Jianjun Cao, Xiao Sun, Yonggui Fu, Xiaodong Fang, Xiaosen Guo, Bo Wang, Rong Hou, Fujun Shen, Bo Mu, Peixiang Ni, Runmao Lin, Wubin Qian, Guodong Wang, Chang Yu, Wenhui Nie, Jinhuan Wang, Zhigang Wu, Huiqing Liang, Jiumeng Min, Qi Wu, Shifeng Cheng, Jue Ruan, Mingwei Wang, Zhongbin Shi, Ming Wen, Binghang Liu, Xiaoli Ren, Huisong Zheng, Dong Dong, Kathleen Cook, Gao Shan, Hao Zhang, Carolin Kosiol, Xueying Xie, Zuhong Lu, Hancheng Zheng, Yingrui Li, Cynthia C. Steiner, Tommy Tsan-Yuk Lam, Siyuan Lin, Qinghui Zhang, Guoqing Li, Jing Tian, Timing Gong, Hongde Liu, Dejin Zhang, Lin Fang, Chen Ye, Juanbin Zhang, Wenbo Hu, Anlong Xu, Yuanyuan Ren, Guojie Zhang, Michael W. Bruford, Qibin Li, Lijia Ma, Yiran Guo, Na An, Yujie Hu, Yang Zheng, Yongyong Shi, Zhiqiang Li, Qing Liu, Yanling Chen, Jing Zhao, Ning Qu, Shancen Zhao, Feng Tian, Xiaoling Wang, Haiyin Wang, Lizhi Xu, Xiao Liu, Tomas Vinar, Yajun Wang, Tak-Wah Lam, Siu-Ming Yiu, Shiping Liu, Hemin Zhang, Desheng Li, Yan Huang, Xia Wang, Guohua Yang, Zhi Jiang, Junyi Wang, Nan Qin, Li Li, Jingxiang Li, Lars Bolund, Karsten Kristiansen, Gane Ka-Shu Wong, Maynard Olson, Xiuqing Zhang, Songgang Li, Huanming Yang, Jian Wang & Jun Wang

Nature 463, 311–317 (2010)

In this Article, the Latin species name of the giant panda was written incorrectly as *Ailuropoda melanoleura*. The correct name is *Ailuropoda melanoleuca*.

CORRIGENDUM

doi:10.1038/nature08847

Dense packings of the Platonic and Archimedean solids

S. Torquato & Y. Jiao

Nature 460, 876–879 (2009)

In the Introduction and in the Figure 4 legend of this letter, it was stated that the truncated tetrahedron is the only Archimedean solid that is not centrally symmetric. The correct statement is that the truncated tetrahedron is the only non-chiral Archimedean solid that is not centrally symmetric. This subtle distinction does not affect any of the results, conclusions or conjectures in our paper.

NEWS

Mixed budget outlook for young scientists

US President Barack Obama's proposed budget for fiscal year 2011 looks to be a mixed bag for young scientists. If Congress accepts the president's budget requests, postdocs funded by the National Institutes of Health (NIH) will receive a significant stipend boost. But biomedical early-career scientists, although bolstered by an ongoing federal initiative to keep their grant application success rates high, are facing a decline in the number of available competing grants. Early-stage researchers in other fields, meanwhile, may benefit from higher allocations in such areas as energy and climate change. The US\$66-billion non-defence research and development budget was announced earlier this month.

Under the proposal, postdoctoral training stipends funded by the NIH's Ruth L. Kirschstein National Research Service Awards (NRSAs) would go up by 6%, on the heels of a 1% increase implemented for fiscal-year 2010 that follows several years without a rise. "If this goes through, it will be fantastic for postdoctoral scholars," says Cathee Johnson Phillips, executive director of the National Postdoctoral Association (NPA). "It is a recognition of their value to the scientific enterprise."

The boost, Johnson Phillips notes, would set a significant precedent, as many universities and research institutions across the nation use the NRSA as a standard for their own postdoctoral pay levels. The proposed increase "will challenge US institutions to pay their postdocs more", she says. Johnson Phillips says that the NPA plans to ask members to advocate for the increase to federal legislators. "We are making this one of our priorities this year," she says.

Overall, Obama's budget request for the NIH seeks \$32.1 billion, up \$1 billion — although it will fund 199 fewer competing grants. An NIH policy established last year calls for 'special consideration' of early-career researchers' grant applications, which means they are guaranteed to be funded at the same success rate as more seasoned investigators, says Sally Rockey, the NIH's acting deputy director for extramural research.

However, fewer available competing grants must inevitably translate into fewer awards for all applicants in 2011 than in 2010. "Success rates will dip for everyone unless the NIH gets a larger appropriation from Congress," says Howard Garrison, director of the office of public affairs of the Federation of American

Societies for Experimental Biology.

The proposed National Science Foundation (NSF) allocation, up about 8% to \$7.4 billion, includes about \$6 billion for core research activities. Two of three programmes aimed specifically at early-career researchers and graduate students would be funded at higher levels under the president's budget proposal. CAREER, the NSF's faculty early-career development programme, which aims to get more young investigators into faculty positions, is up by 6.5% to \$209.2 million, and the Graduate Research Fellowship Program is up by 16.4% to \$158.2 million.

The Department of Energy budget would rise by more than 7% to \$28.4 billion, including a 16% increase to \$370 million for global climate-change research. This and other budget increases could mean significant grant funding opportunities for young investigators who often have the most innovative proposals, says Martin Apple, president of the Council of Scientific Society Presidents.

"If you are a young investigator, there are hundreds of millions of dollars that weren't there before," says Apple.

Karen Kaplan



L. TEDESCHI/IMAGES.COM/CORBIS

PROSPECTS

Salary boost

Negotiating for a pay rise can be a smooth, fruitful process if you follow a few guidelines, says **Deb Koen**.

When it comes to a pay rise, don't expect your superiors to recognize accomplishments without some prompting. Keeping in mind the following steps should help foster the desired outcome.

Make the case

Be on the lookout for opportune times to negotiate a rise — for example, when you have published new results, secured additional funding or noticed that your superior is in a good mood. Having settled on the timing of your request, prepare to make a compelling argument. Frame the request in terms of the value you bring to your employer. Focus on your contributions, including not only specific achievements but also assets that may be overlooked — for example, perhaps you have become the 'go to' scientist for certain areas, or your good humour bolsters the morale of lab mates. If you are a seasoned scientist and valued employee, the costs to recruit and develop your replacement could cost the organization twice your salary.

You may find it useful to prepare a one-page 'highlights' paper that you use as a guide for the conversation.

Anticipate potential responses

Preparing for a variety of outcomes will lead to greater self-assurance in approaching the negotiation. Get an accurate idea of the going rate by checking salaries for comparable roles in and outside your workplace.

If you get an increase, follow up with a brief thank-you note reaffirming your commitment to deliver on performance. If 'maybe', attempt to uncover the underlying objection. Be sure to highlight your contributions, intentions and commitment to the organization.

If a 'no' surfaces, seek feedback on what you can do to position yourself for a rise. Ask for a three-month review. Have a plan B in case you're disappointed. Explore the possibility of additional benefits in lieu of a salary increase (such as new equipment, more holiday, flexible scheduling), and, if all else fails, be ready to network for other job prospects.

Reinforce the relationship

Although negotiation sometimes creates tension, don't lose sight of the ongoing employment relationship. You're looking for a process that will not only advance your agenda but will also preserve or enhance your relationship. Cite your record, your demonstrated commitment and the potential for future contributions.

Make sure that your employer recognizes the value you bring to the organization. If not, you may want to reassess; it may be time to discreetly update your CV. From this point on, keep a record of accomplishments on which you can easily draw to negotiate for future salary increases, prepare for performance appraisals or update your resumé.

Maintain perspective. The discussion doesn't have to be a win-lose encounter but can be a conversation in which you explore options that will benefit both you and your employer.

Deb Koen is president and chief executive of Career Development Services in Rochester, New York.

Q&A

In January, **Zhenrong Zhang** obtained her first faculty position as an assistant professor, at Baylor University in Waco, Texas. She will set up Baylor's first scanning tunnelling microscopy lab.



Did you want to be a scientist from an early age?

To be honest, I never thought I could be a scientist. It seemed so high end. I wanted to go to college for computer science because I thought it would be easier to find a job. Mentors redirected me to the physics department because I was good at it. Even after I started a PhD in China, at the Chinese Academy of Science's Institute of Physics in Beijing, I still was not sure I was going to be a scientist.

The defining moment for me occurred while I was working as a postdoc at the University of Innsbruck in Austria, and was fascinated by the beauty of seeing molecules on the surface of metals using a scanning tunnelling microscopy technique.

What was it about this technique that captured your imagination?

Using scanning tunnelling microscopy, my mentor (Zdenek Dohnalek) at the Pacific Northwest National Laboratory in Richland, Washington, and I developed a methodology to obtain site-specific information at the atomic level in order to learn more about the chemical and physical processes occurring on surfaces. For example, we worked on oxides, such as titanium dioxide, that often have surface defects — reactive sites that can alter chemical reaction rates. Using this technique, we were able to visualize molecules' attraction to the reactive sites. This helped us investigate the dynamics of several reactions important for energy generation and environmental clean-up.

How have you decided to focus your scientific efforts?

I want to connect my research to everyday life somehow. After I went

to Austria, my interest in energy and the environment brought me to a joint postdoc at the Pacific Northwest National Lab and the University of Texas at Austin, where I could focus my research on surface reactions that were important to both energy generation and environmental clean-up. For example, one of our projects was focused on splitting water, in an attempt to find ways to create hydrogen for use as an alternative energy source.

Do you have plans to conduct more applied research?

I do fundamental research. My work won't translate overnight into new energy sources. But it could give rise to the fundamental understanding that provides the guidelines for people to design catalysts that can be used for energy and environmental clean-up.

One of the projects we did at the Pacific Northwest National Lab was to create catalysts that oxidize organic contaminants. In the future, I hope to design catalysts to clean up automotive emissions.

You have just finished that postdoc. Was it a difficult decision not to go back to China?

At the end of the postdoc I had the same pressure as everyone — the need to find a job. I applied for positions in both China and the United States. It was difficult to decide where to go.

I got an offer from one of the best institutes in the Chinese Academy of Sciences, to work with some of the best scientists in the world and be provided with a really good start-up package. I struggled quite a bit over this. Then I got the offer at Baylor University. It came

down to a personal choice.

Baylor attracted me because they put so much emphasis on research and because it is a Christian university. Although I didn't narrow my job search to Christian universities, I feel that the environment Baylor could provide me with is a dream for a scientist and a Christian.

What do you anticipate will be the hardest part of getting the scanning tunnelling microscopy lab up and running?

The hardest part will be physically setting up the space to get optimum performance. The resolution of scanning tunnelling microscope images is extremely sensitive to mechanical and electrical noise. As a result, I have to think about its location and pay extra attention to the selection and operation of the other devices that are necessary to run the apparatus.

Who has been the most influential person in your career?

My previous adviser at the University of Texas, the late Mike White, who had a passion for science. His eyes would sparkle when we had exciting results. I want to be someone like that and feel joyful about what I do.

What has been your biggest challenge to overcome?

I'm a woman and I'm a scientist. I've had two kids in the past five years. Working full time and overtime as a scientist and taking care of young children is a challenge, both physically and emotionally. Luckily, I have support from my husband and mother. ■

Interview by Virginia Gewin

IN BRIEF

Postdocs waltz to Vienna

Announced on 10 February, the Vienna International Post-Graduate Program for Molecular Life Sciences marks a targeted effort to attract young researchers to the city. Based at the Max F. Perutz Laboratories, 18 participants will receive 3–5 years of postdoctoral funding, career-development training and guidance on establishing their own independent research projects and labs. The postdocs will receive an annual salary of around €45,000 (US\$61,000) plus €14,000 for research and travel expenses. The total initial programme funding is €5 million, jointly supported by the city of Vienna and the Austrian Federal Ministry of Science and Research.

Science courses at risk

Science, technology, engineering and maths courses at US public universities and colleges could be imperilled, according to a report on higher-education revenues over the past 25 years. The 11 February report, by the State Higher Education Executive Officers group in Boulder, Colorado, finds that institutions are likely to face a growing budget deficit because of the combined effects of the recession, which has reduced state funding, and a spike in student enrolment. Just 40% of educational revenue is derived from tuition, the report says. "The ability of public colleges and universities to provide quality programmes in science, technology, and other fields is threatened," says Paul Lingenfelter, the group's president.

Biotech beats recession

Despite California's economic woes, its biotech and biomedical industries seem to be thriving. The biotech sector will hire 1,000 clinical scientists, medical lab technicians and medical physicists through a three-year training and placement programme. Funded by a US\$4.95-million federal grant announced on 15 February, it will be administered by San Diego State University and its partners. A 2 February report by the California Healthcare Institute and PricewaterhouseCoopers, which polled 200 of the state's largest biomedical firms, finds promise in that sector too: 81% of firms said that they expect to maintain or expand their local workforce in 2 years. Almost half hope to grow research and development activities in-state by 2011.

Distraction

A fine romance.

Julian Tang

He was there again.

Jenny Landers walked down the steps of the physics lab to where her bicycle was chained, shaking her head and smiling to herself.

It wasn't that he was unattractive, but she wished that he would just come and talk to her.

"Men!" she sighed to herself in exasperation as she bent to unlock her chain, then stood up to put it in her backpack.

"Er, hello," said a quiet, rather nervous male voice from just beside her.

Jenny almost dropped her backpack. Looking up, she was startled to see the subject of her musings.

"Sorry, I didn't mean to give you a fright," he said, self-consciously.

Jenny felt her face getting hot. "Don't worry, it's OK," she began quickly, looking down and fiddling with her pack to allow her to recover some dignity.

He stuck his hand out. "We haven't met. My name's Jeremy — Jeremy Maitland," he started. Then as an afterthought, "I'm an English major here."

Jenny, not knowing what else to do, allowed social etiquette to kick in and shook his hand, firmly. "Jenny Landers, physics PhD, at your service," she laughed, finally breaking the ice.

"Want to go for a drink?" he asked hesitantly. "I've wanted to talk to you for some time, but didn't know how to, um, approach you."

Jenny grinned in relief. "Sure!"

They ended up in one of the local student hang-outs, finding a seat in a quiet corner.

"So, er, what shall I get you?"

Jenny didn't normally drink much, but tonight, she would make an exception. "What about half a cider?"

Jeremy nodded, smiling nervously, and moved off to join the queue at the bar.

Jenny watched him go, curiously. Although he seemed nervous with her, he moved in a sure and assertive manner. He quickly got the attention of the bartender and came back with a pint of draught for himself, her cider and a bag of corn chips.

"So, what area of research are you in?" asked Jeremy, finally, when the silence became awkward.

"Well," she paused, looking into her glass. "My research is in astrophysics, specifically to look for unusual radio-frequency sources from deep space ..."

"You mean like SETI?" he interrupted, excitedly.

"Yes!" she exclaimed, looking at him, incredulously.

Jeremy continued, speculating. "It seems an impossible task. I mean, from what little I've read, you need to search in multiple directions at multiple wavelengths. From a point source, like Earth on the galactic scale, you cannot cover every angle and the possible number of wavelengths is equally vast." As he finished, Jeremy was staring into the distance, as though his mind were elsewhere.

Jenny couldn't take her eyes off him.

And that was that.



They became a couple soon after, were married a few years later and had triplets — at which point Jenny gave up her lifelong dream of joining the SETI Institute to become a full-time mother. Jeremy showed an amazing talent for predicting stock-market trends and became a very successful investment manager. They lived a long and happy life, with many grandchildren.

Later, as Jeremy lay on his death-bed at the ripe old age of 77, Jenny, still spry at 80, sat quietly beside him, holding his hand.

"We had a good life together, didn't we, Jen?" Jeremy whispered.

The cancer had spread throughout his body. They knew he didn't have long now.

With tears in her eyes, Jenny squeezed his hand. "We did OK."

After a short pause, he asked: "You don't regret giving up your dreams of SETI — even just a little bit?"

Jenny waited a little, before replying. She knew she couldn't lie to him to make him feel better, even now. He would know. "Yes,

a little, I guess — but having children is a worthy substitute, my love."

He held her gaze for a while then nodded. He wanted her to know that he understood what she had sacrificed.

The funeral was a simple affair, just family and close friends. Jenny lingered a little longer at the grave as her children waited respectfully a short distance away, then eventually, she left too.

That night, Jenny would have been intrigued and amazed to see Jeremy's body start to glow brightly in the elegant coffin as the clothes in which he was buried began to vaporize. Then the substance of Jeremy's body shimmered briefly before vanishing.

Moments later, Jeremy Maitland was hovering in deep space, with others of his kind.

Your mission was much ... longer than expected.

Yes, but this way ... this distraction ... was kinder — the same ends were achieved.

Are you sure?

There was a pause, as if his peers were conferring, or perhaps ... *sensing*.

About the same time, on Earth, Elena, one of Jenny Lander's youngest granddaughters was sitting at her grandmother's desk PC, looking through university websites, trying to decide which course she wanted to do and where. Looking up from the

screen for a moment, she spotted one of her grandmother's old box-files, marked 'SETI' on one of the upper shelves. Curious, she took it down and started looking inside.

After a few minutes, Jenny walked into the study. "You know, something, Elena," she began, after watching her thoughtfully for a few minutes. "I have some ideas about that project that I haven't told to a soul in over 60 years! Want to hear them?"

Elena looked up, her eyes bright with interest and nodded.

Back in deep space, the *sensing* came to an end. Without any need for further communication, he started on his return journey to Earth.

Julian Tang is a clinical/academic virologist. Like SETI members, he also believes that ET is out there somewhere, but may not want to be found — at least, not yet ...

Join the discussion of Futures in Nature at go.nature.com/QMAM2a

JACEY

Location of corneal epithelial stem cells

Arising from: Majo, F., Rochat, A., Nicolas, M., Jaoude, G. A. & Barrandon, Y. *Nature* **456**, 250–254 (2008).

The longstanding concept that corneal epithelial stem cells reside mainly in the limbus is supported by the absence of major corneal epithelial differentiation markers, that is, K3 and K12 keratins, in limbal basal cells (these markers are expressed, however, in corneal basal cells, thus distinguishing the mode of keratin expression in corneal epithelium from that of all other stratified epithelia), the centripetal migration of corneal epithelial cells, the exclusive location of slow-cycling cells in the limbal basal layer, the superior *in vitro* proliferative potential of limbal epithelial cells, and the transplanted limbal cells' ability to reconstitute corneal epithelium *in vivo* (reviewed in refs 1–4). Moreover, previous data indicate that corneal and conjunctival epithelia represent two separate cell lineages (reviewed in refs 1–4). Majo *et al.*⁵ suggested, however, that corneal and conjunctival epithelia are equipotent, and that identical oligopotent stem cells are present throughout the corneal, limbal and conjunctival epithelia. We point out here that these suggestions are inconsistent with many known growth, differentiation and cell migration properties of the anterior ocular epithelia.

Majo *et al.* suggested that corneal and conjunctival stem cells are equipotent because corneal epithelial cells could form goblet cells, and because cultured (thus somewhat 'de-differentiated') pig corneal and conjunctival cells shared a similar phenotype⁵. They may have overlooked, however, reports showing that cultured rabbit corneal/limbal epithelial cells, but not conjunctival cells, expressed K3/K12 keratins^{6–8}; conversely, conjunctival epithelial cells, but not corneal cells, formed goblet cells when transplanted into athymic mice^{8,9}. Similar phenotypic specificity was preserved in cultured human limbal/corneal and conjunctival cells¹⁰. Moreover, human and rabbit studies showed that limbal epithelial cells, but not conjunctival cells, could restore a true corneal epithelium (reviewed in ref. 4). These data have established that limbal/corneal and conjunctival epithelia are not equipotent and that they represent two distinct cell lineages governed by their own stem cells (reviewed in refs 4, 9 and 10).

Majo *et al.* suggested that corneal epithelium contained stem cells because corneal epithelium gave rise to large colonies, serially transplanted mouse central corneal epithelium could regenerate, and transplanted mouse limbal cells did not migrate centripetally⁵. Although their data showed that some pig corneal cells have significant proliferative potential, this property is not unique to stem cells: some transit amplifying cells such as hair matrix are known to be able to divide numerous times. Hence, a more meaningful test is to compare the growth potential of corneal and limbal cells by serially passaging them under identical culture conditions. Such studies have established that rabbit and human limbal cells have a much greater proliferative capacity than corneal cells^{7,10}. Moreover, Majo *et al.*'s data (see figure 3b in ref. 5) showed that although corneal cells of rabbit, pig and sheep grew well in primary culture, those of human¹⁰ and calf did not. Such a major species variation argues against the idea that corneal epithelium contains stem cells (which, if they exist, cannot be slow-cycling given that they are undetectable as label-retaining cells²). Regarding the ability of corneal epithelium to self-sustain, Huang and Tseng showed that, after limbal removal, rabbit central corneal epithelium can remain apparently intact for a long time until it is wounded, indicating that central corneal cells have a significant maintenance potential until it is perturbed¹¹. Finally, Majo *et al.*'s negative finding that limbal cells do not migrate centripetally contradicts many reports establishing that, in intact human¹² and mouse eyes^{13,14} (that have not been surgically manipulated) corneal

epithelial cells undergo centripetal migration. Collectively, the existing data strongly suggest that corneal epithelial stem cells reside mainly, if not exclusively, in the limbus.

Finally, Majo *et al.*'s model hypothesized that both corneal and conjunctival epithelial cells migrated towards the limbus (the 'tectonic plate confrontation model'). They may have overlooked, however, several reports showing that conjunctival cells do not migrate¹⁵, while corneal cells undergo centripetal, rather than centrifugal, migration^{12–14}. We conclude that this model, which suggests (1) that corneal and conjunctival epithelia are equipotent, (2) that identical oligopotent stem cells are distributed throughout the anterior ocular surface epithelium including the central corneal epithelium, and (3) that corneal and conjunctival epithelial cells migrate towards the limbus, is incompatible with existing data.

Tung-Tien Sun¹, Scheffer C. Tseng² & Robert M. Lavker³

¹Departments of Cell Biology, Dermatology, Pharmacology and Urology, New York University School of Medicine, New York, New York 10016, USA.

e-mail: sunt01@nyumc.org

²Department of Tissue Technology, Ocular Surface Center, Ocular Surface Research and Education Foundation, Miami, Florida 33173, USA.

³Department of Dermatology, Northwestern University, Feinberg School of Medicine, Chicago, Illinois 60611, USA.

Received 24 January 2009; accepted 19 November 2009.

1. Schermer, A., Galvin, S. & Sun, T. T. Differentiation-related expression of a major 64K corneal keratin *in vivo* and in culture suggests limbal location of corneal epithelial stem cells. *J. Cell Biol.* **103**, 49–62 (1986).
2. Cotsarelis, G., Cheng, S. Z., Dong, G., Sun, T. T. & Lavker, R. M. Existence of slow-cycling limbal epithelial basal cells that can be preferentially stimulated to proliferate: implications on epithelial stem cells. *Cell* **57**, 201–209 (1989).
3. Kenyon, K. R. & Tseng, S. C. Limbal autograft transplantation for ocular surface disorders. *Ophthalmology* **96** (5), 709–722; discussion 722–723 (1989).
4. Lavker, R. M., Tseng, S. C. & Sun, T. T. Corneal epithelial stem cells at the limbus: looking at some old problems from a new angle. *Exp. Eye Res.* **78**, 433–446 (2004).
5. Majo, F., Rochat, A., Nicolas, M., Jaoude, G. A. & Barrandon, Y. Oligopotent stem cells are distributed throughout the mammalian ocular surface. *Nature* **456**, 250–254 (2008).
6. Sun, T.-T. & Green, H. Cultured epithelial cells of cornea, conjunctiva and skin: absence of marked intrinsic divergence of their differentiated states. *Nature* **269**, 489–493 (1977).
7. Wei, Z. G., Wu, R. L., Lavker, R. M. & Sun, T. T. *In vitro* growth and differentiation of rabbit bulbar, fornix, and palpebral conjunctival epithelia. Implications on conjunctival epithelial transdifferentiation and stem cells. *Invest. Ophthalmol. Vis. Sci.* **34**, 1814–1828 (1993).
8. Doran, T. I., Vidrich, A. & Sun, T.-T. Intrinsic and extrinsic regulation of the differentiation of skin, corneal and esophageal epithelial cells. *Cell* **22**, 17–25 (1980).
9. Wei, Z. G., Sun, T. T. & Lavker, R. M. Rabbit conjunctival and corneal epithelial cells belong to two separate lineages. *Invest. Ophthalmol. Vis. Sci.* **37**, 523–533 (1996).
10. Pellegrini, G. *et al.* Location and clonal analysis of stem cells and their differentiated progeny in the human ocular surface. *J. Cell Biol.* **145**, 769–782 (1999).
11. Huang, A. J. & Tseng, S. C. Corneal epithelial wound healing in the absence of limbal epithelium. *Invest. Ophthalmol. Vis. Sci.* **32**, 96–105 (1991).
12. Auran, J. D. *et al.* Scanning slit confocal microscopic observation of cell morphology and movement within the normal human anterior cornea. *Ophthalmology* **102**, 33–41 (1995).
13. Collinson, J. M. *et al.* Clonal analysis of patterns of growth, stem cell activity, and cell movement during the development and maintenance of the murine corneal epithelium. *Dev. Dyn.* **224**, 432–440 (2002).
14. Nagasaki, T. & Zhao, J. Centripetal movement of corneal epithelial cells in the normal adult mouse. *Invest. Ophthalmol. Vis. Sci.* **44**, 558–566 (2003).
15. Nagasaki, T. & Zhao, J. Uniform distribution of epithelial stem cells in the bulbar conjunctiva. *Invest. Ophthalmol. Vis. Sci.* **46**, 126–132 (2005).

Competing financial interests: declared none.

doi:10.1038/nature08805

Majo et al. reply

Replying to: T.-T. Sun, S. C. Tseng & R. M. Lavker *Nature* **463**, doi:10.1038/nature08805 (2010)

Our claim is not that there are no stem cells in the limbus, but that there is more to corneal renewal than the limbus and that the double-dome-shaped structure of the cornea and physical constraints have a crucial impact on cell dynamics¹.

Sun and colleagues² imply that in our paper³ we misused the term 'holoclones' that we defined as stem cells⁴; the central cornea of the pig contains numerous true holoclones, meaning that the cornea of the pig has extensive growth potential and the ability to be serially passaged *in vitro*. We agree that there are species differences among mammals; nonetheless, all corneas that we have investigated, including calf and human, contain colony-forming cells. Fifty cell doublings in pig cornea is not trivial and contradicts the model proposed by Sun and colleagues⁵; we quote their abstract "we demonstrate the existence of a hierarchy of TA cells; those of peripheral cornea undergo at least two rounds of DNA synthesis before they become post-mitotic, whereas those of central cornea are capable of only one round of division". It also does not agree with Huang and Tseng's experiment⁶ showing "that, after limbal removal, rabbit central corneal epithelium can remain apparently intact for a long time until it is wounded, indicating that central cornea cells have a significant maintenance potential".

Our results show that corneal cells can form goblet cells when they migrate onto a conjunctival environment (in mouse) or generate true goblet cell colonies when cloned (in pig). Corneal differentiation is found in human conjunctiva⁷, conjunctival cells may be successfully transplanted in the human to replace cornea⁸, and there are reports of cornea remaining transparent for years in limbal deficiency⁹. Furthermore, corneal cells¹⁰, like conjunctival cells (our unpublished results), can form hairy skin when exposed to an inductive skin microenvironment, indicating a greater plasticity than anticipated and that stem cell fate strongly depends on stromal signals.

We are not aware of any paper that clearly demonstrates stem cell migration from the limbus. Buck¹¹ in his landmark paper has not demonstrated basal cell migration; we quote his abstract: "the median distance migrated was about 17 μ m per day. This figure represents the distance through which superficial and wing cells had migrated; the distance migrated by basal cells was not determined". Nagasaki and Zhao¹² have presented evidence of movement in the cornea but not that the migrating cells actually originated from the limbus ('from' is not the same as 'near'). An overcrowding of the corneal epithelium, a source of tension and sliding as previously emphasized by Sun and colleagues¹³, or sequential activation of the β -actin promoter can easily explain these observations. Similarly, the spiral stripe organization mixing clockwise and counterclockwise clones¹⁴ is highly reminiscent of centrifugal growth originating from a small number of stem cells originally located in central cornea. This biological model occurs widely in nature, for instance in the growth of a daisy, as the easiest and

most efficient way to fill space, a notion supported by mathematical models¹⁵ and a clothoid growth model (Euler spiral).

François Majo¹, Ariane Rochat^{2,3}, Michael Nicolas¹, Georges Abou Jaoudé⁴ & Yann Barrandon^{2,3}

¹Hôpital Ophtalmique Jules Gonin, Avenue de France 15, 1004 Lausanne CH, Switzerland.

²Department of Experimental Surgery Lausanne University Hospital (CHUV), 1011 Lausanne CH, Switzerland.

³Laboratory of Stem Cell Dynamics, Ecole Polytechnique Fédérale de Lausanne (EPFL), 1015 Lausanne CH, Switzerland.

e-mail: yann.barrandon@epfl.ch

⁴Laboratory of Informatics and Visualization, Ecole Polytechnique Fédérale de Lausanne (EPFL), 1015 Lausanne CH, Switzerland.

- Dupps, W. J. Jr & Wilson, S. E. Biomechanics and wound healing in the cornea. *Exp. Eye Res.* **83**, 709–720 (2006).
- Sun, T.-T., Tseng, S. C. & Lavker, R. M. Location of corneal epithelial stem cells. *Nature* **463**, doi:10.1038/nature08805 (2010).
- Majo, F., Rochat, A., Nicolas, M., Jaoude, G. A. & Barrandon, Y. Oligopotent stem cells are distributed throughout the mammalian ocular surface. *Nature* **456**, 250–254 (2008).
- Barrandon, Y. & Green, H. Three clonal types of keratinocyte with different capacities for multiplication. *Proc. Natl Acad. Sci. USA* **84**, 2302–2306 (1987).
- Lehrer, M. S., Sun, T. T. & Lavker, R. M. Strategies of epithelial repair: modulation of stem cell and transit amplifying cell proliferation. *J. Cell Sci.* **111**, 2867–2875 (1998).
- Huang, A. J. & Tseng, S. C. Corneal epithelial wound healing in the absence of limbal epithelium. *Invest. Ophthalmol. Vis. Sci.* **32**, 96–105 (1991).
- Kawasaki, S. et al. Clusters of corneal epithelial cells reside ectopically in human conjunctival epithelium. *Invest. Ophthalmol. Vis. Sci.* **47**, 1359–1367 (2006).
- Di Girolamo, N. et al. A contact lens-based technique for expansion and transplantation of autologous epithelial progenitors for ocular surface reconstruction. *Transplantation* **87**, 1571–1578 (2009).
- Dua, H. S., Miri, A., Alomar, T., Yeung, A. M. & Said, D. G. The role of limbal stem cells in corneal epithelial maintenance: testing the dogma. *Ophthalmology* **116**, 856–863 (2009).
- Ferraris, C., Chevalier, G., Favier, B., Jahoda, C. A. & Dhoubilly, D. Adult corneal epithelium basal cells possess the capacity to activate epidermal, pilosebaceous and sweat gland genetic programs in response to embryonic dermal stimuli. *Development* **127**, 5487–5495 (2000).
- Buck, R. C. Measurement of centripetal migration of normal corneal epithelial cells in the mouse. *Invest. Ophthalmol. Vis. Sci.* **26**, 1296–1299 (1985).
- Nagasaki, T. & Zhao, J. Centripetal movement of corneal epithelial cells in the normal adult mouse. *Invest. Ophthalmol. Vis. Sci.* **44**, 558–566 (2003).
- Lavker, R. M. et al. Relative proliferative rates of limbal and corneal epithelia. Implications of corneal epithelial migration, circadian rhythm, and suprabasally located DNA-synthesizing keratinocytes. *Invest. Ophthalmol. Vis. Sci.* **32**, 1864–1875 (1991).
- Collinson, J. M. et al. Clonal analysis of patterns of growth, stem cell activity, and cell movement during the development and maintenance of the murine corneal epithelium. *Dev. Dyn.* **224**, 432–440 (2002).
- Stewart, I. Mathematical recreations: Daisy, Daisy, give me your answer, do. *Sci. Am.* **272**, 96–99 (1995).

Competing financial interests: declared none.

doi:10.1038/nature08806

Location of corneal epithelial stem cells

Arising from: Majo, F., Rochat, A., Nicolas, M., Jaoude, G. A. & Barrandon, Y. *Nature* **456**, 250–254 (2008).

The longstanding concept that corneal epithelial stem cells reside mainly in the limbus is supported by the absence of major corneal epithelial differentiation markers, that is, K3 and K12 keratins, in limbal basal cells (these markers are expressed, however, in corneal basal cells, thus distinguishing the mode of keratin expression in corneal epithelium from that of all other stratified epithelia), the centripetal migration of corneal epithelial cells, the exclusive location of slow-cycling cells in the limbal basal layer, the superior *in vitro* proliferative potential of limbal epithelial cells, and the transplanted limbal cells' ability to reconstitute corneal epithelium *in vivo* (reviewed in refs 1–4). Moreover, previous data indicate that corneal and conjunctival epithelia represent two separate cell lineages (reviewed in refs 1–4). Majo *et al.*⁵ suggested, however, that corneal and conjunctival epithelia are equipotent, and that identical oligopotent stem cells are present throughout the corneal, limbal and conjunctival epithelia. We point out here that these suggestions are inconsistent with many known growth, differentiation and cell migration properties of the anterior ocular epithelia.

Majo *et al.* suggested that corneal and conjunctival stem cells are equipotent because corneal epithelial cells could form goblet cells, and because cultured (thus somewhat 'de-differentiated') pig corneal and conjunctival cells shared a similar phenotype⁵. They may have overlooked, however, reports showing that cultured rabbit corneal/limbal epithelial cells, but not conjunctival cells, expressed K3/K12 keratins^{6–8}; conversely, conjunctival epithelial cells, but not corneal cells, formed goblet cells when transplanted into athymic mice^{8,9}. Similar phenotypic specificity was preserved in cultured human limbal/corneal and conjunctival cells¹⁰. Moreover, human and rabbit studies showed that limbal epithelial cells, but not conjunctival cells, could restore a true corneal epithelium (reviewed in ref. 4). These data have established that limbal/corneal and conjunctival epithelia are not equipotent and that they represent two distinct cell lineages governed by their own stem cells (reviewed in refs 4, 9 and 10).

Majo *et al.* suggested that corneal epithelium contained stem cells because corneal epithelium gave rise to large colonies, serially transplanted mouse central corneal epithelium could regenerate, and transplanted mouse limbal cells did not migrate centripetally⁵. Although their data showed that some pig corneal cells have significant proliferative potential, this property is not unique to stem cells: some transit amplifying cells such as hair matrix are known to be able to divide numerous times. Hence, a more meaningful test is to compare the growth potential of corneal and limbal cells by serially passaging them under identical culture conditions. Such studies have established that rabbit and human limbal cells have a much greater proliferative capacity than corneal cells^{7,10}. Moreover, Majo *et al.*'s data (see figure 3b in ref. 5) showed that although corneal cells of rabbit, pig and sheep grew well in primary culture, those of human¹⁰ and calf did not. Such a major species variation argues against the idea that corneal epithelium contains stem cells (which, if they exist, cannot be slow-cycling given that they are undetectable as label-retaining cells²). Regarding the ability of corneal epithelium to self-sustain, Huang and Tseng showed that, after limbal removal, rabbit central corneal epithelium can remain apparently intact for a long time until it is wounded, indicating that central corneal cells have a significant maintenance potential until it is perturbed¹¹. Finally, Majo *et al.*'s negative finding that limbal cells do not migrate centripetally contradicts many reports establishing that, in intact human¹² and mouse eyes^{13,14} (that have not been surgically manipulated) corneal

epithelial cells undergo centripetal migration. Collectively, the existing data strongly suggest that corneal epithelial stem cells reside mainly, if not exclusively, in the limbus.

Finally, Majo *et al.*'s model hypothesized that both corneal and conjunctival epithelial cells migrated towards the limbus (the 'tectonic plate confrontation model'). They may have overlooked, however, several reports showing that conjunctival cells do not migrate¹⁵, while corneal cells undergo centripetal, rather than centrifugal, migration^{12–14}. We conclude that this model, which suggests (1) that corneal and conjunctival epithelia are equipotent, (2) that identical oligopotent stem cells are distributed throughout the anterior ocular surface epithelium including the central corneal epithelium, and (3) that corneal and conjunctival epithelial cells migrate towards the limbus, is incompatible with existing data.

Tung-Tien Sun¹, Scheffer C. Tseng² & Robert M. Lavker³

¹Departments of Cell Biology, Dermatology, Pharmacology and Urology, New York University School of Medicine, New York, New York 10016, USA.

e-mail: sunt01@nyumc.org

²Department of Tissue Technology, Ocular Surface Center, Ocular Surface Research and Education Foundation, Miami, Florida 33173, USA.

³Department of Dermatology, Northwestern University, Feinberg School of Medicine, Chicago, Illinois 60611, USA.

Received 24 January 2009; accepted 19 November 2009.

1. Schermer, A., Galvin, S. & Sun, T. T. Differentiation-related expression of a major 64K corneal keratin *in vivo* and in culture suggests limbal location of corneal epithelial stem cells. *J. Cell Biol.* **103**, 49–62 (1986).
2. Cotsarelis, G., Cheng, S. Z., Dong, G., Sun, T. T. & Lavker, R. M. Existence of slow-cycling limbal epithelial basal cells that can be preferentially stimulated to proliferate: implications on epithelial stem cells. *Cell* **57**, 201–209 (1989).
3. Kenyon, K. R. & Tseng, S. C. Limbal autograft transplantation for ocular surface disorders. *Ophthalmology* **96** (5), 709–722; discussion 722–723 (1989).
4. Lavker, R. M., Tseng, S. C. & Sun, T. T. Corneal epithelial stem cells at the limbus: looking at some old problems from a new angle. *Exp. Eye Res.* **78**, 433–446 (2004).
5. Majo, F., Rochat, A., Nicolas, M., Jaoude, G. A. & Barrandon, Y. Oligopotent stem cells are distributed throughout the mammalian ocular surface. *Nature* **456**, 250–254 (2008).
6. Sun, T.-T. & Green, H. Cultured epithelial cells of cornea, conjunctiva and skin: absence of marked intrinsic divergence of their differentiated states. *Nature* **269**, 489–493 (1977).
7. Wei, Z. G., Wu, R. L., Lavker, R. M. & Sun, T. T. *In vitro* growth and differentiation of rabbit bulbar, fornix, and palpebral conjunctival epithelia. Implications on conjunctival epithelial transdifferentiation and stem cells. *Invest. Ophthalmol. Vis. Sci.* **34**, 1814–1828 (1993).
8. Doran, T. I., Vidrich, A. & Sun, T.-T. Intrinsic and extrinsic regulation of the differentiation of skin, corneal and esophageal epithelial cells. *Cell* **22**, 17–25 (1980).
9. Wei, Z. G., Sun, T. T. & Lavker, R. M. Rabbit conjunctival and corneal epithelial cells belong to two separate lineages. *Invest. Ophthalmol. Vis. Sci.* **37**, 523–533 (1996).
10. Pellegrini, G. *et al.* Location and clonal analysis of stem cells and their differentiated progeny in the human ocular surface. *J. Cell Biol.* **145**, 769–782 (1999).
11. Huang, A. J. & Tseng, S. C. Corneal epithelial wound healing in the absence of limbal epithelium. *Invest. Ophthalmol. Vis. Sci.* **32**, 96–105 (1991).
12. Auran, J. D. *et al.* Scanning slit confocal microscopic observation of cell morphology and movement within the normal human anterior cornea. *Ophthalmology* **102**, 33–41 (1995).
13. Collinson, J. M. *et al.* Clonal analysis of patterns of growth, stem cell activity, and cell movement during the development and maintenance of the murine corneal epithelium. *Dev. Dyn.* **224**, 432–440 (2002).
14. Nagasaki, T. & Zhao, J. Centripetal movement of corneal epithelial cells in the normal adult mouse. *Invest. Ophthalmol. Vis. Sci.* **44**, 558–566 (2003).
15. Nagasaki, T. & Zhao, J. Uniform distribution of epithelial stem cells in the bulbar conjunctiva. *Invest. Ophthalmol. Vis. Sci.* **46**, 126–132 (2005).

Competing financial interests: declared none.

doi:10.1038/nature08805

Majo et al. reply

Replying to: T.-T. Sun, S. C. Tseng & R. M. Lavker *Nature* **463**, doi:10.1038/nature08805 (2010)

Our claim is not that there are no stem cells in the limbus, but that there is more to corneal renewal than the limbus and that the double-dome-shaped structure of the cornea and physical constraints have a crucial impact on cell dynamics¹.

Sun and colleagues² imply that in our paper³ we misused the term 'holoclones' that we defined as stem cells⁴; the central cornea of the pig contains numerous true holoclones, meaning that the cornea of the pig has extensive growth potential and the ability to be serially passaged *in vitro*. We agree that there are species differences among mammals; nonetheless, all corneas that we have investigated, including calf and human, contain colony-forming cells. Fifty cell doublings in pig cornea is not trivial and contradicts the model proposed by Sun and colleagues⁵; we quote their abstract "we demonstrate the existence of a hierarchy of TA cells; those of peripheral cornea undergo at least two rounds of DNA synthesis before they become post-mitotic, whereas those of central cornea are capable of only one round of division". It also does not agree with Huang and Tseng's experiment⁶ showing "that, after limbal removal, rabbit central corneal epithelium can remain apparently intact for a long time until it is wounded, indicating that central cornea cells have a significant maintenance potential".

Our results show that corneal cells can form goblet cells when they migrate onto a conjunctival environment (in mouse) or generate true goblet cell colonies when cloned (in pig). Corneal differentiation is found in human conjunctiva⁷, conjunctival cells may be successfully transplanted in the human to replace cornea⁸, and there are reports of cornea remaining transparent for years in limbal deficiency⁹. Furthermore, corneal cells¹⁰, like conjunctival cells (our unpublished results), can form hairy skin when exposed to an inductive skin microenvironment, indicating a greater plasticity than anticipated and that stem cell fate strongly depends on stromal signals.

We are not aware of any paper that clearly demonstrates stem cell migration from the limbus. Buck¹¹ in his landmark paper has not demonstrated basal cell migration; we quote his abstract: "the median distance migrated was about 17 μ m per day. This figure represents the distance through which superficial and wing cells had migrated; the distance migrated by basal cells was not determined". Nagasaki and Zhao¹² have presented evidence of movement in the cornea but not that the migrating cells actually originated from the limbus ('from' is not the same as 'near'). An overcrowding of the corneal epithelium, a source of tension and sliding as previously emphasized by Sun and colleagues¹³, or sequential activation of the β -actin promoter can easily explain these observations. Similarly, the spiral stripe organization mixing clockwise and counterclockwise clones¹⁴ is highly reminiscent of centrifugal growth originating from a small number of stem cells originally located in central cornea. This biological model occurs widely in nature, for instance in the growth of a daisy, as the easiest and

most efficient way to fill space, a notion supported by mathematical models¹⁵ and a clothoid growth model (Euler spiral).

François Majo¹, Ariane Rochat^{2,3}, Michael Nicolas¹, Georges Abou Jaoudé⁴ & Yann Barrandon^{2,3}

¹Hôpital Ophtalmique Jules Gonin, Avenue de France 15, 1004 Lausanne CH, Switzerland.

²Department of Experimental Surgery Lausanne University Hospital (CHUV), 1011 Lausanne CH, Switzerland.

³Laboratory of Stem Cell Dynamics, Ecole Polytechnique Fédérale de Lausanne (EPFL), 1015 Lausanne CH, Switzerland.

e-mail: yann.barrandon@epfl.ch

⁴Laboratory of Informatics and Visualization, Ecole Polytechnique Fédérale de Lausanne (EPFL), 1015 Lausanne CH, Switzerland.

1. Dupps, W. J. Jr & Wilson, S. E. Biomechanics and wound healing in the cornea. *Exp. Eye Res.* **83**, 709–720 (2006).
2. Sun, T.-T., Tseng, S. C. & Lavker, R. M. Location of corneal epithelial stem cells. *Nature* **463**, doi:10.1038/nature08805 (2010).
3. Majo, F., Rochat, A., Nicolas, M., Jaoude, G. A. & Barrandon, Y. Oligopotent stem cells are distributed throughout the mammalian ocular surface. *Nature* **456**, 250–254 (2008).
4. Barrandon, Y. & Green, H. Three clonal types of keratinocyte with different capacities for multiplication. *Proc. Natl Acad. Sci. USA* **84**, 2302–2306 (1987).
5. Lehrer, M. S., Sun, T. T. & Lavker, R. M. Strategies of epithelial repair: modulation of stem cell and transit amplifying cell proliferation. *J. Cell Sci.* **111**, 2867–2875 (1998).
6. Huang, A. J. & Tseng, S. C. Corneal epithelial wound healing in the absence of limbal epithelium. *Invest. Ophthalmol. Vis. Sci.* **32**, 96–105 (1991).
7. Kawasaki, S. et al. Clusters of corneal epithelial cells reside ectopically in human conjunctival epithelium. *Invest. Ophthalmol. Vis. Sci.* **47**, 1359–1367 (2006).
8. Di Girolamo, N. et al. A contact lens-based technique for expansion and transplantation of autologous epithelial progenitors for ocular surface reconstruction. *Transplantation* **87**, 1571–1578 (2009).
9. Dua, H. S., Miri, A., Alomar, T., Yeung, A. M. & Said, D. G. The role of limbal stem cells in corneal epithelial maintenance: testing the dogma. *Ophthalmology* **116**, 856–863 (2009).
10. Ferraris, C., Chevalier, G., Favier, B., Jahoda, C. A. & Dhoubilly, D. Adult corneal epithelium basal cells possess the capacity to activate epidermal, pilosebaceous and sweat gland genetic programs in response to embryonic dermal stimuli. *Development* **127**, 5487–5495 (2000).
11. Buck, R. C. Measurement of centripetal migration of normal corneal epithelial cells in the mouse. *Invest. Ophthalmol. Vis. Sci.* **26**, 1296–1299 (1985).
12. Nagasaki, T. & Zhao, J. Centripetal movement of corneal epithelial cells in the normal adult mouse. *Invest. Ophthalmol. Vis. Sci.* **44**, 558–566 (2003).
13. Lavker, R. M. et al. Relative proliferative rates of limbal and corneal epithelia. Implications of corneal epithelial migration, circadian rhythm, and suprabasally located DNA-synthesizing keratinocytes. *Invest. Ophthalmol. Vis. Sci.* **32**, 1864–1875 (1991).
14. Collinson, J. M. et al. Clonal analysis of patterns of growth, stem cell activity, and cell movement during the development and maintenance of the murine corneal epithelium. *Dev. Dyn.* **224**, 432–440 (2002).
15. Stewart, I. Mathematical recreations: Daisy, Daisy, give me your answer, do. *Sci. Am.* **272**, 96–99 (1995).

Competing financial interests: declared none.

doi:10.1038/nature08806